The Strain Manipulation of Nickel and Permalloy Spin Valves

Mohammed Salim Humaid Al-Qayoudhi

School of Physics and Astronomy

University of Nottingham

This dissertation is submitted for the degree of

Doctor of Philosophy

July 2020

Acknowledgements

This study would not have been possible without the guidance and supervision of Dr Andrew Rushforth, to whom I offer tremendous thanks for his commitment, patience, support, encouragement, great discussions, and caring for every detail from my first day throughout my PhD. I would also like to thank my supervisor Dr Kevin Edmonds for his excellent supervision.

Special thanks go to Dr Staurt Cavil from York University for his collaboration for the FMR measurements, and sincere appreciation to Dr Debi Pattnaik for his discussion and support with the magnetotransport system, Dr Mu Wang for the SQUID training, Syamashree Roy for helping with sputtering and experiments, and Oliver Amin for MATLAB discussion. I would like to express my gratitude to the many support staff in the School of Physics, starting with the cleanroom team, Jas Chauhan for his great support on fabrication, David Taylor for the fabrication training, and Natalia Alexeeva for always being helpful. I also wish to thank all staff from the Electronic and Mechanical Workshop, the Cryogenic Team, and Mike Parker for his IT support. I also wish to show my gratitude to Dr Richard Cousins for his time with the calibration of EBL fabrication of nanowires. I would like to express my deep thanks to all people in the spintronic group, Prof Bryan Gallagher, Dr Richard Campion, Dr Peter Wadely, Dr Khalid Omari. Special acknowledgements go to the past and present members of room C26 for great life discussion, fun, wonderful coffee and tea time, Dr Duncan Parkes (for the first tour in the physics building!), Dr Stuart Bowe, Luke Barton (the best coffee maker), Stuart Poole, Alex Lewis, Sonka Riemers, and Sam Parker. Very special thanks go to BROS WhatsApp group members for the motivation and fun: Carl Andrews, Michal Grzybowski, and Srikanth Reddy.

I would like to take the opportunity to express my gratitude to the Omani Ministry of Higher Education for the scholarship and financial support they awarded me, and special thanks to staff from the Omani Embassy in London for their help and kindness. I dedicated this work to my mother for her tremendous love and to my father, who could not be with us at the end of this work. This work could not be accomplished without the continuous support of my beloved wife and for keeping my spirit up always. Thank you to my lovely children, Salim and Reema, for a wonderful time in Nottingham and the joy around me. Finally, I want to express my gratitude to my sisters and brothers for continuous support throughout my PhD.

Abstract

In spintronics devices, the manipulation of magnetisation in magnetic films and spin valves can play a crucial role in the development of novel technologies. The usage of strain-induced anisotropy utilised in spintronics devices can devise new methods for low-power storage and logic devices. One of these methods is using a multiferroic device to introduce strain throughout the magnetic materials. In this study, strain induced in ferromagnetic layers is accomplished by using a hybrid structure of piezoelectric transducer/ magnetic multi or single layers. The main aim of this thesis is to study the strain effect on the magnetisation and magnetic reversal of spin valves consisting of permalloy and nickel layers (with different magnetostriction values and sign) through the strain-induced magnetoelastic coupling.

Initially, this thesis examines the role of the strain on single layers of microdevices of sputtered permalloy ($Ni_{80}Fe_{20}$) and nickel layers using magnetotransport measurements. Varying strain in the permalloy sample rotates the magnetisation by 90^o when varying the strain between tensile and compressive. The induced magnetic anisotropy modulates the magnetic properties of the permalloy sample, particularly the anisotropic magnetoresistance (AMR), switching field, magnetic reversal, and remanent magnetisation. The coherent rotation model enables calculation of magnetic anisotropy as a function of applied voltage, showing positive magnetostriction of the permalloy layer, possibly enhanced by surface anisotropy, which shows dominance at low thickness. The stoichiometry divergence from 20:80 ratio might also explain the magnetostriction boost. The nickel layer under strain effect showed zero magnetostriction, which might be due to the critical thickness at which there is an inversion of the value of magnetostriction between positive and negative value.

Spin valves with incorporated IrMn layers, S548 (PZT/Cr/NiFe/Cr/Ni/IrMn/Cr), and S549 (PZT/Cr/Ni/Cr/NiFe/IrMn/Cr) were investigated under varying voltages through the transducer. The permalloy in these spin valves shows positive magnetostriction in S548, but no effect in S549, as the permalloy is coupled partially to the IrMn layer, while the nickel exhibited zero

magnetostriction, similar to that in single layer sample. Despite the magnetisation reversal of both spin valves exhibiting two-step reversal, these multilayer systems' magnetoresistance is dominated by AMR; applying strain does not enhance the giant magnetoresistance (GMR) effect in both spin valves. This might be attributed to the spacer suppressing of the flow of electron spins.

The core of this thesis is the investigation of the strain effect in sputtered pseudo spin valve with Cu spacer: IM008 (PZT/Ta/NiFe/Cu/Ni/Ta) and IM009 (PZT/Ta/Ni/Cu/NiFe/Ta), which is demonstrated using magnetotransport and ferromagnetic measurements. These spin valves show clear GMR curves responding to the strain. The GMR modulated with the tuning strain in the spin valves for both magnetic layers shows a dependence of strain. The nickel layer possesses negative magnetostriction in these spin valves opposite to the sign of the magnetostriction of the permalloy layer. The effect of strain on each layer manifested differently in the magnetic properties of the whole spin valves (i.e. coercivity, remnant magnetisation, and spin valve stiffness). The strain affects each magnetostrictive layer differently, which can be utilised for certain applications with low power cost. Finally, in addition to the transport measurements, the static and dynamic properties of pseudo spin valves were investigated using modulated FMR. The resonance field H_{res} of the permalloy varies with the strain in both spin valves. The anisotropy as a function of strain is extracted for the permalloy layer, showing positive magnetostriction in agreement with transport measurement. For IM008, the spectra show only one clear resonance, which might be related to the dynamic interaction between magnetic layers, while for IM009, the nickel spectra showed negative magnetostriction extracted for certain voltages. The linewidth ΔH of permalloy shows in-plane dependence, caused by extrinsic damping contributions. The strain control of FMR could be used as a basis for bringing faster, lighter, and energy-efficient prototype devices that could be used in communication and space technology.

Table of Contents

List of Figures

List of Tables

Chapter 1: Introduction and Background Theory

1.1 Introduction

1.1.1 Introduction to spintronics

Spintronics is a promising field of physics and engineering that aims to understand the interaction of electron spin in solid-state materials. Nowadays, scientists are trying to exploit the intrinsic spin of the electron rather than using its charge to make new spintronics devices, particularly in magnetic memory, sensor, and recording devices, which can contribute to novel and remarkable devices that are faster, smaller, and cheaper, with higher density and low energy costs. The discovery of anisotropic magnetoresistance (AMR) by William Thomson in 1857 was the starting point of spintronics [1]. He found that the resistance of nickel and iron is changed when the magnetisation orientation of these materials is changed with respect to the electric current. This phenomenon ascribed to the spin-orbit coupling, where the conduction electrons anisotropically scattered [2].

AMR was used in the early 1990s when IBM manufactured a commercially available sensor in the hard disk drive (HDD) read head. At that time the AMR read head was better than the induction head, which had been used since the 1970s, with the former achieving superior signal from the recording film, due to higher sensitivity compared to the induction head [3]. The AMR value is of the order of 2% for some ferromagnetic materials at room temperature, increasing the areal recording density (ARD) of HDD by 30% - 60% annually. Permalloy alloy (NiFe) was one of the first ferromagnetic materials used as a magnetoresistive read head due to a fairly large AMR signal at room temperature, and low saturation field [4].

In 2008, Fert [5] and Grunberg [6] were awarded with a Nobel prize for the discovery of the giant magnetoresistance (GMR). The discovery in 1988 galvanised spintronics and precipitated a flurry of scientific research and technological applications. This phenomenon was explained by the Mott's two current model of conductivity [7]. In ferromagnetic materials, the density of state at Fermi level is different for each spin due to the split in d bands, and there is a difference in scattering probability between the spin-up and spin-down electrons. The resistance in spin channels is different due to the scattering probability, being greater for minority spin electrons [8]. As shown in figure 1.1, the simplest model for the exploitation of the GMR is two magnetic layers (F_1 and F_2) sandwiching a non-magnetic material (N). When spins in both magnetic layers are aligned in parallel, the two spin channels have different spin scattering, with one having a majority spin with less scattering probability in both layers, while the other channel has more probability of scattering in both layers. Consequently, the conductivity is dominated by one channel, which results in low net resistance, see figure 1.1. In contrast, when magnetic layers are in antiparallel alignment, both channels can be either minority or majority, through spin travelling through each layer. Consequently, the resistance in this orientation is greater than in the previous alignment.

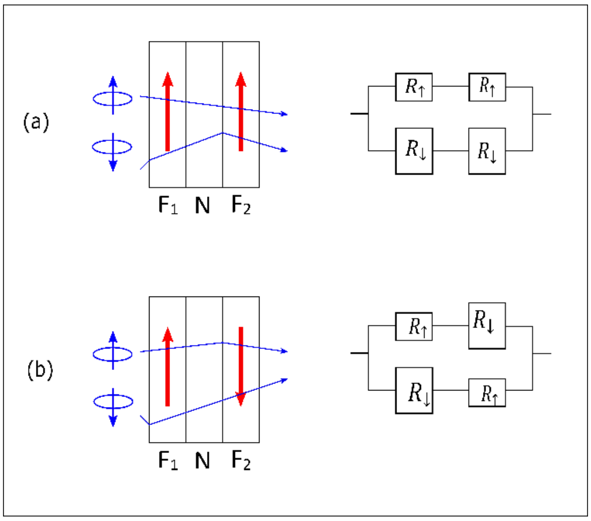

Figure 1.1: An illustration of the GMR mechanism, (a) the parallel and (b) the antiparallel configurations of the spin valve. The red arrows represent the magnetisation direction in ferromagnetic layers F1 and F2 while the blue arrows represent the spins. The resistance in (b) is higher than that in (a), N is the non-magnetic layer, $R^{\uparrow}$, and $R^{\downarrow}$ are the resistance for the spin-up and spin-down channels.

For this bilayer structure, the GMR occurs when the magnetisation alignment switches between the parallel and antiparallel alignment, with magnetoresistance expressed as $\frac{\Delta R}{R} = \frac{R_{AP} - R_p}{R_p}$, where R_{AP} and R_p represent the resistance of the antiparallel and parallel configuration (respectively). The magnetoresistance value was enhanced by the discovery of multilayer structure whereby its value for the first discovery by Grunberg was at 1.5% (at room temperature (RT)) for a trilayer structure of Fe/Cr/Fe, and 80% (at $4.2K$) for multilayer structure $[(Fe/Cr)]_{40}$ by Fert [5, 6]. Most experiments at that time focused on magnetoresistance at low temperatures, showing high values of magnetoresistance, increasing the complexity involved with applications. Increasing the number of layers increases the value of the magnetoresistance ratio. Parkin et al. [9, 10] reported that for two systems of multilayers, $[Co/Cu]_{60}$ and $[Co\text{-}Fe/Cu]_{120}$, the magnetoresistance values exceed 65% and 110% at room temperature, respectively. The magnetoresistance for same structures at $4.2K$ reach 110% for $[Co/Cu]_{60}$, and 220% for the $[Co\text{-}Fe/Cu]_{120}$. Many multilayer systems were grown with different magnetic materials and spacers, with correspondingly varied magnetoresistance values, due to differing structural and magnetotransport properties. Parkin [11] found that changing the non-magnetic spacer material thickness changes the interlayer coupling between the magnetic layers, which oscillates between the ferromagnetic and antiferromagnetic coupling.

Despite the great difference observed between the AMR and GMR values, GMR was not exploited in the hard drive industry before the appearance of the spin valve structure, as the magnetic field needed to change the alignment in GMR devices is larger than that produced by the magnetic medium [4]. The use of the spin valve solves this problem, as it comprises a free layer and a layer pinned by the antiferromagnetic layer (AFM). This was first demonstrated by Dieny et al. [12] using an AFM layer of FeMn to pin a permalloy layer while another permalloy layer was free. The same idea of the spin valve can be reached using multilayers with different coercivity (pseudo spin valve), like Co/Cu/NiFe system, where the NiFe is a soft layer that can switch easily with small magnetic field [13].

A decade after the discovery of GMR, the spin valve was considered a practical concept that significantly contributed to commercial data storage technology, with the first read-head hard drive based on GMR manufactured and brought to market by IBM in 1997 [14]. The GMR read head sensor replaced the AMR sensor and increased the ARD from 1 to $20\ Gb/inch^2$ to reach $600Gb/inch^2$ in 2007, reducing the HDD disk diameter to $0.85inch$ [15]. Figure 1.2 shows a schematic for the GMR read head reading the media stores as magnetised regions. The GMR sensor has also been used in the automotive and biomedical industries [16, 17].

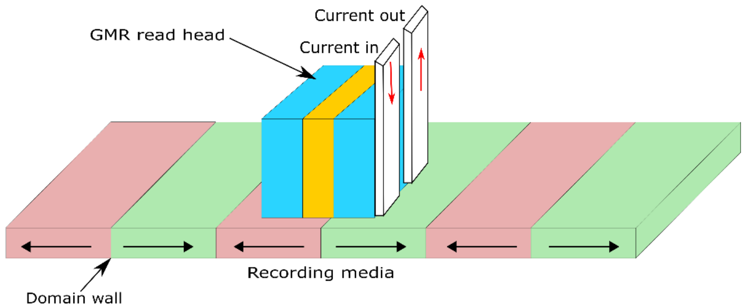

Figure 1.2*:* Schematic of GMR read head where the head passes over the recording media.

The value of the GMR is surpassed by the tunnelling magnetoresistance (TMR), in which the two magnetic electrodes sandwich an insulating layer. This device is called a magnetic tunnel junction (MTJ), where the electrons tunnel through the insulating barrier from one layer to another layer depending on the available states for electrons in each layer. This tunnelling phenomenon depends on the matching of spin selective bands, unlike the GMR, which depends on spin-dependent scattering. The value of the TMR dependent on the magnetisation orientation is the same as the GMR, whereby it is maximum for the antiparallel configuration and minimum for parallel configuration. TMR was discovered prior to the GMR in 1975 by Julliere et al. [18], and it showed a small value at low temperature using the structure of Fe/Ge/Co. Interest in TMR was stimulated during the mid-1990s after an increase in GMR research, and after the improvement in growth techniques enabled the growth of thin insulating barriers. In 1995, room temperature TMR values were reported by two groups: 12% by Moodera et al. [19] using MTJ structure of CoFe/Al_2O_3/Co; and 18% by Miyasaki et al. [20] using a junction structure of Fe/Al_2O_3/Fe. In 2004, two groups from IBM [21] and Japan [22] succeeded to use epitaxial MgO barrier with a huge TMR value of 200% at room temperature. A dramatic increase in TMR ratio was found by Lee et al. [23] in a pseudo spin valve of MTJ with the structure of $(Co_{25}Fe_{75})_{80}B_{20}/MgO/(Co_{25}Fe_{75})_{80}B_{20}$, with a value of 500% at RT and 1010% at $5K$.

The usage of TMR in the HDD industry increased the ARD to reach a value close to $1Tb/inch^2$ in 2011 [24]. MTJs were first commercialised in 2006, when they were used as a basis of the new memory technology called Magnetic Random Access Memory (MRAM). MRAM uses MTJ or GMR spin valves as cells; the bits in the MRAM are arranged and connected in array in two perpendicular lines, with MTJ unit cells at crossing points of conducting lines. The information 0 and 1 is recorded in the free layer as two different orientations (states) with respect to the pinned layer, typical MRAM architecture is illustrated in figure 1.3. For the writing process, two orthogonal fields from two current lines are applied to a certain cell to control the magnetic orientation of the free layer. A schematic of the conventional MRAM unit cell is shown in figure 1.4 (a). For the reading process, the magnetoresistance (either TMR or GMR) of the addressed magnetic cell is measured between the two lines connected to the cell [15].

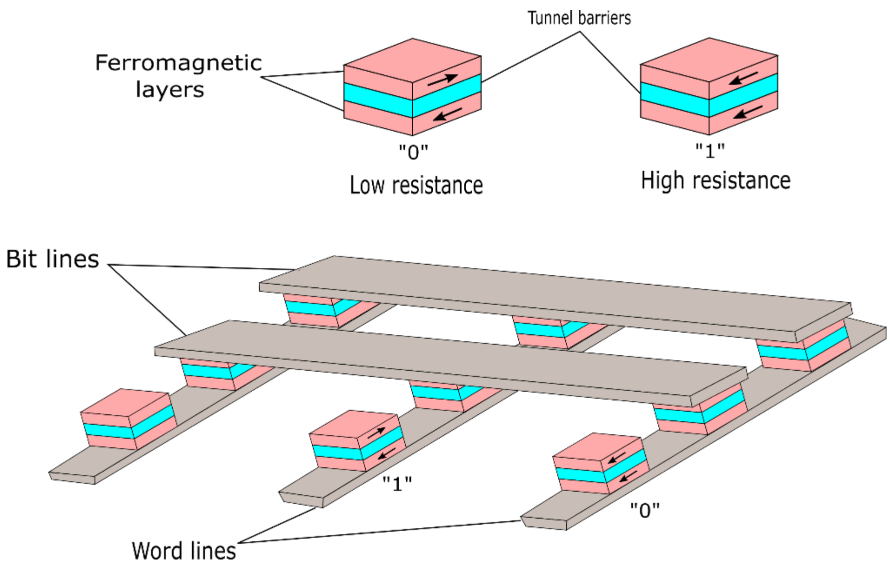

Figure 1.3: A schematic of a typical MRAM architecture, consisting of bit and word lines with the unit cell representing a spin valve with two magnetic states at the top with low and high resistance states.

The early proposals by Berger [25] and Slonczewski [26] in 1996 of the spin polarised current introducing spin-transfer torque were able to change the magnetisation orientation of magnetic layer without using a magnetic field, and subsequent experiments by Katine et al. [27] led to introducing new MRAM memory called spin-transfer torque MRAM (STT-MRAM). In this experiment, two Co layers with different thicknesses were used and separated by a Cu layer. When the layers are in antiparallel alignment state, the spin polarisation moves from the thick layer to the thin layer, to rotate and align with the thin layer moments. However, the spin is conserved, the spin exerts a torque on the ferromagnetic layer and causes a switch in the magnetisation of the thin layer. In contrast, when the magnetisation is aligned in parallel in the two layers, the spin current flows from the thin to the thick layer, and this causes a switch of the thin layer moment antiparallel to the thick layer if the current density is high enough (typically around $10^{10} Am^{-2}$) [4]. The change in the moments' status in both layers could be read using the GMR or TMR resistance. This switching of the magnetisation using spin polarised current instead of the magnetic field was the idea behind the STT MRAM, with the free layer only changing the magnetisation direction with respect to the pinned layer (using STT to write information). The current density needed to switch the free layer is given by equation [27]:

$$J_C = \left(\frac{\alpha}{\eta}\right)\left(\frac{2e}{\hbar}\right) M_s t (H_K + 2\pi M_s) \tag{1.1}$$

where α is the gilbert damping, η is the spin-transfer torque efficiency, e is the electron charge, M_s is the saturation magnetisation, and H_K is the anisotropy field. The design of the STT MRAM is easier than the conventional MRAM (field-assisted MRAM), since there is no need for a magnetic field to switch the cell. A schematic of the STT-MRAM unit cell is shown in figure 1.4 (b). In conventional MRAM, the scalability is limited due to the high current needed to produce a magnetic field for smaller storing elements, as the field increases with a smaller area to reach a smaller unit of $90nm$ [4]. In order to decrease the writing current, materials with low damping factor can be used (see equation 1.1). The writing current can also be reduced by increasing the efficiency η, which could be achieved by increasing the spin polarisation of the material used in the unit cell with different interfaces in the MTJ, Heusler alloy, and multireference layers [28, 29].

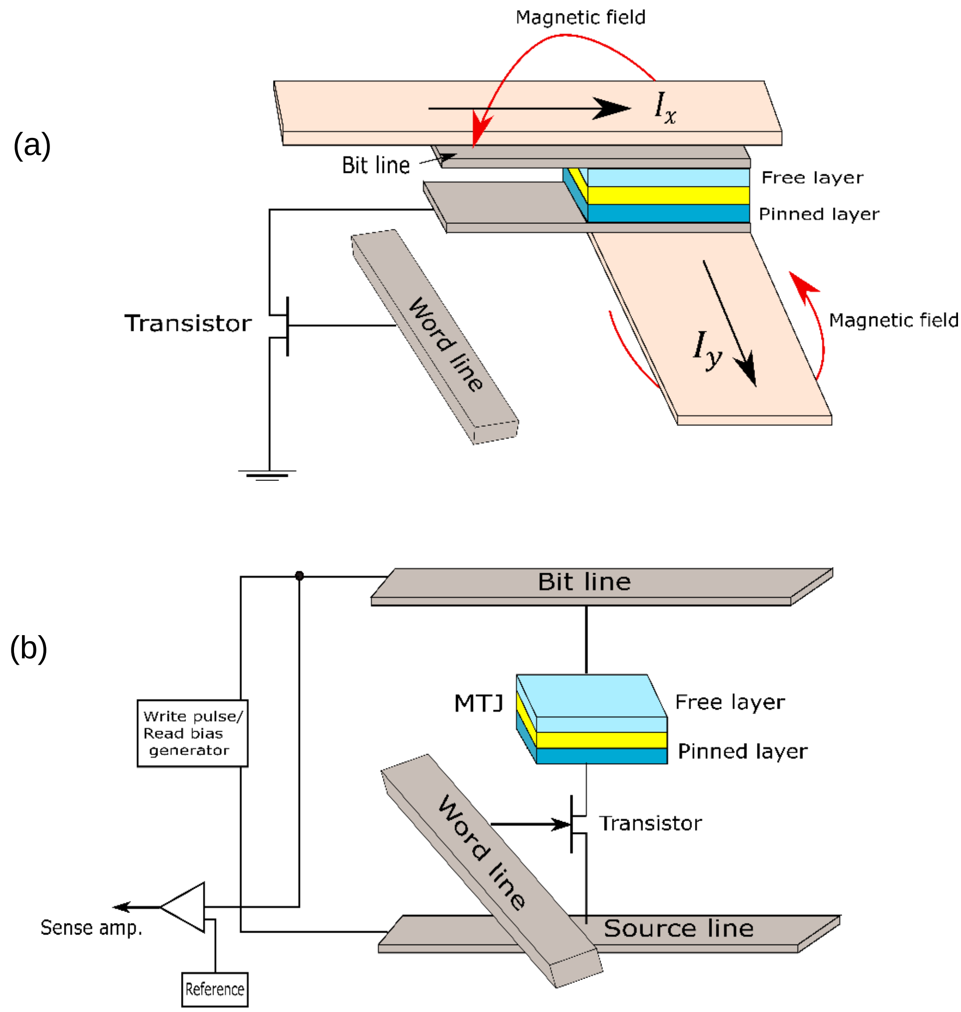

Figure 1.4: Schematic of the (a) conventional MRAM and (b) STT MRAM.

Using MgO barrier instead of Al_2O_3 increases the lifetime of the MTJ, as MgO has a higher voltage breakdown [30]. The switching time depends on the damping factor, which could play an opposite effect where the switching speed leads to higher speed switching, but it needs high writing current. The writing current in MRAM is high compared to some other memories, which leads to high energy consumption. Different spintronics memories were proposed to face high energy consumption, like Spin Hall Effect memory (SHE-MRAM) and spin-orbit torque MRAM (SOT-MRAM) [4]. Another way to reduce the power consumption of STT-MRAM is to use the electric field to control the magnetic anisotropy of the free layer and decrease the anisotropy field, and hence the power needed for the switching [31, 32].

Hu et al. [33] proposed a design for the voltage-controlled MRAM (strain-mediated magnetoelectric coupling SME RAM) shown in figure 1.5, by integrating a magnetic unit of MTJ or GMR spin valve in ferroelectric material of PMN-PT. Applying an electric field perpendicular to the PMN-PT layer induces an in-plane strain that rotates the free layer (Ni) by 90^o, and the non-volatile switching of the Ni can be achieved even after switching off the voltage. This design shows an ultralow-power consumption of $1.6 \times 10^{-4}\text{pJ per bit}$ compared to 0.1pJ per bit for STT-MRAM, and 70pJ per bit for MRAM.

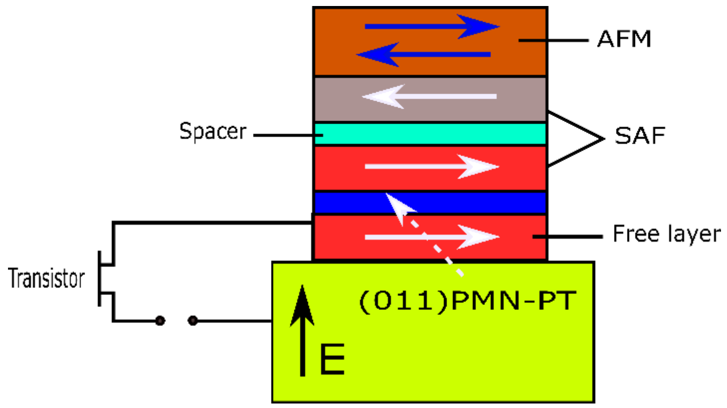

Figure 1.5: Schematic of the structure of SME MRAM for integrating spin valve device in the ferroelectric layer, where the free layer at the bottom can switch by using only the electric field without a magnetic field. SAF is synthetic antiferromagnetic.

Sixtus and Tonks were the first to observe the propagation of domain walls in magnetic materials, and to measure their velocity, during the early 1930s [34, 35]. Domain wall memories are also promising memories with ultra-high-density and fast operation. Parkin et al. [36] proposed a racetrack memory based on controlling a train of magnetic domain walls in a ferromagnetic wire, using pulses of spin-polarised current to move the domain wall while the data is read using MTJs. Domain wall-based devices are a promising technology, offering increasingly fast, cheap, and high-density solutions.

1.1.2 Electric field control spintronics

Controlling the local magnetic properties of ferromagnetic materials using different methods is an attractive field in spintronics science. One of these methods is applying an electric field through magnetoelectric coupling between the ferroelectric and magnetic materials. This method can be used as a basis for low-power spintronic devices to avoid the use of high current densities which dissipate energy as heat [37, 38, 39]. Magnetoelectric coupling arises at the interface between the ferroelectric and magnetic components, mainly from charge, exchange coupling, and strain.

The magnetic properties of magnetic materials depends on the carriers' density, hence artificial multiferroic systems have been designed to offer a change in carrier density through modulation of the electric field (charge-mediated magnetoelectric coupling), which leads to a modification of the magnetic behaviour of this materials. For instance, for $3d$ metals (Fe, Co, and Ni), a change in electrons density in $3d$ levels could modulate the magnetic anisotropy prominently. As the magnetic properties are related to the carrier density, the change in the electrons' density alters the magnetic anisotropy K_u and the corresponding energy, magnetocrystalline anisotropy energy MAE. Applying an electric field with a value less than $1MV/cm$ to Fe/MgO changed the electrons' occupancy in different orbitals, which led to a change in the spin-orbit coupling and shifted the Fermi level [40, 41]. Stolichnov et al. [42] found that the diluted magnetic semiconductor (Ga, Mn)As channel could be controlled using a copolymer polyvinylidene fluoride with trifluoroethylene P(VDF-TrFE) as a dielectric gate, leading to non-volatile control of magnetism. They successfully manipulate the Curie temperature T_C and the coercivity as a function of the multiferroic polarisation state, as a result of the electric field controlling the holes density.

The exchange bias mediated magnetoelectric coupling links the ferroelectric polarisation with the ferromagnetic spins at the interface of antiferromagnetic/ferromagnetic heterostructure using multiferroic materials, like $BiFeO_3$ [43], $YMnO_3$ [44], and Cr_2O_3 [45]. Reversible switching of Cr_2O_3 at the interface with the ferromagnetic layer Co/Pd is achieved at room temperature using electric means. The direction of the exchange bias and the net magnetisation of the uncompensated spin that pins the magnetic layer at the interface depends on the electric field value and direction [46]. For another system of NiFe/$YMnO_3$, biasing the multiferroic layer with biasing voltage tunes the exchange bias and hence modifies the magnetisation and magnetotransport properties. This is ascribed to the clamping of the ferroelectric and antiferromagnetic domain walls, accompanied by the pinning of the NiFe with AFM interface [44].

Using strain mediated magnetoelectric coupling brought intensive research interest during the last two decades, showing promising features of using ferroelectric/ferromagnetic heterostructures. When a voltage is applied to a ferroelectric material, the lattice of the ferroelectric material is deformed through the inverse piezoelectric effect, whereby strain is transferred from this material to the adjacent magnetic layer, resulting in modulation of the magnetic properties of the latter. The strain mediated magnetoelectric coupling is the main focus of this thesis; using strain in the manipulation of magnetic materials is discussed in the next section.

1.1.3 Strain mediated magnetoelectric coupling

1.1.3.1 Ferroelectric/magnetic heterostructure

Magnetoelastic coupling allows the magnetostrictive and ferroelectric materials to interact in such a way that magnetic properties of the magnetic material are modulated when the electric field is tuned through the ferroelectric material. This coupling is achieved by choosing suitable magnetostrictive and ferroelectric materials accompanied by a good interface, to make sure that most of the strain is transferred through the heterostructure interface. Magnetic materials have different magnetostriction values (the magnetic material property at which its dimensions change during the magnetisation process); table 1.1 compares between polycrystalline ferromagnetic materials' magnetostrictions for bulk form, focusing on transition metals (Co, Fe, and Ni) and some of their alloys.

Galfenol $Fe_{81}Ga_{19}$ shows high magnetostriction compared to other materials in the table, while permalloy shows zero magnetostriction. On the other hand, nickel shows negative magnetostriction with a quite high elastic constant $c_{11} -$

c_{12}. This is changing at the low thickness of thin films. Kim and Silva [47] found that for the permalloy with thickness below $7nm$, the absolute value of magnetostriction increases and shows an abrupt enhancement. On the other hand, for nickel, Bochi et al. [48] demonstrated that for Cu/Ni/Cu, the magnetostriction sign changes at a thickness of $8nm$; consequently, at that thickness, nickel magnetostriction goes to zero. These changings of the magnetostriction at low thicknesses are related to the surface anisotropy, which shows dominance rather than bulk anisotropy at low thickness, as proposed by the Néel model [49].

Table 1.1: Comparison of magnetisation saturation $\boldsymbol{M_s}$ magnetostriction constants $\boldsymbol{\lambda_s}$ and elastic constants $\boldsymbol{c_{11}} - \boldsymbol{c_{12}}$ between $3d$ ferromagnetic material and some of their alloys.

Material	$\boldsymbol{M_s}$ $(\boldsymbol{A/m} \times \mathbf{10^3})$	$\boldsymbol{\lambda_s}$ $(\times \mathbf{10^{-6}})$	$\boldsymbol{c_{11}} - \boldsymbol{c_{12}}$ $(\boldsymbol{GPa})$
		Polycrystalline	
Fe	1712 [50]	-7 [50]	95 [55]
Co	1431 [50]	-62 [50]	141 [56]
Ni	509 [51]	-34 [50]	90 [55]
$Fe_{19}Ga_{81}$	1380 [52]	65 [54]	39.4 [57]
$Ni_{80}Fe_{20}$	844 [53]	0 [53]	8.6 [58]

On the other hand, for Ni_xFe_{100-x}, the magnetostriction varies with modifying the Ni to Fe ratio. Bonin et al. [53] demonstrated that by varying the stoichiometry of polycrystalline Ta/Ni_xFe_{100-x} (5nm)/Ta, they were able to change the magnetostriction of the Ni_xFe_{100-x} between -6.6×10^{-6} and $+1.5 \times 10^{-5}$ with the Ni percentages of 86.7% and 61.9%, respectively. For the composition of $Ni_{80}Fe_{20}$, the magnetostriction is equal to zero. Varying the Ni percentage changes the magnetostriction sign and value; this also affects the magnetisation saturation and dynamic damping of the permalloy.

Many approaches were used to couple magnetostrictive materials with ferroelectric materials for strain mediated magnetoelastic coupling. One of these approaches is sintering particulate composites [59]; another method used by Zheng et al. [60] to embed uniform magnetic nanopillars in $BaTiO_3$ matrix. Direct deposition of magnetic films directly on the ferroelectric substrate, such as Pb(Zr, Ti)O_3 (PZT) [61], BaTiO3 (BTO) [62], PMN-PT [63], and polyethylene terephthalate (PET) [64] have been demonstrated with different magnetostrictive materials. In this thesis, the method used to couple the ferromagnetic layers with the ferroelectric material is that described by Rushforth et al. in 2008 [37], by bonding a fabricated device of the ferromagnet on the top of the lead zirconate titanate (PZT) piezoelectric transducer slab using two components of epoxy. Tuning the voltages across the transducer introduces sizeable uniaxial strain in the magnetic films, thereby modulating the magnetic anisotropy as a function of the voltage applied to the transducer. The same method was used by Cavil et al. [65], where an L-shape device was bonded into the piezoelectric transducer to study the competition between magnetocrystalline, magnetostatic, and strain-induced in the L-shape device. Strain controls various magnetic properties and features of magnetic materials, and the next subsections briefly summarise the strain effect on certain features related to this thesis.

1.1.3.2 Strain control of magnetoresistance

The control of magnetoresistance in single film AMR and spin valves (GMR and TMR) using strain mediated magnetoelastic coupling is demonstrated by using heterostructures of ferroelectric and ferromagnetic materials. Phenomenologically, the AMR depends on the angle between the magnetisation direction and the electric current; applying an electric field to a ferroelectric/magnetic structure could modulate the AMR value. For a structure of a magnetic layer of $Ni_{80}Co_{20}$ deposited directly on ferroelectric layer PZN-PT using a sputtering magnetron, the AMR periodically modulates between the maximum and minimum values when the electric field is changing, as a square wave field in the absence of the magnetic bias field. The magnetisation orientation rotates by 90^o, when applying the electric field induces magnetic anisotropy in $Ni_{80}Co_{20}$, which results in changing the magnetisation orientation [66]. Brandlmaier et al. [67] showed that for a polycrystalline Ni/piezoelectric transducer structure, the AMR changes by 0.5% when the voltage cycles at certain magnitudes, and the Ni magnetisation switches by 15^o between two remnant states at $0V$ and $0mT$.

The following sections will focus on the strain control of magnetic properties of spin valves as it is the core of this thesis. The findings of previous researches that use the strain to control spin valve magnetisation are presented in figure 1.6. The first panel (figure 1.6(a)) represents the results of a study [66] conducted on a Ta/FeMn/$Ni_{80}Fe_{20}$/Cu/Co/Ta spin valve deposited onto a single crystal substrate of PZN-PT; the permalloy layer (with zero magnetostriction) is pinned to FeMn, with Co (with negative magnetostriction) as the spin valve's free layer. Two configurations are grown with different easy axis direction of Co depends on the magnetic field direction applied during the deposition (refer to the schematic at the top of figure 1.6(a)). When the strain is along the easy axis, and magnetic field direction, the coercivity of the Co layer is enhanced. Enhancement was demonstrated by broader magnetoresistance peaks of the spin valve without GMR enhancement, whereby Co magnetisation switched by 180^o. On the other hand, when the strain is perpendicular to the easy axis, GMR decreased to 50%, as Co magnetisation rotated by 90^o from the former direction. The graph on the left of this panel represents magnetoresistance curves at different electric field value, while the graph on the right depicts the fluctuation of the magnetoresistance with the electric field at zero magnetic field for the perpendicular measurement direction. It should be noted that in this spin valve, the NiFe layer does not respond to the strain as its magnetostriction is zero.

The schematic at the left side of figure 1.6(b) represents one of two spin valve geometries reported in reference [68]. This spin valve utilised the same layers structure for both configurations, with different easy axis directions introduced during growth and deposited onto a PZT substrate. Strain effects on spin valve configurations demonstrated opposing trends of changing spin valve properties. The two graphs in this panel illustrate the extent to which the GMR and the field needed to reach the maximum resistance, decrease as the strain is increased, when the field is parallel to the easy axis of the layers. However, in the perpendicular direction, both quantities are increased. Given that the magnetostrictive layer in this structure is pinned by the IrMn layer, the effect of the strain may be inhibited, while the free layer is at the bottom with zero magnetostriction. However, it should be noted that the upper layer rotated slightly in response to the strain and that subsequent GMR enhancement or suppression is dependent on the magnetisation alignment in both layers, which is also affected by the spin valve configuration (easy axis direction).

Rizwan et al. [69] reported a structure for a spin valve (figure 1.6(c)) grown on PMN-PT substrate with the CoFe as both free and pinned layers. The graph on the left of the 1.6(c) panel depicts the GMR value change as a function of magnetic field direction with respect to the easy axis at various electric field values, and the GMR decreased as the electric field (strain) increased. This is ascribed to the distribution of the magnetic domains when applying strain, as magnetic anisotropy is weakened. Rizwan et al. considered this effect to be the result of the ferroelectric substrate's domain structure, which could affect the grown magnetic structure's crystallinity. To prevent this reduction of the GMR with strain, the same group [70] reported another study by growing a set of samples with various growth field directions, where the antiparallel alignment enhanced with strain. The graph at the left side of panel 1.6 (c) shows increased GMR as a function of strain for most directions of the growth (with different initial magnetic anisotropy), whereby the strain rotates the lower free layer, which enhances the GMR. All studies in panels 1.6 (a), (b) and (c) utilised more than one geometry with various easy axes to optimise and obtain an enhanced GMR with strain.

Zhao et al. [71] investigated a pseudo spin valve with two free layers of Co and Ni grown onto PMN-PT; the structure is depicted at the top of panel 1.6(d). This study showed non-volatile magnetisation rotation by 90^o of the Co layer magnetisation as a response to the strain, while Ni magnetisation at the bottom did not demonstrate a strain response. The GMR increased with the strain, as shown in the lower graph in panel 1.6 (d). The letters in the graph represent various strain stages, while ER represents the spin valve's resistance ratio with respect to zero strain. Although this structure shows non-volatile manipulation of magnetoresistance, it should be noted that this study was conducted at a low temperature ($80K$); the results of strain modulation at room temperature are more easily generalisable to practical applications.

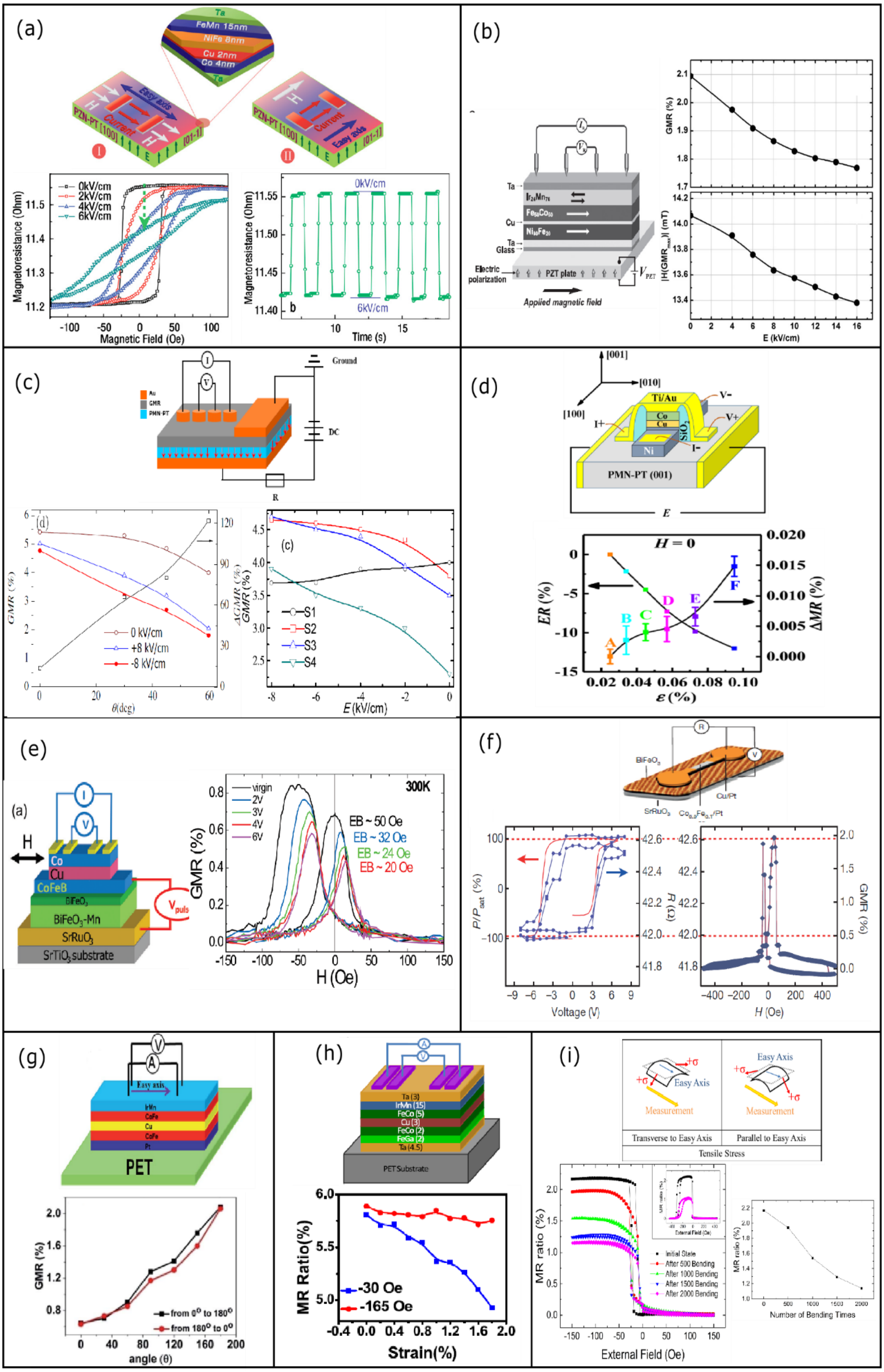

Figure 1.6: Previous research conducted to study the strain control of spin valves structures (a)[66], (b) [68], (c) [69, 70], (d) [71], (e)[72], (f) [73], (g) [64], (h) [76], and (i) [77].

$BiFeO_3$ (BFO) multiferroic has been utilised in two previous studies considered here panels 1.6.(e) and (f). Change in the magnetic status of the magnetic structures is related to BFO polarisation status and depends on ferroelectric domains and domain-walls type. The first study [72] was conducted on a structure shown at the left side of figure 1.6(e). Exchange bias decreased with strain, affecting the GMR value with the same trend as shown in the right side of the graph in the same panel. This process is irreversible; the exchange bias could not be restored, including by changing voltage polarity. A piezoresponse force microscopy investigating the BFO's domains and domain walls revealed a correlation between the domain walls and FE-AFM-type domains with the strain effect on the magnetic status of the spin valve. The measurements of voltage versus current of this study showed a quite large leakage current, which is a challenge in using BFO substrate and needs to be addressed for using this material when applying an electric field to control magnetic structures. For the same multiferroic substrate, Heron et al. [73] demonstrated the concept of high-density magnetoelectric RAM (MeRAM) using a Pt/$Co_{90}Fe_{10}$/Cu/$Co_{90}Fe_{10}$ spin valve device patterned on a single phase of BFO (figure 1.6(f)). Regarding the magnetoresistance of the spin valve, varying the voltage applied to the BFO (a $4V$ range) produced a non-volatile change between the two switching states of low and high resistance; a change of $\Delta R = 1.4\%$ is observed without using a magnetic field (as shown in the left graph in 1.6(f)). This value is close to the value obtained when applying a magnetic field to the spin valve (see the graph on the right of the same panel). The findings indicate that the energy consumption per switch per area of the heterostructure equals $480\mu J/m^2$, which is less by an order to the memory using spin polarisation when compared to other studies with a value of 3 to $4\ mJ/m^2$ [74, 75]

Various studies have used flexible polyethene terephthalate (PET) substrate to study the strain effect on spin valve magnetisation (the bottom row of figure 1.6). The study [64] presented in figure 1.6(g) utilised the structure illustrated at the top of the figure. As the bending angle changed between $\theta = 0^o$ and $\theta = 180^o$, GMR increased monotonically from 0.64% to 2.08%, and the opposite trend (decreased GMR) was observed for the opposing bending direction. The strain-induced magnetic anisotropy in both free and pinned layers in the spin valve, and that affected the GMR value depends on the layers' orientation. Regarding the study [76] in panel 1.6(h), a spin valve was grown onto PET with FeCo as a pinned layer, while a composite free layer of FeGa/CoFe was utilised; FeGa was used to enhance the magnetostriction of the free layer, while FeCo to enhance the scattering and thus the GMR (refer to the illustration of the spin valve at the top of figure 1.6(h)). This structure demonstrated decreased GMR with the strain (at two different field values; shown in the lower figure in the same panel), which is attributed to the spin spiralling at the interface between the two free layers as an effect of the varying magnetostrictions between them. In the third study [77] with a flexible PET substrate, the spin valve bent repetitively in two directions with respect to the magnetic easy axis, as shown at the top of panel 1.6(i). Two layers with positive magnetostriction $Ni_{80}Fe_{20}$ and $Co_{70}Fe_{30}$ were selected; magnetoresistance demonstrated decrease or increase depending on the bending direction. The graphs in figure 1.6(i) represent the measurement when the bending is parallel to the easy axis, which shows a decreased GMR with strain. Although using flexible PET substrate demonstrated enhanced GMR values in some cases, the roughness of the PET substrate could affect the magnetic structure to distribute the anisotropy when mechanical strain is applied. On the other hand, the bending angle of the spin valve is difficult to measure and hence it is difficult to measure the actual strain induced in the film [64, 77].

This thesis extends on the body of previous research on strain effect on spin valves by conducting an investigation that utilises two magnetostrictive layers with different magnetostriction values and signs. Using a permalloy layer with positive magnetostriction, and nickel with negative or zero magnetostriction facilitates a sizeable change in the magnetic and magnetoresistance properties of the spin valves. This could contribute to the low power spintronics devices and in controlling domain walls propagation in storage and logic devices. Results indicate that the strain affected the reversal of the permalloy and nickel differently to align them perpendicular to each other (at zero magnetic field) when maximum tensile or compressive strain values are applied. Magnetoresistance curve features could then be controlled, and thus the magnetic properties vary and depend on the difference of the layers magnetostriction constants sign. One previous study [78] based on the same principle, intended to exploit the difference in magnetostriction values in layers of a spin valve using two galfenol layers with different compositions of $Fe_{84}Ga_{16}$\Cu\$Fe_{88}Ga_{12}$ in order to introduce varying magnetic anisotropy and magnetelastic constants. Findings indicated a change in the magnetic reversal and switching field values of each layer, which manifest as different features in magnetoresistance curves. Although both layers evidenced higher magnetostriction values in response to the strain, this did not enhance the GMR value of this spin valve which might be related to different factors. In the present study, the majority of the magnetoresistance is mainly due to the GMR effect, which shows a distinct response to the strain. On the other hand, to avoid complications encountered in previous studies where the domain structure of the ferroelectric is responsible for some of the observed effects, an approach is used where spin valves grown on semiconductor substrates which are then glued to piezoelectric transducers.

There is still a lack in the literature of studies that investigate the magnetic reversal and induced anisotropies of each layer separately in multilayer samples under the effect of the strain. This study investigates the impact of the strain on magnetoresistance, ferromagnetic resonance and on reversal features of each layer in the spin valves. A quantitative study of the induced anisotropy is provided by studying the impact of strain on single layers of permalloy and nickel using magnetotransport measurement. The induced anisotropy in spin valves for each layer is studied using ferromagnetic resonance (FMR) measurment.

1.1.3.3 Strain control ferromagnetic resonance

Using strain-mediated magnetoelectric is one of the most efficient ways to tune the ferromagnetic resonance (FMR) rather than using electric current-driven electromagnet. Strain-induced anisotropy modulates the FMR properties in a reversible and reproducible way. Lou et al. [79] demonstrated the ability to tune the microwave frequency under no bias magnetic field. They deposited a layer of $100nm$ of FeGaB on a ferroelectric slab of PZN-PT, and by using vector network analyser FMR, they were able to tune the FMR frequency between $1.75GHz$ and $7.57GHz$ at zero magnetic fields when varying the electric field between $0kV/cm$ and $6kV/cm$, respectively, with mean tunable frequency per electric field unit of $970MHz.cm.k/V$. Figure 1.7 (a) shows the S21 spectra of the FeGaB/PZN-PT heterostructure, with the frequency tuned with the electric field at zero magnetic field. The strain-induced by ferroelectric slab into FeGaB induces an effective anisotropy, varying with the voltage, as also shown in figure 1.7(b) by the VSM measurement with the same corresponding voltages with the largest anisotropy at $8KV/cm$ and the lowest at $0KV/cm$, with anisotropy field values of $700\mathrm{Oe}$ and $20\mathrm{Oe}$, respectively.

Previous researchers [80] used a hybrid structure of Ni and transducer actuator of $Pb(Zr_xTi_{1-x})O_3$ to conduct a modulated FMR measurement for Ni/PZT structure, by varying the voltages between $-30V$ and $+50V$ in two different directions of the magnetic field with respect to the transducer axis (with 90^o difference). Figure 1.7(c) shows the angular dependence of the resonance field H_{res} at two voltages of $+20V$ and $-30V$, where the Ni easy axis shows in-plane rotation by 90^o, and the sign of magnetic anisotropy can be inverted by varying the voltage. Using strain to tune the ferromagnetic resonance brings scope for potential prototype devices that can be used in communication and space technology, like aircraft and satellites, as conventional items (electromagnet components) are replaced by lighter items based on multiferroic heterostructure, thus producing faster, lighter, more energy-efficient solutions that can be integrated into one-chip devices such as phase shifters, resonators, and tuneable filters [81, 82, 83] .

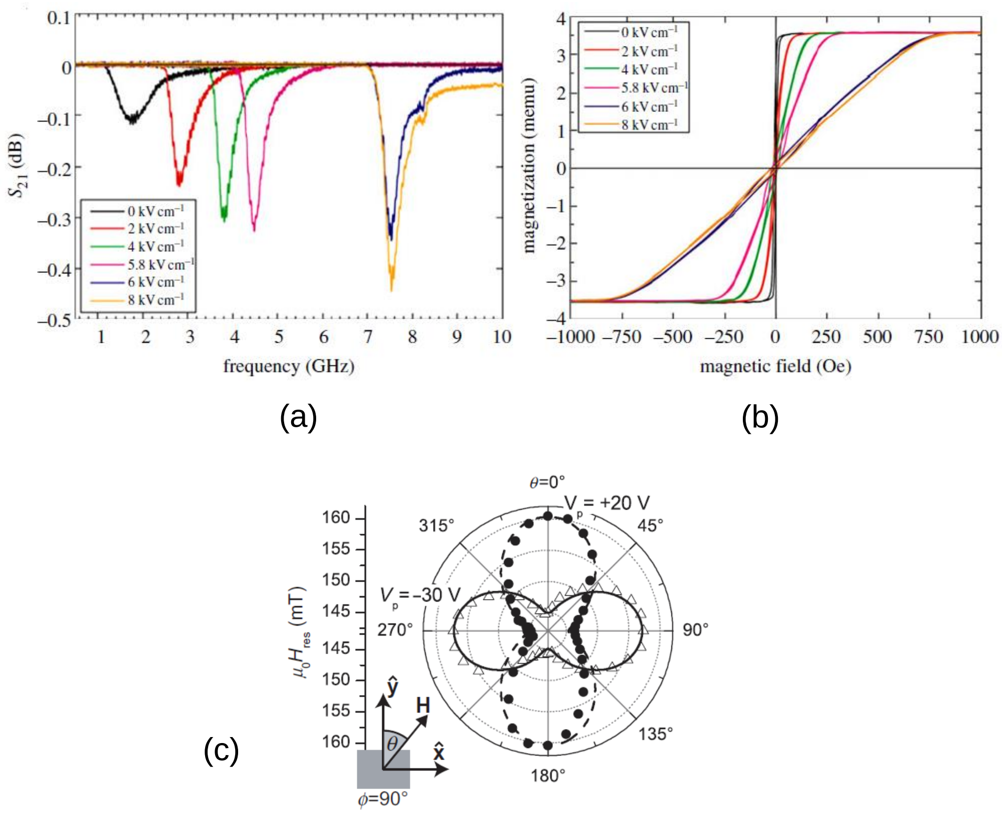

Figure 1.7: (a) Electric field control of ferromagnetic resonance of FeGaB/PZN-PT with zero bias magnetic field. (b) The corresponding hysteresis loops measured by the VSM for the same structure in (a) for the same values of the electric field, shows the largest anisotropy when applying $8kV/cm$ [72]. (c) The angular dependence of H_{res} when applying two voltages of $-30V$ and $+20V$ to the actuator in Ni/PZT structure [80].

1.1.3.4 Strain control of domain wall propagation

Domain walls manipulation in spintronics devices is a very promising field that could be used in storage and logic devices. Using a magnetic field and electric current to propagate domain wall costs huge energy due to Joule heating. Magnetoelastic coupling is one of the most efficient methods to control the propagation of the magnetic domain [84, 85, 86]. Parkes et al. [87] demonstrated strain-induced non-volatile switching of epitaxial FeGa at zero magnetic fields, whereby a sizable anisotropy induced by the strain controls the domain walls motion in the patterned devices.

Lei et al. [88] proposed a low power storage and logic device used a hybrid structure of magnetic spin valve/ferroelectric by pattering a hall bar device of the spin valve with layers shown in figure 1.8(a) on the top of PZT, by applying a lateral electric field, as shown in figure 1.8(b), to induce a local strain to control domain walls locally. Controlling the free layer coercivity by applying strain at certain position controls the domain wall propagation, whereby the domain walls are pinned at the gate voltage. Measurements also show that the propagation field is increasing with voltage, and gives complete control of the domain walls position, which can be monitored using the GMR to detect the motion. This device can be used as a promising idea for logic devices, as the gates can be controlled by the strain. This pioneered idea could be used in racetrack memory to replace the complicated construction of the pinning sites of domain walls that needed high current density to move. Rather, the electric field can control the domain wall by pinning at a certain position with less energy cost.

(a)

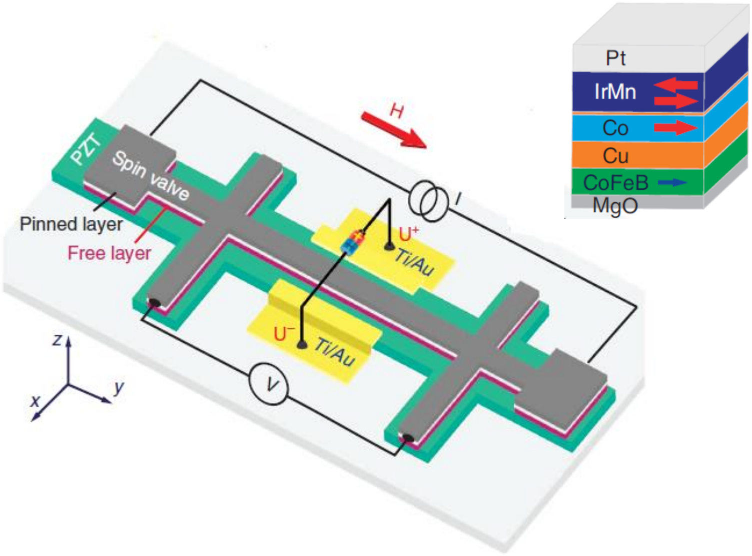

(b)

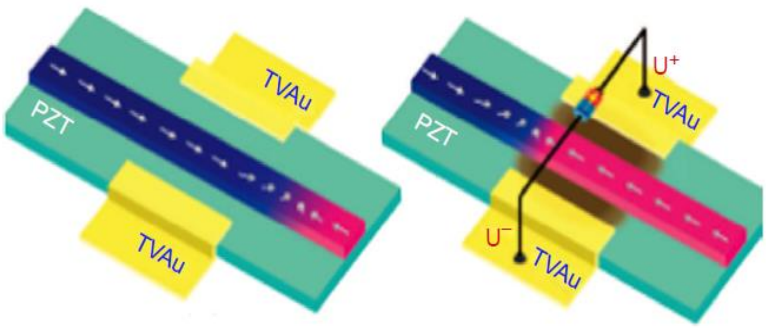

Figure 1.8: (a) The design of the experiment used by Lei et al. [83], where the spin valve (top right) is deposited on the top of the ferroelectric material of PZT. (b) The domain walls propagate freely when no voltage is applied and the walls are pinned at voltage gates.

The spintronics field brought intensive interest in developing a wide range of technologies that can be used in storage and logic devices. The need for high-density storage, ultra-fast, low-cost energy is behind the motivation for obtaining new spintronics devices to cope with the demands of high-performance computing. Multilayer structure systems are behind most of the storage devices that are used these days, such as HDD and MRAM. The main aim of this thesis is to investigate the strain-induced anisotropy on magnetisation and magnetic reversal of the nickel and permalloy spin valves using a hybrid structure of piezoelectric/spin valve. This can be used for the basis of low power spintronics devices in HDD, MRAM, sensors, and microwave devices, as discussed in detail in the previous sections. The investigation uses magnetotransport and ferromagnetic resonance to study the strain mediated magnetoelectric in the hybrid structures.

This thesis outlines the theory and background of ferromagnetic materials and their magnetostriction focussing on $3d$ metals, along with the theory behind magnetotransport phenomena of multilayer structure and dynamic properties in second part of this chapter. Chapter 2 describes the experimental and computational techniques used to study the samples in this thesis. Single-layer samples of permalloy and nickel were first investigated in chapter 3 as reference samples for the investigated spin valves using magnetotransport measurements. A comparison study of pseudo spin valves and exchanged bias spin valve using SQUID and magnetotransport measurement using zero voltage is presented in chapter 4. Chapters 5 and 6 study the strain effect on spin valves using magnetotransport and ferromagnetic resonance measurements. The effect on the magnetic reversal and magnetoresistance is studied in detail for all spin valves in chapter 6. The strain investigation on pseudo spin valves using ferromagnetic resonance is studied in chapter 6. This study ends with the conclusion and identifies areas for future work in chapter 7.

1.2 Background theory

1.2.1 Ferromagnetism and exchange energy

Ferromagnetic materials exhibit spontaneous magnetisation where a long-range ordering of atomic moments is aligned in parallel. The ferromagnetic substances show spontaneous magnetisation even in the absence of an external magnetic field. In spite of that the ferromagnetic material might show zero magnetic moments when no field is applied. However, applying a small magnetic field initiates a magnetic moment bigger than that produced in paramagnetic materials. Weiss postulates that this spontaneous magnetisation is attributed to the internal field, called the molecular field (H_m), with a value [50, 89]:

$$\boldsymbol{H_m} = \gamma \boldsymbol{M} \tag{1.2}$$

where $\boldsymbol{M}$ is the substance magnetisation and γ is the molecular field constant. Weiss also assumed that the ferromagnetic specimen consists of small regions called domains where the atomic moments aligned in parallel and reach saturation magnetisation. In the demagnetising state, the net magnetisation might equal zero, as the moments' direction changes from domain to other, figure 1.9 illustrates the deference between demagnetised and magnetised states in ferromagnetic material. The magnetic domains and domain walls are discussed in section 1.2.3. The spontaneous magnetisation of the ferromagnetic material vanishes above certain temperature, called Curie temperature T_c, and becomes paramagnetic material thereafter, whereby the material loses parallel alignment. The paramagnetic susceptibility of a ferromagnet above T_C (χ) follows the Curie-Weiss law as follows:

$$\chi = \frac{C}{T - T_C} \tag{1.3}$$

where C is the Curie constant, the Curie temperature is the temperature at which the thermal agitation destroys the magnetic moments coupling, and the molecular field below T_c is very strong [50]. The Curie temperature varies among ferromagnetic materials; for instance, it is equal to $627K$ and $872K$ for the fcc phase of Ni [90] and NiFe [91].

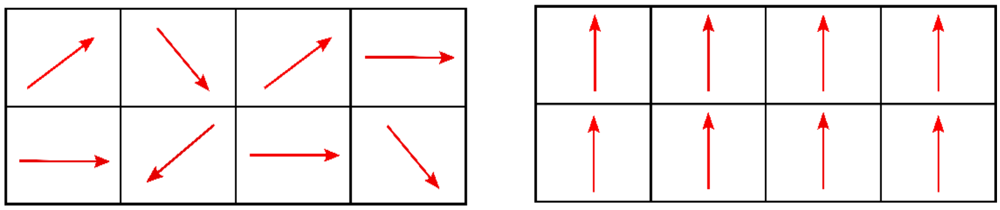

(a) (b)

Figure 1.9: Magnetic domains of a ferromagnetic substance in (a) demagnetised, and (b) magnetised states.

The origin of the molecular field postulated by Wiess theory was not clear until Heisenberg related that to a quantum exchange force called exchange energy. In ferromagnetic materials, the quantum mechanical exchange interaction leads to the alignment of atomic spins and spontaneous magnetisation. The exchange interaction is a powerful force for short-range of neighbouring spins, while it decreases sharply when the distance increases. The Heisenberg Hamiltonian [50] is used to calculate the exchange energy between two adjacent spins, as shown below:

$$E_{exch} = -\sum_{i<j} 2J_{ij}\boldsymbol{S_i}.\boldsymbol{S_j} = -2J_{ij}S^2 \sum_{i<j} cos\psi \tag{1.4}$$

where $\boldsymbol{S_i}$, $\boldsymbol{S_j}$ are the spin vectors of the interacting atoms i, and j, S is the magnitude of the spin, J_{ij} is the exchange integral, and ψ is the angle between adjacent spins. For ferromagnetic materials, J_{ij} is positive, which means the energy is minimised when neighbouring moments are parallel to each other. For negative exchange integral, the antiparallel configuration of the spins gives the lowest energy value, and hence yields antiferromagnetic ordering. Figure 1.10 shows the Bethe-Slater [50, 92] curve where J_{ij} varies with the ratio r_{ab}/r_{3d}, where r_{ab} is an inter-atomic distance and r_{3d} is the radius of $3d$ shell of electrons. Ferromagnetic materials (e.g. Fe, Co, and Ni) have positive exchange integral, depending on the radius ratio, while for smaller distance Mn and Cr exhibit negative integral. For positive values of J_{ij}, it is proportional to the ferromagnetic Curie temperature; Co has the highest T_C while Ni has the lowest T_C of the room temperature elemental ferromagnets[50].

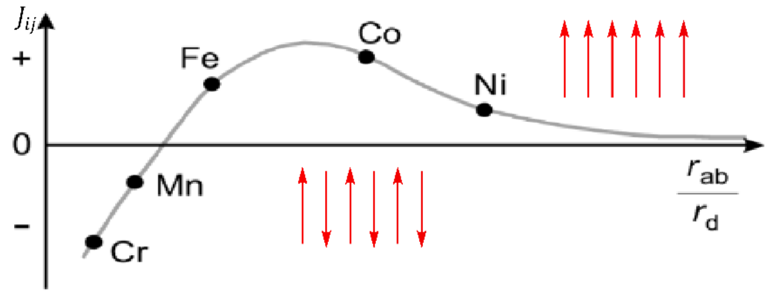

Figure 1.10: Bethe-Slater curve describing the relation between the exchange J_{ij} and the ratio r_{ab}/r_d, where r_{ab} is the inter-atomic distance and r_d is the radius of $3d$ shell of electrons. For ferromagnetic material, J_{ij} is positive for ferromagnets with moment parallel aligned, as shown by upper arrows, while J_{ij} is negative for antiferromagnets with moment antiparallel aligned, as shown by lower arrows (arrows are added to the curve from [50] for comparison between ferromagnetic and antiferromagnetic materials).

Band theory for the electronic structure of solid materials [93, 94] is applied to explain the magnetic properties of the $3d$ ferromagnetic metals, Ni, Co, and Fe, in which the ferromagnetism arises from the spin-split d band results in a different density of state of the spin-up and spin-down electrons at Fermi level. The theory postulated that for these transition materials, the spin in $3d$ band is unbalanced, never completely full due to unoccupied levels, while the $4s$ band is completely full. Hence the magnetic properties in these metals are related to this unbalanced spin in $3d$ band. Table 1.2 shows the electron distributions of different metals in relation to differences in spin between $3d$ and $4s$ bands, which also illustrated in figure 1.11. It is worth mentioning that $3d$ band has a capacity of 10 electrons, while $4s$ has only 2 electrons' capacity, see figure 1.11. According to the Pauli exclusion, for each level in the band, the two electrons should have different spin directions; hence the spins in $4s$ cancel each other [95].

Table 1.2: Distribution of the electrons in 3d and 4s in different metals.

Band	**Number of electrons**					
	Cr	Mn	Fe	Co	Ni	Cu
$\mathbf{3d}$	5	5	6	7	8	10
$\mathbf{4s}$	1	2	2	2	2	1

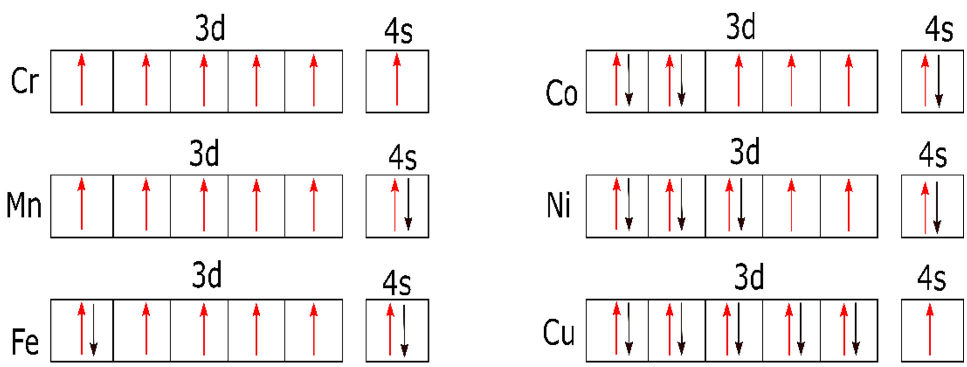

Figure 1.11: Electronic configuration of some metals where black arrows represent the spin-down electrons and red arrows represent spin-up electrons.

1.2.2 Magnetic anisotropies

Magnetic anisotropy means the preference of the magnetisation direction in a ferromagnetic sample lies along a certain direction where the free energy is minimum. In this section, the origins and different contributions of the free energy are discussed, along with how they influence the magnetisation of the ferromagnetic material. The magnitude and direction of these anisotropies determine the magnetisation processes when applying an external magnetic field.

1.2.2.1 Zeeman energy

When a ferromagnetic material is placed in an external magnetic field, the magnetic spins within the material, interact and tends to align with that field due to Zeeman energy, which is given by:

$$E_{zeem} = -\mu_o \int_V \boldsymbol{M}.\boldsymbol{H}_{\boldsymbol{ext}} dV \tag{1.5}$$

where μ_o is the permeability of free space and $\boldsymbol{H}_{\boldsymbol{ext}}$ is the external magnetic field. The Zeeman energy vanishes when the applied field is equal to zero, while it is minimised when the magnetic moments are aligned parallel with the direction of the external magnetic field.

1.2.2.2 Shape anisotropy

Shape anisotropy is caused by the existence of a demagnetising field in non-spherical samples. The demagnetising field H_d is the field inside the magnetic substance generated as a result of the divergence of the magnetisation, and it is sensitive to the material's geometries and proportional to the magnetisation. This field originates from the set of magnetic poles at the surface of a ferromagnetic material, and can be written as:

$$\boldsymbol{H_d} = -N.\boldsymbol{M} \tag{1.6}$$

where N is the demagnetising factor determined from the material geometry, with a value of 1 for thin-film magnetised perpendicular to the film plane, while it is equal to 0 for in-plane magnetisation [96, 97]. The magnetostatic energy or shape anisotropy can be written as:

$$E_{demg} = -\frac{\mu_o}{2}\int_V \boldsymbol{M}.\boldsymbol{H_d}dV \tag{1.7}$$

For thin-film system, the magnetostatic energy is higher along the thickness of the film, and hence the magnetisation tends to lie along the film plane axis. Hence, it needs a lower magnetic field to magnetise the material along the film plane and costs less energy.

1.2.2.3 Magnetocrystalline anisotropy

Magnetocrystalline anisotropy arises from spin-orbit interaction due to the coupling between the spin and orbital momentum of the electron. Due to this coupling, a specific crystalline direction becomes energetically preferable for the spin direction, which is known as the magnetisation easy axis, while the other orientations are harder axes. The magnetocrystalline anisotropy is the energy required to change the direction of the magnetisation from the preferred (easy) axis to the direction of the hard axis. This energy is small compared to the exchange energy (spin-spin coupling), which works just for short-range neighbouring moments, while the crystal anisotropy aligns the moments along a certain direction in the crystal [98].

The magnetocrystalline anisotropy of cubic system can be expressed in a series expansion of the direction cosines of the magnetisation M_s with respect to the cube axis as follows [98, 55]:

$$\epsilon_c = K_o + K_1(\alpha_1^2\alpha_2^2 + \alpha_2^2\alpha_3^2 + \alpha_3^2\alpha_1^2) + K_2(\alpha_1^2\alpha_2^2\alpha_3^2) + \cdots \tag{1.8}$$

where K_o, K_1, and K_2 are the magnetocrystalline constants for a specific material at a particular temperature; and α_1, α_2, α_3 are the direction cosines of the angles between the magnetisation and the cubic crystal. The first term (K_o) is neglected, as it is independent of the orientation, and K_2 is sometimes ignored as it is so small. The lowest order of the anisotropy can be written as:

$$\epsilon_u = K_1 \sin^2\theta \tag{1.9}$$

In this case, the magnetocrystalline anisotropy is called uniaxial anisotropy, whereby the crystal has a single easy axis, as shown in figure 1.12.

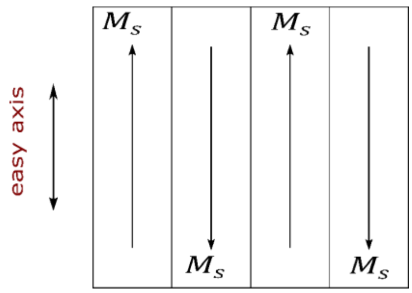

Figure 1.12: Demonstration of uniaxial anisotropy in a ferromagnetic material with magnetisation aligned along the easy axis.

The magnitude and the sign of the $K_1$and K_2 determine the magnetisation easy axis direction and the magnitude of the anisotropy. Table 1.3 shows the values of $K_1$and K_2 for different ferromagnetic materials at room temperature.

Table 1.3: Magnetic anisotropy constants for some ferromagnetic materials at RT[55].

	Fe	**Co**	**Ni**	**NiFe**
$\boldsymbol{K_1}$ (J/m^3)	4.8×10^4	4.1×10^5	-4.5×10^3	-3×10^2
$\boldsymbol{K_2}$ (J/m^3)	-1×10^4	1.5×10^5	-2.3×10^3	-

As shown in table 1.3, nickel with fcc structure, as shown in figure 1.13, has negative K_1, thus $\epsilon_{100} > \epsilon_{110} > \epsilon_{111}$. In this case, the easy axis is along the [111] direction, while [100] is the hard axis of the nickel crystal [98]. The magnetisation hysteresis loop is also affected by the magnetocrystalline anisotropy, as shown for the nickel in figure 1.13. The easy axis needs less field to saturate at around $150Oe$, while the hard axis saturates at $250Oe$. The field needed to saturate the magnetisation in the hard direction called anisotropy field H_K, and can be obtained from:

$$H_K = \frac{2K}{M} \tag{1.10}$$

Permalloy with a stoichiometry of $\mathrm{Ni_{80}Fe_{20}}$ shows a small negative K_1, which means that it needs a very small field to change the magnetisation direction. For this composition, permalloy is a soft material (a magnetic material that needs very small field value to reach saturation magnetisation) with a magnetisation easy axis along [111] direction. Bozarth [99] demonstrated that by changing this composition, the K_1 is changed, and the sign changes from positive to negative when the nickel percentage is around 80%, as shown in figure 1.14, hence the easy axis changes from [111] to [100]. The K_2 for this stoichiometry shows zero value, while it changes as the stochiometry changes to reach the maximum for less Ni concentration.

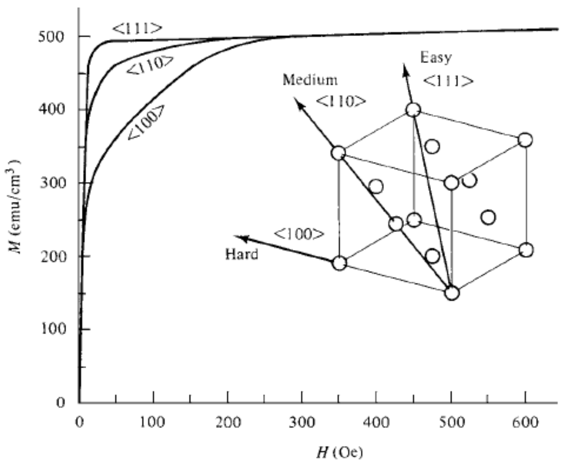

Figure 1.13: Magnetisation curves for the Ni at different directions with the respective crystal structure (fcc) showing that [111] is the easy axis [55].

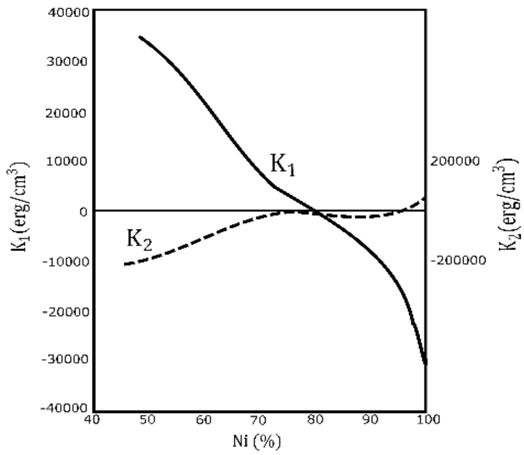

Figure 1.14: Anisotropy constants of the NiFe at the different compositions of the nickel and iron showing that both $K_1$and K_1 have small values for permalloy composition of around $\mathrm{Ni_{80}Fe_{20}}$ [99].

All samples used in this study are polycrystalline for single and multilayer samples. For polycrystalline sample, the magnetisation orientation is isotropic, as the crystal direction is oriented randomly in sample crystallites, and the crystal anisotropy averages out, so the sample shows zero net anisotropy. However, magnetic anisotropy could be induced in the polycrystalline sample during different stages of growth, fabrication [14], preparing the sample for the measurements, and by inducing strain.

1.2.2.4 Magnetoelastic anisotropy

When a magnetostrictive material is subjected to an external magnetic field, its dimensions may change. Hence, its magnetic properties could change due to spin-orbit coupling, where the distance between atoms is influenced. The magnetostriction λ is the fractional change in the length of the magnetic specimen to reach the magnetisation saturation under the effect of an external magnetic field, while the saturation magnetostriction (λ_s) is the strain value at saturation magnetisation. For material with positive magnetostriction, it elongates along the field direction, while for negative magnetostriction, it contracts along the field direction. This phenomenon is called the Joule effect, and the fractional change in the material length is very small, in the range of 10^{-5} to 10^{-6}. Alternatively, the magnetisation of the magnetic material changes under the influence of external mechanical stress (strain), which is called the

Villari effect [96, 55, 100]. In this case, the strain induces anisotropy in the ferromagnetic material. In cubic materials, the magnetostriction (magnetoelastic) term in the free energy is given by [96, 100]:

$$\epsilon_{me} = B_1\left[\varepsilon_{xx}\left(\alpha_1^2 - \frac{1}{3}\right) + \varepsilon_{yy}\left(\alpha_2^2 - \frac{1}{3}\right) + \varepsilon_{zz}\left(\alpha_3^2 - \frac{1}{3}\right)\right]$$
$$+B_2\left[\varepsilon_{xy}\alpha_1\alpha_2 + \varepsilon_{yz}\alpha_2\alpha_3 + \varepsilon_{zx}\alpha_1\alpha_3\right] \quad (1.11)$$

where $B_1$and B_2 are the magnetoelastic constants, α_1, α_2 and α_3 represent the direction cosines of the magnetisation along the cube axes in which the change in the length is measured, and ε_{xx}, ε_{yy}, …. are the strain tensor components. Assuming the magnetisation is in the plane of the film, $\alpha_3 = 0$, and ε_{xy}, ε_{yz}, and ε_{zx} are very small and can be neglected compared to ε_{xx}, ε_{yy}, and ε_{zz}. Hence, equation 1.11 can be written as:

$$\epsilon_{me} = B_1\left[\varepsilon_{xx}\left(\alpha_1^2 - \frac{1}{3}\right) + \varepsilon_{yy}\left(\alpha_2^2 - \frac{1}{3}\right)\right] \quad (1.12)$$

where B_1 can be defined as [96, 100, 101]:

$$B_1 = \frac{3}{2}\lambda_{100}(c_{12} - c_{11}) \quad (1.13)$$

where λ_{100} is the magnetostriction constant measure of the strain along the [100] direction, and $c_{12}$and c_{11} are the elastic constants. In this case, the magnetoelastic energy can be written as:

$$\epsilon_{me} = \frac{3}{2}\lambda_{100}(c_{12} - c_{11})(\varepsilon_{xx} - \varepsilon_{yy})\cos^2\varphi \quad (1.14)$$

where φ is the angle between the magnetisation and [010] axis. This equation describes the energy change with the angle φ. In this thesis, since all samples are polycrystalline, this angle represents the angle between the magnetisation and the strain. The magnetoelastic energy can be written as:

$$\epsilon_{me} = B_1\Delta\varepsilon\cos^2\varphi \quad (1.15)$$

where $\Delta\varepsilon = \varepsilon_{xx} - \varepsilon_{yy}$ is the in-plane strain, ε_{xx} , and ε_{yy} are connected by Poisson's ratio, given by the relation:

$$\upsilon = -\frac{\varepsilon_{xx}}{\varepsilon_{yy}} \tag{1.16}$$

This is discussed more in chapter 3. Comparing the magnetoelastic energy in equation 1.15 to the uniaxial anisotropy in equation 1.9 yields the elastic energy applied as uniaxial anisotropy:

$$K_u = K_S = B_1\Delta\varepsilon \tag{1.17}$$

Hence, the magnetoelastic anisotropy can be written as:

$$\epsilon_{me} = K_S cos^2\varphi \tag{1.18}$$

For polycrystalline material, the magnetostriction can be calculated using the following equation:

$$\lambda_s = \frac{2}{5}\lambda_{100} + \frac{3}{5}\lambda_{111} \tag{1.19}$$

where λ_{111} is the magnetostriction constant measuring the strain along the [111] direction. Figure 1.15 shows that when a strain is applied to the magnetostrictive material at zero field (demagnetised state), the magnetisation direction of the material depends on the magnetostriction sign. The magnetisation easy axis is aligned along the tensile strain direction for the positive magnetostriction material (figure 1.15 (a)). On the other hand, the magnetisation is aligned perpendicular to the strain when applied to the negative magnetostriction material (figure 1.15 (b)).

As mentioned in in section 1.1.3, the permalloy with the stoichiometric $\mathrm{Ni_{80}Fe_{20}}$ has near-zero magnetostriction properties, while nickel has negative magnetostriction for the bulk form, with a value of -34×10^{-6}. However, this could be changed in thin films, whereby the magnetostriction and other anisotropies' values show changes at low thicknesses [50, 91, 102]. In ultra-thin films there is another anisotropy called surface anisotropy, which was discussed first by Néel in 1956 [49]. It arises from the monolayer at the surface of the film, where it has a broken symmetry. In general, for any uniaxial energy term [55, 14]:

$$\epsilon = K_{eff} sin^2\theta \quad (1.20)$$

where K_{eff} is the effective anisotropy constant, with a value of:

$$K_{eff} = K_V + K_s/t \quad (1.21)$$

where the anisotropy constant includes two-terms: K_V is volume or bulk term; K_s is the surface term, and t is the thickness of the film. For ultra-thin films, the surface contribution of the anisotropy can be dominant.

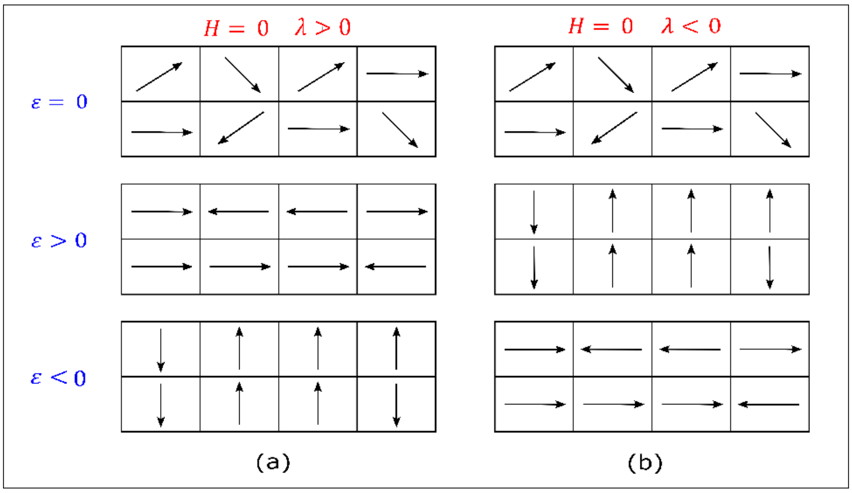

Figure 1.15: Schematic of the difference in the strain effect between (a) Material with positive magnetostriction $\lambda > 0$; (b) Material with negative magnetostriction $\lambda < 0$ (right) when $H = 0$. The effect of the strain on the magnetisation direction depends on the magnetostriction sign, applying a positive strain aligns the magnetisation easy axis in both materials to be perpendicular to each other.

1.2.2.5 Total energy

From the previous sections, the total free energy that can describe the behaviour of the energy of a system can be written as follows:

$$E_{total} = E_{exch} + E_{zeem} + E_{demg} + E_{mc} + E_{me} \quad (1.22)$$

where E_{exch} is the exchange energy associated with neighbouring spins, E_{zeem} is the Zeeman energy, E_{demg} is the demagnetising energy (shape energy), E_{mc} is the magnetocrystalline energy density, and E_{me} is the magnetoelastic energy density. For the ferromagnetic materials, the competition between these energies determines the system's magnetic properties, mainly the magnetisation direction, magnetic domain types, and the magnetisation reversal. Specific terms are used to discuss the magnetic reversal and ferromagnetic resonance of the ferromagnetic layers used in this study, as discussed in the next chapters.

1.2.3 Magnetic Domain and Magnetisation Reversal

1.2.3.1 Magnetic Domains and Domain Walls

In ferromagnetic materials, in the absence of applied magnetic field, magnetic anisotropy contributions determine the direction of the magnetisation in the sample. The magnetic moments tend to align along a preferential direction (easy axis), which generates a stray magnetic field outside the sample, which costs energy accordingly. The magnetisation splits into multiple regions called magnetic domains (as postulated firstly by Weiss) to minimise the stray magnetic field. Magnetic domains are formed as a result of minimising the free density energy of the ferromagnetic material. Figure 1.16 shows how the stray field decreases with increasing magnetic domains. A large variety of domain patterns exist in ferromagnetic samples, depending on properties and shapes.

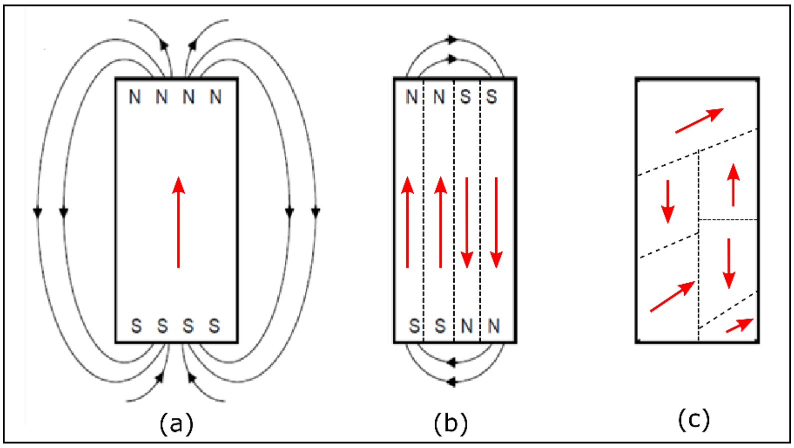

Figure 1.16: Schematic of magnetic domains in a magnetic material, (a) The magnetic material with one domain and large stray field; (b) Increasing magnetic domains decreasing the stray field; (c) No stray field, as more magnetic domains are formed to minimise free energy.

A domain wall exists in this case of the transition from one magnetic domain to another in the sample. The domain wall incurs an energy cost due to the exchange energy associated with pairs of non-parallel adjacent magnetic moments, and the magnetocrystalline anisotropy energy associated with magnetic moments lying away from the easy axes. The exchange energy prefers wide domain walls to reduce the angle between neighbouring magnetic moments, while the magnetocrystalline energy favours narrow domain walls to decrease the number of magnetic moments lying in non-easy directions. In general, the width and energy of the domain wall are determined by the competition between the exchange and magnetocrystalline energy [97, 103]. The domain wall energy can be expressed by the following equation:

$$E_{DW} = 2\pi\sqrt{AK_u} \tag{1.23}$$

where A is the stiffness constant, and K_u is the uniaxial anisotropy. The domain wall thickness that gives the minimum value from the energy in equation 1.23 is given by the equation:

$$\sigma = \pi\sqrt{\frac{A}{K_u}} \tag{1.24}$$

Two eminent domain wall types are shown in figure 1.17, Bloch wall and Néel wall. In both cases, the wall separates two regions with opposite magnetisation direction, and the moments in the wall rotate by 180^o from one domain to another. For Bloch wall, the rotation is out of the plane of the wall, and it is more common in the bulk material. The Néel wall is more common in thin films where the magnetisations rotate in the plane to minimise the stray field, whereby no surface charges [97, 103]. Figure 1.18 shows a phase diagram for the permalloy ($Ni_{80}Fe_{20}$) film for the energy density at different thicknesses, showing that Néel wall is preferred for thickness of less than $50nm$, as shown by the Neel-Bloch crossover [104].

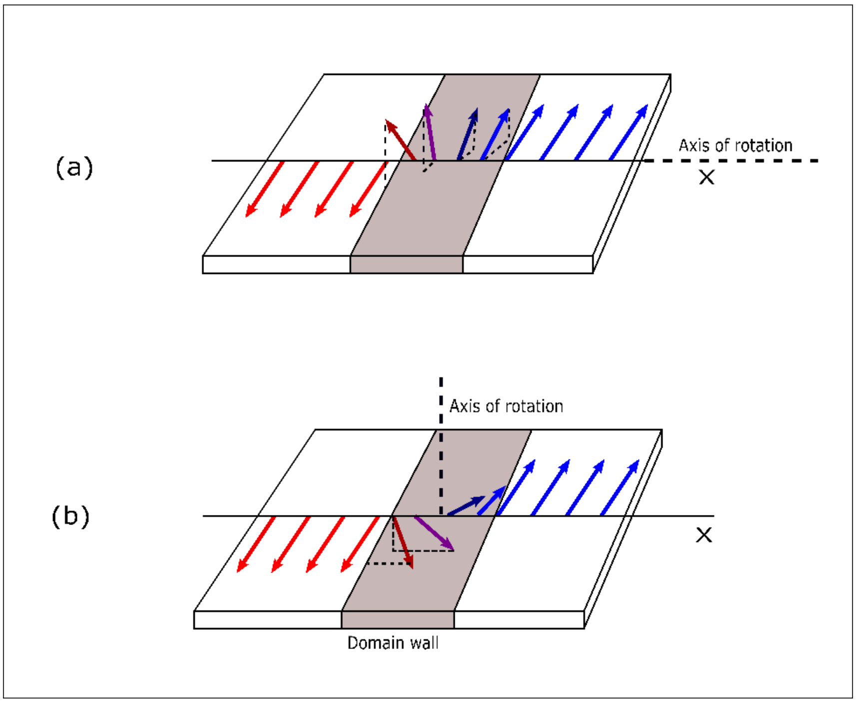

Figure 1.17: Schematic of domain walls type, (a) Bloch wall where the magnetisation rotates out of the planes; (b) Néel wall, where the magnetisation rotates in the same plane of the domain wall. The dashed lines represent the rotation axis, and the colour of the arrows represent changing in magnetisation directions.

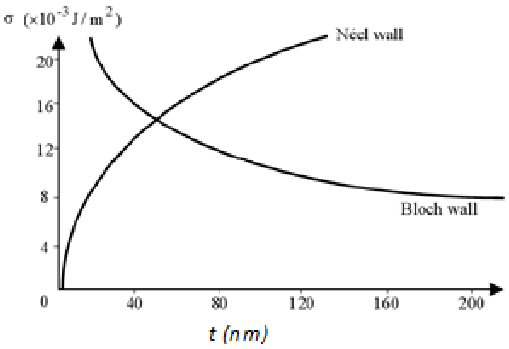

Figure 1.18: Phase diagram for the permalloy film showing that permalloy favours Néel walls for thickness less than $50nm$, where σ is the domain wall energy and t is the film thickness [104].

1.2.3.2 Magnetisation reversal

During the reversal of the magnetisation, the magnetic domains and domain walls undergo different movements, including nucleation, coherent rotation, pinning, and domain wall motion. When a polycrystalline (material with no easy axis preference) ferromagnetic material is localised in an increasing magnetic field, the magnetisation of the domains aligns along the field direction to reach a value of saturation magnetisation [96]. Figure 1.19 (a) shows the magnetisation reversal of a polycrystalline sample showing polar direction for the magnetisation at different points. At zero field value shown by O point, the material with net-zero magnetisation has no preferred magnetisation direction (i.e. it is isotropic), as shown by the circular schematic with arrows of the magnetisation averaging out to give zero magnetisation. As the magnetic field increases from zero to the positive field value at point B, the magnetisation, in this case, is aligned along the positive hemisphere, where the domain walls move erratically near the knee at point B, and the magnetisation direction of the magnetic domains point mostly towards the field direction. As the field increases to reach a value near the saturation field at point C, most of the moments align with the field.

In polycrystalline material, for the magnetisation reversal between $H = 0$ to the saturation field H_s (point (O) to point (C), it is hard to discern reasons behind the magnetisation change, which could be due to the domain walls' motion or domains' rotation or both. In general, the magnetisation changes from point O to point B is predominantly dominated by domain wall motion, while from B to C is dominant by domain rotation. The two processes could function in tandem to change the magnetisation direction in some regions completely. Figure 1.19 (b) shows an assumption of the magnetisation reversal processes between point O and point C, with the domain wall motion dominant over the magnetisation change until the knee, after which the reversal by domains rotation is dominated the magnetisation reversal until saturation status [50].

The field changes direction and decreases to zero at point D, which is called the remnant state, where the magnetisation (M_r) shows hysteresis. At this point, most of the magnetisation is still aligned with the positive field direction, and the single magnetic domain starts to nucleate in multi-domains. The remanence ratio of M_r/M_s could be calculated to distinguish between materials with different anisotropies [96]. Increasing the field in the negative direction to reach point E gives zero magnetisation value, where unstable domains reverse, and the ferromagnetic material reaches the demagnetisation state (where no direction is preferred). When the field reaches zero magnetisation it is known as the coercive field (H_C). When the field increases beyond point E in the negative direction, the domains start to grow and point towards the field direction, combined with the domain walls' propagation, and the magnetisation domains start to point to the direction of the saturation field. Then, the domains rotate coherently to the saturation field at negative saturation field. The point E' shown in the figure is the same as point E with opposite direction.

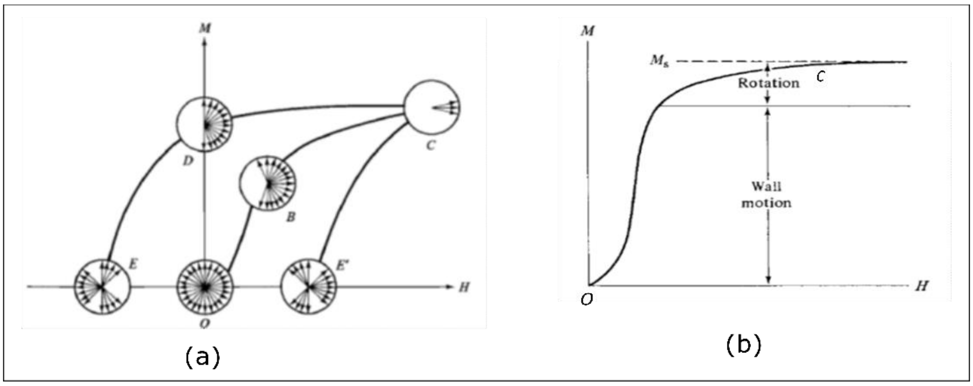

Figure 1.19: (a) Magnetisation reversal of polycrystalline material showing different points in the hysteresis with schematics of magnetisation direction [96]; (b) The curve of the magnetisation reversal represents the domain wall motion and domains rotation regions between $H = 0$ to $H = H_s$ [50].

In this study, a model based on Stoner-Wohlfarth model [105] of coherent rotation (single domain model) is used to model the magnetisation reversal of the permalloy layer to study the strain effect on the magnetostrictive properties of the permalloy. This model deals with the magnetisation of the ferromagnetic material as a uniform magnet during the magnetisation reversal process. The Stoner Wohlfarth model assumed ellipsoid particles uniformly magnetised throughout the magnetisation process. The easy axis lies along the long axis of the particle with uniaxial magnetic anisotropy which has an origin of a shape or a magnetocrystalline energy. When a magnetic field is applied along angle φ with respect to the easy axis, the free energy density is given by the equation:

$$\epsilon_{tot} = K_u \sin^2 - MHcos(\varphi - \theta) \tag{1.25}$$

The first term is the uniaxial term, the second term is the Zeeman energy, and θ is the angle between the magnetisation and easy axis, with coordinates illustrated in figure 1.20 (a). Minimising the energy ϵ_{tot} with respect to the θ

yields one or two energy minima. For a field range of two minima, the hysteresis is present and irreversible jump (switching) from one minimum to another minimum occurs. The hysteresis loops for Stoner-Wohlfarth particle at different angles φ are shown in figure 1.20 (b). For $\varphi = 0^o$ when the field is along the easy magnetisation direction, the M-H loop shows a square loop while for perpendicular direction $\varphi = 90^o$, the magnetisation only rotates toward the field direction with no switching.

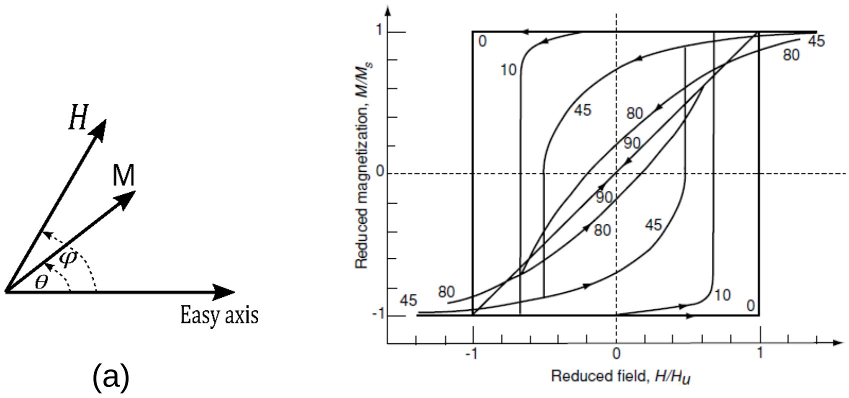

(a)

(b)

Figure 1.20: (a) Coordinate system used in the Stoner-Wohlfarth model, and (b) hysteresis loops for Stoner-Wohlfarth particles at different angles φ between the field and the easy axis [14], H_u represents the uniaxial field.

1.2.4 Magneto-Transport phenomena

1.2.4.1 Anisotropic magnetoresistance (AMR)

Magnetoresistance was first discovered by Lord Kelvin in 1956; he observed that the resistance of nickel and iron changes when the magnitude and direction of the applied magnetic field are changed [1]. This transport property later named anisotropic magnetoresistance (AMR) by Smit [106] concerns the resistivity of the magnetic material depending on the angle between the magnetisation M and the current density J. The AMR arises from the spin-orbit coupling, which introduces anisotropic scattering between the spin-up and spin-down electrons [2]. In magnetic transition metals (Ni, Fe, and Co), both s and d states are at the Fermi level, and the spin-up and spin-down electrons are not necessarily equal. Figure 1.21 shows the band structure of the transition metal (Fe, Co, and Ni), where it can be seen that there is a shift in the sub-bands of d states, and hence the two current densities of spins are different. The hybridisation of s and d levels leads to more scattering between localised d electrons and free s electrons [55]. The scattering probabilities at the Fermi level are different for the spin-up and spin-down electrons, which determines the magnetic properties of the material. For instance, from the band structure of iron, the Fermi level intersects both d sub-levels, hence iron exhibits week ferromagnetism compared to Ni and Co [107]. The AMR ratio from the developed model of two currents by Campbell, Fert, and Joual [108] is equal to:

$$\frac{\Delta R}{R} = \frac{R_{\parallel} - R_{\perp}}{R_{\perp}} = \gamma[\left(\frac{R_{\downarrow}}{R_{\uparrow}}\right) - 1] \tag{1.26}$$

where $R_{\parallel}$ is the longitudinal resistance when the current direction is parallel to the magnetisation of the material, $R_{\perp}$ is the transverse resistance when the current is perpendicular to the magnetisation, γ is proportionality with a value of 0.01 for $3d$ transition metals [109], and $\frac{R_{\downarrow}}{R_{\uparrow}}$ is the ratio between the resistance of the spin-up and spin-down electrons. The values of $\frac{\Delta R}{R}$ and $\Delta \mathrm{R}$ for different metals at room temperature show very small values with low percentages at room temperature.

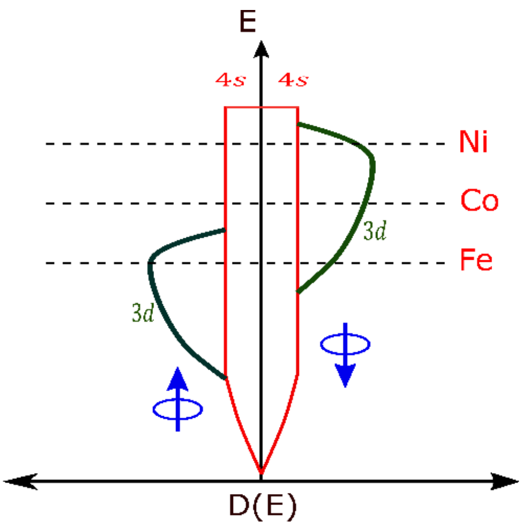

Figure 1.21: Schematic representation of the densities of states of transition metals (Fe, Co, and Ni), showing different densities of the spin-up and spin-down electrons (blue arrow) at the Fermi level.

The longitudinal and transverse resistances can be understood phenomenologically from figure 1.22, where a ferromagnetic sample has magnetisation $\boldsymbol{M}$, localised in the electric field $\boldsymbol{E}$ with two components, parallel $E_{\parallel}$ and perpendicular$E_{\perp}$. The current density that flows in the sample is J and can be decomposed into two components, $J_{\parallel}$ and $J_{\perp}$. From Ohm's law, the electric field can be written as [110]:

$$\boldsymbol{E} = \boldsymbol{J}\rho \tag{1.27}$$

where ρ is the resistivity of the sample; hence, the two components of $\boldsymbol{E}$ can be written as:

$$E_{\parallel} = J_{\parallel}\rho_{\parallel} \tag{1.28}$$

$$E_{\perp} = J_{\perp}\rho_{\perp} \tag{1.29}$$

where $\rho_{\parallel}$ is the longitudinal resistivity when the current direction is parallel to the magnetisation of the material and $\rho_{\perp}$ is the longitudinal resistivity when the current is perpendicular to the magnetisation. The longitudinal electric field can be given by:

$$\boldsymbol{E_x} = E_{\parallel}\cos\theta + E_{\perp}\sin\theta$$

$$E_x = |J|\rho_{\parallel}\cos\theta\cos\theta + |J|\rho_{\parallel}\sin\theta\sin\theta$$

$$E_x = |J|(\rho_{\parallel}cos^2\theta + \rho_{\perp}sin^2\theta) \tag{1.30}$$

From equation 1.28 and 1.29 in equation 1.30, the angular dependence of the longitudinal resistivity is given by [111]:

$$\rho_{xx}(\theta) = \rho_{\parallel}\cos^2\theta + \rho_{\perp}\sin^2\theta$$

$$\rho_{xx}(\theta) = \frac{(\rho_{\parallel}+\rho_{\perp})}{2} + \frac{1}{2}(\rho_{\parallel} - \rho_{\perp})\cos2\theta$$

$$\rho_{xx}(\theta) = \rho_{avg} + \Delta\rho\ cos2\theta \tag{1.31}$$

Hence, the angular dependence of the longitudinal resistance can be written as:

$$R_{xx}(\theta) = R_{avg} + \Delta R\ \cos2\theta \tag{1.32}$$

where θ is the angle between the current and the magnetisation, as shown in figure 1.22, and ρ_{avg} and R_{avg} are the average resistivity and resistance of the material when the magnetisation rotates by 360^o. Figure 1.23 shows an example of rotational R_{xx} for the permalloy (S476) sample fitted to equation 1.32. Similarly, for the transverse resistance:

$$\rho_{xy}(\theta) = (\rho_{\parallel} - \rho_{\perp})\cos\theta\sin\theta$$

$$\rho_{xy}(\theta) = \frac{1}{2}(\rho_{\parallel} - \rho_{\perp})\, sin2\theta$$

$$\rho_{xy}(\theta) = \Delta\rho\,\sin2\theta$$

or

$$R_{xy}(\theta) = \Delta R\,\sin2\theta \tag{1.33}$$

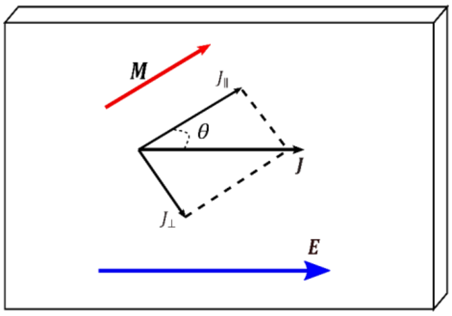

Figure 1.22: The schematic used to derive the longitudinal and transverse resistance, representing a ferromagnetic sample localised in an electric field $\boldsymbol{E}$. $\boldsymbol{J}$ is the current density that flows in the sample, and θ is the direction between the magnetisation and the current.

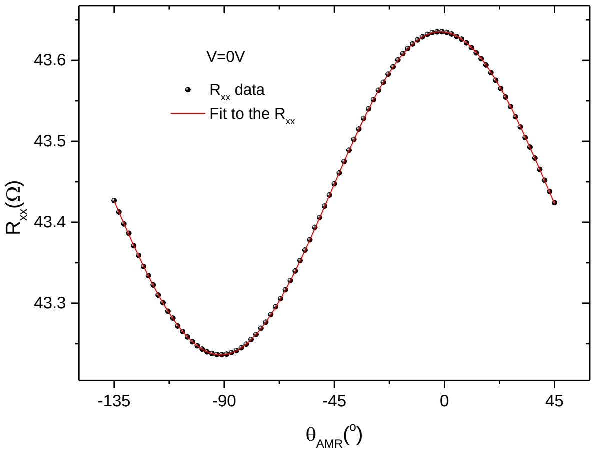

Figure 1.23: The rotation R_{xx} measurements at $0V$ for the sample S476, along with the fit from equation 1.32.

1.2.4.2 Giant magnetoresistance (GMR)

The giant magnetoresistance (GMR) is one of the most significant discoveries in spintronics found by two separate groups, one led by P. Grünberg [6] and the other by A. Fert [5]. They found a remarkable change in the resistance of the multilayered system of ferromagnetic layers separated by a non-magnetic spacer. The Grünberg group studied the role of Cr layer thickness in Fe/Cr/Fe sandwich, where the interlayer between the ferromagnetic changes to give the maximum value for the antiferromagnetic coupling. The Fert group measured the resistance of multilayers (superlattices) with different numbers of layers of Fe/Cr at $4.2K$ as a function of the magnetic field, examples of the measurements of which are shown in figure 1.24 (a). They found that the GMR change was in the range of 80% for the structure [(Fe 30Å/Cr 9Å)]$_{40}$. Unlike AMR, GMR does not depend on the direction of the magnetisation with respect to the current direction; rather, it depends on the magnetisation orientation of the successive magnetic layers. Figure 1.24 (b) shows a schematic of multilayers with different magnetisation direction, and how that reflects on the magnetoresistance curves shown in figure 1.24 (a). On the other hand, it has a bigger value; for instance, Parkin et al [10]. found that for multilayer system of Co/Cu, the GMR can reach 110% and 220% at RT and $4.2K$, respectively, compared to lower percentages for AMR. The GMR value also depends on the material choices and thickness (F/NM), where F is the ferromagnetic material, and NM is the non-magnetic material, like Cr, Cu, Ru, Au, and Ag. The GMR magnitude (MR ratio) is given by [50, 55, 112]:

$$GMR = \frac{\Delta R}{R} = \frac{R_{AP} - R_P}{R_P} \tag{1.34}$$

where the R_{AP} is the resistance when the magnetisations in the successive layers are anti-parallel, while R_P is the resistance when the magnetisation in the ferromagnetic layers are aligned in parallel. The MR ratio varies as the magnetisation orientation on the adjacent layers changes, as explained in the following [112]:

$$\frac{\Delta R(\psi)}{R} = (\frac{\Delta R}{R})_{GMR} \frac{(1 - cos\psi)}{2} \tag{1.35}$$

where ψ is the angle between the magnetisation in successive ferromagnetic layers. The GMR reaches its maximum value when the magnetisations in successive layers are in the opposite direction to each other with $\psi = 180^o$.

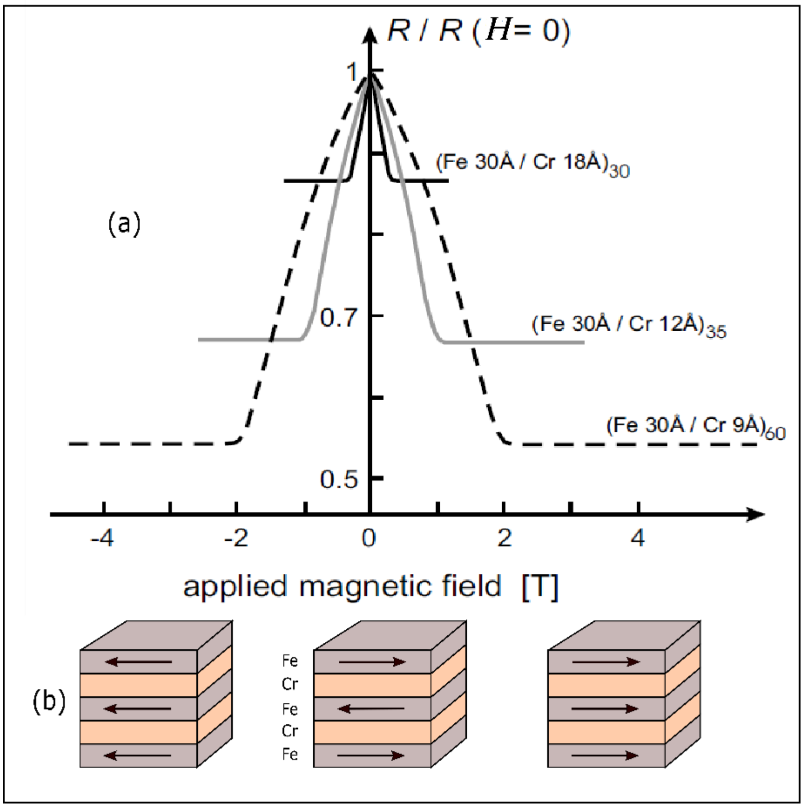

Figure 1.24: (a) Magnetoresistance curves for three superlattices of Fe/Cr measured at $4.2K$ by Fert group [5]. The magnetic field is applied parallel to the plane of layers and to the electric current. (b) Schematics of the Fe layers orientations showing that the maximum value of the GMR is given for the antiparallel alignment, while it is minimum when the magnetisations are parallel to each other.

1.2.4.2.1 Mott's two current model

GMR can be understood using Mott's two-current model for conductivity in magnetic materials and band structure [7, 113]. The total conductivity can be expressed from the spin-up electrons S↑ and spin-down electrons S↓, both of which are considered separate channels. As mentioned previously, for ferromagnetic material at the Fermi level, the density of state (DOS) is different for spin-up and spin-down electrons, as shown in figure 1.21. In this case (given the majority spin direction when the spin polarisation is parallel to the magnetisation direction of the ferromagnetic layer), the scattering is less due to less empty states for majority spin direction, and hence the resistance in that channel is low. Scattering increases for the minority spin as there are more empty states for this spin direction when the spin polarisation is opposite to the magnetisation direction in the ferromagnetic layer, and the resistance in that channel increases. Figure 1.25 shows band structures of an example of ferromagnetic layers separated by a non-magnetic layer for two magnetic configurations: when the magnetisations of the layers are parallel (a); and antiparallel (b).

As can be seen for the parallel configuration, the scattering is always greater in one channel (spin-down) since the electron spin polarisation is the opposite to the magnetisation direction in both layers. For another configuration in 1.25 (b), the scattering in both channels is the same, since the direction of magnetisation with respect to the spin polarisation is opposite in both cases, hence the scattering is high in both channels. For the non-magnetic layer, the spin-up and spin-down have the same scattering probability at the Fermi level; thus, the spin electrons pass the non-magnetic layer with equal probability [110]. The resistance series for the corresponding layers in 1.25 (a) and (b) related to the scattering in both channels is discussed above. $R^{\uparrow}$ represents the spin-up channel and $R^{\downarrow}$ represents the spin-down channel resistance, both of which are connected in parallel. For the parallel configuration, there is less resistance for spin-up $R^{\uparrow}$ compared to spin-down $R^{\downarrow}$, as the scattering is only in the spin-up direction. For the antiparallel alignment in 1.25 (b), the scattering is in both spin directions, hence it shows a bigger resistance compared to the parallel configuration.

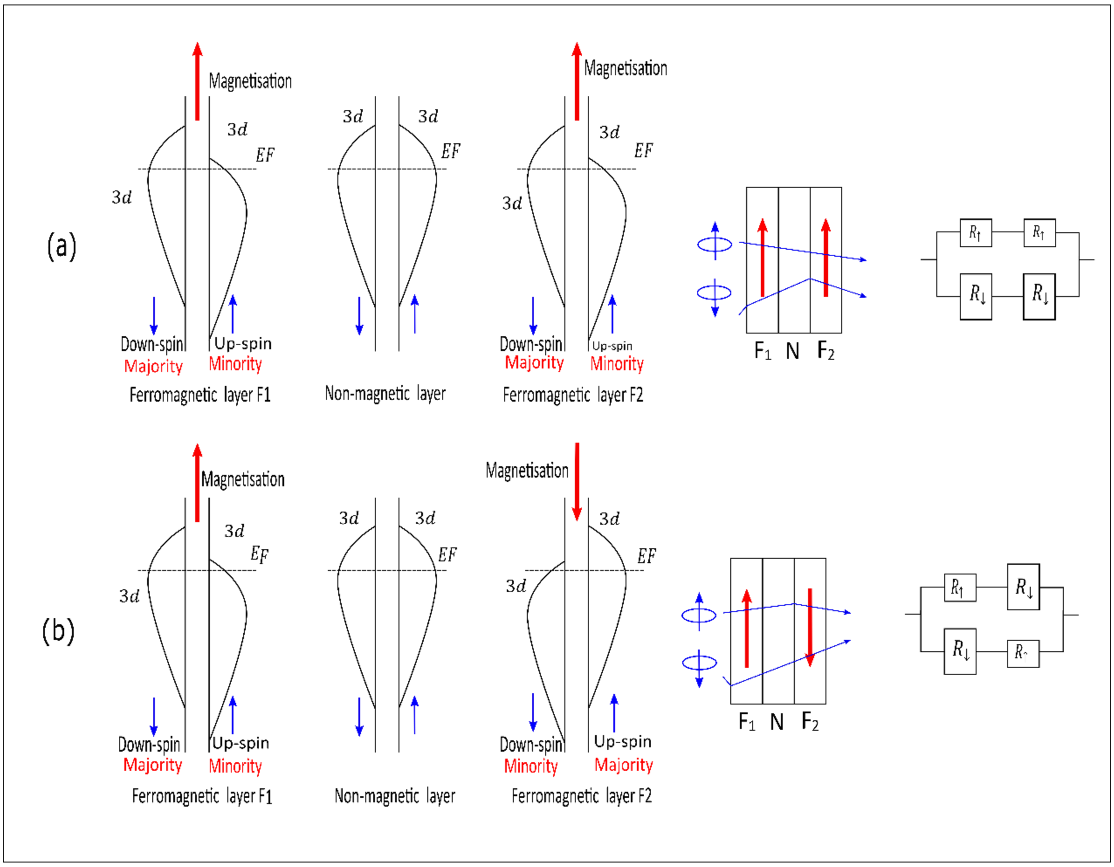

Figure 1.25: Schematics of the two spin currents model of (a) Parallel configuration and (b) Antiparallel configuration using the band theory of materials. For antiparallel configuration, the spin scattering is in both channels, while it is just in one channel for the parallel configuration. Hence the antiparallel configuration shows more resistance.

The resistance of the parallel and antiparallel states can be expressed, respectively, as [112]:

$$R_P = (\frac{1}{R^{\uparrow}} + \frac{1}{R^{\downarrow}})^{-1} \tag{1.36}$$

and

$$R_{AP} = (R^{\uparrow} + R^{\downarrow})/4 \tag{1.37}$$

where $R^{\uparrow}$and $R^{\downarrow}$ are the resistance of spin-up and spin-down channels. The GMR ratio can be expressed as:

$$GMR = \frac{R_{AP} - R_P}{R_P} = \frac{(1-\alpha)^2}{4\alpha} \tag{1.38}$$

where $\alpha = \frac{R^{\uparrow}}{R^{\downarrow}}$ is introduced as the scattering asymmetry. The GMR ratio increases when the difference between the spin-up and spin-down resistance increases [14, 112].

1.2.4.2.2 Spin-valve System

A spin valve is a structure in which two ferromagnetic layers are separated by a non- magnetic material, as illustrated in Figure 1.26. The first layer, called the reference, or pinned layer, which is pinned by an exchange bias to an antiferromagnetic layer (AFM), while the second is called the free, sensor, or soft layer. A small magnetic field could switch the magnetic moment's direction of the soft layer to be parallel or antiparallel to the reference layer magnetisation, depending on the exchange bias field direction. Changing the direction of the magnetisation leads to changes in resistance (i.e. the GMR effect) [50, 112]. The non-magnetic spacer between the ferromagnetic layers is used to eliminate the coupling between the free and pinned layers.

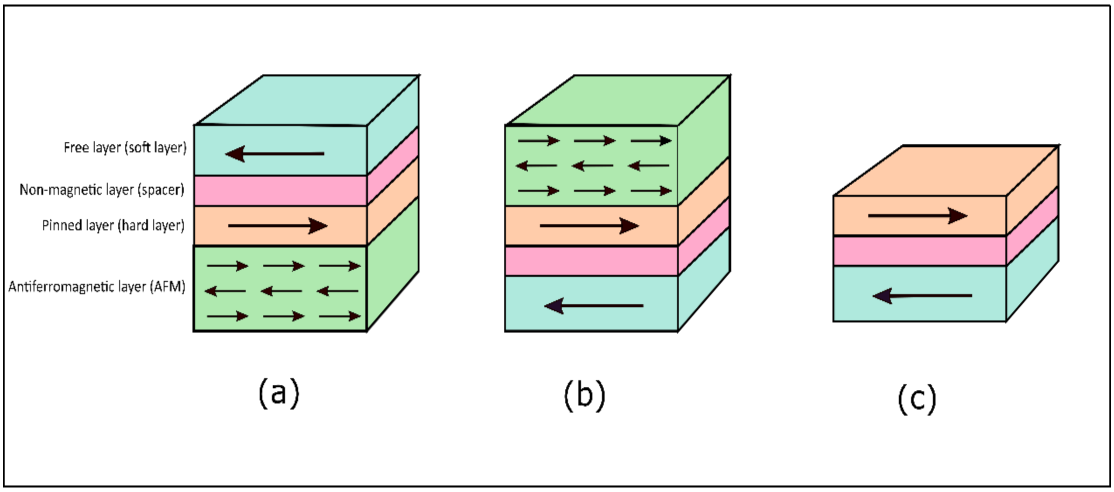

Figure 1.26: (a) Bottom spin valve structure with antiferromagnetic layer at the bottom to pin one ferromagnetic layer while the other magnetic layer is free, (b) Top spin valve; and (c) pseudo spin valve, with two free magnetic layers having different coercivities.

There are two types of spin valves depending on the position of the antiferromagnetic material. The first is the bottom spin valve (BSV), for which the AFM is deposited on the bottom of the spin valve, as shown in figure 1.26. The second type is the top spin valve (TSV), for which the AFM is deposited on the top of the multilayer structure, and hence the hard layer is lower than the AFM layer. In this thesis, for the strain study purpose, the TSV structure was used, whereby the strain can affect the ferromagnetic layers directly. There is another classification of spin valves that depends on the current direction with respect to the layers: current in plane (CIP) and current perpendicular to the plane (CPP) spin valve, as shown in figure 1.27 (a) and (b) (respectively). The CIP configuration gives a smaller GMR effect, since each layer has its conductivity, which could shunt the GMR effect, while for the CPP, the spin current has to pass the whole spin valve [98]. In this thesis, CIP spin valve is used since it is easier to prepare for fabrication and measurement. Furthermore, for the strain measurement, applying a strain to a specific layer could control the effect of the strain in the whole spin valve (according to which layer is in the direct response to the strain effect).

There is another type of spin valve called the pseudo spin valve, which includes free ferromagnetic layers without an antiferromagnetic layer, as shown in figure 1.26 (c). In this case, these layers should have different switching fields to achieve antiparallel alignment. To achieve this, two different materials with different coercivities should be chosen, or changing thickness or compositions when using the same metal [14]. In this study, two pseudo spin valves were used with two different materials, $Ni_{80}Fe_{20}$ and Ni. Figure 1.28 shows a magnetoresistance curve for IM008 pseudo spin valve sample with free Ni and $Ni_{80}Fe_{20}$. The magnetoresistance in this case shows symmetric curves around zero field, as both layers are free. The magnetoresistance curve exhibits a defined plateau when the two magnetic materials have two different coercivities, with no coupling through the non-magnetic spacer. The magnetoresistance value of the spin valve could be enhanced by varying the types and thicknesses of ferromagnetic and non-magnetic materials; however, this is out of the scope of this study.

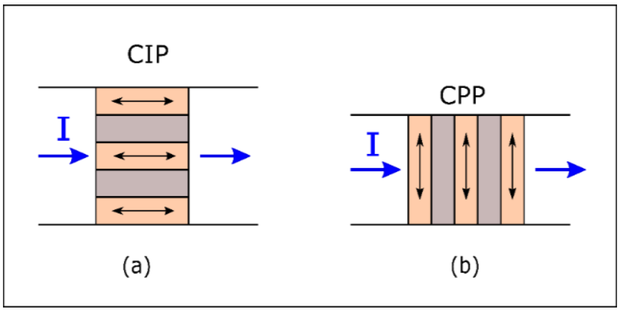

Figure 1.27: (a) Current in plane (CIP) spin valve; (b) Current perpendicular to the plane (CPP) spin valve.

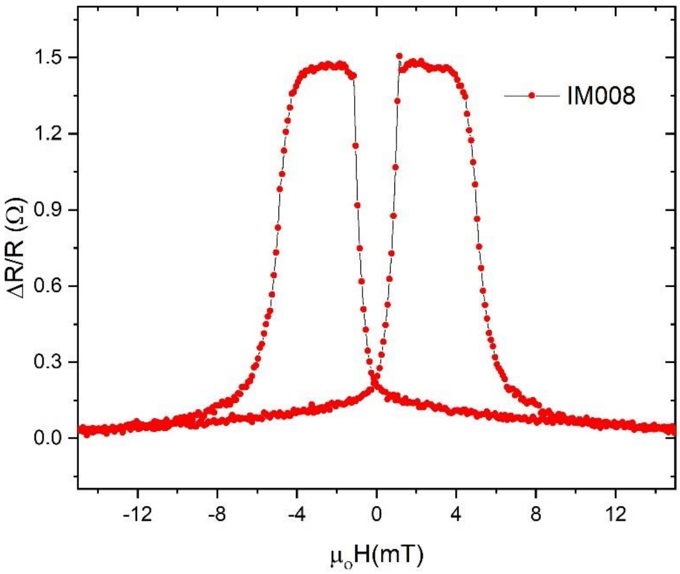

Figure 1.28: The magnetoresistance curve for the IM008 pseudo spin valve with two free layers, Ni and NiFe. The MR curves are symmetric around the zero-field, as there is no exchange bias in the spin valve. The plateau in the curves represents the different coercivities of Ni and NiFe.

1.2.5 Antiferromagnetism and exchange bias

1.2.5.1 Antiferromagnetism

An antiferromagnet is a substance in which magnetic moments are aligned antiparallel. Antiferromagnetic material has a small positive susceptibility, and it increases to reach its maximum at Néel temperature T_N, as shown in figure 1.29. The paramagnetic susceptibility of the antiferromagnetic material (AFM) above T_N follows the Curie-Weiss law discussed in section 1.2.1 for the ferromagnetic material, to follow [55]:

$$\chi_{AFM} = \frac{C}{T-\theta_W} \tag{1.39}$$

In AFM material, θ_W is the Weiss constant with $\theta_W < 0$. Antiferromagnetic substances are paramagnetic above the T_N. As described in section 1.2.1, the exchange interaction plays a crucial role in determining the alignment of neighbouring moments. Figure 1.10 shows that for low distance ratio ${r_{ab}}/{r_d}$, $J_{ex} < 0$, hence the adjacent moments are aligned antiparallel to each other (see the inset at the bottom of figure 1.10). Antiferromagnetic materials have different T_N values. Table 1.4 states selected antiferromagnetic materials with their Néel temperature.

Table 1.4: Néel temperature of selected antiferromagnetic material in K [14]

	Cr	Mn	FeMn	IrMn
T_N (K)	311	96	510	690

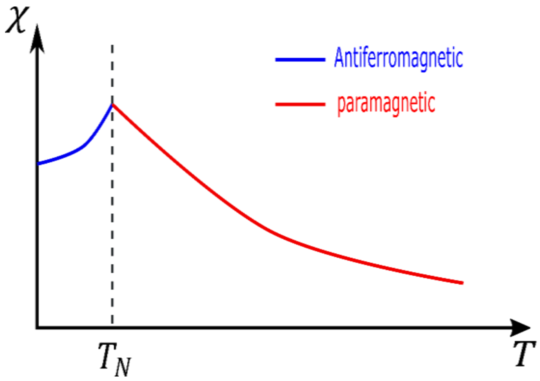

Figure 1.29: Temperature dependence of the magnetic susceptibility of AFM material.

1.2.5.2 Exchange bias

Exchange bias was discovered in 1956 by Meiklejohn and Bean [114], they observed a shift in magnetic hysteresis loop in the H-axis of cobalt nanoparticles after cooling in a magnetic field, and subsequently found that Co particles' oxidised and were partially coated by an antiferromagnetic layer of CoO. Exchange bias (unidirectional anisotropy) refers to the pinning effect between ferromagnetic (FM) and antiferromagnetic (AFM) layers in which the magnetisation of FM is pinned to the AFM layer. The exchange bias is obtained by cooling the system from temperature $T_N < T < T_C$ in a saturation magnetic field of the ferromagnetic layer [110]. In this case, the ferromagnetic material is aligning along the field direction, while the antiferromagnetic material is randomly oriented (paramagnetic state). When the temperature decreases to $T_B < T < T_N$, T_B is the blocking temperature where the antiferromagnetic layer cannot pin the neighbouring ferromagnetic layer [115]. At the interface between the ferromagnetic and antiferromagnetic layers, the moments align ferromagnetically with the antiferromagnetic layer for the ideal situation. From the experiment conducted by Meiklejohn and Bean for Co particles [114], figure 1.30 shows the difference between two hystereses; the symmetric hysteresis loop around zero field represents the hysteresis of particles when cooling down in the absence of the magnetic field, while the shifted hysteresis loop (solid line) represents when the particles cooled down in a saturation magnetic field. The shift in the hysteresis loop represents the exchange bias field (H_{eb}), and can be calculated using the following equation [116]:

$$H_{eb} = \frac{H_{c1}+H_{c2}}{2} \tag{1.40}$$

where $H_{c1}$and H_{c2} are the coercive fields in both sides of the hysteresis loop. The exchange anisotropy term in the free energy density of an exchanged biased system can be written as:

$$E_{eb} = -J_{eb}\cos(\theta_{eb}) \tag{1.41}$$

where $-J_{eb}$is the interlayer exchange coupling constant between the ferromagnetic and antiferromagnetic layers, and θ_{eb} is the angle between the uniaxial anisotropy of the pinned ferromagnetic material and the biased field. The exchange bias field depends linearly on the interfacial constant in the following equation:

$$H_{eb} = \frac{-J_{eb}}{M_F t_F} \tag{1.42}$$

where the M_F and t_F are the saturation magnetisation and the thickness of the ferromagnetic pinned layer, respectively. The H_{eb} shows inverse dependence with the pinned layer thickness [116, 117]. On the other hand, the value of T_B varies and depends on the structure and thickness of AFM material [118, 119]. The thickness of the AFM material also affects the H_{eb} and H_c. Two exchange biased systems in two different studies show that the H_{eb} and H_c have a clear dependence on the thickness of the AFM, IrMn/FeNi [120] and IrMn/Co [115]. In this study, a layer of IrMn is used in two spin valves to pin the ferromagnetic layer to enhance the antiparallel alignment of the magnetic layers. As shown in table 1.4, IrMn has high T_N compared to most AFM materials, with a value of $690K$.

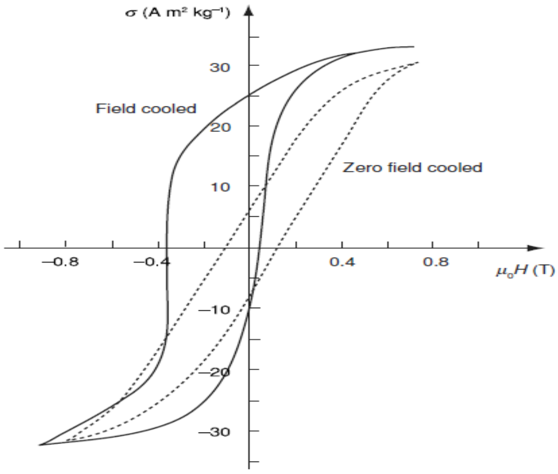

Figure 1.30: Hysteresis loops of the Co particles coated with CoO. The symmetric hysteresis around zero field represents the magnetisation reversal of the particles cooled without saturation field, while the shifted hysteresis is for the Co particles cooled in a saturation field [114].

The coercive field H_c in an exchange biased system is also connected to the exchange bias field. H_c can be expressed as:

$$H_c = \frac{-H_{c1}+H_{c2}}{2} \tag{1.43}$$

The coercivity of the pinned layer usually increases below the blocking temperature T_B, as proven in many comparable systems with the same ferromagnetic and antiferromagnetic materials and thickness [121, 122, 123]. This is attributed to the anisotropy of the AFM material. For AFM material with weak anisotropy, below T_B, the ferromagnetic material can drag the AFM moments irreversibly, which increases the coercivity of the ferromagnetic material [124].

1.2.6 Magnetisation dynamics

This section discusses magnetisation dynamics, starting with the motion of magnetic moments in relation to the theory and mathematical understanding of ferromagnetism. Magnetisation damping and its relation with the field linewidth along with the reasons behind intrinsic and extrinsic damping are described in detail.

1.2.6.1 Motion of magnetic moments

In order to explain the dynamic of the magnetisation, Landau and Lifshitz [125] described a model to discuss the effect of the microwave field $\boldsymbol{H_{rf}}$ perturbation on the magnetic dipoles in an effective field $\boldsymbol{H_{eff}}$. The time-evolutions of the magnetisations can be expressed by the first term of Landau and Lifshitz's equation:

$$\frac{dM}{dt} = -\gamma M \times H_{eff} \tag{1.44}$$

where γ is the gyromagnetic ratio with a value of $\frac{ge}{2m_e}$ [126], and g is the Landé-g factor, with $g \simeq 2$ for the free electron. The effective field $\boldsymbol{H_{eff}}$ can be introduced as:

$$\boldsymbol{H_{eff}} = \frac{1}{\mu_o}\frac{\partial \epsilon_{tot}}{\partial M} \tag{1.45}$$

where ϵ_{tot} is the free energy density discussed in section 1.2.2.5, consisting of different contributions as stated in equation 1.22. The first term of Landau and Lifshitz's equation describes the precessional motion of the magnetisation around the effective field, as induced by the torque experienced by the magnetic moments as it moves around the effective field. The angular velocity of the magnetisation around the effective field yielded from equation 1.44 is called Larmor angular velocity:

$$\omega_L = \gamma \boldsymbol{H_{eff}} \tag{1.46}$$

The first term of Landau and Lifshitz's equation assumes that there is no dissipation and the motion will remain in the trajectory of the magnetisation away from its equilibrium, as shown in figure 1.31 (a)[127, 128]. In reality, there is always a dissipation term in the magnetisation motion that leads the magnetisation to align along the effective field direction as proposed by Gilbert [129] in 1955, added as a second term in the equation of motion as follows:

$$\frac{d\boldsymbol{M}}{dt} = -\gamma \boldsymbol{M} \times \boldsymbol{H_{eff}} - \frac{\gamma\alpha}{M_s}\left[\boldsymbol{M} \times (\boldsymbol{M} \times \boldsymbol{H_{eff}})\right] \tag{1.48}$$

This is now known as the Landau-Lifshitz-Gilbert (LLG) equation, where α is the Gilbert damping parameter, which is responsible for bringing the magnetisation to equilibrium, as shown in figure 1.31 (b).

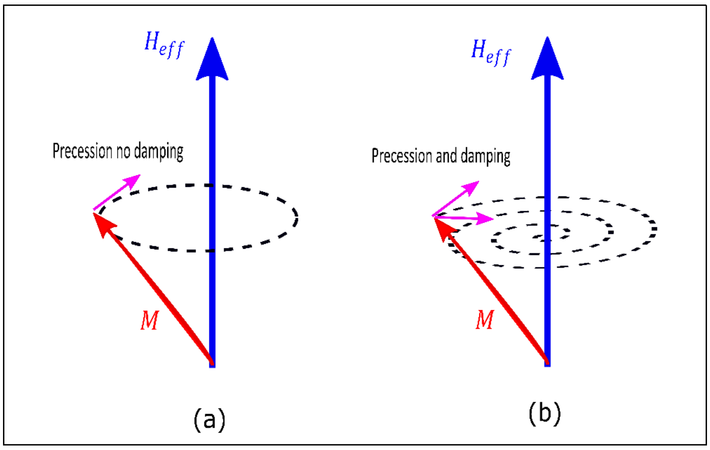

Figure 1.31: Schematic representations of the magnetisation dynamic around the effective field showing (a) The precessional motion without damping and (b) The magnetic moments spiralling down to align the effective field because of the damping term.

1.2.6.2 Ferromagnetic resonance FMR

The ferromagnetic resonance phenomenon occurs when the magnetisation vector of a ferromagnetic material is perturbed with a microwave field $\boldsymbol{H_{rf}}$ and experiences a torque in $\boldsymbol{H_{eff}}$; the magnetisation precesses and the resonance condition are fulfilled when the precession frequency of the magnetisation coincides with the microwave frequency of the $\boldsymbol{H_{rf}}$ [126]. The FMR absorption of microwave power lineshape is used to determine the ferromagnetic properties, namely magnetic anisotropies, saturation magnetisation, damping parameter, and curie temperature [130, 131]. The resonance condition can be solved using the LLG equation to extract the magnetic properties of the ferromagnetic material [132, 133]. Equation 1.44 is used to determine the resonance condition [134], using the spherical coordinates shown in figure 1.32, where the magnetisation and magnetic field directions are represented by azimuthal and polar angles to give the resonance condition as follows:

$$\left(\frac{\omega_{res}}{\gamma}\right)^2 = \frac{1}{\boldsymbol{M}^2 \sin^2\theta}\left[\frac{\partial^2\epsilon}{\partial\theta^2}\frac{\partial^2\epsilon}{\partial\varphi^2} - \left(\frac{\partial^2\epsilon}{\partial\theta\partial\varphi}\right)^2\right]_{\varphi_o,\theta_o} \tag{1.49}$$

where φ and θ are the azimuthal and polar angles of the magnetisation, while φ_o and θ_o are the equilibrium angles of $\boldsymbol{M}$. To solve the ferromagnetic resonance, the second derivative of the free energy density ϵ (equation 1.22) with respect to the spherical coordinates of the magnetisation is needed. This is discussed in detail in section 2.5.1 for the energy of the system used in this study to find the field resonance H_{res}. The linewidth of the absorption ΔH (full-width half maximum of the absorption) is calculated by [135]:

$$\Delta H = \frac{\alpha}{d\omega_{res}/dH}\frac{\gamma}{\boldsymbol{M}}\left(\frac{\partial^2\epsilon}{\partial\theta^2} + \frac{1}{\sin^2}\frac{\partial^2\epsilon}{\partial\varphi^2}\right) \tag{1.50}$$

The calculation for ΔH is also discussed in section 2.5.1 for the system used in this study.

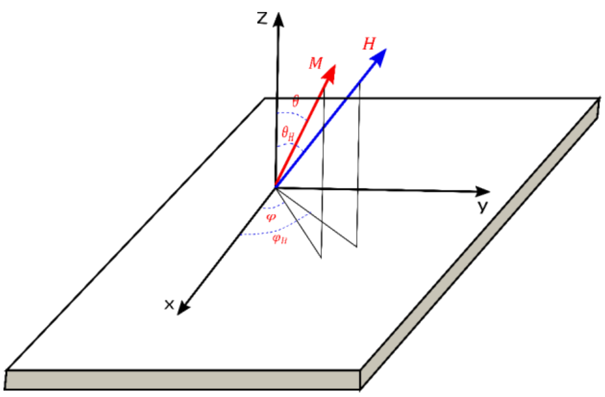

Figure 1.32: Schematic representation of the magnetisation and field direction in the coordinates used to calculate the ferromagnetic resonance.

1.2.6.2.1 Ferromagnetic resonance damping

As mentioned for the FMR phenomenon, the magnetisation vector precesses around the effective magnetic field until it is damped to lie parallel to the effective field direction. The damping in the second term of the LLG equation (equation 1.48) is behind the alignment of the magnetic vector along the field direction. In the FMR measurement, damping can be characterised by the linewidth ΔH [136]:

$$\Delta H = \Delta H_o + \frac{2\pi\alpha f}{\gamma} \qquad (1.51)$$

where ΔH_o is the extrinsic contribution to the damping, while the second term is the intrinsic contribution to the damping and is dependent on the frequency. The intrinsic term is usually isotropic for the $3d$ transition metals, while the extrinsic term is strongly dependent on the crystallographic defect and magnetic inhomogeneity in the ferromagnetic sample. The intrinsic damping is raised due to eddy currents, phonon drag mechanism, and electron spin-orbit-relaxation processes. On the other hand, the extrinsic term is related to different factors such as magnetic inhomogeneity, mosaicity, two magnon scattering (TMS), and spin pumping. The next subsection discusses intrinsic and extrinsic damping in detail [136].

1.2.6.2.1.1 Intrinsic damping

The intrinsic damping in ferromagnetic films can be related to the different contributions. Eddy currents contribute to the magnetisation vector relaxation. These currents are produced in the film when applying an alternating field, which appears as an extra relaxation term in the Gilbert damping, manifest as a broadening in the linewidth. The damping contribution introduced by eddy currents is given by [137]:

$$\alpha_{eddy} = \frac{1}{6} M_s \gamma \left(\frac{4\pi}{c}\right)^2 \sigma t_F^2 \qquad (1.52)$$

where c is the velocity of light in the free space, σ is the ferromagnetic film conductivity (which is proportional to dissipation), and t_F is the film thickness. The films used in this study (Ni ($5nm$) and $Ni_{80}Fe_{20}$ ($4nm$)) are very thin, and the eddy current contribution to the damping is negligible for thin films [136].

Another contribution to the intrinsic damping is the magnon-phonon scattering. Suhl studied the effect of phonon drag on magnon relaxation using small geometries to assume that the magnetisation and strain are homogeneous. Using the LLG equation and equation of motion for strain gives the Gilbert phonon damping [136]:

$$\alpha_{phonon} = \frac{2\eta\gamma}{M_s}\left(\frac{B_2(1+\nu)}{\Upsilon}\right)^2 \tag{1.53}$$

where η is the magnon phonon viscosity, B_2 is the magnetoelastic shear constant, ν is the Poisson ratio, and Υ is the Young's modulus. The most important contribution to the intrinsic damping is the spin-orbit coupling, first proposed by Heinrich et al. [138], which is related to the itinerant electrons and the interaction between sp like electrons with static d spins. Two electron mechanisms (intraband and interband transitions) are proposed with two different damping parameters [136]:

$$\alpha_{SO}^{intra} \simeq \frac{\langle S\rangle^2}{M_S\gamma}\left(\frac{\xi}{\hbar}\right)^2\left(\sum\chi_P^{\mu}\langle\mu|L^+|\mu\rangle\langle\mu|L^-|\mu\rangle\right)\tau_m \tag{1.54}$$

$$\alpha_{SO}^{inter} \simeq \frac{\langle S\rangle^2}{M_S\gamma}(\Delta g_\alpha)^2\frac{1}{\tau_m} \tag{1.55}$$

where $\langle S\rangle$ is the reduced spin $M_s(T)/M_S(0)$, ξ is the spin-orbit interaction coefficient, χ_P^{μ} is Pauli susceptibility for a given Fermi sheet, L^+ $|L^-|$ are the right and left-handed components of the atomic site transverse angular momentum, τ_m is the momentum relaxation time, and Δg_α is the deviation from g-factor value [136].

1.2.6.2.1.2 Extrinsic damping

There are different contributions to extrinsic damping, which are related to the quality of the sample. As discussed for the linear equation in 1.51, ΔH_o represents the extrinsic term damping, while $\frac{2\pi\alpha f}{\gamma}$ represents the intrinsic damping. This equation can be extended to include different external contributions of linewidth as follows:

$$\Delta H = \frac{2\pi\alpha f}{\gamma} + \Delta H^{inhom} + \Delta H^{mosaic} + \Delta H^{2mag} \tag{1.56}$$

where the first term represents the intrinsic part of the linewidth, while others represent the extrinsic contributions to the damping (mosaicity, inhomogeneity, and TMS). The extrinsic terms could cause in-plane or out of plane angular dependence of the linewidth.

The second contribution is the inhomogeneity, which is related to the fluctuation of the magnitude and direction of the demagnetising field in the film. This contribution is called field dragging, as the magnetisations are dragged behind the field because of the anisotropy effect. Which can be expressed as [139]:

$$\Delta H_{inhom} = \frac{\partial H}{\partial 4\pi M_{eff}} \Delta 4\pi M_{eff} \tag{1.57}$$

where M_{eff} is the effective magnetisation and $\Delta 4\pi M_{eff}$ stands for the inhomogeneity of the demagnetising field. The third term in equation 1.56 is the mosaicity term, caused by the variation of the thin film thickness, internal field, and different crystallite orientation, the variations of these properties from region to region vary the resonance field within the film, and hence broaden the linewidth and increase the magnetisation relaxation. This term could cause an angular dependence of the field linewidth as it depends on the crystalline directions, which can be expressed as follows [139]:

$$\Delta H_{mosaic} = \frac{\partial H}{\partial \varphi} \Delta \varphi \tag{1.58}$$

where $\Delta\varphi$ stands for the inhomogeneity of the crystal axes orientation among various grains in the film.

TMS is one of the most important reasons for broadening the linewidth of FMR spectrum and hence increasing the damping. TMS is related to the magnon scattering, whereby at resonance condition magnons precess as a spin wave with uniform mode $(k = 0)$ to scatter in scattering centres (caused by magnetic properties of inhomogeneity in the film). These uniform spin waves degenerate into non-uniform modes $(k \neq 0)$, and consequently dissipate energy to the lattice [140, 141, 142]. TMS can be examined by studying the dependence of the FMR spectra linewidth in the microwave frequency, exhibiting a nonlinear curve for the range of frequencies used in the experiment. The TMS could show an in-plane contribution to the field linewidth, as can be expressed by the equation [143]:

$$\Delta H_{TMS} = \left(\frac{2}{\sqrt{3}}\right)[\Gamma_{EA}\cos^2(\varphi) + \Gamma_{HA}\cos^2(\varphi - \pi/2)].\sin^{-1}\left(\sqrt{\frac{H}{H+4\pi M_S+H_S}}\right) \quad (1.59)$$

where Γ_{EA} and Γ_{HA} are parameters that measure the TMS intensity scattering at easy and hard axes, respectively, and H_S is the surface anisotropy field. The TMS does not have a contribution when the field is applied out of the film plane [144].

1.2.6.2.1.3 Spin pumping

For multilayer systems, spin pumping could enhance the damping of the system. For a system with two ferromagnetic layers separated by non-magnetic layer (spacer). When the magnetisation precesses at the ferromagnetic layer (F_1), the spin current generates at the interface of (F_1) and the normal metal (N), thus the interface (F_1/N) acts as a spin pump [144, 145]. The spin current flows toward the normal metal and perpendicular to the F_1/N interface, hence the momentum of the spin that carried by the spin current is [146]:

$$j_{spin} = \frac{\hbar}{4\pi} A_r \hat{\boldsymbol{m}} \times \frac{d\hat{\boldsymbol{m}}}{dt} \quad (1.60)$$

where $\hat{\boldsymbol{m}}$ is a unit vector along $\boldsymbol{M}$, while A_r is a scattering matrix:

$$A_r = \sum_{m\,n}\left(\left|r^{\uparrow}_{m,n} - r^{\downarrow}_{m,n}\right|^2 + \left|t^{\uparrow}_{m,n} - t^{\downarrow}_{m,n}\right|^2\right) \quad (1.61)$$

where $r_{m,n}^{\uparrow}$ and $t_{m,n}^{\uparrow}$ are the reflection and transmission parameters of the spin-up and spin-down electrons into the non-magnetic layer. The longitudinal component of the spin current is absorbed at the interface of the second ferromagnetic material (F_2) and the non-magnetic layer (N/F_2). When the precession angle is very small, most of the spin current is transverse, and hence it is all absorbed at the (N/F_2) interface, and the magnetisation relaxed to enhance the damping of the layer [147-148].In this case, the N/F_2 interface acts as a spin sink for the dissipated spin current, and hence a brake for F_1 precessing spin [147]. The damping caused by spin pumping can be expressed by [146]:

$$\alpha_{sp} = \frac{G_{sp}}{\gamma M_s} = g\mu_B \frac{g^{\uparrow\downarrow}}{4\pi M_s}\frac{1}{d_1} \tag{1.62}$$

where G_{sp} is the spin pump Gilbert parameter, $g^{\uparrow\downarrow}$ is the interface mixing conductivity, and d_1 is the thickness of the first ferromagnetic layer, F_1. One would expect that both ferromagnetic layers are coupling dynamically, whereby both act as a mutual spin pump and spin sink. The equation of motion for ferromagnetic F_1 can be given by [146]:

$$\frac{1}{\gamma}\frac{\partial M_1}{\partial t} = \left[-\boldsymbol{M_1} \times \boldsymbol{H_{eff,1}}\right] + \frac{G_1}{\gamma^2 M_S^2}\left[\boldsymbol{M_1} \times \frac{\partial \boldsymbol{M_1}}{\partial t}\right] + \frac{\hbar}{4\pi d_1} g_1^{\uparrow\downarrow} \boldsymbol{\widehat{m}_1} \times \frac{\partial \boldsymbol{\widehat{m}_1}}{\partial t} - \frac{\hbar}{4\pi d_1} g_2^{\uparrow\downarrow} \boldsymbol{\widehat{m}_2} \times \frac{\partial \boldsymbol{\widehat{m}_1}}{\partial t}$$

where $\boldsymbol{M_1}$ is the magnetisation vector of F_1, $\boldsymbol{H_{eff,1}}$ is the effective field in the layer F_1, $G_1$is the Gilbert parameter for F_1, and $g_1^{\uparrow\downarrow}$ and $g_2^{\uparrow\downarrow}$ are the interface mixing conductivity for F_1 and F_2 (respectively). The sign of the third (+) and fourth (-) term in the right-hand side represent the spin current direction from the first layer to the second layer [146]. The spin pumping could cause an angular dependence to the field linewidth arises from the magnetisation alignment between magnetic layers in a multilayer system, and from the precession magnitude of the magnetisation in each layer [149, 150].

Chapter 2: Experimental and Computational Methods

This chapter describes all experimental techniques used to grow, fabricate, and investigate the single and multilayer samples used in this thesis.

2.1 Samples growth and fabrication

2.1.1 Material used

The details of the investigated samples', such as layers, thicknesses, and substrates are shown in table 2.1. All substrates used in this thesis were very thin ($150\mu m$), to make sure that most of the strain transferred from the piezoelectric transducer to the magnetic layers. All samples were grown by Dr Andrew Rushforth at University of Nottingham, except S548 and S549, which were grown by the author.

Table 2.1: A summary of samples used in this study

Sample number	**substrate**	**Material (thickness nm)**	**Machine**
S475	Si/SiO2	Ta(4)/**Ni**(5)/Ta(3)	1
S476	Si/SiO2	Ta(4)/**NiFe**(4)/Ta(3)	1
S548	GaAs (001)	Cr(4)/**NiFe**(4)/Cr(4)/**Ni**(5)/IrMn(8)/Cr(3)	1
S549	GaAs (001)	Cr(4)/**Ni**(5)/Cr(4)/**NiFe**(4)/IrMn(8)/Cr(3)	1
IM008	GaAs (001)	Ta(4)/**NiFe**(4)/Cu(4)/**Ni**(5)/Ta(3)	2
IM009	GaAs (001)	Ta(4)/**Ni**(5)/Cu(4)/**NiFe**(4)/Ta(3)	2

1 is for Mantis QPrep500_1 and *2* is for Mantiss QPrep500_2

2.1.2 Magnetron sputtering

Sputtering is an effective coating technique using physical vapour deposition, where a target is bombarded by energetic inert gas ions. The atoms or molecules of the target are then ejected from it by energetic Argon ions , and are deposited onto the substrate. The sputtering process starts by applying a bias voltage between the target and the substrate inside the chamber where the target clusters accelerate to the substrate. The plasma is generated in the chamber when the electric field is applied to the inert gas (inside the chamber) at very low pressure. Ions and electrons are subjected to a strong magnetic field near to the target, making them spiral around the magnetic flux, as shown in figure 2.1. This process stabilises the plasma and makes the sputtering process more efficient by increasing the plasma density near the target, which increases the deposition yields. DC sputtering is used to sputter conductive material, while RF sputtering can be used to grow non-conductive films. The alternating electric field prevents the accumulation of charges on targets.

Although the quality of film grown with sputtering magnetron technique is inferior to that achieved using molecular beam epitaxy (MBE) technique, the sputtering system has demonstrated very good quality growth for epitaxial and polycrystalline single and multilayer films [151, 78, 152]. The sputtering system is preferable because of its faster growth deposition rate and lower equipment cost. The growth of samples in this thesis was performed using two sputtering systems, Mantis QPrep500_1 (with six deposition ports), and Mantis QPrep500_2 (with five deposition ports). The thickness of grown films was monitored using Quartz Crystal Monitor (QCM) inside the sputtering chamber. Preliminary sets of calibration samples were first grown before samples growth, and a set of samples was grown for each target. Calibration samples' thicknesses were then measured using a profilometer after the deposition and were compared with the deposition rate and the time of deposition. The results of these measurements were used to adjust the tooling factor and growth rate of the sputtering system for each target.

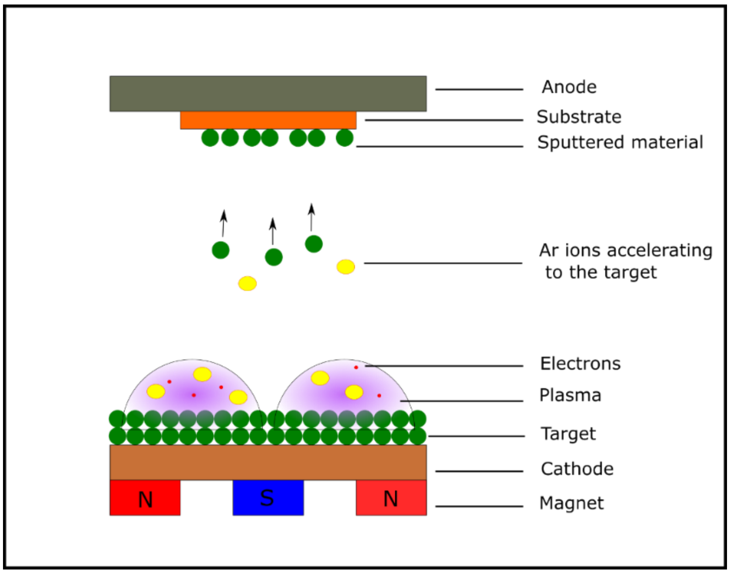

Figure 2.1: Schematic of the magnetron sputtering system with target atoms moving to stick on the substrate when bombardments hit the target surface. The magnetic field near the target traps the plasma to allow a faster sputtering rate.

All samples growth in this thesis was done using the sputtering system from a single target except the IrMn layer, where a co-sputtering deposition was carried out using a composition of $20:80$. For the permalloy, a target of the nominal composition of $Ni_{80}Fe_{20}$ was used to grow all permalloy layers. All used targets had very high purity (approximately 99.99%). The chamber base pressure and growth pressures were around 1×10^{-9} Torr and 1×10^{-3} Torr, respectively. For all spin valves grown in this study, expect for IM008 and IM009 samples, an external magnetic field with a value of $4mT$ was used, and the substrate was placed between two magnets fixed to the substrate table to introduce a uniaxial anisotropy in the free layer, and to pin another layer by introducing an exchange bias field by sputtering the IrMn at the top of the upper ferromagnetic layer. The substrate stage rotated for all samples with a speed of $20rpm$ to ensure uniform growth.

2.1.3 Microfabrication

In order to proceed with transport measurements, all samples were fabricated using photolithography technique. Photolithography is a microfabrication technique that uses UV light to transfer patterns through a mask on the top of films by using light-sensitive materials called photoresist. The fabrication was performed in the cleanroom facility at the University of Nottingham. A summary of the fabrication process is illustrated in figure 2.2, showing the two stages. The mesa stage at the left side shows how the film is patterend to the desired shape using a certain mask under UV exposure. The first stage ends with dry itching (ion milling) to get rid of the film around the devices. The second stage is to make contacts using thermal deposition by depositing an adhesive layer (Ti) followed by a gold layer. A schematic diagram of the device and its dimensions is shown in figure 2.3. The design of this device enables magnetic transport measurements at different directions of the electric current and strain with respect to the magnetic field.

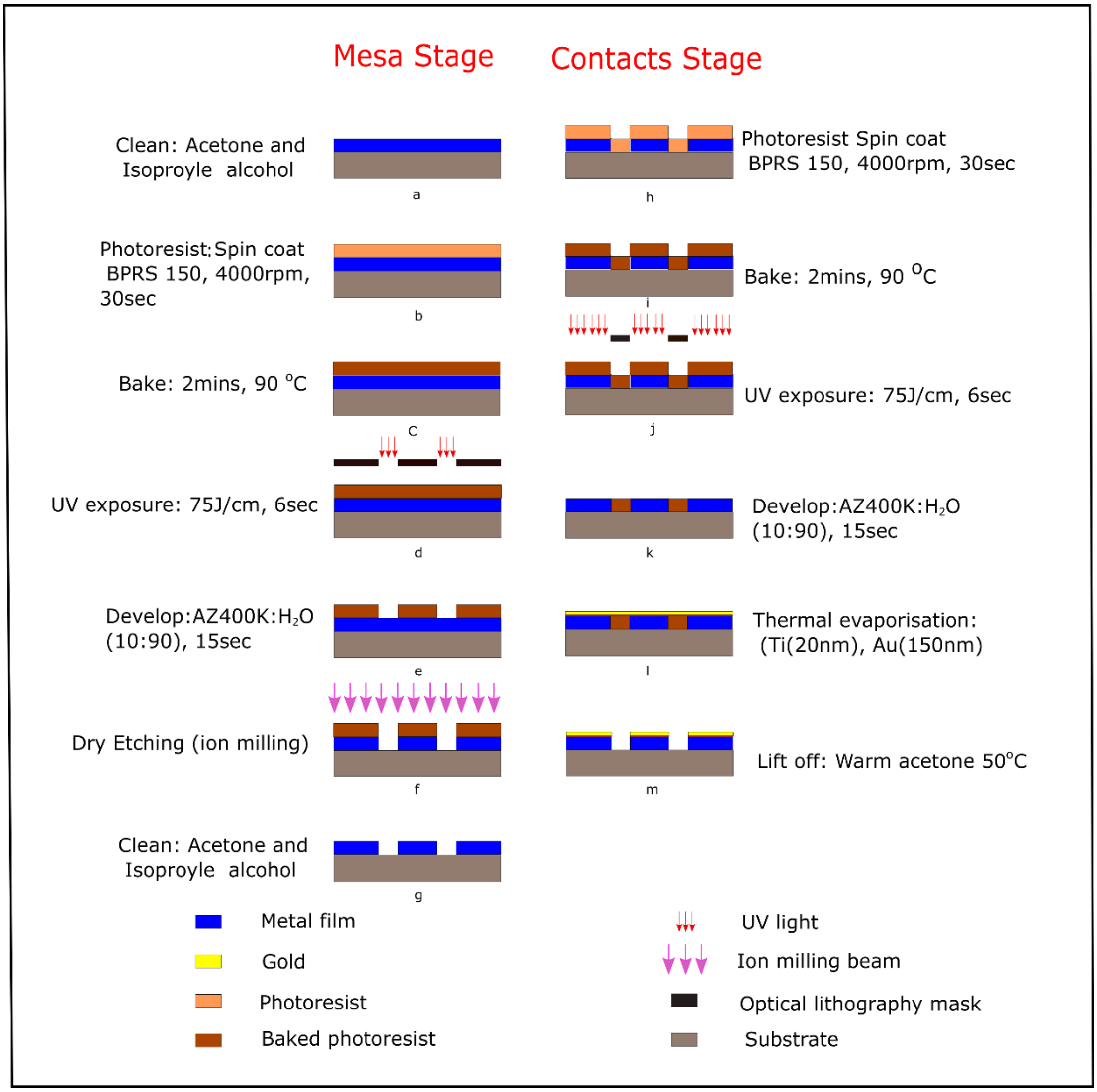

Figure 2.2: Microfabrication sequence steps (a-m) of the samples using photolithography. The process started by cutting a chip of size $5 \times 7mm$ from the grown wafer to end with microdevices having the shape shown in figure 2.3. Two stages are shown in the fabrication, mesa stage (left) and contact stage (right).

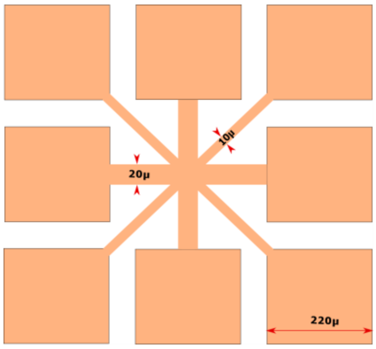

Figure 2.3: Schematic diagram of the micro-device used in the transport measurements fabricated using the optical-lithography technique. The design of this device allows transport measurements when applying an electric current and strain along different directions with respect to the magnetic field.

2.1.4 Ion milling

In order to get a good definition of the fabricated micro-devices, ion (dry) etching was used to etch the films around the devices as a step of the microfabrication process (step f in figure 2.2). Ion milling is an etching technique that uses the energetic ion (Argon) as a beam, hitting the surface of the samples, with the desired pattern covered by photoresist in the microfabrication process. In order to control the depth of milling, the power of the ion beam and the time of the milling should be considered carefully. Dry etching is preferred for etching multilayer films, as it is not selective and is known to be an anisotropic way to etch the device edge with a very good quality profile. Mantis RFM60 ion miller was used to mill all samples in this thesis. Argon gas was introduced in an ion source tube, and RF power of 100W at $13.56MHz$ was applied to a coil enclosed inside the source tube, to generate a plasma. Applying a bias of order $200V$ between the transparent outer and inner grids that enclose the source tube launches a plasma beam through the outer grid to bombard the substrate and mill the sample. A Faraday cup was used in the chamber to measure the ion beam current, and hence to control the beam flux. Electrons are also ejected to the ion beam from the neutraliser to reduce the beam charge to zero, to avoid increasing the charge of the substrate.

The RFM60 was attached at the bottom of the sputtering system (Mantis QPrep500_2), and the neutraliser was attached to the ion source. In the milling process, the patterns that need to be fabricated are protected and covered by the photoresist, while the rest of the film is removed by the bombardments. The table of the substrate was rotated at $20rpm$ to ensure homogeneous and uniform milling for the whole substrate. In this thesis, the photoresist $PBRS150$ ($1500nm$ thickness) was used to cover the micro-patterns (steps b-e in figure 2.2). The milling time and power were adjusted for the samples studied, according to the calibration test performed for the same layers and substrates. After each milling for the calibrated samples, the milling depth was measured by a profilometer, with varying power and time of milling in order to reach the perfect milling conditions. Figure 2.4 (a) shows an example of the milling depth of one pad of a micro-device after the milling, measured using a profilometer; the measurement shows a good profile for the device after the milling. Figure 2.4 (b) shows an example of a device image taken directly after milling, while 2.4 (c) shows an image of a device after cleaning the photoresist with acetone (step g in figure 2.2 at the end of the mesa stage). The resistance of the chips was measured and compared before and after milling to check if there was any trace for the film around the devices on the chip, along with a careful microscope checking. The milling process was performed by Dr Andrew Rushforth with my assistance.

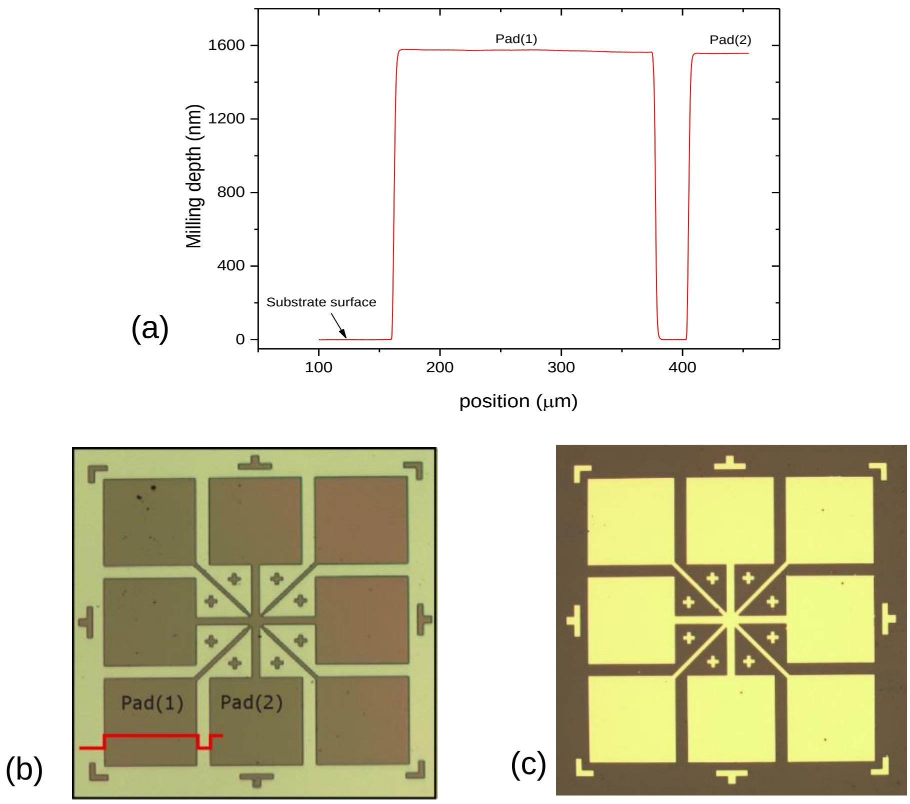

Figure 2.4: (a) An example of measuring milling depth as a function of device width. The measurement is done using the device shown in (b), where the red line indicates the area scanned by the profilometer measurement shown in (a). (c) The device after cleaning the photoresist using the acetone (step g in figure 2.2). The depth measurement and shape of the devices shows that the dry milling gives very anisotropic etching, with a high-quality definition.

2.1.5 Thermal deposition

The thermal evaporation technique is a physical deposition where a target material placed in a resistive coil or boat and is heated by passing a high current. The material is melted and vaporised to stick onto the substrate. The chamber was pumped down to a pressure of around $1 \times 10^{-7}\mathrm{Torr}$, so the mean free path of the vaporised materials was between $10cm$ and 1m (longer than the distance between the target and the substrate). In this study, the thermal evaporator was used to deposit the contacts metals for the transport measurements of the devices where Ti $(20nm)$ and Au $(120nm)$ were deposited, respectively, on the top of the magnetic layers films (see figure 2.5), as the last step microfabrication process represented by step m in figure 2.2. Figure 2.5 shows an image for a microdevice ready for the transport measurement after the last step of the microfabrication, with a layer of gold on the top.

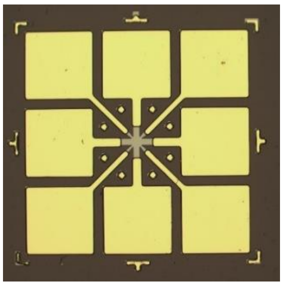

Figure 2.5: The microdevice fabricated using the photolithography with a contact layer of gold at the top.

2.2 Samples preparation for measurements

Samples were prepared for different measurements techniques; SQUID and ferromagnetic resonance measurements were performed using unpatterned thin film samples, while the transport measurements were carried out using patterned micro-devices. The details about preparing samples for each measurement are discussed in detail in the next sections. The transport and ferromagnetic resonance measurements were performed using a piezoelectric transducer device to study the strain effect on magnetic properties of single and multilayer nickel and permalloy. The next subsections discuss the piezoelectric transducer concept, whereby the voltage is used to control the strain in magnetic layers and induce magnetic anisotropy in the magnetic structure.

2.2.1 Piezoelectric transducer

Figure 2.6 shows the concept of the device used to study the strain effect on ferromagnetic films and devices in this thesis. A commercial piezoelectric transducer from Piezomechanik GmbH [153], Pst 150/5x5/7, with a capacitance of $800nF$ was used. It operates safely between $-30V$ and $+150V$, and can apply a tensile force of $2000N$ when a maximum voltage is applied to the actuator. In order to protect the ferromagnetic samples from damage, a range of voltages between $-30V$ and $+50V$ were applied to the piezoelectric stacks. Applying a voltage $V>0$ to the actuator expands it along the dominant direction along the y-axis (tensile strain), while applying a negative voltage $V<0$ expands the short axis of the piezoelectric transducer along the x-axis (compressive strain) and contracts the long axis, as shown in figure 2.6. At room temperature, this transducer gives a maximum uniaxial strain of value around $1x10^{-3}$, however, not all of this strain can be transmitted to the ferromagnetic layers due to the elastic properties of the substrate and the epoxy used to fix the device (or film) on the piezoelectric transducer. The value of the strain transmitted to the film is in the range of $2x10^{-4}$, as discussed in the next chapters.

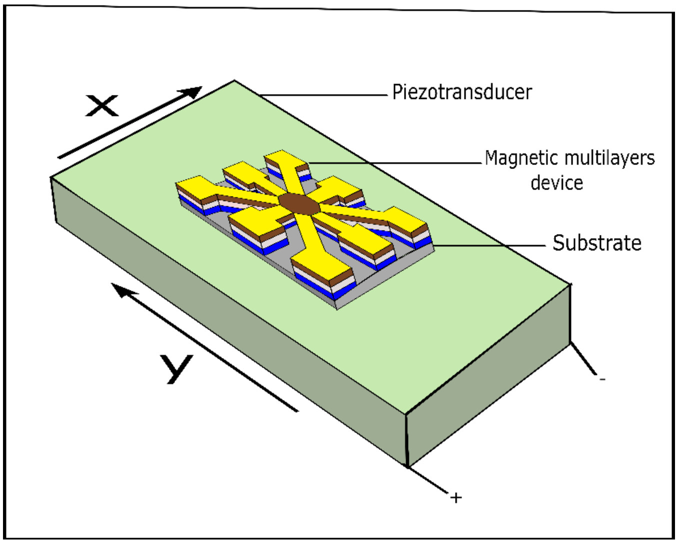

Figure 2.6: The hybrid structure of the ferroelectric material (piezoelectric transducer) and the magnetic device mounted on the top of the piezoelectric transducer. The voltage applied through the positive and negative terminals at the edge of the transducer.

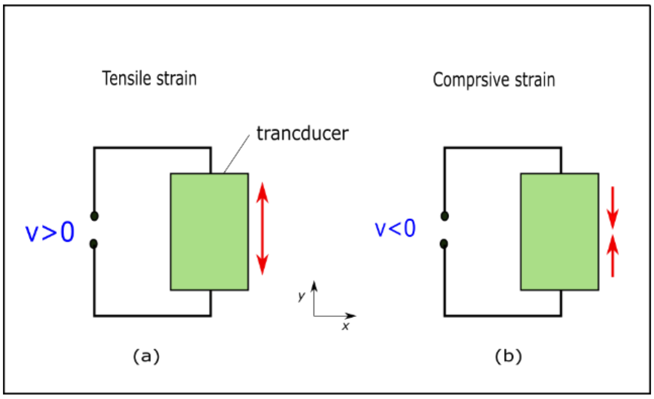

Figure 2.7: Schematic of the actuator when applying a positive or negative voltage with the corresponding strain type.

2.2.2 Mounting the sample onto the transducer

The hybrid structures of piezoelectric transducers and ferromagnetic films or devices were prepared firstly by removing the coating polymer material that covered both sides of the transducer from one side, using sandpaper. Isopropyl alcohol (IPA) was then used to clean the transducer surface to make sure the surface was clean from dust, and was smooth to mount the sample. For the transport measurements, the transducer was mounted on a 12-pin header using GE varnish glue. The glue was put at the edge of the transducer under the casing part, to prevent any clamping of the transducer stacks to the header. After checking the polarity of the terminals carefully, both negative and positive terminals were soldered to the header pins. Epo-Tek H70E epoxy resin mixture of $9:5$ was used to affix the device onto the transducer and was left for 24 hours at room temperature to cure. For ferromagnetic resonance experiments, instead of using devices, unpatterned thin films of size $4 \times 5mm$ were mounted on the actuators for the IM008 and IM009 samples. Figure 2.8 shows an image for a micro-device mounted on the top of the piezoelectric transducer, while the piezoelectric transducer was mounted on a 12-pin header for the transport measurements. The image also shows that microwires bonded the pads of the device to the pins of the header for the transport measurements.

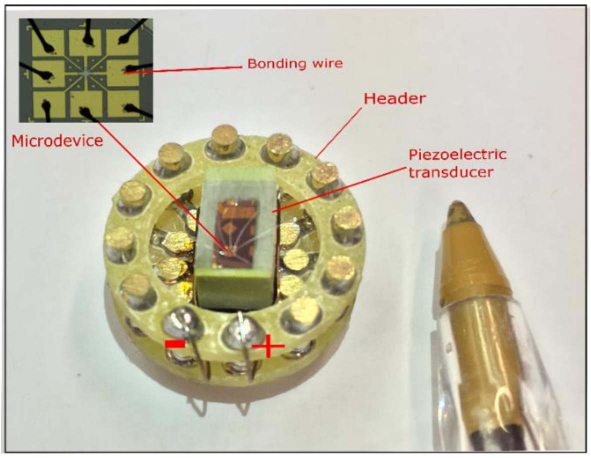

Figure 2.8: Image for the hybrid structure of the devices mounted on the piezoelectric transducer, and the transducer mounted on the 12-pin header. The two terminals of the piezoelectric transducer $\pm$ were soldered to the header to apply a range of voltages, while other pins were bonded to the microdevice (as shown top-left) using aluminium wires with $25\mu m$ thickness.

2.2.3 Strain calibration

In order to measure the actual strain transferred to the magnetic devices, transport measurements were carried out to measure the relation between the voltages applied to the piezoelectric transducer and strain-induced into the magnetic material, using the longitudinal resistance to get the strain value. The hybrid structure was placed in a magnetic field of $300mT$ to make sure all magnetisations of the ferromagnetic material were saturated, and the changes in resistance were due only to the geometrical distortion of the sample. A current was applied along the x-direction, as shown in figure 2.9, and the voltage was ramped from $-30V$ to $+50V$ (in steps of $+1V$), and from $+50V$ to $-30V$ (in steps of $-1V$), while recording the longitudinal resistance R_{xx}. Assuming the initial length of the device is x_0, inducing an anisotropy by applying a strain to this device in the x-direction changes the length of the device to be x_1. The strain in x-direction is given by:

$$\varepsilon = \frac{x_1 - x_0}{x_0} \tag{2.1}$$

Defining the Poisson's ratio ν as the negative ratio between the lateral strain and the longitudinal strain, in our case, applying strain along the x-axis gives the Poisson ratio as:

$$\nu = -\frac{\varepsilon_y}{\varepsilon_x} = -\frac{\varepsilon_z}{\varepsilon_x} \tag{2.2}$$

In order to find the relation between the device resistance and its change in length, the following equation is used:

$$R = \frac{\rho l}{A} \tag{2.3}$$

where ρ is the film resistivity, l and A are the film length and area. This is applied to the magnetic device dimensions using the following:

$$R = \frac{\rho x}{yz} \tag{2.4}$$

The resistance is partially differentiated in the three directions to get the change of the resistance on the device volume using the resistance from 2.4 equation:

$$\Delta R = \frac{\rho \Delta x}{yz} - \frac{\rho x \Delta y}{y^2 z} - \frac{\rho x \Delta z}{y z^2} \quad (2.5)$$

Equation 2.5 is divided by R from equation 2.4 to get:

$$\frac{\Delta R}{R} = \frac{\Delta x}{x} - \frac{\Delta y}{y} - \frac{\Delta z}{z} \quad (2.6)$$

Using equation 2.1 and 2.2 in equation 2.6:

$$\frac{\Delta R}{R} = (1 + 2\nu)\varepsilon_x \quad (2.7)$$

Hence the strain is given by the equation:

$$\varepsilon_x = \frac{(1+2\nu)}{\Delta R/R} \quad (2.8)$$

The Poisson's ratio is different from one material to another, as discussed in chapters 3 and 5 for each material.

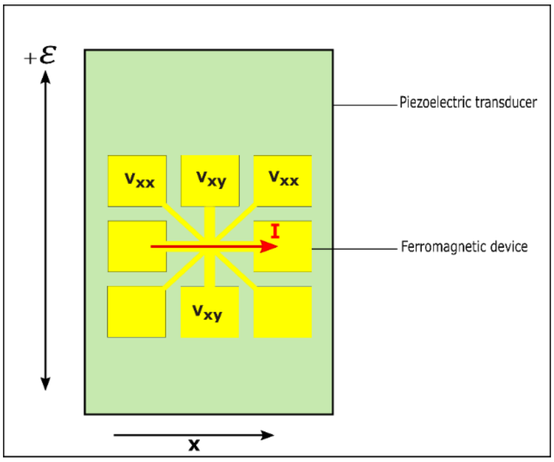

Figure 2.9: Schematic diagram for the hybrid structure used for the strain calibration and the magnetotransport measurements, showing the notation of the current I, transverse V_{xy} and longitudinal V_{xx} voltages, and the direction of the tensile strain.

2.3 Magnetotransport measurements

In-plane magnetotransport measurement was performed on the hybrid structure described in section 2.2.2. After wire bonding of the device contacts to the header pins (shown in the microscopic image in figure 2.8), the header was mounted on a rotatable probe capable of rotating 360^o in-plane of the devices, between two electromagnet poles. The measurements were carried out using the four-point probe experiment. For the sweep measurements, the magnetic field was swept between $+40mT$ and $-40mT$ in steps of $0.2mT$. The magnetic field with respect to the long axis of the transducer is the reference for the direction of the measurement with angle φ. For instance, for the measurement when the magnetic field is perpendicular to the long axis of the transducer, the angle $\varphi = 90^o$. On the other hand, the magnetic field direction with respect to the electric current varied with the angle α. The current value used was $1mA$, with a current density less than $9 \times 10^{+9} Am^{-2}$ for all samples used in this thesis.

For most of the devices, the current was probed through different directions of the device arms, to check if the strain-induced properties of the device changed with changing current direction with respect to the strain direction. For every field sweep, the voltage applied to the piezoelectric transducer was fixed. A range of voltages between $-30V$ and $+50V$ ($+80V$ in one case for IM008 sample) was used, with steps varying for different samples. The magnetotransport setup was carried out using two Keithley multimeters measuring longitudinal (V_{xx}) and transverse (V_{xy}) voltages, a Keithley 2400 current source, and a Keithly 2400 voltage source for the piezoelectric transducer. MATLAB codes were used to control the experiments and record the data.

Figure 2.10 (a) shows an example of the sweep of the transverse resistance (R_{xy}) for the permalloy sample (S476) when the magnetic field was $\varphi = 45^o$ with the long axis of the transducer, and current was applied $\alpha = 90^o$ to the field, while a range of voltages between $-30V$ and $+50V$ was applied to the piezoelectric transducer. For the rotational measurements of the transverse R_{xy}, longitudinal R_{xx}, $\mathrm{resistances}$, and strain calibration, a field of $300mT$ was used, to make sure all moments were saturated. Figure 2.10 (b) shows an example of the rotational R_{xy} measurements of the S548 spin valve sample when a magnetic field of $300mT$ was rotated in the plane around the multilayer film.

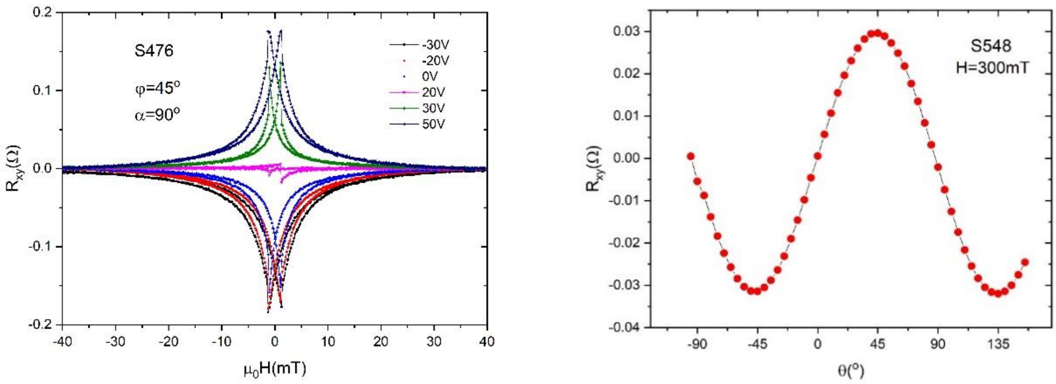

(a) (b)

Figure 2.10: (a) Transverse resistance R_{xy} measurements for S476 sample, when the magnetic field $\varphi = 45^o$ with the long axis of the transducer, and the current is applied along $\alpha = 90^o$ to the field, while a range of voltages between -30V and +50V are applied to the piezoelectric transducer. (b) Rotational R_{xy} as a function of angle, when a magnetic field of $300mT$ rotates in a plane by 250^o in steps of 5^o around the hybrid structure of the piezoelectric transducer and S548 spin valve.

2.3.1 Modelling the M-H loops

In order to study the strain effect on the magnetic properties of permalloy sample, a model was used to study the change in the magnetic anisotropies as a function of strain induced by the piezoelectric transducer. This section is just for the study of the strain effect on the permalloy single layer sample (S476), which was studied using magnetotransport measurement. The magnetic hysteresis loops at different strain value were constructed from magnetoresistance curves. This process is discussed more in detail in chapter 3, whereby it is easier for the reader to follow with examples and comparisons of magnetoresistance curves for different strains and directions. The transverse magnetoresistance curves were used, and the angles between the magnetisation and the current were determined using equation 1.32:

$$\theta_{AMR} = \frac{1}{2}\arcsin\left(\frac{R_{xy}}{\Delta R}\right) \qquad (2.9)$$

The angles between the magnetisation and the magnetic field (θ_M) were then determined, to find the projection M of the M_s, and hence $\frac{M}{M_s}$ was plotted as a function of the applied field (H). Figure 2.11 (a) shows examples of magnetoresistance curves used to extract hysteresis loops when the magnetic field is parallel to the transducer for the permalloy sample, applying $-30V$ and $+50V$, and the corresponding extracted magnetisation hysteresis loops are shown in figure 2.11 (b).

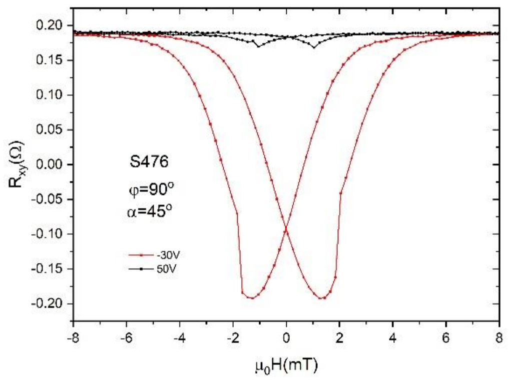

(a)

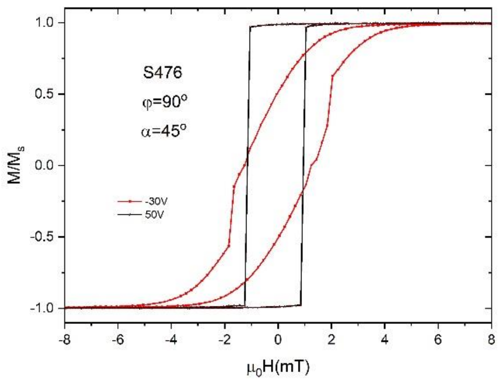

(b)

Figure 2.11: Extracting the magnetic hysteresis loop. (a) The R_{xy} of the S476 sample measured when voltages of $-30V$ and $+50V$ were applied to the piezoelectric transducer with the direction shown in both figures. (b) The magnetic hysteresis loop (M/M_s) extracted from the transport data in (a).

The magnetisation curves obtained from the magnetoresistance curve were simulated using the equation of free energy density (1.22) for the permalloy sample using the single domain model [105] as follows:

$$\epsilon = -MHcos(\varphi - \theta) + K_s sin^2(\theta) \quad (2.10)$$

where the first term is the Zeeman term, the second term is the magnetoelastic term introduced in the sample by the piezoelectric transducer (uniaxial term), φ is the angle between the magnetic field and the long axis of the transducer, θ is the angle between the magnetisation easy axis and the long axis of the actuator, and K_s represents the magnetoelastic anisotropy constant. The directions are shown in figure 2.12, where the long axis of the traducer as a reference direction in the simulation. The magnetic field swept between $-40mT$

and $+40mT$, while angle θ varied between 0^o and 360^o in steps of 0.20^o. The saturation magnetisation used in this simulation was obtained from the SQUID measurement for the permalloy sample. As the magnetic field swept from the maximum value, the value of the angle θ_{min} at the minimum free energy was determined. As the field changed to the next lower value, θ_{min} was changed by $\mp\Delta\theta_{min}$ to obtain a new energy minimum. The values of θ_{min} were collected and used to plot the magnetisation projection:

$$M = M_s \cos(\varphi - \theta_{min}) \tag{2.11}$$

The simulation was performed for hard magnetisation hysteresis loops, while the easier loop was excluded due to the high uncertainty of this model for the permalloy sample. The switching region was not included in this simulation since it does not give a good fit to the model, as discussed later in chapter 3. The simulated curves were fit to the experimental hysteresis loops using the least sum squares method, using the equation:

$$C = \sum_{i=1}^{n}(X_i - Y_i)^2 \tag{2.12}$$

where X_i and Y_i are points in the simulated and experimental curves, respectively, with a total of n points. A range of values of K_s were used to find the best fit between the experimental and simulated data. Figure 2.13 shows examples of the fitting when the magnetic field was parallel to the long axis of the transducer, to which $-30V$ was applied.

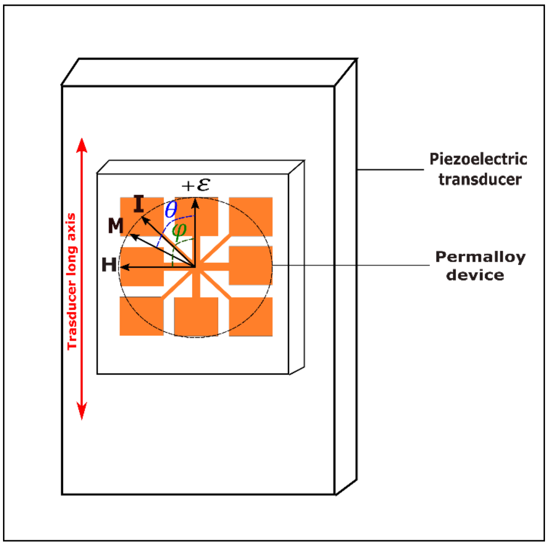

Figure 2.12: The illustration of the hybrid device along with the magnetic field and the current direction to the long axis of the piezoelectric transducer. The angles used in equations 2.10 are illustrated in the figure.

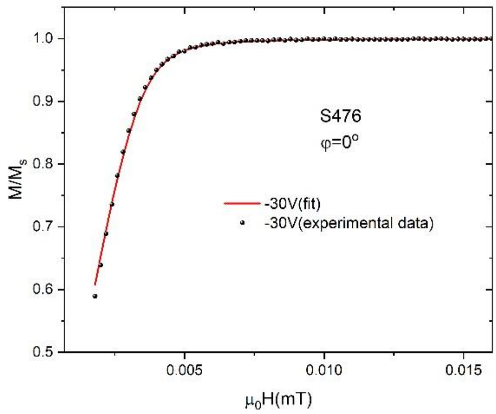

Figure 2.13: Demonstration of the fitting for S476 sample when the field is parallel to the long axis of the transducer, with $-30V$ applied to the transducer.

2.4 SQUID magnetometry

Superconducting Quantum Interference Device (SQUID) magnetometry is an ultrasensitive technique used to measure the magnetic properties of materials as a function of the magnetic field or temperature. In this thesis, a Quantum Design magnetometer was used to measure the magnetisation of the samples without applying strain. Films of size $(4x4mm)$ were used and mounted inside a drinking straw, which was then connected to the sample rod and moved inside the sample chamber using the stepper motor. When the magnetic sample moves through the superconducting detection coil, as shown in figure 2.14, the magnetisation of the sample induces an inductive electric current in the coil, and hence any change in the sample magnetic flux changes the current in the coil. The detection coil is a superconducting wire wound in a second derivative gradiometer. The upper and lower coils were wound oppositely to the centre coils, to cancel noise. The detection coil is coupled with the Josephson junction; the change in the current in the detection coil changes the magnetic flux in the Josephson junction. The SQUID consists of one or two Josephson junctions, where it is a tunnelling junction of thin insulator film sandwiched between two superconductors. As long as the magnetic flux is trapped in the Josephson junction, the magnetic flux converts to a voltage in the rf circuit. The voltage signal changes when the sample is moving in the detection coil. The ultra-sensitivity of the SQUID measurement comes from the Josephson junction, which can detect a very low magnetic flux of $\phi = 2.079 \times 10^{-15} Wb$ [154].

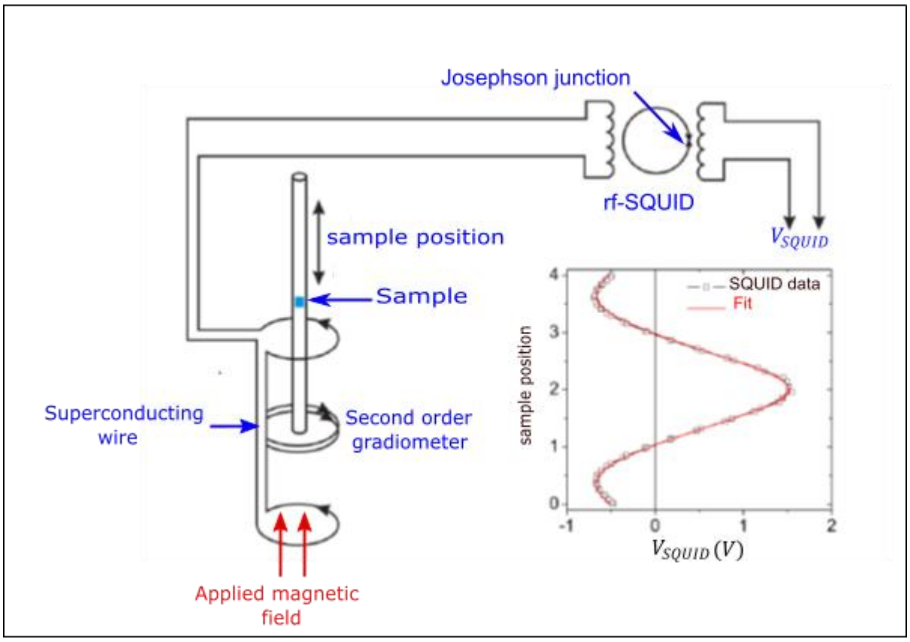

Figure 2.14: Schematic diagram showing the SQUID magnetometer, where the magnetic sample moves in the detection coil to induce a current in the coil. The change in the flux detected in the Josephson junction to produce an output voltage is related proportionally to the magnetisation of the magnetic sample that moved in the detection coil.

The SQUID magnetometer measures the long moment m of the sample along the gradiometer axis, as shown an example of the SQUID measurements in figure 2.15 for S549 spin valve sample. The magnetisation is calculated using $\boldsymbol{M} = m/V$, where $\boldsymbol{M}$ is the magnetisation and V is the sample volume. The diamagnetic background of the measurements was subtracted using the linear fitting of the graph above the saturation in the M-H loop. The SQUID magnetometer used in this thesis provides a controllable magnetic field between $\pm 1T$, and covers a range of temperature between $2K$ and $300K$. All samples in this thesis were measured by the SQUID except the nickel sample S475. For all spin valves in this thesis, the measurements were performed at $300K$ and $2K$. In addition, the spin valves with IrMn layer (S548 and S549) were measured at $300K$, $50K$, and $2K$, to investigate exchange bias and coercivity change with varying temperatures.

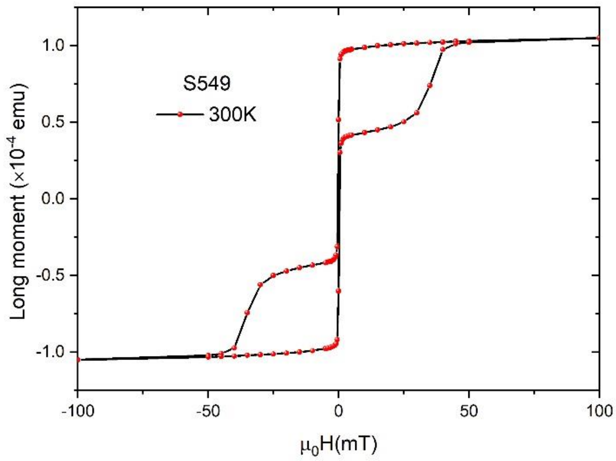

Figure 2.15:: Example of SQUID hysteresis loop for the S549 spin valve sample performed at room temperature. The field swept between $+500mT$ and $-500mT$, to make sure all moments were saturated with the field.

2.5 Ferromagnetic resonance

FMR is a powerful technique used to study the dynamic and static properties of ferromagnetic materials. The measurements were carried out at the University of York by Dr Stuart Cavill. The setup used is a custom-designed FMR spectrometer that can be used with two different modes: Vector Network Analyser FMR (VNA-FMR), and the Modulation FMR mode. The Modulation FMR technique was used to study the strain effect on the static and dynamic properties of multilayers samples IM008 and IM009. In the FMR measurement, an RF magnetic field applied to perturb the magnetisation field, so the ferromagnetic material magnetisation precesses around the effective field. A basic schematic design for the FMR spectrometer running under modulation FMR mode is shown in figure 2.16. The static magnetic field up to $2T$ is induced by two Helmholtz coils, where a soft iron pole is connected to the centre of each coil to focus the magnetic field in the area between the coils. The magnets can be rotated azimuthally using a DC servo motor. In the air gap between the poles, the sample was mounted in a custom-built co-planar waveguide CPW, supported by SMA connector, and connected to the RF generator. The CPW was designed to operate over a wide frequency range, consisting of a conductor line placed at the middle of two grounded gaps, all of which are situated on a dielectric surface. The RF current passed through the conductor wire and hence generates RF field perpendicular to the wire, and the sample which is placed on the top of the wire.

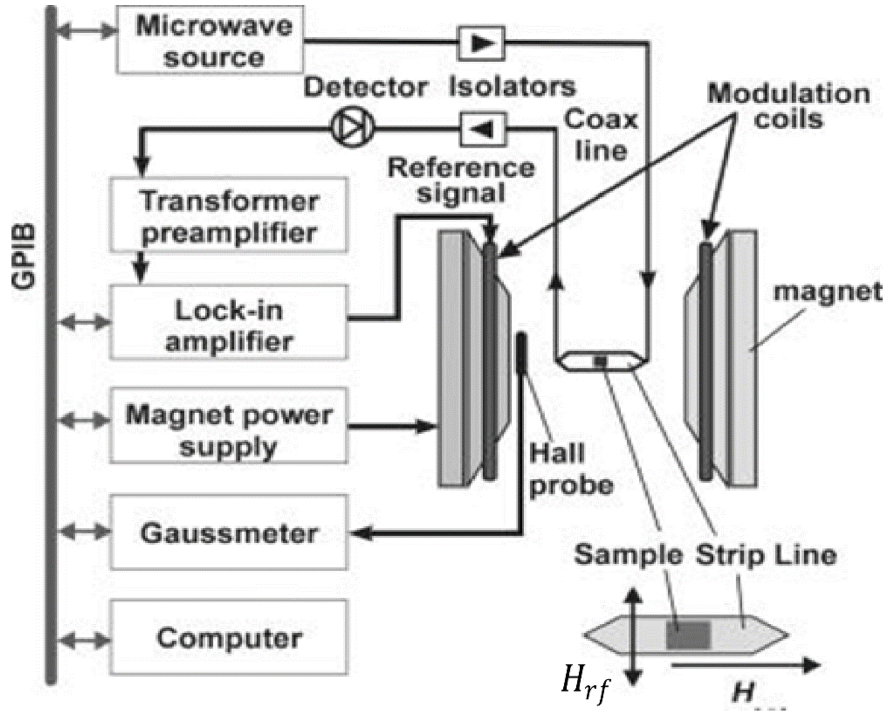

Figure 2.16: Typical modulation ferromagnetic resonance system used to perform the FMR of IM008 and IM009 samples.[155].

Due to the weak signals of the FMR in the ultra-thin films, two modulation coils powered by ac source are inserted in the electromagnet cavity, along with the lock-in amplifier technique, to detect and get a better signal to noise ratio [156].

A modulation coil system measures the first derivative of the absorption spectrum. Figure 2.17 shows a typical modulated FMR spectrum (first derivative of the FMR absorption), showing the linewidth ΔH (full width half maximum) and the resonance field H_{res} for IM009 spin valve using a frequency of $8GHz$ at $-25V$ with direction $\varphi = 10^o$. The FMR modulation mode capable of extracting a range of magnetic properties of ferromagnetic material. The FMR spectrum can be generated typically by applying a frequency and step the field through the resonance.

Rotating the magnet in-plane at different angles with respect to the magnetic film enables measurement of the magnetic anisotropies of the film and the magnetisation saturation M_s, an example of which is shown in figure 2.19 (a). In our measurements, the magnet was rotated by 180^o around spin valves used in this measurement at $8GHz$ and $14GHz$ for IM008, while $8GHz$ applied for IM009. Different voltages were applied for both samples at these angular measurements; for IM008 the voltages are $0, +25V, +50V$, while for IM009, the voltages are $-25V, 0, +50V$. A range of frequencies were applied ($6GHz - 15GHz$) for both samples for the measurement when the external field was parallel to the long axis of the transducer ($\varphi = 0$), applying $0V$ and $+50V$ for IM008, and $0V$ for IM009. An example is shown in figure 2.19 (b).

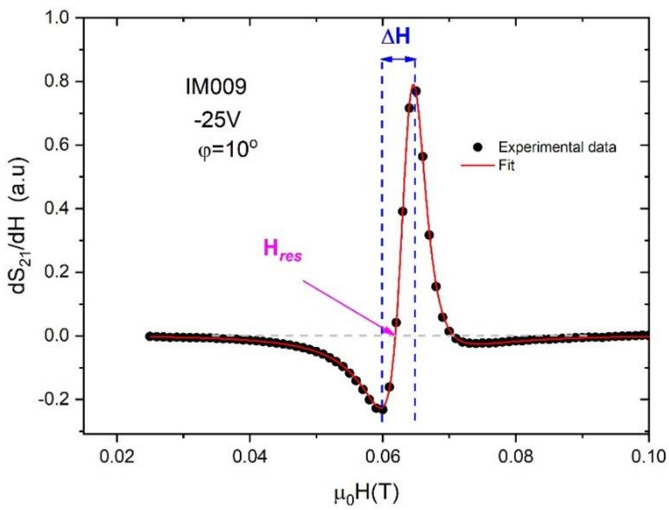

Figure 2.17: Modulation ferromagnetic resonance signals of IM009 spin valve measured at $8GHz$ at $-25V$ with direction $\varphi = 10^o$. The red line is fitted to equation 2.13.

2.5.1 Modelling of ferromagnetic resonance:

To extract ΔH and H_{res} from the normalised derivative of the spectrum, as shown in figure 2.17, the spectrum is fitted to the first derivative of the asymmetric Lorentzian function as follows[157,158]:

$$\frac{d(+\chi' \sin(\epsilon)+\chi'' \cos(\epsilon))}{dH} = A\left[-\frac{2(H-H_{res})\Delta H cos(\epsilon)}{[\Delta H^2(H-H_{res})^2]^2} - \frac{[\Delta H^2-(H-H_{res})^2]\sin(\epsilon)}{[\Delta H^2(H-H_{res})^2]^2}\right] + \mathrm{B} \qquad (2.13)$$

where $\chi'$and χ'' are the real and imaginary components of the AC susceptibility, respectively, A and B are constants, H is the external dc-magnetic field, H_{res} is the resonance field, ΔH is the line width, and ϵ is the mixing angle between the dispersive and absorptive components of the distorted FMR line shape.

In order to extract the magnetic anisotropies and the saturation magnetisation (i.e. static properties) of the IM008 and IM009 spin valves layer (NiFe and Ni), the data extracted from the FMR experiments is modelled for each layer separately. As mentioned in section 1.2.6, the resonance condition is obtained in terms of the second derivative of the free energy of the magnetisation using the Smit, Suhl, and Beljers approach, with the following equation [132,133]:

$$\left(\frac{\omega_{res}}{\gamma}\right)^2 = \frac{1}{\boldsymbol{M}^2 \sin^2\theta}\left[\frac{\partial^2\epsilon}{\partial\theta^2}\frac{\partial^2\epsilon}{\partial\varphi^2} - \left(\frac{\partial^2 E}{\partial\theta\partial\varphi}\right)^2\right]_{\varphi_{o},\theta_o} \qquad (2.14)$$

where φ and θ are the polar and azimuthal angles of the magnetisation, and φ_o and θ_o are the equilibrium angles of $\boldsymbol{M}$. To extract the resonance field H_{res} from the FMR spectra, the second derivative needs to be obtained first for the free energy equation. The free energy (discussed previously in section 1.2.2.5) is given for the system in this study by:

$$E_{total} = E_{zeem} + E_{demg} + E_{me} \qquad (2.15)$$

where the first term represents the Zeeman energy, the second term is the demagnetising energy, and the last term is the magnetoelastic term introduced by the transducer in the ferromagnetic layer, which can be considered as a uniaxial term, as denoted in the magnetisation hysteresis modelling. The demagnetisation term is introduced in the equation of the free energy density, since a stray field is generated perpendicular to the layer as a result of the precessing magnetisation. The free energy density in the spherical coordinates is given by:

$$\epsilon = -H_{ext}M_s[\sin\theta_H \sin\theta \cos(\varphi_H - \varphi) + \cos\theta_H \cos\theta] \\ + \frac{1}{2}H_u M_s \sin^2\theta \cos^2(\varphi - \varphi_o) + \frac{1}{2}4\pi M_s^2 \cos^2\theta \qquad (2.16)$$

where H_{ext} is the applied field, and $H_u = 2K_u/M_s$ is the uniaxial field. The coordinates and angles are shown in figure 2.18.

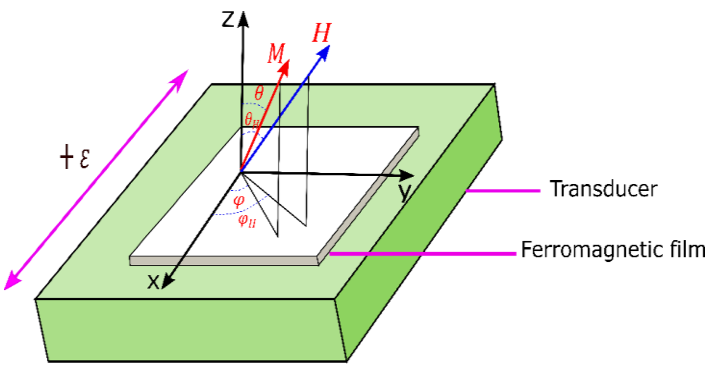

Figure 2.18: The coordinates and angles used for the FMR simulation for the hybrid device of the transducer and the magnetic film.

The first derivatives of the energy density equalise to zero for the equilibrium conditions, and are given by:

$$\frac{\partial \epsilon}{\partial \theta} = -H_{ext}M_s[\sin\theta_H \cos\theta \cos(\varphi_H - \varphi) - \cos\theta_H \sin\theta] \\ + \frac{1}{2}H_u M_s \sin 2\theta \cos^2(\varphi - \varphi_o) - \frac{1}{2}4\pi M_s^2 \sin 2\theta = 0 \qquad (2.17)$$

$$\frac{\partial \epsilon}{\partial \varphi} = +H_{ext}M_s \sin\theta_H \sin\theta \sin(\varphi_H - \varphi) \\ - \frac{1}{2}H_u M_s \sin^2\theta \sin 2(\varphi - \varphi_o) = 0 \qquad (2.18)$$

With the field is in the direction of $\theta_H = \frac{\pi}{2}$, the equilibrium condition of the magnetisation is obtained when the angle $\theta = \frac{\pi}{2}$, hence:

$$-H_{ext}M_s \sin(\varphi_H - \varphi) + \frac{1}{2}H_u M_s \sin 2(\varphi - \varphi_o) = 0$$

The second derivatives in this case are:

$$\frac{\partial^2 \epsilon}{\partial \theta^2} = H_{ext}M_s \cos(\varphi_H - \varphi) - H_u M_s \cos^2(\varphi - \varphi_o) + 4\pi M_s^2 \quad (2.19)$$

$$\frac{\partial^2 \epsilon}{\partial \varphi^2} = H_{ext}M_s \cos(\varphi_H - \varphi) - H_u M_s \cos 2(\varphi - \varphi_o) \quad (2.20)$$

$$\frac{\partial^2 \epsilon}{\partial \theta \partial \varphi} = 0 \quad (2.21)$$

Using equation 2.19, 2.20 and 2.21 in 2.14 at the resonance condition:

$$\left(\frac{\omega_{res}}{\gamma}\right)^2 = [H_{res}\cos(\varphi_H - \varphi) - H_u \cos^2(\varphi - \varphi_o) + 4\pi M_s] \times [H_{res}\cos(\varphi_H - \varphi) + H_u \cos 2(\varphi - \varphi_o)] \quad (2.22)$$

where $H_{ext} = H_{res}$ at the resonance condition, $4\pi M_s \gg H_{res} \gg H_u$, hence from equation 2.22 the H_{res} can be obtained by:

$$H_{res} = \frac{\omega_{res}^2}{4\pi M_s \gamma^2} - H_u \cos 2(\varphi - \varphi_o) \quad (2.23)$$

The uniaxial field (and hence the magnetic anisotropy induced by the transducer) and the magnetisation saturation can be extracted from equation 2.23 for each layer in the spin valve. Figure 2.19 (a) shows an example for the in-plane angular dependence curve of the H_{res} for the permalloy layer in IM008 spin valve ($14GHz$ and $+50V$) along with the fitting to equation 2.23.
For the dynamic properties, the equation used by Suhl is used to extract the linewidth [135]:

$$\Delta H = \frac{\alpha}{d\omega_{res}/dH}\frac{\gamma}{\boldsymbol{M}}\left(\frac{\partial^2 \epsilon}{\partial \theta^2} + \frac{1}{\sin^2}\frac{\partial^2 \epsilon}{\partial \varphi^2}\right) \quad (2.24)$$

Using equation 2.19 and 2.20 in 2.24 to find the linewidth:

$$\Delta H = \Delta H_o + \frac{2\pi\alpha f}{\gamma} \tag{2.25}$$

where ΔH_o is the extrinsic contribution to the damping, while the second term is the intrinsic contribution to the damping and is dependent on the frequency. Figure 2.19 (b) shows an example for the linear fitting of the linewidth for obtaining the intrinsic and extrinsic contributions of the damping for the permalloy layer in IM009 sample at $0V$.

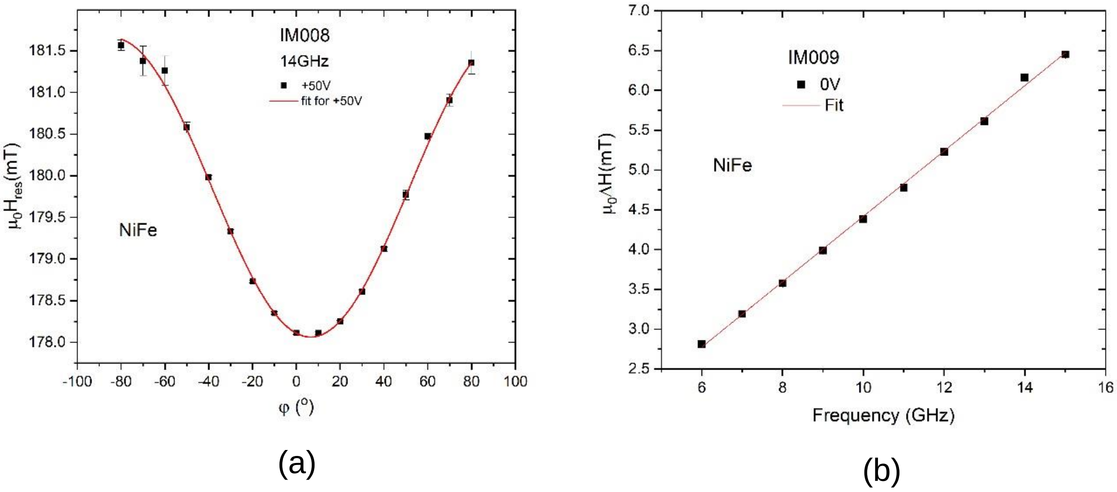

Figure 2.19: Examples of fitting (a) In-plane dependence of H_{res} of permalloy layer in IM008 spin valve applying +50V to the transducer at 14GHz frequency to extract the magnetisation saturation and magnetic anisotropies. (b) The linear fit of the linewidth as a function of frequency for the permalloy in IM009 spin valve at $0V$. The curve in (a) is fitted to equation 2.23, while the line in (b) is fitted to equation 2.25.

Chapter 3: An investigation of the effect of voltage-induced strain on ultrathin films of permalloy and nickel

3.1 Introduction

This chapter investigates the effect of the voltage-induced strain on single layers of polycrystalline ferromagnetic materials, permalloy ($Ni_{80}Fe_{20}$), and nickel (Ni). For both samples, ferromagnetic devices were mounted on the top of piezoelectric transducers to induce a controllable magnetic anisotropy that can change the magnetic properties of the material. Permalloy (Py) is a soft magnetic material known by small magnetocrystalline anisotropy and near-zero magnetostriction in bulk form [159]. Nickel is a soft magnetic material that has high magneto-elastic constants in bulk form, which means that its magnetisation has a very high response to strain [50]. In this study, ultrathin films of permalloy and nickel were grown using a magnetron sputtering system, fabricated into micro-scale devices, in order to conduct magneto-transport measurement to examine the strain effect on their magnetism. The measurements show that the voltage-induced strain control of the magnetic properties of the permalloy was manifest as a large change in the magnetoresistance curves. By extracting magnetic hysteresis loops from the transport data, it was possible to understand how the strain affects the magnetisation reversal of the permalloy under changing voltage (strain). The strain could change the magnetisation easy axis, switching field, switching directions, and magnetoresistance value. The magnetic easy axis was changed by 90^o when changing the strain from tensile to compressive, or vice versa. At the end of the study of the permalloy sample, a model was suggested to calculate the magnetoelastic constants B_1 for the ultra-thin film of permalloy. For the nickel film, it was shown that the voltage-induced strain has a negligible effect on the magnetisation reversal. For ultrathin films, the magnetic properties changed dramatically due to the surface term that dominates at this thickness, according to the Nèel model [160].

This chapter discusses the effect of strain on magnetic properties of ultrathin films of permalloy (sample S476) and nickel (sample S475). The magneto-transport measurements were carried out for both samples by mounting the fabricated micro-devices on the piezoelectric transducer, as described in section 2.2.2. Magnetic hysteresis loops were extracted from the transport data, then calculations were performed to simulate the hysteresis loops and fit them to the experimental loops, to find the anisotropy constants, and hence the magnetostriction constants. SQUID magnetometry was used to measure the anisotropy of the deposited film of the permalloy.

3.2 Strain control of magnetoresistance and magnetism of the permalloy ultrathin film

3.2.1 Magnetotransport measurements without strain

After mounting the permalloy micro-device S476 (Ta [4nm]/NiFe [4nm]/Ta [3nm]) on top of the piezoelectric transducer, as discussed in section 2.2.2, the direction of the magnetotransport measurement configuration of the device on the transducer was as illustrated in figure 3.1. The hybrid structure (piezoelectric transducer and the permalloy device) was placed in a magnetic field of $300mT$, which was rotated in the plane of the film in increments of 2^o. Four terminal resistance measurements were performed, and the values of the longitudinal (R_{xx}) and transverse (R_{xy}) resistances were measured for a range of 180^o. These measurements were performed to characterise the anisotropic magnetoresistance (AMR). The result of the rotational measurements is shown in figure 3.2, where the R_{xx} and R_{xy} resistances changed with the direction of the magnetic field. The rotational resistances graphs could be described by the following equations:

$$R_{xx} = R_{av} + \Delta R \cos{(2\theta_{AMR})} \quad (3.1)$$

$$R_{xy} = \Delta R \sin{(2\theta_{AMR})} \quad (3.2)$$

where R_{av} is the average resistance of the material when the magnetisation rotates by 360^o, and θ_{AMR} is the angle between the direction of the magnetisation and the electric current. The fitting of these equations to the resistance is shown in figure 3.2 (a) and (b). The values of the sample resistance R, $\Delta R = R_{//} - R_{\perp}$ (where $R_{//}$ is the film resistance when the current along the magnetic field, and $R_{\perp}$ is the resistance when the current is perpendicular to the magnetic field). For the permalloy sample, the value of ΔR extracted from R_{xx} and R_{xy} curves in figure 3.2 is equal to 0.41Ω. All measurements shown were conducted at $0V$ applied to the transducer; voltages of $-30V$, $+30V$, and $+50V$ were also applied to the rotation measurements, but the strain induced in the film was insufficient to make any change compared to the high saturating magnetic field applied to the sample.

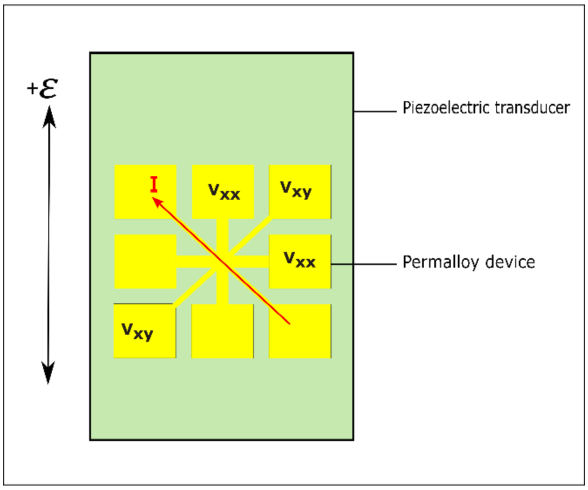

Figure 3.1: The magnetotransport measurement configuration of the micro-device of the permalloy sample S476 mounted on the piezoelectric transducer.

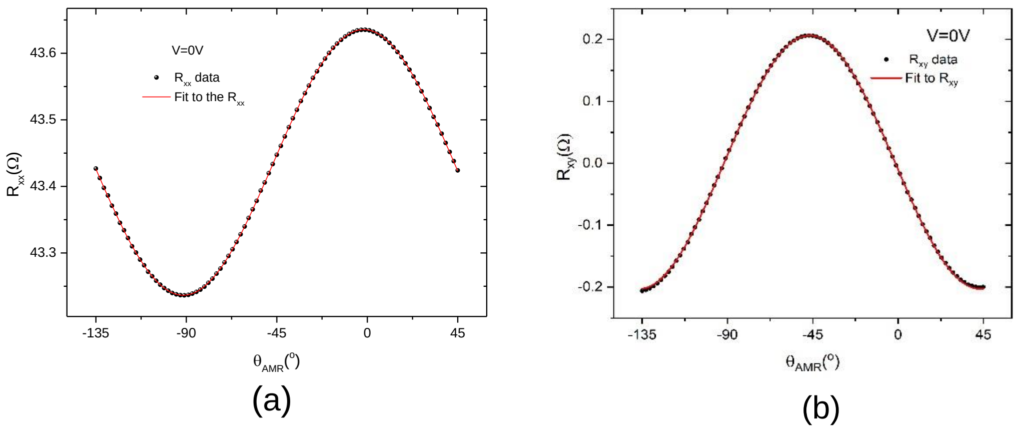

Figure 3.2**:** The rotation measurements at $0V$ for the sample S476, (a) R_{xx}, and (b) R_{xy} along with the fit for both graphs from equations 3.1 and 3.2, respectively. The curves show a dependence of the resistance on the angle between the magnetisation and current.

Sweep measurements were carried out for the permalloy sample. A magnetic field swept between $-40mT$ and $+40mT$ while applying a current of $1mA$, and the longitudinal and transverse resistance were measured using the same configuration as in figure 3.1. Two angles are used to describe the experiments configurations in this chapter and other chapters, whereby φ is the angle between the magnetic field and the long axis of the transducer, and α is the angle between the magnetic field and the electric current as shown by the schematic in figure 3.3. The magnetic field always rotated around the stage of the hybrid device, and that changes the two angles accordingly. Figures 3.4 (a) and (b) show the sweep measurements of the R_{xx} and R_{xy} at $0V$ applied to the piezoelectric transducer. The lowest R_{xx} observed is when the magnetic field is perpendicular to the electric current $\alpha = 90^o$, while the maximum value when the field is parallel to the current $\alpha = 0^o$. For R_{xy}, the maximum resistance is when the current made an angle of $\alpha = 45^o$, whereas the minimum was when the angle was $\alpha = -45^o$. The significant change of the resistance at the low field is due to the magnetisation rotation or switching, while the linear value at the higher field is due to the parallel alignment between the magnetisation and the magnetic field. The magnitude of the change of the magnetoresistance (AMR) agreed with the rotation measurements for the R_{xx} and R_{xy}.

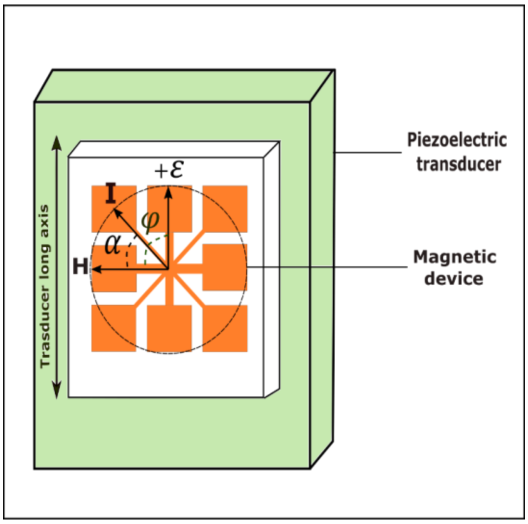

Figure 3.3: A schematic for the angles that used to describe the experiments configurations in this thesis.

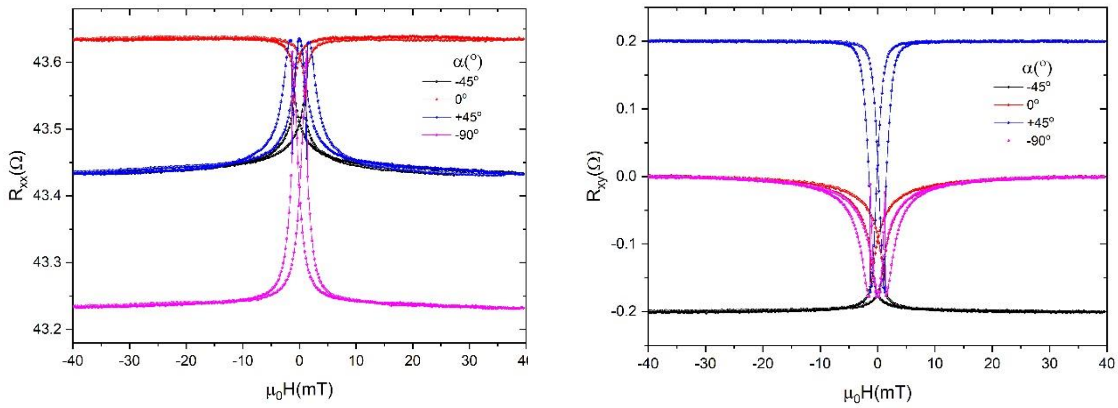

(a) (b)

Figure 3.4: Field sweep data for the permalloy sample S476 (a) R_{xx}, and (b) R_{xy} along four directions of the current with respect to the magnetic field at $0V$ applied on the transducer.

3.2.2 Strain control of the magnetoresistance and magnetisation reversal of permalloy

For measurements with an induced strain, a range of voltages between $-30V$ and $+50V$ was applied to the piezoelectric transducer. The first step was to find out the actual strain value induced in the sample by the varying voltage applied to the transducer. The measurements procedure (as described in section 2.2.2) involved cycling the voltages between $-30V$ and $+50V$. A saturating magnetic field was applied to ensure that the measured changes of resistance were not due to the rotation of the magnetisation. The voltages were swept up between $-30V$ and $+50V$ with steps of $+1V$, and were then swept down from $+50V$ to $-30V$, with $-1V$ steps. The bias voltage was ramped up or down to the next voltage when the current across the piezoelectric transducer was less than $10\mu A$, to prevent any damage in the ferromagnetic device by charging the piezoelectric transducer and hence rapidly inducing a large strain through the device. Figure 3.5 shows the relation between the strain induced in the permalloy sample S476 and the voltage applied to the transducer. It is equal to 1.78×10^{-4} when a voltage of $+50V$ is applied, while for $-30V$ it is equal to -1.78×10^{-4}. For all magnetotransport measurements performed with the application of a strain in this thesis, the voltage swept up from $-30V$ as a starting point, to end with $+50V$.

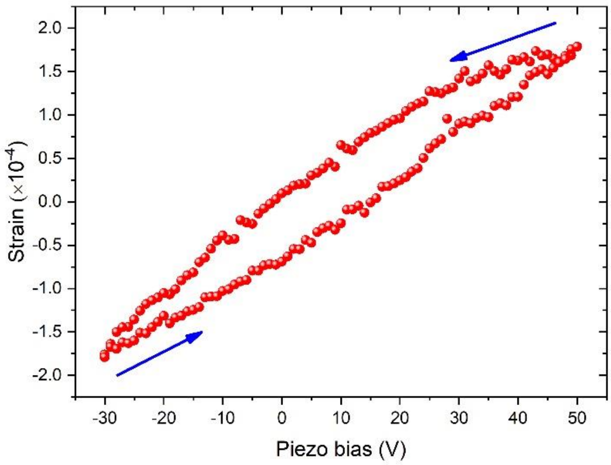

Figure 3.5: Strain loop for sample S476 with voltage bias across the piezoelectric transducer swept up and down between $-30V$ and $+50V$. The strain extracted from the R_{xx} is as discussed in section 2.2.2. Blue arrows show the direction of the measurement.

The following subsections discuss the effects of the strain on the magnetoresistance and magnetisation reversal of the permalloy sample. The direction of the magnetic field with respect to the long axis of the transducer is used to describe the direction of the measurement. The measurements were carried out along four directions of the magnetic field with respect to the transducer (φ), 0^o, $+45^o$, -45^o, and 90^o. For all measurements presented in the next sections, the current was applied at -45^o from the long axis of the transducer, as shown in figure 3.1.

3.2.2.1 Magnetic field perpendicular to the long axis of the transducer ($\boldsymbol{\varphi = 90^o}$)

The experimental configuration of these measurements is illustrated in figure 3.6 (a), where the magnetic field is perpendicular to the transducer, and the electric current is $\alpha = -45^o$ to the field. The R_{xy} and R_{xx} data when a range of voltages between $-30V$ and $+50V$ was applied to the transducer are presented in figure 3.6 (b) and (c), respectively. It is known that the bulk permalloy has a magnetostriction value near zero for the composition used in this study [53, 162]; however, the R_{xx} and R_{xy} resistances depend significantly on the voltages applied to the transducer. It is clear that for the R_{xy} at switching event, the value of the maximal resistance increases with increasing voltages. For instance, the maximal magnetoresistance ($\frac{\Delta R_{xy}}{R_{xx}} = \frac{R_{xy(\max)} - R_{xy(min)}}{R_{xx}}$) is equal to 0.9% when a voltage of $+50V$ is applied to the transducer, while it is equal to 0.09% when the voltage is equal to $-30V$. The relation between the $\Delta R_{xy}/R_{xx}$ and the voltage is shown in figure 3.7 (a), while figure 3.7 (b) shows the corresponding strain effect on the $\Delta R_{xy}/R_{xx}$. The $\Delta R_{xy}/R_{x}$ increased promptly when the strain value changed polarity (positive strain values represent tensile strain while negative values represent compressive strain), while it showed a gradual change in the same strain sign. That could be ascribed to the magnetostriction properties of the permalloy as a response to the tensile or compressive strain values induced by the piezoelectric transducer in the device. Gao et al. [163] found that the strain control magnetoresistance value of a film of NiFe with a thickness of $10nm$ exhibited a change of 0.17% on the difference of the maximal $\Delta R_{xy}/R_{xx}$ when they swept the electric field between $+80V$ and $-200V$. In this study, the difference between -$30V$ and $+50V$ reached 0.8%. According to the R_{xy} equation (equation 3.2), this could happen due to the changing angle of the magnetisation with respect to the current, and hence the magnetic field, as discussed in detail with regard to magnetic reversal directions (figure 3.12).

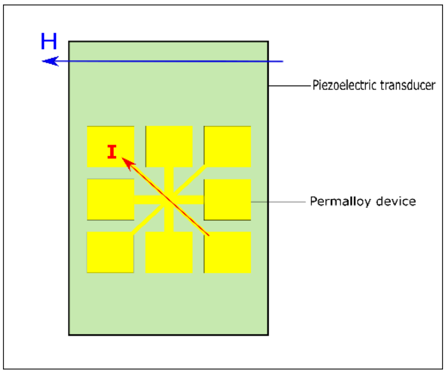

(a)

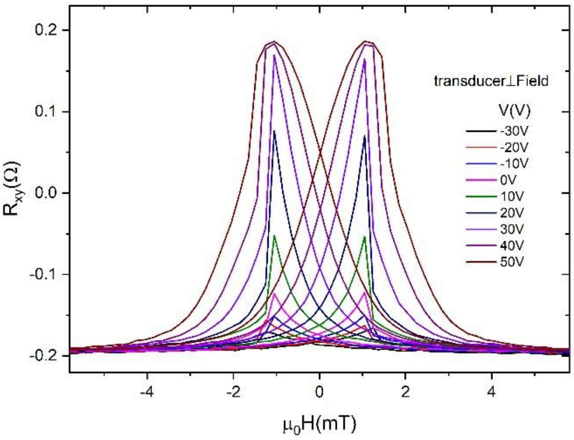

(b)

(c)

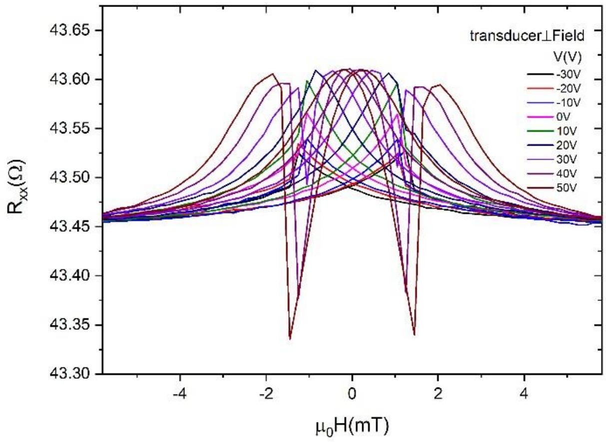

Figure 3.6: (a) A schematic of the hybrid device configuration with respect to the magnetic field, where the magnetic field is perpendicular to the long axis of the actuator ($\varphi = 90^o$), with a current direction $\alpha = -45^o$. (b) R_{xy} and (c) R_{xx} when voltages between $-30V$ and $+50V$ are applied to the piezoelectric stressor to induce a strain in the permalloy film. The value of the resistances and shape changed with changing strain.

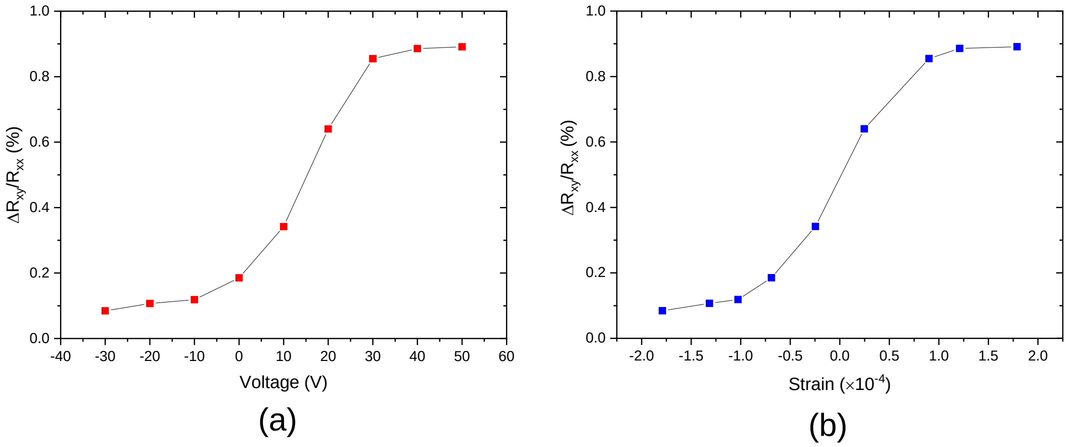

Figure 3.7**:** The dependence of the $\Delta R_{xy}/R_{xy}$ on the (a) voltages applied to the transducer and (b) the corresponding strain when the transducer is perpendicular to the magnetic field ($\varphi = 90^o$).

To understand the effect of strain in the magnetism of the permalloy sample, the magnetoresistance data were used to plot the magnetisation hysteresis loops using equation (3.2) to get the angle between the current and the magnetisation (θ_{AMR}) as follows:

$$\theta_{AMR} = \frac{1}{2}\arcsin\left(\frac{R_{xy}}{\Delta R}\right) \tag{3.3}$$

For instance, transverse resistance data when a voltage of $+50V$ is applied to the transducer (as shown in figure 3.8 (a)) is used to extract the angles θ_{AMR}. These angles are then used to obtain the magnetisation directions with respect to the magnetic field (θ_M), as illustrated in figure 3.8 (b). The magnetisation projection to the saturation field can be obtained from the following equation:

$$M = M_s \cos(\theta_M) \tag{3.4}$$

where M_s is the saturation magnetisation. The magnetisation hysteresis loop can then be plotted for this data, as shown in figure 3.8 (c). This method was used to extract the magnetic hysteresis loops for all resistance data at different voltages when the magnetic field is perpendicular to the piezoelectric transducer.

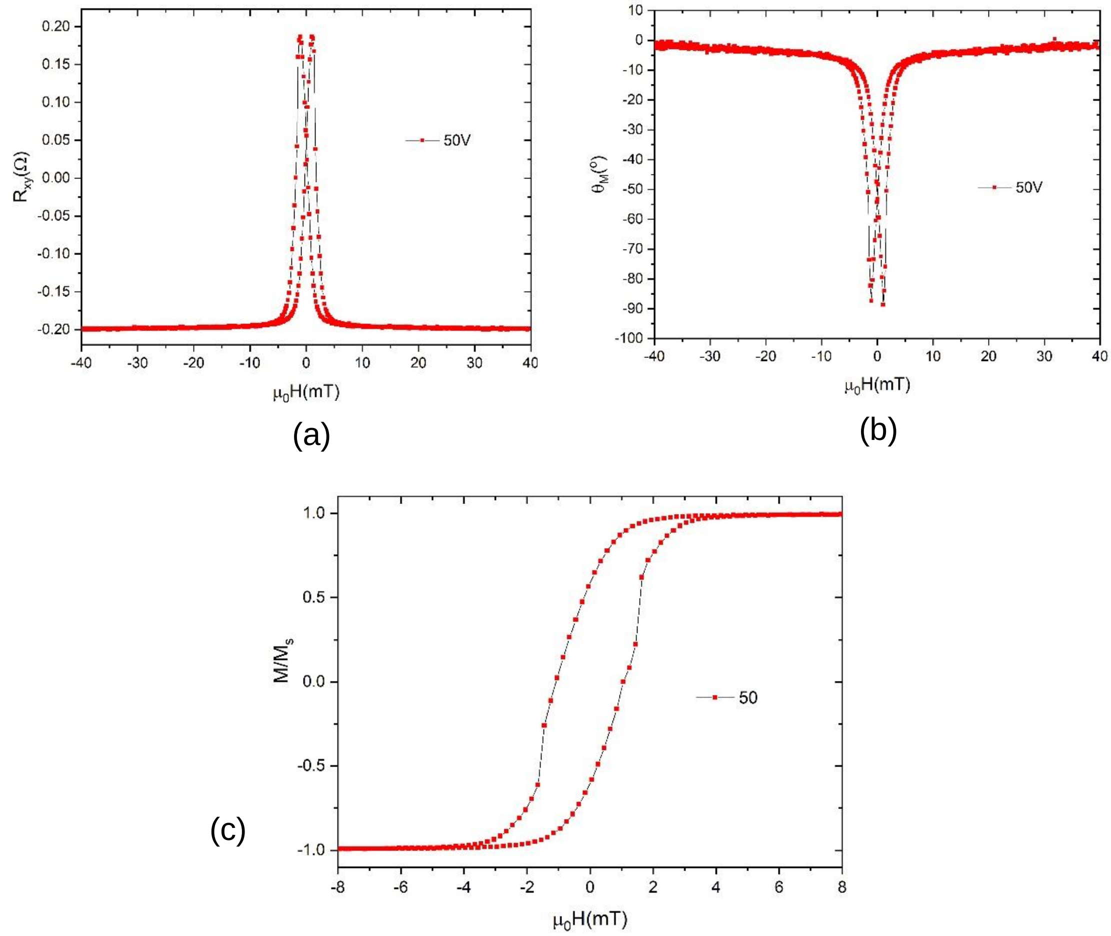

Figure 3.8: Extracting the magnetic hysteresis loop. (a) The R_{xy} of the S476 sample measured when a voltage of $+50V$ was applied to the piezoelectric transducer with the direction shown in the schematic in figure 3.5 (a). (b) The direction of the magnetisation with respect to the magnetic field. (c) The magnetic hysteresis loop ((M/M_s) extracted from the transport data.

The magnetic hysteresis loops at different voltages extracted from the data of the transverse resistance shown in figure 3.6 (b) are illustrated in figure 3.9. It shows that the magnetisation reversal depends significantly on the voltage applied to the transducer. The corresponding strain of each voltage is given in the inset of figure 3.9. It is shown that for the voltage equal to $-30V$, the magnetisation reversal has a very rectangular shape with a normalised remanence magnetisation (M_r/M_s) equal to ~1. This indicates that the magnetisation remains aligned with the magnetisation easy axis and switches abruptly by 180^o. For $+50V$, the shape has an s-shape, where a higher field is required to saturate the magnetisation, indicating that the field direction is now along a hard axis [95]. The inset in figure 3.9 shows a schematic of the hybrid device where the magnetic field is perpendicular to the long axis of the piezoelectric actuator. The magnetisation prefers to lie along the direction of the field when a compressive strain is applied (with the voltages shown in figure 3.9 with a value of $+10V$ and less), while for the tensile strain (for the voltages shown in figure 3.9 with a value of $+20V$ and more), the loops became harder, as the easy axis prefers to lie perpendicular to the magnetic field.

It is clear that applying a voltage to the transducer induces a strain in the permalloy sample, and that changes the magnetic free energy of the film, as the strain induces anisotropy. This is manifest as a change in the magnetic hysteresis loop, and hence a change in the magnetism of the permalloy sample [65]. Figure 3.10 (a) shows the variation of the normalised remnant magnetisation M_r/M_s at different voltages applied to the transducer, while 3.10 (b) shows the corresponding dependence on the strain. It can be seen that as the voltage increases from $-30V$ to $+50V$, the M_r/M_s decreases steadily for negative voltages, while for the voltage equal to $+20V$ and more, the M_r/M_s decreases significantly, indicating that the magnetisation easy axis changes with changing strain, from compressive to tensile strain values. For a compressive strain of value -1.78×10^{-4} $(-30V)$, the normalised remnant magnetisation was 0.98, and this decreased linearly to 0.95 for the strain of -0.24×10^{-4} $(+10V)$. In that case, the easy axis of the magnetisation preferred the direction along the short axis of the transducer (i.e. along the magnetic field direction). On the other hand, applying a tensile strain to the permalloy sample altered the preferred magnetisation direction to be along the long axis of the transducer (perpendicular to the magnetic field direction), and hence the M_r/M_s shows a dramatic change to reach 0.56 when a maximum tensile strain of value 1.78×10^{-4} $(+50V)$ is applied to the device.

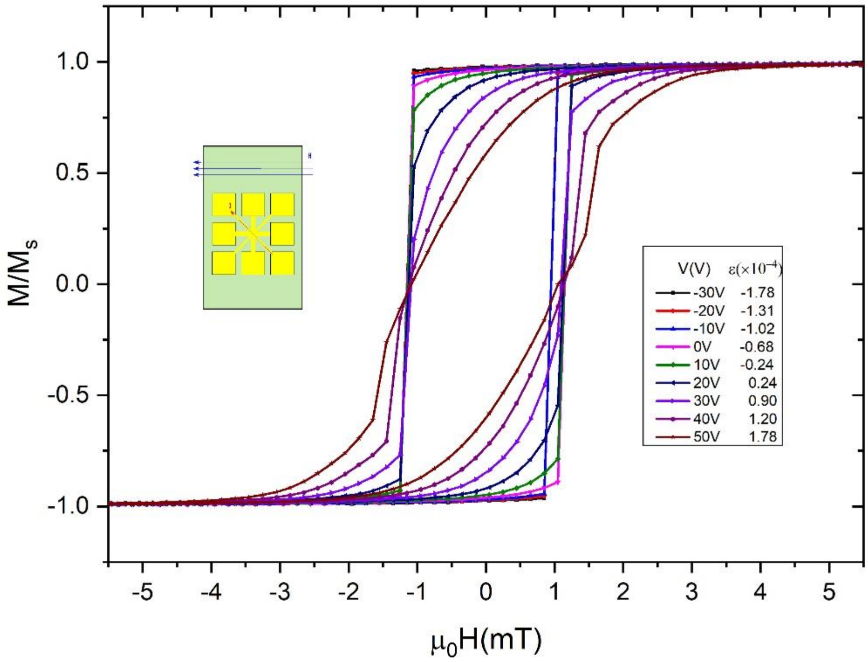

Figure 3.9: Magnetic hysteresis loops extracted from the transport measurements. The inset to the right shows the voltages applied to the transducer, and corresponding strain induced in the film. The schematic on the left illustrates the measurement configuration directions of the field and current, represented by blue and red arrows, respectively. The hysteresis loops change with the strain; magnetisation loops show harder reversal for the tensile strain values, as the magnetisation direction lies along the long axis of the transducer.

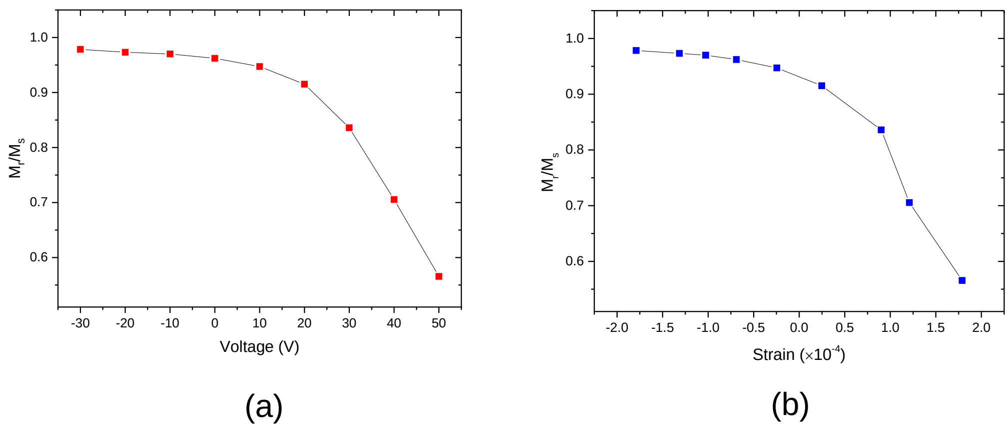

Figure 3.10**:** Normalized remnant magnetisation M_r/M_s as a function of (a) voltage applied to the piezoelectric actuator and as a function of (b) strain induced in the film.

To study the magnetisation reversal at selected voltages ($-30V$, $0V$, $+30V$, and $+50V$), the magnetotransport data and the extracted hysteresis loops for these voltages are shown in figure 3.11. The angle of the magnetisation as a function of the magnetic field as swept from large negative to large positive values during the reversal process is depicted schematically in figure 3.12 for each voltage. The hysteresis loops consist of regions where the magnetisation changes gradually, which we identify as a gradual reversal of the magnetisation, and represent these regions by red arrows in figure 3.12 for the reversal between (a) and (b) points before the switch, and between (c) and (d) after the switch. There is also a region where the magnetisation switches abruptly, represented by blue arrows between (b) and (c) points. When a voltage of $-30V$ is applied to the transducer, the reversal shows a very easy direction (figure 3.11 (c)). In this case, the magnetisation easy axis is along the field direction. The reversal angles are represented schematically in figure 3.12 (a); when the magnetic field swept from the saturation from the negative field direction, the magnetisation rotated (reversed gradually) away from the field direction by only $\sim 20°$ (see the red arrow (1)), before switching abruptly by $\sim 180°$ (see the blue arrow (2)). This was followed by a region of coherent rotation (see the red arrow (3)) as the magnetisation rotated towards the positive magnetic field, when the field swept to large positive values. For the $0V$ measurement, as shown in figure 3.11 (c), both $-30V$ and $0V$ show similar reversal with a bigger region (arrows (1) and (3)) where the magnetisation reverses slowly, as shown in figure 3.12 (b). On the other hand, at the largest positive voltages ($+30V$ and $+50V$), the reversal of the magnetisation became harder, as shown in the magnetisation hysteresis in figure 3.11 (c), as the magnetisation easy axis changed to lie along the tensile strain direction (perpendicular to the field direction), as the field was reduced to zero. Figure 3.12 (c) and (d) show the schematic reversal of $+30V$ and $+50V$, where the red arrow (1) indicates that the magnetisation reverses slowly to the easy axis direction (perpendicular to the field), followed by an abrupt switch (blue arrow (2)). It is worth noting that in the region where the magnetisation rotates towards saturation (represented by region 3 in figures 3.12 (c) and 3.12 (d)), the magnetisation follows a different path to that followed in the region where the magnetisation is rotating away from the field as it reduces from saturation (region 1 in figures 3.12 (c) and 3.12 (d)). One can assume that, for the tensile measurements, the reversal after the abrupt switch (represented by the red arrow (3)) shows harder reversal than the reversal before the switching (red arrow (1)) (see figures 3.11 (c), 3.12 (c) and (d)). As explained in section 3.2.3, this was not expected within the model of the coherent rotation, and we are not able to model the whole data in the magnetisation reversal. The region (1) does not follow the coherent rotation model, and we speculate that might be related to the built-in strain due to the Joule magnetostriction as inducing an anisotropy varies with the magnetic field value. Hence a single uniaxial anisotropy is not valid for the reversal part as the reversal could be due to the domain wall motion, this is discussed in detail in section 3.2.3. The rotation of the magnetisation (as represented by arrows (1) and (3)) for $-30V$ and $0V$ measurements in figure 3.12 (a) and (b) could be explained due to a small offset between the magnetic field and the new easy axis induced by the strain, since perfect alignment is difficult to achieve practically. For the tensile strain, the magnetisation started to rotate away from the field direction at a higher negative field, as shown in magnetoresistance and magnetisation measurements in figure 3.11 (a), (b), and (c) for $+30V$ and $+50V$ measurements. The magnetisation reversal shows that the magnetisation rotated by 90^o, or more than that when applying $+30V$ and $+50V$, respectively. On the other hand, the field needed to saturate the magnetisation along the positive field direction at point (d) increases with increasingly positive voltages. This provides a clear idea about what strain does to the magnetisation reversal; for compressive strain, the magnetisation prefers to lie along the short axis of the piezoelectric transducer (parallel to the magnetic field), while it favours lying along the long axis of the transducer (perpendicular to the field direction) when a tensile strain is applied.

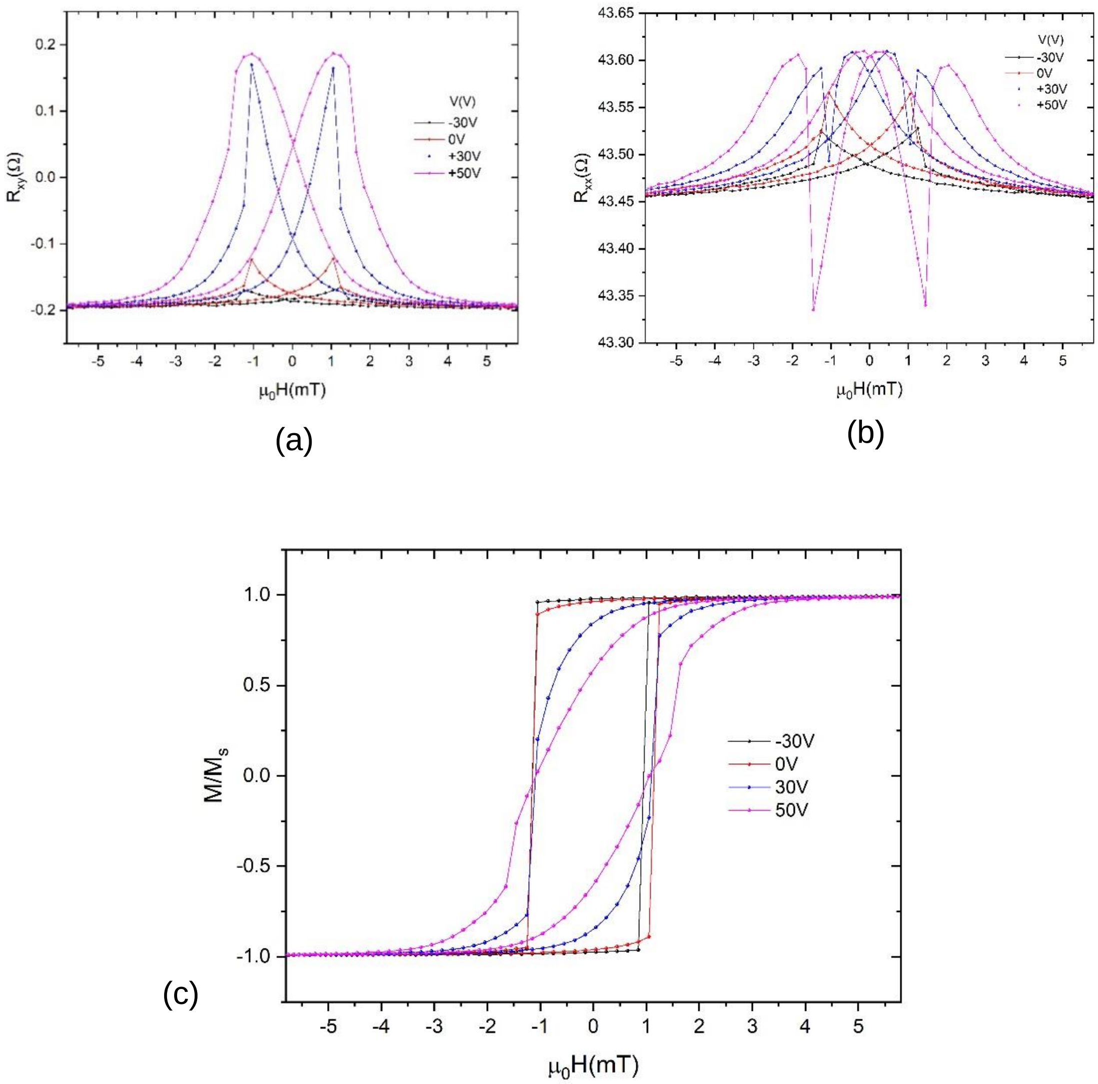

Figure 3.11*:* *A* comparison between (a) R_{xy}, (b) R_{xx}, and (c) the extracted magnetic hysteresis loops when voltages of $-30V$, $0V$, $+30V$, and $+50V$ are applied to the transducer for the measurements of the permalloy sample S476 when the magnetic field is perpendicular to the transducer ($\varphi = 90^o$). Note that small scale is used for all graphs to accentuate different features of the reversal.

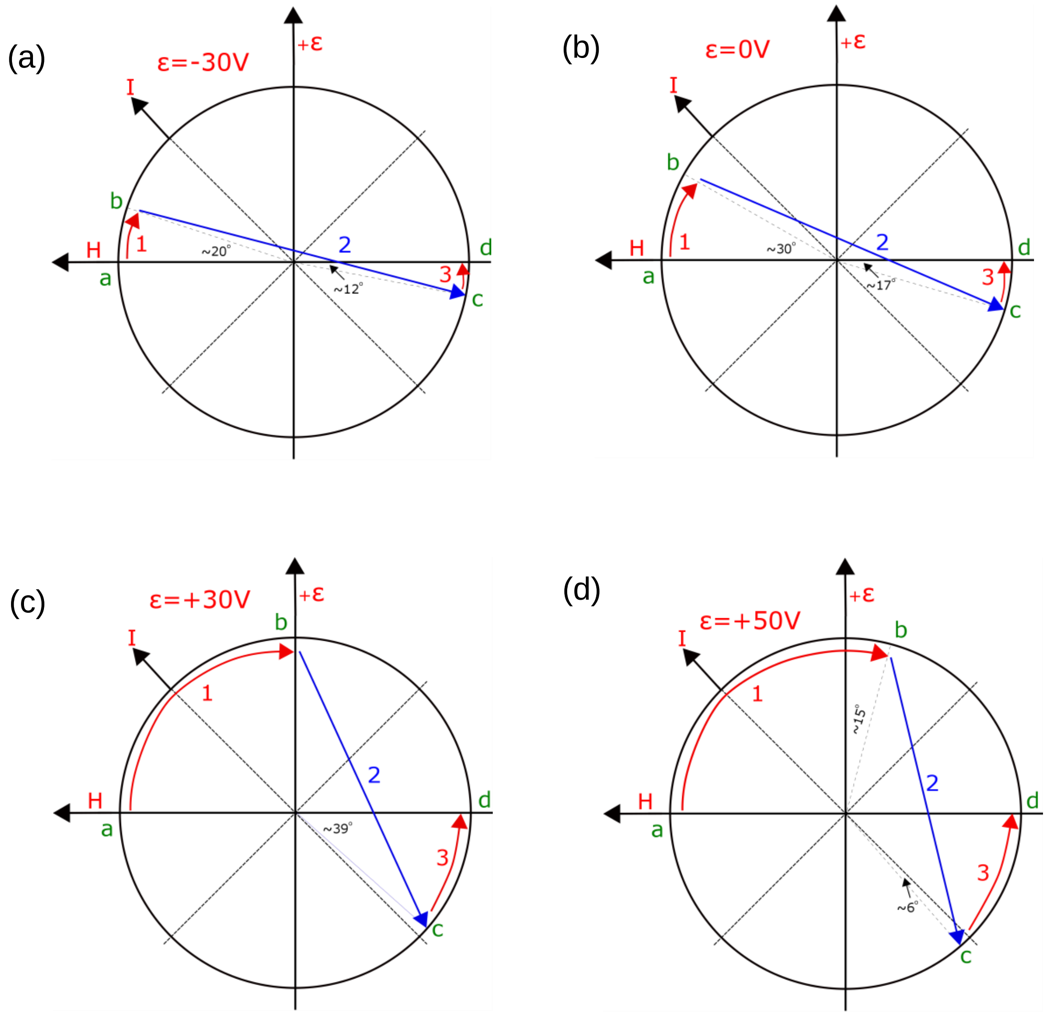

Figure 3.12: Illustrations of the magnetisation reversal for sample S476 when different voltages are applied (a) $-30V$, b) $0V$, c) $+30V$, and (d) $+50V$. Red arrows represent the slow reversal of the magnetisation, and blue arrows represent the abrupt switching of the magnetisation. The directions of strain, magnetic field, and electric current are shown in the figures. The angles of magnetisation are determined from the R_{xx}, and R_{xy} curves.

3.2.2.2 Magnetic field parallel to the long axis of the transducer ($\varphi = 0^o$)

When the magnetic field is rotated by 90^o from the previous position, the magnetic field is parallel to the long axis of the transducer ($\varphi = 0^o$), and the current is along $\alpha = +45^o$ to the field (figure 3.13 (a)). Figures 3.13 (b) and (c) show R_{xx} and R_{xy} as the field is swept in the plane of the device, while the corresponding magnetic hysteresis loops are shown in figure 3.14. It is clear that the magnetisation reversal strongly depends on the voltages applied to the transducer. The strain affects the magnetoresistance value in the opposite way compared with the case when the magnetic field makes an angle $\varphi = 90^o$ to the transducer. At large positive voltage, the easy axis of the permalloy is in the same direction of the field (along the long axis of the transducer), while at a large negative voltage, the magnetisation favours the direction perpendicular to the field (along the short axis of the transducer). Figure 3.15 (a) shows a comparison of the M_r/M_s for the two field directions as a function of the voltage applied to the transducer, and figure 3.15 (b) shows the angle of the magnetisation with respect to the field (θ_M) at $0mT$ when the magnetic field is swept from the negative to the positive direction. Both plots reveal that the magnetisation reversal of the permalloy is dependent on the strain type and direction. The crossing of the curves at approximately $+20V$ indicates that the absolute value of the voltage-induced strain is near zero (as mentioned before, $+16V$ is the zero strain). The magnetisation reversal loops when a voltage of $+20V$ is applied to the transducer when the field is perpendicular and parallel to the transducer are shown in figure 3.15 (c), where it is shown the near-zero strain value gives the same loops in both directions. The schematic illustrations of the reversal of the magnetisation at different voltages are not shown for these measurement directions since it gives the opposite effect to the reversals shown in figure 3.12 for the previous measurement.

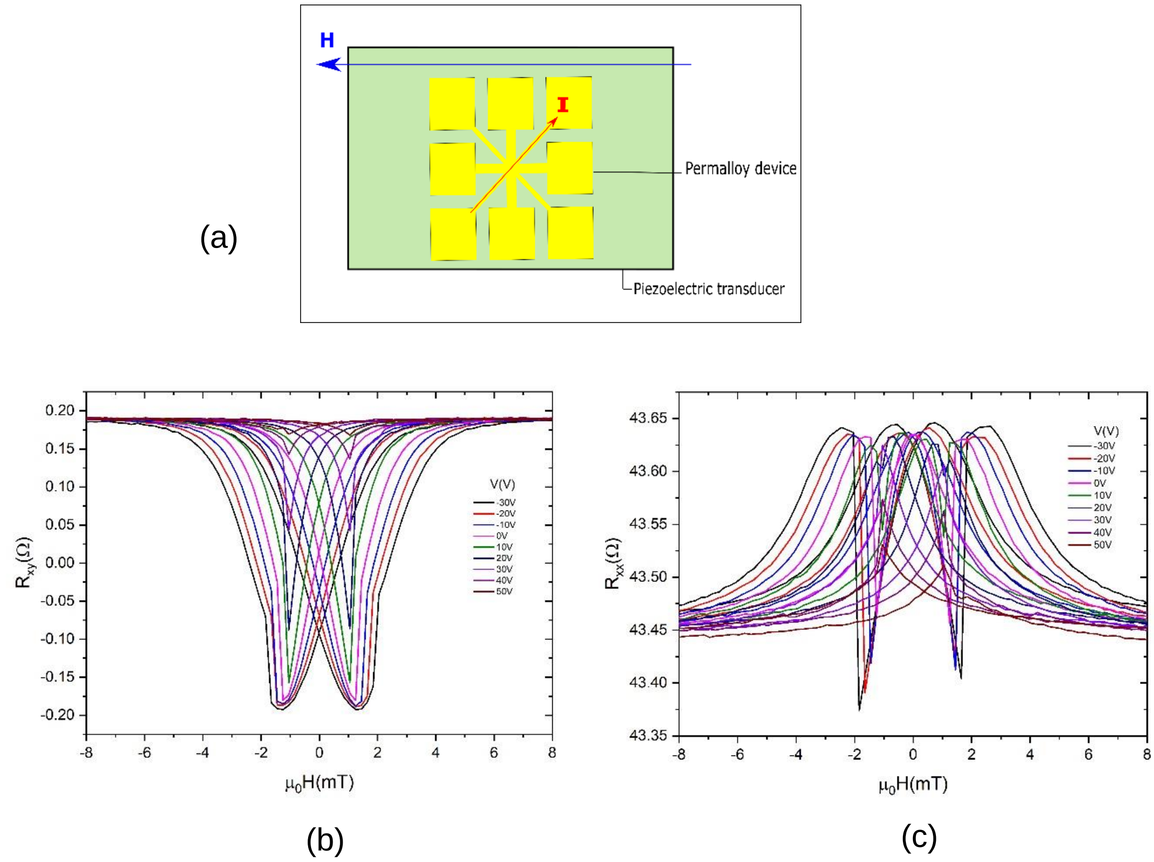

Figure 3.13: (a) A schematic of the hybrid device configuration with respect to the magnetic field where the magnetic field is parallel to the long axis of the actuator ($\varphi = 0^o$), with a current direction $\alpha = +45^o$. (b) R_{xy} and (c) R_{xx} when voltages between $-30V$ and $+50V$ are applied to the piezoelectric device to induce a strain in the permalloy film. The values of the resistance and shapes were changed with changing strain.

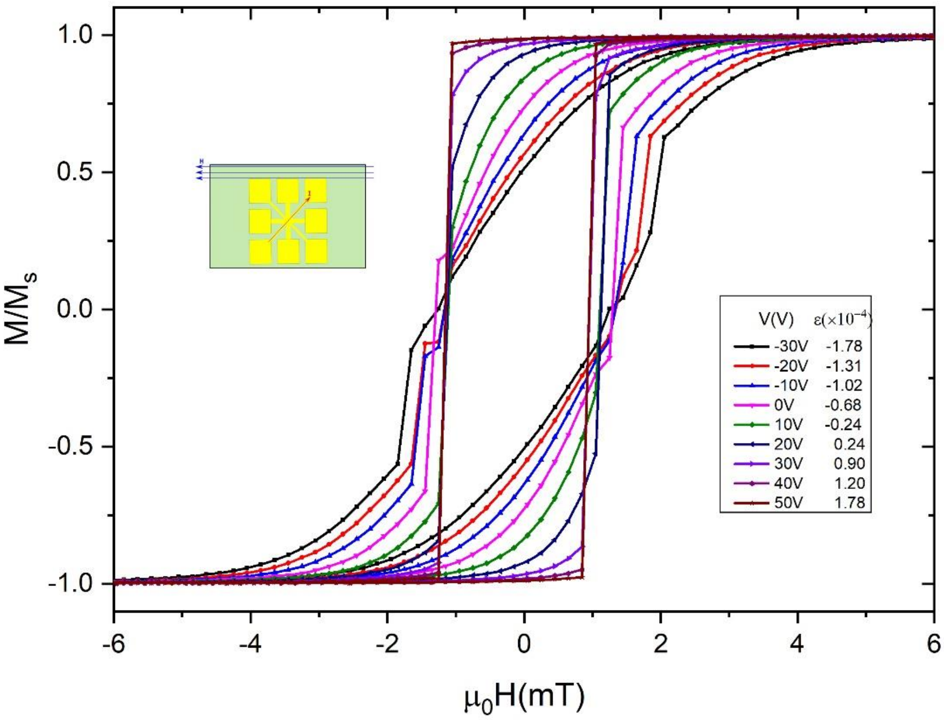

Figure 3.14: Magnetic hysteresis loops extracted from the transport measurements and the inset to the right shows the voltages applied to the transducer, and corresponding strain induced in the film. The schematic on the left illustrates the measurement configuration directions with the current and field represents by red and blue arrows, respectively. The hysteresis loops changing with the strain; the magnetisation loops show harder reversal for the compressive strain as the magnetisation direction is along the short axis of the transducer.

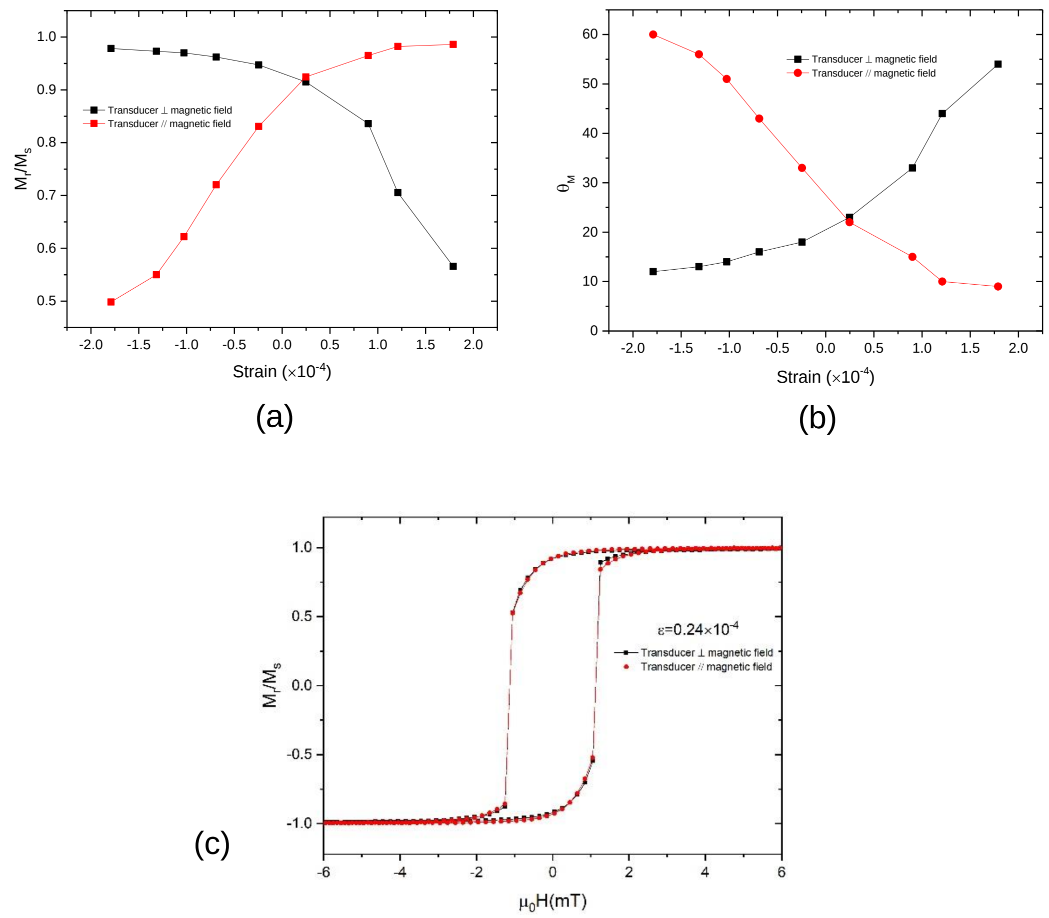

Figure 3.15**:** (a) A comparison of M_r/M_s as a function of strain induced in the film, showing that the value of the M_r/M_s depends on the strain direction with respect to the magnetic field. (b) A comparison of the θ_M for the S476 sample when the magnetic field decreased to $0mT$, when the field swept up between $-40mT$ and $+40mT$ for measurements when the magnetic field is parallel and perpendicular to the transducer. (c) hysteresis loops when a voltage of $+20V$ is applied to the transducer for the measurements when the field is making angles of $\varphi = 0^o$ and $\varphi = 90^o$ to the transducer.

3.2.2.3 Strain control switching field of the permalloy

As discussed in the previous sections, strain-controlled the magnetoresistance and magnetisation reversal of the permalloy sample. It was clear that the magnetisation easy axis changed in both directions' measurements when the magnetic field was parallel and perpendicular to the transducer. Figure 3.16 (a) shows a zoomed section of the longitudinal resistances curves (see the whole image in figure 3.13 (c)) for the measurements when the field was parallel to the transducer ($\varphi = 0^o$) at different voltages; the switching field changed with varying voltages, as indicated by black arrows in the image. For this measurement, the magnetisation lay on the new axis introduced by compressive strain, perpendicular to the field. As discussed before, the range of the field where the magnetisation reverses gradually increased by increasing the strain when it was perpendicular to the field direction. Consequently, a higher magnetic field is needed to switch the magnetisation to another field direction. In figure 3.16 (a), the switching field is changed between $1.8mT$ to $0.8mT$ when changing the voltages between $-30V$ and $+50V$. The relation between applied voltages and strain with the switching field is shown in figure 3.16 (b) and (c) for measurements when the magnetic field is parallel and perpendicular to the transducer. It is obvious that the effect of strain on switching became significant when the strain direction is perpendicular to the field in both direction measurements. For the strain values around 0, the switching field tends to be unchanged, which could be attributed to the weak strain at these values for both measurement directions. It is clear that when the field is parallel to the transducer, the change in the switching field is more than in another direction, which could be due to the intrinsic anisotropy introduced in the sample during the sample growth, as discussed in section 3.2.3 with regard to SQUID measurements.

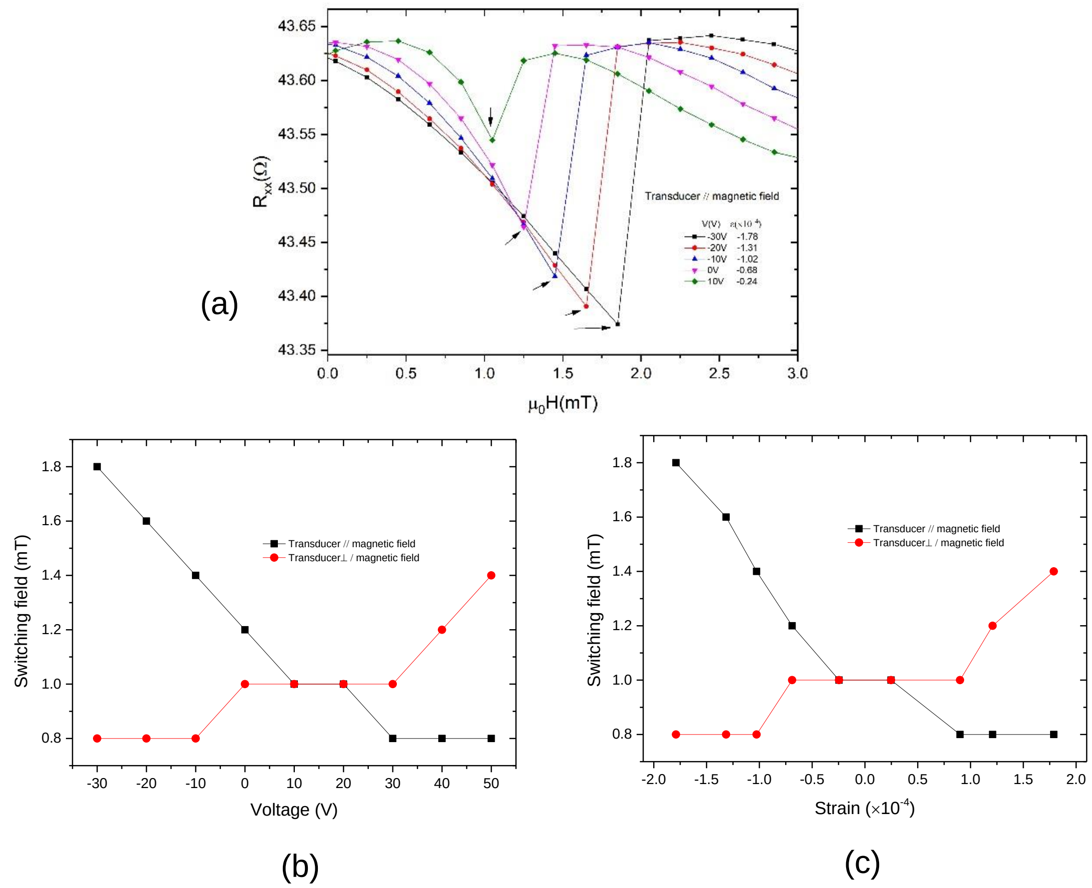

Figure 3.16**:** (a) Zoomed section of the R_{xx} curves for the S476 sample when the field is parallel to the transducer ($\varphi = 0^o$) at different applied strain (voltages) (see the original image in figure 3.12 (c)). The switching field values when the transducer is parallel and perpendicular to the magnetic field as a function of (b) voltage and (c) strain.

3.2.2.4 Strain control switching direction when the magnetic field is $\boldsymbol{\varphi = +45^o}$ and $\boldsymbol{\varphi = -45^o}$ to the long axis of the transducer

Other measurements were performed using different directions for the field with respect to the long axis of the transducer. The magnetic field was aligned to be along $\varphi = +45^o$ and $\varphi = -45^o$ to the long axis of the transducer while the current was along $\alpha = 90^o$ and $\alpha = 0^o$, respectively. The R_{xy} curves for both directions with different voltages applied to the transducer are shown in figures 3.17 (a) and (b). For both measurements, the resistance curves show different directions as the strain changes from compressive to tensile strain. This might be related to the magnetisation reversal direction as the field swept between the two directions of the magnetic field; it reverses clockwise or anticlockwise in the plane of the film, depending on the strain type and direction. As an example of how the strain affects the switching direction, illustrations of the magnetic reversals of the permalloy sample are shown in figure 3.18 (a) and (b) for the measurements when the field was $\varphi = -45^o$ to the transducer. When a compressive strain of -1.78×10^{-4} $(-30V)$ was applied to the sample, the magnetisation preferred to lie along the short axis of the transducer, where it is clear that magnetisation rotated a way hardly to the new easy axis, along the short axis, as illustrated by the red arrow (1) from point (a) to (b) in figure 3.18 (a). The magnetisation then switched by 180^o, as indicated by the blue arrow (2). As the magnetic field starts to increase in the positive direction, the magnetisation reverses slowly (which could be a rotation) to lie along the field direction. In contrast, when a strain of $+1.78 \times 10^{-4}$ $(+50V)$ was applied, the magnetisation rotated away by 45^o from the decreasing negative field to reach the long axis of the transducer, and the magnetisation's new easy axis favoured lying in that direction. Subsequent switching and rotation to the field positive direction, as illustrated in figure 3.18 (b), clarifies that the magnetisation's easy axis direction changes by tuning the strain from compressive to tensile values. As the compressive strain was ramped down (changing the voltage from $-30V$ to reach $+10V$), the magnetisation reversal became less hard, as can be seen from the curvature changes of the rotation in resistance curves. On the other hand, as the voltage increased from $+20V$ (ramping up the strain), the magnetisation became harder, as reflected in the resistance curves. When a voltage of $+20V$ $(+0.24 \times 10^{-4})$ was applied, both measurements showed a very distinct case, with the magnetisation showing very easy reversal between the two magnetic field directions (negative and positive) (see figures 3.18 (a) and (b)). This agreed with the previous measurements when the transducer was perpendicular and parallel to the magnetic field. This strain value is very close to the zero strain value. One can assume that there is no preferable axis for the magnetisation at this strain, and that the sample has more polycrystalline properties with an easy plane. It is difficult to extract the direction of the magnetisation reversal at this strain value, since it showed some complicated peaks in the transverse resistance for both measurements when the magnetic field is $\varphi = +45^o$ and $\varphi = -45^o$ to the long axis of the transducer.

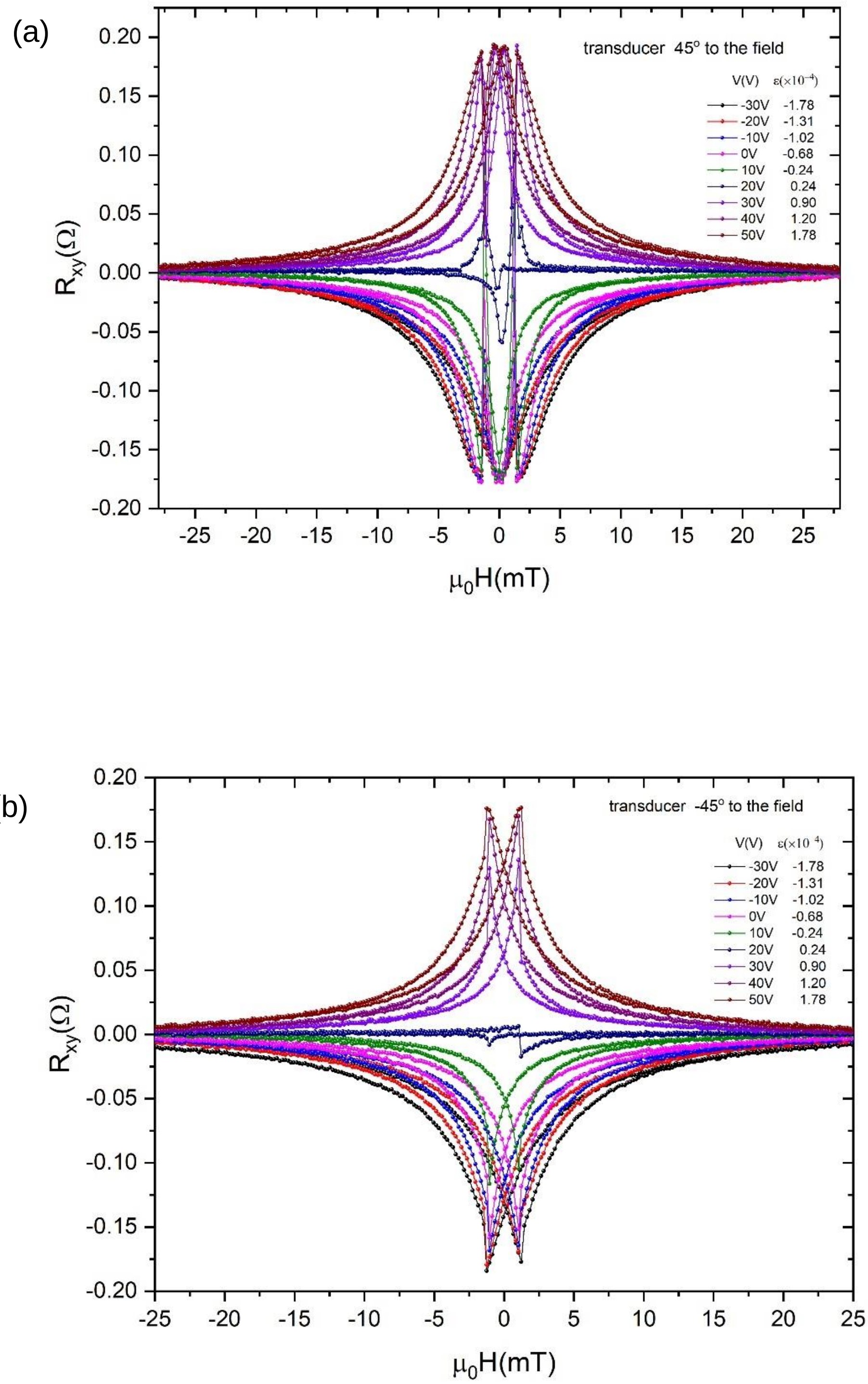

Figure 3.17: R_{xy} curves for different voltages (strain) when the transducer is along (a) $\varphi = +45^o$ and (b) $\varphi = -45^o$ to the magnetic field. The $+20V$ (0.24×10^{-4}) curves in both figures (shown in blue) indicate distinct behaviour, with an easier switching curve.

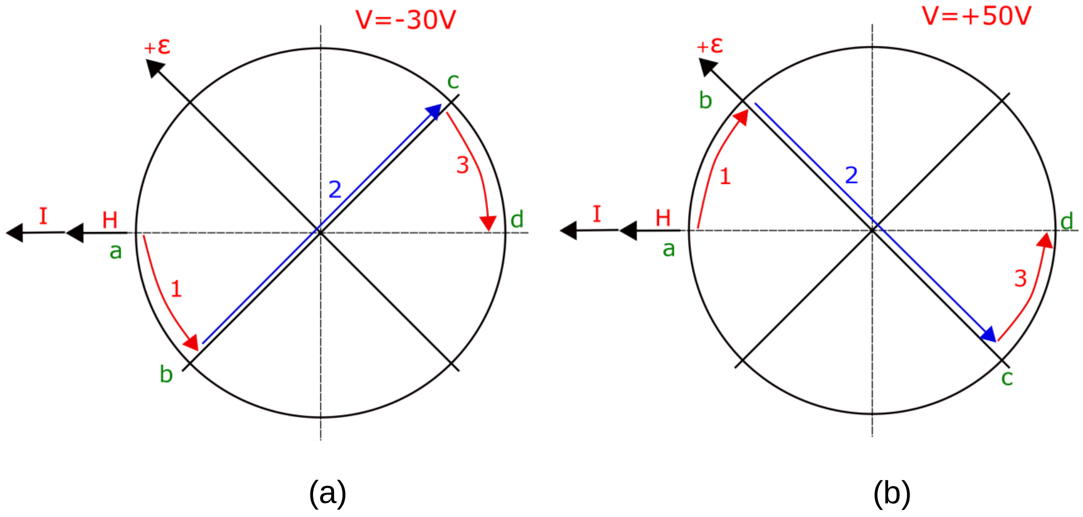

Figure 3.18**:** Magnetisation reversal when the magnetic field is along $\varphi = -45^o$ to the transducer, with voltages of (a) $-30V$ and (b) $+50V$ applied to the transducer. The switching direction of the magnetisation changed with changing strain, from compressive to tensile.

3.2.3 Modelling the magnetisation reversal of the permalloy sample

In this section, an attempt to model the data of magnetisation hysteresis loops of the permalloy sample was performed in order to determine the anisotropy values induced by the piezoelectric transducer in the permalloy film. The simulation was applied to the experimental data when the magnetic field is parallel and perpendicular to the transducer. The simulation focused on the voltage range where hard hysteresis loops were observed because in those regions, the voltage-induced strain had the greatest effect on the shapes of the magnetic hysteresis.

Figure 3.19 (a) shows an example of the data used for the fitting. It showed a hysteresis loop when a voltage of $+50V$ was applied to the piezoelectric transducer for the perpendicular configuration of the magnetic field to the transducer. The corresponding illustration for the magnetisation reversal of sweep-up loop is shown in figure 3.19 (b). Colours in figure 3.19 (a) and (b) represent the same magnetisation movement. The black colour region in 3.19 (a) represents the sweep-down measurement, which is symmetric to the sweep-up measurement, and hence the discussion will focus on one sweep of the hysteresis (sweep-up). The sweep-up of the hysteresis loop is divided into three regions:

1) The reversal before the switching, shown as region number (1) in both figures, with red colour.

2) The switching area is shown by the blue colour (2).

3) The coherent rotation after the switching shown by red colour is indicated as number (3).

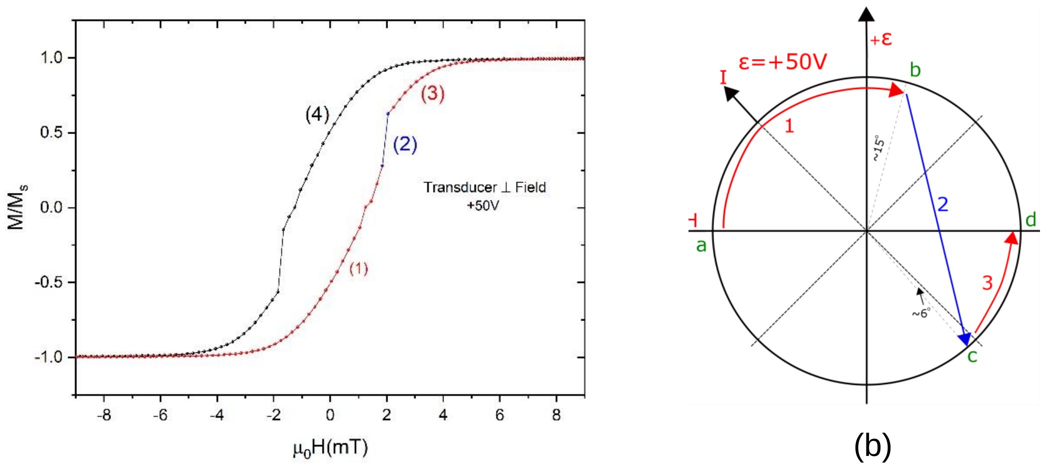

(a)

Figure 3.19**:** (a) The magnetic hysteresis loop when a voltage of $+50V$ was applied to the transducer, where the field is perpendicular to the transducer direction ($\varphi = 90^o$). (b) A schematic for magnetisation reversal for the same measurement configuration at the same voltage applied to the transducer. The same colours of red and blue regions shown in (a) and (b) represent the same magnetisation reversal.

Focusing on the hysteresis loop in figure 3.19 (a), it is clear that the curves before and after switching are not symmetric, where is the reversal in the region (3) is harder than the region (1). It was difficult to simulate the whole loop since it did not give a good fit when including the switching region (2) along with regions (1) and (3). The single-domain Stoner-Wolfarth model [164] was used to model curves (1) and (3) separately. The coherent rotation model does not work for the curve (1) since the magnetisation does not show zero value when the field is zero for the hard axis ($\varphi = 90^o$). According to this model, the single uniaxial anisotropy must force $M = 0$ when $H = 0$ for the hard reversal direction. We speculate that could be related to the Joule magnetostriction, whereby the saturation of the magnetisation at negative field induces a strain that varies as a function of the field, and this induces an anisotropy that competes with the anisotropy induced by the transducer[55]. This strain is then released when the magnetisation switches in region 2. As a result of this induced anisotropy, the material reversal is more complicated, which could be attributed to multi-domains reversal, and hence the coherent rotation is not the main reversal at the region (1). Many attempts were performed to simulate the curve (1) with one or two anisotropies, but the coherent rotation model does not work for the curve (1). On the other hand, curve (3) simulated separately using the coherent rotation model as follows [164]:

$$\epsilon = -MHcos(\varphi - \theta) + K_s sin^2(\theta) \tag{3.5}$$

where ϵ is the energy density for the curve (3), the first term is the Zeeman term; the second term is the magnetoelastic term introduced in the sample by the piezoelectric transducer (uniaxial term), φ is the angle between the magnetic field and the long axis of the actuator, θ is the angle between the magnetisation easy axis and the long axis of the actuator, and K_s represents the magnetoelastic anisotropy constant. The direction of the magnetic field with respect to the long axis of the actuator direction was used here as a reference for the directions of the simulation, as shown in figure 3.20.

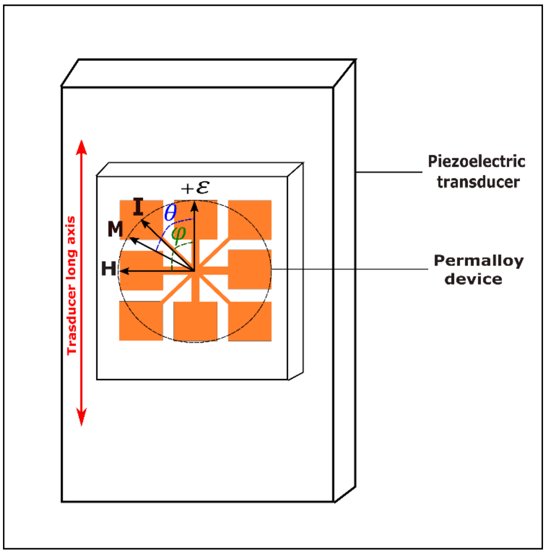

Figure 3.20: The illustration of the hybrid device along with the magnetic field and the current direction to the long axis of the piezoelectric transducer. The angles used in equations 3.5 are illustrated in the figure.

To find the magnetisation projection M used to simulate the hysteresis loops, the free energy equation was solved numerically to find its minimum. For the simulation, the magnetic field varies between $-40mT$ and $+40mT$, and a saturation magnetisation M_s of the permalloy (measured using SQUID, as discussed later) is used in the simulation (equation 3.5). The angle θ varies between 0^o and 360^o in steps of 0.20^o. The simulated curves were fit to the experimental hysteresis loops using the least sum squares method, as follows:

$$C = \sum_{i=1}^{n}(X_i - Y_i)^2 \qquad (3.6)$$

where X_i and Y_i are points in the simulated and experimental curves, respectively, with a total of n points. Range of values of K_s is varied to find the best fit between the experimental and simulated data. Fits to the experimental data when $+50V$ and $+30V$ are applied to the piezoelectric transducer for the curve (3) are shown in figure 3.21 (a) and (b). Two different anisotropy constants were obtained from these fitting for the curve (3) with values of $K_s = 1020 \mp 40 J/m^3$ and $K_s = 720 \mp 70 J/m^3$ when applied $+50V$ and $+30V$, respectively. The C (cost function) is in the range of 1×10^{-4} to 9×10^{-4} for the range of voltages data used to extract the anisotropy values when K_s is used for fitting. For this measurement direction ($\varphi = 90^o$), voltages of range between $+50V$, and $+20V$ in steps of $+5V$ were used to determine the anisotropies constant K_s as shown in figure 3.22 (a). Figure 3.22 and (b) show the relation between the anisotropy K_s and the strain applied by the transducer into the film when the magnetic field is perpendicular to the transducer. As discussed in section 1.2.2.4, K_s can be expressed as:

$$K_s = B_1\left(\varepsilon_{xx} - \varepsilon_{yy}\right) + K_{so} \qquad (3.7)$$

where B_1 is the magnetoelastic constant (proportional to the magnetostriction constant λ_s), and K_{so} is the intercept since K_S does not go to zero at zero strain. The magnetoelastic constant represented by the linear fit in figure 3.22 (b) with a value of $B_1 = (2.9 \mp 0.2) \times 10^6 J/m^3$ for the direction when the field is perpendicular to the long axis of the transducer. Song et al. [160] found that for the permalloy ultrathin films with the same composition used in this study, for films that have a thickness less than $2nm$, $B_1 \cong 1\ \times 10^5 J/m^3$ to $4 \times 10^5 J/m^3$, while for films that have a thickness of $4nm$ and above (i.e. bulk thickness), it is equal to $B_1 = -0.76 \times 10^5 J/m^3$. For a thickness between $3nm$ and $4nm$, the B_1 value is changed between positive and negative, and it should be equal to zero at a certain thickness. In the present study, the value of the magnetoelastic constants are quite high compared to those of Song et al. [160], as the strain could change the direction of the magnetisation by 90^o when changing the strain type and direction.

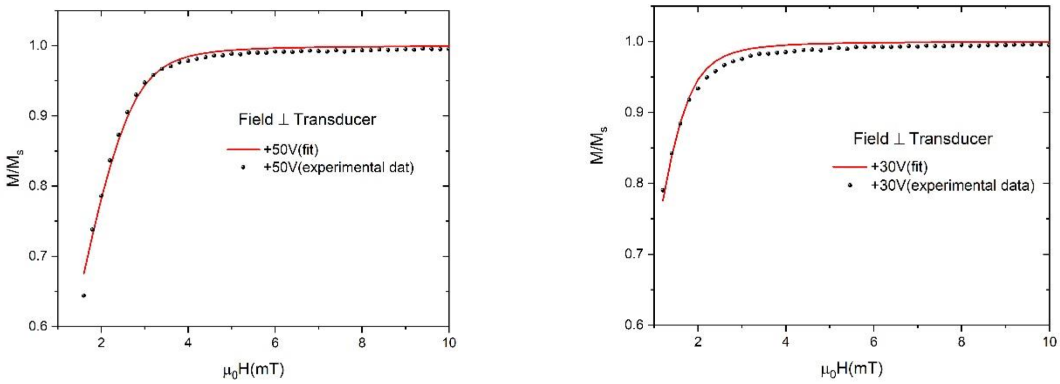

(a) (b)

Figure 3.21: (a) Demonstration of the magnetic hysteresis loop fitting for region 3 when voltages of (a) $+50V$ and (b)+30V are applied to the transducer for the measurement $\varphi = 90^o$.

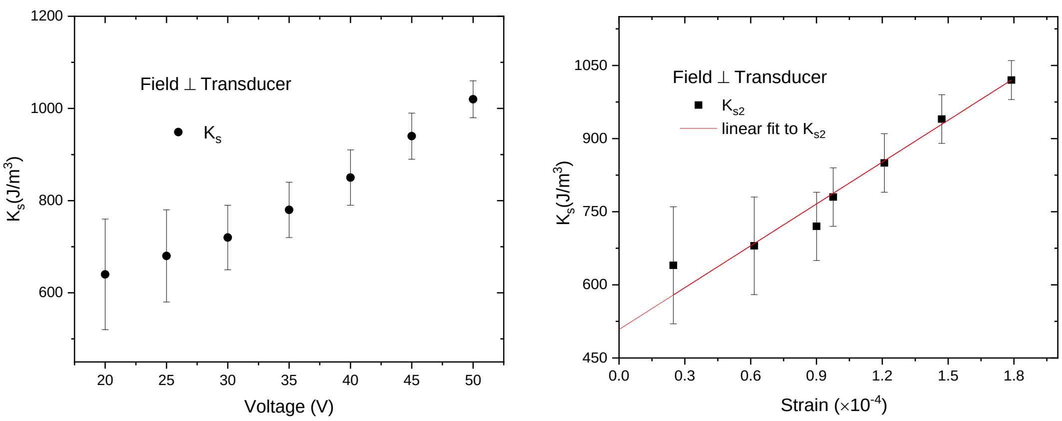

(a) (b)

Figure 3.22: (a) The magnetoelastic anisotropies constants K_s for the permalloy sample when the magnetic field is perpendicular to the transducer ($\varphi = 90^o$) as a function of (a) voltage, and (b) strain. The linear fit of the points in (b) gives the value of the magnetoelastic constants (B_1).

On the other hand, when the magnetic field is parallel to the piezoelectric transducer ($\varphi = 0^o$), the anisotropies constants value (for the curve (3)) varies with voltage, as shown in figure 3.23 (a). It shows the maximum value of $K_s = -1370 \mp 20 J/m^3$ when a voltage of $-30V$ is applied, while $K_s = -1020 \mp 60 J/m^3$ when -5V is applied. The linear fits for K_s with the strain is shown in figures 3.23 (b), given the value of the magnetoelastic constant of $B_1 = (3.8 \mp 0.3) \times 10^6 J/m^3$.

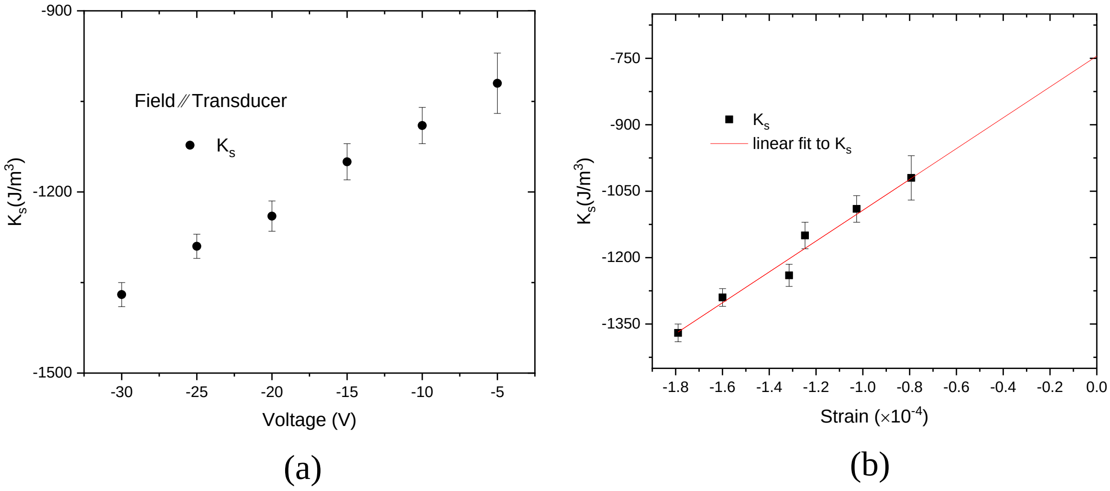

Figure 3.23: (a): (a) The magnetoelastic anisotropies constants K_s for the permalloy sample when the magnetic field is parallel to the transducer ($\varphi = 0^o$) as a function of (a) voltage, and (b) strain. The fit of the points in (b) gives the value of the magnetoelastic constants (B_1).

In both measurements of $\varphi = 90^o$ and $\varphi = 0^o$, the fit in figure 3.22 (b) and 3.23 (b) is extrapolated to zero strain value intercepting with values of $K_s = 510 \mp 30 J/m^3$ and $K_s = -750 \mp 50 J/m^3$ for both directions, respectively. These anisotropies constants are quite large compared to the anisotropy of the permalloy film measured by the SQUID as discussed later in this section with a value of $K_u = 320 \mp 10 J/m^3$. Furthermore, the difference in the intercept between the two directions ($\varphi = 90^o$ and $\varphi = 0^o$) in value and sign is quite high, rather it should be equal. This could be attributed to the residual strain induced by the joule magnetostriction even after the switching event which could affect differently in both measurement directions. On the other hand, this might be related to the applicability of the coherent rotation model to the polycrystalline material as the reversal could not be due to the rotation of the magnetic domains. Rather, the reversal of the permalloy sample could be more complicated due to the domain wall motion as the anisotropy varies inhomogeneously through the film.

A SQUID measurement was performed for the thin film (with no patterns) of the permalloy sample using the method described in section 2.4 to determine the saturation magnetisation and to investigate any intrinsic anisotropy induced during the growth. The SQUID data for two directions of the film is shown in figure 3.24, where the sample dimension used was $4mm \times 4mm$ (to exclude any shape anisotropy that could appear in the measurement). It can be seen that the coercivity of the film is equal to $0.2mT$, which is ~5 times less that of the micro-device, which could be attributed to the pinning sites of the magnetic domains that appeared during fabrication. It is also clear that one direction showed an easier direction for the magnetisation, whereas another showed harder magnetisation direction. It is known that during the deposition of polycrystalline material a small uniaxial anisotropy K_u might be introduced in the film as an intrinsic strain, where the deposition rate, vacuum level, or any deposition parameters could affect the structure of polycrystalline materials [65,165,166]. To find the value of the intrinsic stress in the film, the SQUID data is simulated and fitted using the equation:

$$\epsilon = -MHcos(\varphi_m - \theta_1) + K_u sin^2(\theta_1) \quad (3.8)$$

where φ_m is the angle between the magnetisation easy axis and the magnetic field, θ_1 is the direction between the magnetisation and the easy axis, and K_u is the uniaxial anisotropy. In this case. The least-square fit in the simulation of the loop is used to fit with the SQUID data. The fit is shown in figure 3.25 for the hard axis, where $K_u = 320 \mp 10J/m^3$, which might be introduced in the film during the deposition as an intrinsic strain [14]. As mentioned before that this anisotropy is different than those anisotropies extracted from the extrapolation of the strain at zero value, as shown in figures 3.22 (b) and 3.23 (b). However, this also could explain the difference in the absolute values of the maximum K_s

anisotropies in both fitting directions. Comparing the absolute values of the difference between $K_s = 1370J \mp 30/m^3$ and $K_s = 1020 \mp 40J/m^3$, for $\varphi = 0^o$ and $\varphi = 90^o$, gives $\Delta K_s = 350 \mp 70J/m^3$, which is very close to the uniaxial anisotropy $K_u = 320 \mp 10J/m^3$ extracted from the SQUID measurement. It is worth mentioning here that the uniaxial anisotropy was not independently included in equations 3.5 and 3.6, where it was included with the magnetoelastic term, since it is quite small compared to the external magnetoelastic term, and its omission makes the equations easier for the simulation (by reducing the variables). The saturation magnetisation of the permalloy was calculated from the SQUID data with a value of $(1030 \mp 20) \times 10^3 A/m$.

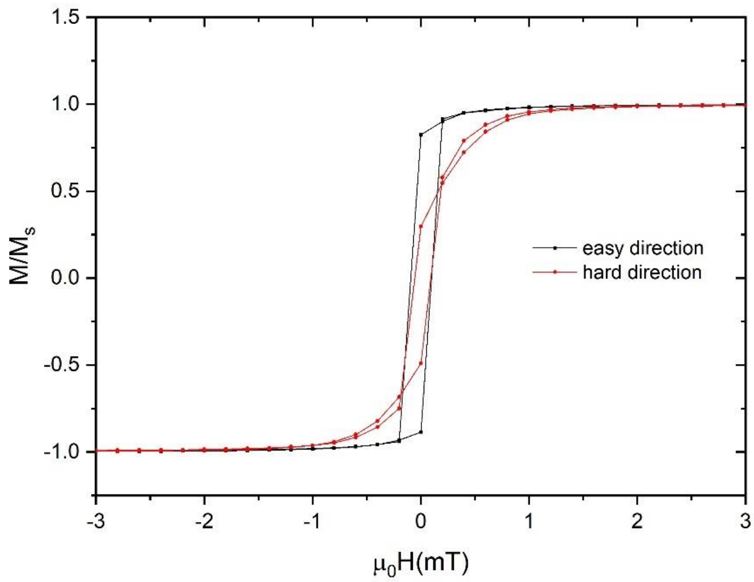

Figure 3.24: SQUID magnetic hysteresis loop data for the permalloy sample S476 thin film (with no patterns) measured for two directions perpendicular to each other. The measurements show that one direction is harder than the other direction when a uniaxial anisotropy $K_u = 320 \mp 10J/m^3$ is introduced in the film during growth.

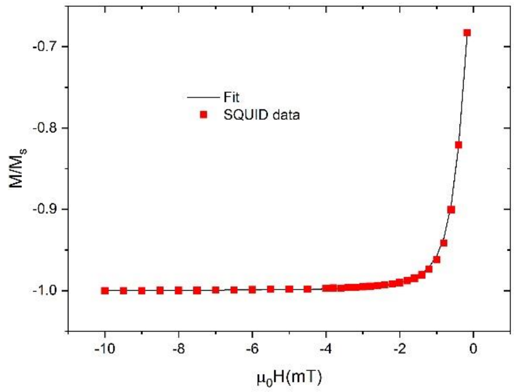

Figure 3.25: Demonstration of the SQUID magnetic hysteresis loop fitting for the permalloy sample (as-deposited thin film) for the harder direction of the magnetisation with a uniaxial anisotropy value of $K_u = 320 \mp 10 J/m^3$.

As mentioned in chapter 1 that permalloy is an alloy of nickel and iron with different composition Ni_xFe_{100-x}, whose magnetic properties vary with changing x. For the compositions shown in table (3.1), the saturation magnetisation M_S, saturation magnetostriction λ_S, and uniaxial anisotropy field H_K are compared [53].

Table 3.1: A comparison of the magnetic properties of the permalloy with different composition of iron and nickel [53].

Permalloy composition	M_S **(**$\times 10^3 A/m$**)**	$\mu_0 H_K$ **(mT)**	λ_S
$Ni_{86.7}Fe_{13.3}$	754.01	0.62	-6.58×10^{-6}
$Ni_{79.9}Fe_{20.1}$	843	0.60	0
$Ni_{61.9}Fe_{39.1}$	1058.7	0.86	1.47×10^{-5}

It is clear that the composition of the permalloy plays a crucial role in magnetic properties. Focusing on the magnetostrictive properties, the magnetostriction changed with the composition, whereby a composition of around $Ni_{80}Fe_{20}$ had near-zero magnetostriction [53,165]. In the present study, the sample was grown from a source of composition that has a nominal ratio of $Ni_{80}Fe_{20}$. It is obvious from the magnetotransport measurements that the strain controls the magnetoresistance features of the permalloy thin-film device. To compare the magnetostriction values in table 3.1 with the permalloy in this study, equation 1.13 and 1.19 are used as follows:

$$B_1 = \frac{3}{2}\lambda_{100}(c_{12} - c_{11}) \tag{3.9}$$

$$\lambda_s = \frac{2}{5}\lambda_{100} + \frac{3}{5}\lambda_{111} \tag{3.10}$$

Using $c_{12} - c_{11} = 8.6\text{GP}$ [58] gives $\lambda_s = (8.8 \mp 0.6) \times 10^{-6}$ and $\lambda_s = (1.2 \mp 0.1) \times 10^{-5}$ for the measurement of $\varphi = 90^o$ and $\varphi = 0^o$, respectively. Comparing the values of the magnetostriction in the present study with values in table 3.1 from reference [53] shows that the magnetostriction in this study is in the range of the third composition $Ni_{61.9}Fe_{39.1}$ from reference [53]. Thus, the magnetostrictive properties of the permalloy sample in this study could be attributed firstly to the composition of the permalloy, where according to the SQUID data, the saturation magnetisation of the permalloy sample is equal to $(1030 \mp 20) \times 10^3 A/m$. This is in the same range of permalloy magnetisation with the stoichiometric ratio of $\mathrm{Ni}_{61.9}\mathrm{Fe}_{39.1}$, as stated in the table (3.1), where it has higher magnetostriction compared to the $Ni_{80}Fe_{20}$. The reason behind this could be related to the sputtering process, whereby the ejected atoms of Fe and Ni are not ideally $20{:}80$.

Secondly, the thickness grown for this sample was $4nm$, which is considered to be an ultra-thin film. Kim and Silva [47] found that the magnetostriction constant λ_s increased rapidly in permalloy ultra-thin film below $7nm$, as illustrated in figure 3.26. They proposed that applying an electric field to an ultra-thin film induced an anisotropy due to the surface term, as presented by the Néel model, and hence the magnetostriction of the material is:

$$\lambda_{total} = \lambda_{bulk} + \lambda_{surface}/t \tag{3.11}$$

Where the magnetostriction has two terms, bulk term λ_{bulk} and surface term $\lambda_{surface}$, and t is the film thickness. The surface term induces magnetostriction that dominates the bulk term.

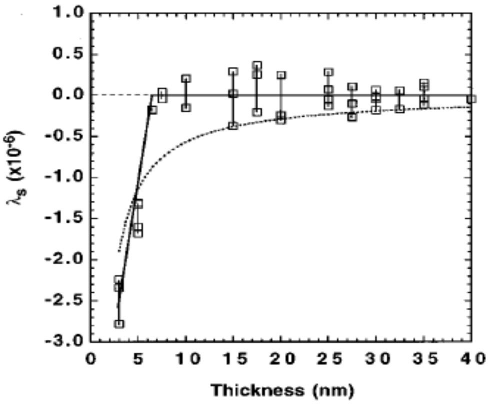

Figure 3.26: The surface magnetostriction λ_s as a function of film thickness for permalloy, where the dashed line represents the Neél model results, and the solid line represents the experimental results [47].

On the other hand, Song et al. [160] reported that for NiFe/Ag/Si and NiFe/Cu/Si of less than 3nm thickness, the magnetoelastic constant B is positive, while its sign changed near $4nm$, and the magnetoelastic constant becomes negative for all other thicknesses, including the bulk samples. They fit the data to the Néel model equation for magnetoelastic constants as follows:

$$B(t) = B_{bulk} + B_{surface}/t \qquad (3.12)$$

where B_{bulk} is the magnetoelastic constant for the bulk term, and $B_{surface}$ is the surface term. The critical thickness at which the magnetoelastic constants changed from positive to negative through the zero value could change and vary with the film deposition parameters. The thickness of the sample used in this study was $4nm$; the associated magnetostriction was positive and could be decreased with increasing thickness. The surface term of the magnetostriction plays a critical rule for changing the magnetic properties of permalloy ultrathin films. On the other hand, the interlayer and capping could affect the magnetic properties of the magnetic layers. Ueno and Tanoue found that sandwiching permalloy with different layers of Ti, Ta, and Cu while varying the film thickness gives different magnetic properties as the interlayer and capping layer change [167]. Further investigation is needed to study the thickness dependence of the permalloy on the magnetostrictive properties.

3.3 Investigation of the strain effects on the magnetic properties of nickel ultrathin film

3.3.1 Magnetotransport measurements without strain

The nickel thin film sample S475 was grown as a single film layer with the structure of $Ta(4nm)/Ni(5nm)/Ta(3nm)$. The sample was then fabricated into micro-devices and mounted onto the top of the surface of a piezoelectric transducer, as described in section 2.2.2. The configuration for the magnetotransport measurements is illustrated in figure 3.27 (a). Figure 3.27 (b) and figure 3.27 (c) show the R_{xx} and R_{xy}, respectively when a voltage of $0V$ was applied to the transducer. It is clear for the nickel sample that ΔR is less than that for the permalloy sample, with a value of 0.05Ω, compared to 0.4Ω for the permalloy film. It is shown for the R_{xx} that the resistance baselines are not straight. The reason for this is unclear; it could be due to an intrinsic property of the sample, or it could be caused by the experimental setup. On the other hand, the R_{xy} curves are hardly saturating at around $30m$T, where it seems that nickel is harder than the permalloy sample. The switching field for the nickel sample is around $1mT$, similar to the permalloy sample switching field.

Using the transverse resistance to extract the magnetic hysteresis loops (as described for the permalloy sample in section 3.2.2.1), figure 3.28 shows results when $\alpha = +45^o$ and $\alpha = -45^o$. It can be seen that the hysteresis loops have similar shapes and features, which means that the anisotropies in both directions are the same in both directions' measurements, with no preferred direction.

3.3.2 Magnetotransport measurements when applying strain

For the strain measurements, figure 3.29 shows the relation between the voltage applied to the piezoelectric transducer and the strain induced in the nickel layer, measured with the same procedures as performed for the S476 sample. It can be seen that the value of the strain in this sample is less than that for the permalloy sample, in the range of $\sim \times 10^{-5}$, while for the permalloy, it is in the range of $\sim \times 10^{-4}$. On the other hand, the strain loop for the nickel shows no hysteresis for the nickel sample, which could be attributed to strain relaxation in the glue layer. To investigate the strain effect on the magnetotransport measurement of the nickel sample, a range of voltage between $-30V$ and $+50V$ was applied to the actuator. It is shown that for all voltages in figure 3.30, there was no change in the R_{xy} or R_{xx} curves in all directions, and the three voltages are only shown here since all are same, $-30V$, $0V$, and $+50V$.

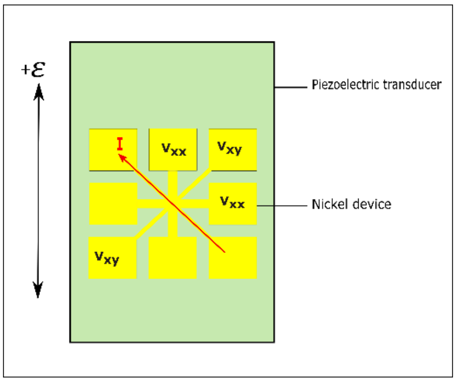

(a)

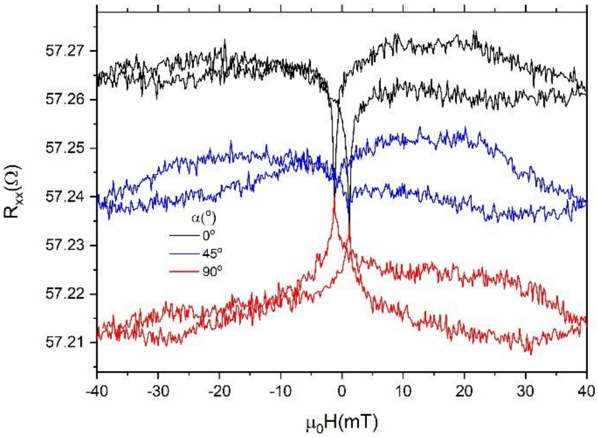

(b)

(c)

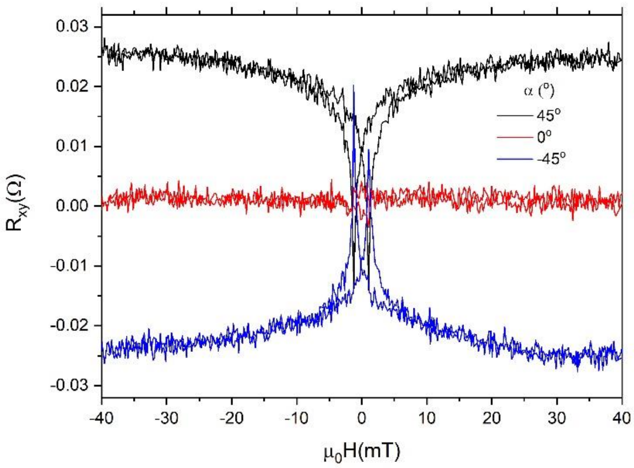

Figure 3.27**:** (a) The configuration of the magnetotransport measurement of S475 sample. (a) R_{xx} and (b) R_{xy} measurements when $0V$ was applied to the transducer, and different current directions (α) are indicated in the inset.

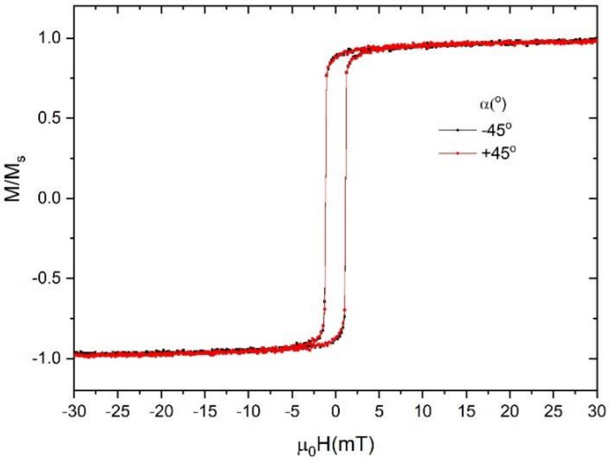

Figure 3.28**:** Magnetic hysteresis loops extracted from the transport curves when the current $\alpha = +45^o$ and $\alpha = -45^o$ was applied to the magnetic field. The hysteresis loops for both directions show the same shape and magnetic properties.

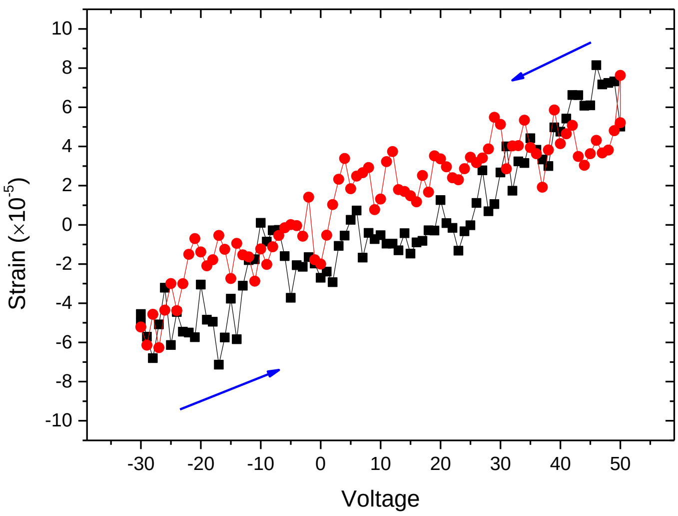

Figure 3.29: Strain loop for sample S475 with voltage bias across the transducer swept up and down between $-30V$ and $+50V$, with steps of $+1V$ and $-1V$. The strain extracted from the longitudinal resistance R_{xx} is discussed in section 2.2.2. Blue arrows show the direction of measurements, starting at $-30V$.

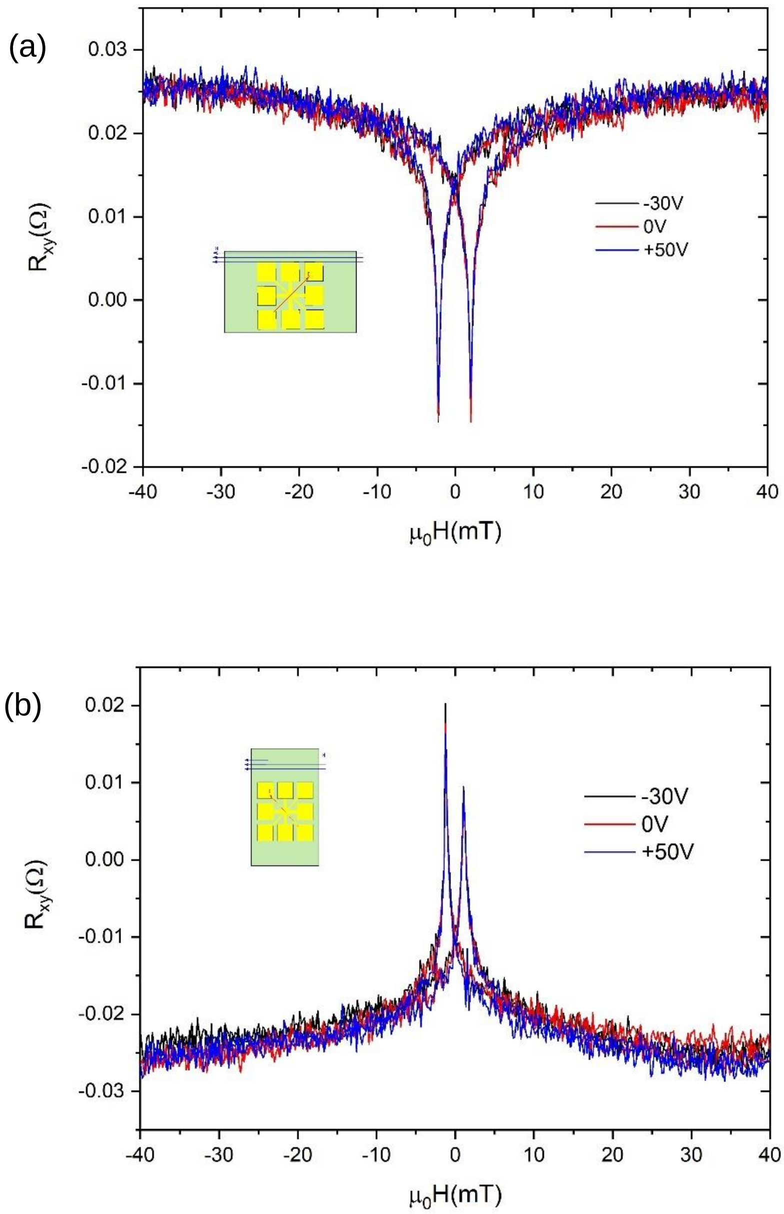

Figure 3.30: The R_{xy} curves at different voltages applied to the transducer. A schematic of the hybrid device configuration with respect to the magnetic field are shown inside the figures when the field is (a) parallel ($\varphi = 0^o$) and (b) perpendicular ($\varphi = 90^o$) to the long axis of the transducer. The resistance values and shapes do not change for all voltages measurements.

As mentioned in section 1.1.3, nickel has magnetostrictive properties with high elastic constants that enable it to respond to any value of strain. However, in ultra-thin ferromagnetic films, as thickness decreases, the magnetic properties change drastically. Vaz et al. [168] reported that as the thickness of the Ni film decreases, its magnetic moment also decreases. Magnetic anisotropies are also affected by the reduction of thickness, which could break the symmetry at the surface and change the electronic structure of the material. As mentioned for the permalloy sample, the Néel model proposed an extra term to represent the surface term for the ultrathin films. Bochi et al. [48] stated that the effective magnetoelectric coefficient B_{eff} changes its sign at a certain thickness for the nickel, at approximately $8nm$, as shown in figure 3.31. In general, the effective anisotropy K_{eff} for the ultra-thin film is:

$$K_{eff} = -2\pi M_s^2 + K_{MC}^b + B_b\varepsilon + (K_s + B_s\varepsilon)/h \tag{3.13}$$

The first three terms are the bulk magnetostatic, magnetocrystalline, and magnetostriction terms, respectively, while ε represents the strain tensor. The last term represents the surface term for the magnetocrystalline and magnetoelastic anisotropies. To sum up, with ultra-thin film, the magnetisation and magnetic anisotropies can be affected, and the properties of the film could change significantly compared to the bulk properties. For the Ni film in this study, the magnetostrictive properties at a thickness of $5nm$ show zero magnetostriction. Hence, applying strain to this film does not show any response in magnetotransport measurements.

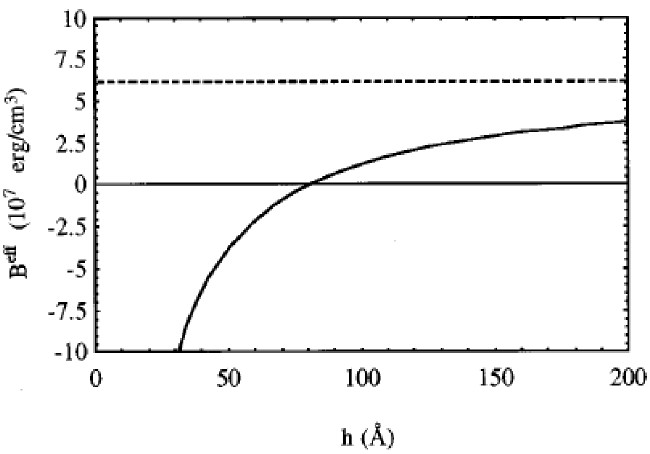

Figure 3.31: Magnetoelectric constant B_{eff} variation with Ni thickness, indicating the value change from positive to negative as the film thickness decreases; hence, the magnetostriction decreases to near zero with this change [48].

3.4 Conclusion

This study examines the strain effects on the magnetic properties of polycrystalline permalloy and nickel single layers by varying the voltage through the piezoelectric transducer to induce a strain in these samples and hence tune magnetic properties. Magnetotransport measurements were conducted for both samples under different strain values by varying the voltages on the transducer. For the permalloy sample, the strain calibration measurements showed that a maximum compressive strain of value -1.76×10^{-4} was induced in the film when a voltage of $-30V$ was applied to the transducer, while the maximum tensile value of 1.76×10^{-4} was obtained when a voltage of $+50V$ was applied to the transducer. The magnetoresistance measurements show responses to the strain induced in the film, where $\Delta R_{xy}/R_{xx}$ changed from 0.09% to 0.9% when voltages of $-30V$ to $+50V$ were applied to the transducer for the measurements when the magnetic field was perpendicular to the long axis of the transducer. The remnant magnetisation of the permalloy sample varied. For instance, when the magnetic field was parallel to the long axis of the transducer, the M_r/M_s changed from 0.99 to 0.49, when the voltage changed from $+50V$ to $-30V$, respectively. The switching field was also affected by the strain, decreasing from $1.8mT$ when a voltage of $-30V$ was applied, to reach $0.8mT$ when a voltage of $+50V$ was applied to the actuator for the last direction of the measurement.

The magnetic reversal illustration (figure 3.11 and 3.17) showed that the strain induced in the permalloy sample was able to change the direction of the magnetic easy axis, and it depended on the strain direction with respect to the magnetic field direction. Applying a strain perpendicular to the magnetic field made the magnetisation direction harder at the magnetic field direction, and easier along the strain direction. An assumption was made to extract the magnetoelastic anisotropy constants, whereby the magnetic hysteresis upsweep curve divided into two fitting curves, as the curve of magnetic reversal after the magnetisation switching is harder than the one before switching. The coherent rotation model was used to extract magnetic anisotropies from the region (3). The magnetoelastic anisotropies were determined with the maximum values of $K_s = -1370 \mp 20J/m^3$ and $K_s = 1020 \mp 40J/m^3$ for $\varphi = 0^o$

and $\varphi = 90^o$ measurements, respectively. The magnetoelastic anisotropy constants B_1 were extracted from the linear fit of anisotropies vs strain curves, with values varying between $B_1 = (3.8 \mp 0.3) \times 10^6 J/m^3$ and $B_1 = (2.9 \mp 0.2) \times 10^6 J/m^3$. The extrapolation to zero strain resulted in a different intercept for the residual anisotropy, which may indicate that the sample is in a different strain state. We speculate that this might arise from a strain induced in the sample by saturating the magnetisation along a particular direction.

The strain did not show any response on the magnetic properties of the nickel sample; the magnetoresistance measurements did not show any change in the value or shape of the curves. Hence, the nickel sample shows zero magnetostriction at this thickness. To sum up, for both samples, as ultrathin films, the magnetic properties of films changed dramatically from the bulk properties, including in terms of magnetisation saturation, magnetostriction, and anisotropy field. At this range of thickness, the surface term of the material plays a crucial role in changing the properties of the sample, whereby the interface is dominantly led to unique properties at the very low nanoscale.

Chapter 4: Magnetisation and Magnetotransport Measurements of Permalloy and Nickel Spin Valves

4.1 Introduction

Spin valves are multilayered structures consisting of ferromagnetic layers separated by non-magnetic material layers (spacers). An important transport effect of this structure is called giant magnetoresistance (GMR), which differs from the anisotropic magnetoresistance (AMR) of single ferromagnetic material, and which has attracted much interest in the past three decades. One of the main mechanisms giving rise to assumptions of this phenomenon is spin-dependent scattering, whereby the magnitude of the GMR depends on the contrast of the scattering in two independent conduction channels [5-169]. The magnitude of the GMR is maximum when successive ferromagnetic layers are aligned antiferromagnetically (i.e. antiparallel) to each other, being minimal when the spin configuration of these layers is ferromagnetically aligned [12]. Different non-magnetic layers have been used for inter-layers including: Cu, Au, Al, Cr, and Ta. Each metallic material has optimal thickness depending on the contextual ferromagnetic materials and the growth condition conducive to the giant magnetoresistance effect and changing the thickness of these layers gives an oscillatory value of the GMR [169, 12, 170].

This chapter studies the magnetic reversal and magnetotransport properties of sets of spin valves consisting of permalloy and nickel layers and correlates the features in magnetotransport data with the reversal of the magnetisation in the individual layers within the spin valve. The thickness of nickel and the permalloy layers are the same as used in the study of the single films in chapter 3. Some samples incorporate an IrMn layer in order to provide exchange bias. The IrMn was also grown with the same thickness ($8nm$) for all spin valves with IrMn. Two metallic spacers were used in different spin valves, Cu and Cr. All spin valves that used Cu as a non-magnetic spacer showed the giant magnetoresistance effect, with values of around 1.5%. The stiffness of these spin valves (the field required to overcome the antiparallel alignment) is different and depends on the growth sequence and the nature of the interfacial layers. The spin valves with Cr spacer show just an anisotropic magnetoresistance without GMR, which is attributed to the suppression of electron spin flow through the Cr layer. All samples with IrMn layer show higher coercivity than the spin valves with free nickel and permalloy layers. All spin valves with IrMn layer show zero exchange bias at room temperature, while exchange bias emerges at lower temperatures of $50K$ and $2K$. All magnetisation measurements were carried out using the SQUID magnetometry, performed using as-deposited films of these spin valves, while the transport measurements were performed using the micro-fabricated devices and mounted onto piezoelectric transducers, as discussed in section 2.2.2.

This chapter comprises two main parts (sections 4.2 and 4.3). Firstly, starting with two pseudo samples (i.e. not containing an antiferromagnetic exchange biasing layer), IM008, and IM009 spin valves, the magnetisation loops and transport measurements are discussed and compared to each other since they have reversed growth order of the magnetic layers. The second part is for the spin valves with IrMn layer and Cr spacer, S548, and S549. SQUID magnetometry measurements were performed for these samples at different temperatures. For all spin valves, magnetic properties extracted from magnetisation and transport measurements were discussed and illustrated, namely: magnetoresistance features, magnetic reversal, exchange bias, magnetisation process.

4.2 Magnetisation and magnetotransport measurements of pseudo spin valve of permalloy and nickel layers

Two pseudo spin valves were grown using the sputtering system as discussed in chapter 2, with the structure of Ta (4nm)/ $Ni_{80}Fe_{20}$ (4nm)/ Cu (4nm)/ Ni (5nm)/ Ta (3nm), called IM008, and Ta (4nm)/ Ni (5nm)/ Cu (4nm)/ $Ni_{80}Fe_{20}$ (4nm)/ Ta (3nm), called IM009, as shown in figure 4.1. The thicknesses of NiFe and Ni layers used in all spin valves in this chapter are the same thicknesses of the permalloy and nickel single layers studied in chapter 3. The spin valves are then fabricated as microdevices using a photolithography technique, as discussed in the steps described in section 2.1.3, then mounted on the top of the piezoelectric transducer to prepare it for the strain and magnetotransport measurements.

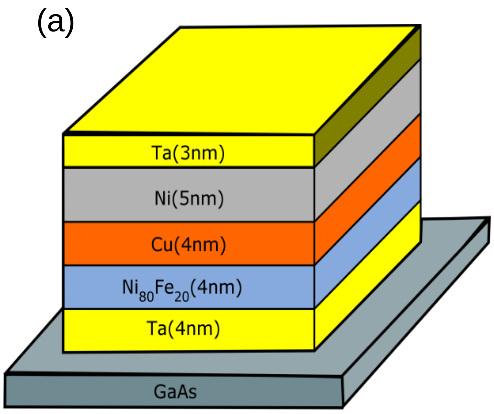

Figure 4.1: Schematic of the multi-layered structures of the spin valves films grown using the sputtering system, (a) IM008 and (b) IM009. The thickness of each layer is shown.

4.2.1 SQUID magnetometry measurements for the IM008 and IM009 spin valves

For the pseudo spin valves of nickel and permalloy multilayers magnetisation reversal was investigated using SQUID magnetometry. Figure 4.2 (a) shows the magnetisation hysteresis loops for the IM008 sample at $300K$. It shows two distinct magnetisation reversals, where the abrupt switching at around $0.5mT$ could be attributed to the permalloy layer, which is softer and has a longer step in the hysteresis loop, since the saturation magnetisation of the permalloy is bigger than that of the nickel, while the more gradual step at around $4mT$ is ascribed to the Ni layer. In the magnetic hysteresis loop, the permalloy reversal percentage (abrupt switching) is identified as ΔM_{NiFe} and consists of 61% of the whole reversal, whereas the nickel layer reversal percentage (slow reversal) is indicated by ΔM_{Ni}, and comprises 39% of the reversal (note that the percentage of ΔM_{NiFe} and ΔM_{Ni} are calculated an average from both sides of the hysteresis loop). As measured in chapter 3, the saturation magnetisation of the permalloy layer is measured with a value of $1030 \times 10^3 A/m$, whereas the nickel saturation magnetisation as found by Neugebauer with a value of $509 \times 10^3 A/m$ [51].

Comparing nickel and permalloy saturation magnetisation as single layers with the percentages calculated from the hysteresis loop gives 67% for the permalloy and 33% for the nickel layer. The difference in coercivity between the bottom layer (NiFe) and the upper layer (Ni) enhances the region of field where antiparallel magnetisation occurs, which could be useful for the giant magnetoresistance effect. As the magnetic field is swept from a high positive magnetic field at $+300mT$, the permalloy layer magnetisation switches at a very low magnetic field of $-0.5mT$ to align antiparallel to the nickel layer. The nickel layer starts to reverse slowly (could be magnetic domains nucleation or rotation) to align with the permalloy and the saturation field is approximately $8mT$. Since the nickel magnetisation is reversing gradually, instead of clear switching, an assumption was made to measure the coercivity of the nickel taking the field value at which 50% of the layer has reversed, giving a nickel coercivity value of $4.25mT$. A symmetric curve is shown for the descending field for the opposite direction of the field sweep for both layers. For this spin valve, since there is no antiferromagnetic layer to pin one of the two ferromagnetic layers, the difference in coercivities between the permalloy and the nickel layers enhances the spin valve effect (GMR), as discussed in section 1.2.4.2. GMR depends on the magnetisation alignment of the ferromagnetic layers, and it gives the maximum value when the two adjacent layers' magnetisations are aligned in antiparallel formation [5-169].

On the other hand, IM009 spin valve shows different reversal characteristics where the two layers have very similar switching field values, as can be seen in figure 4.2 (b) for the $300K$ measurements. The coercivity of the permalloy layer is equal to $0.5mT$, which is the same as the permalloy in IM008 spin valve, while it is $0.9mT$ for the nickel layer. The ΔM_{NiFe}, and ΔM_{Ni} percentages from the whole reversal are different slightly from the IM008, with a value of 72% for the permalloy layer and 28%for the nickel. This difference could be ascribed to the interface between the layers, as suggested by Gritsenko et al. [171], who confirmed intermixing between layers using the TEM images.

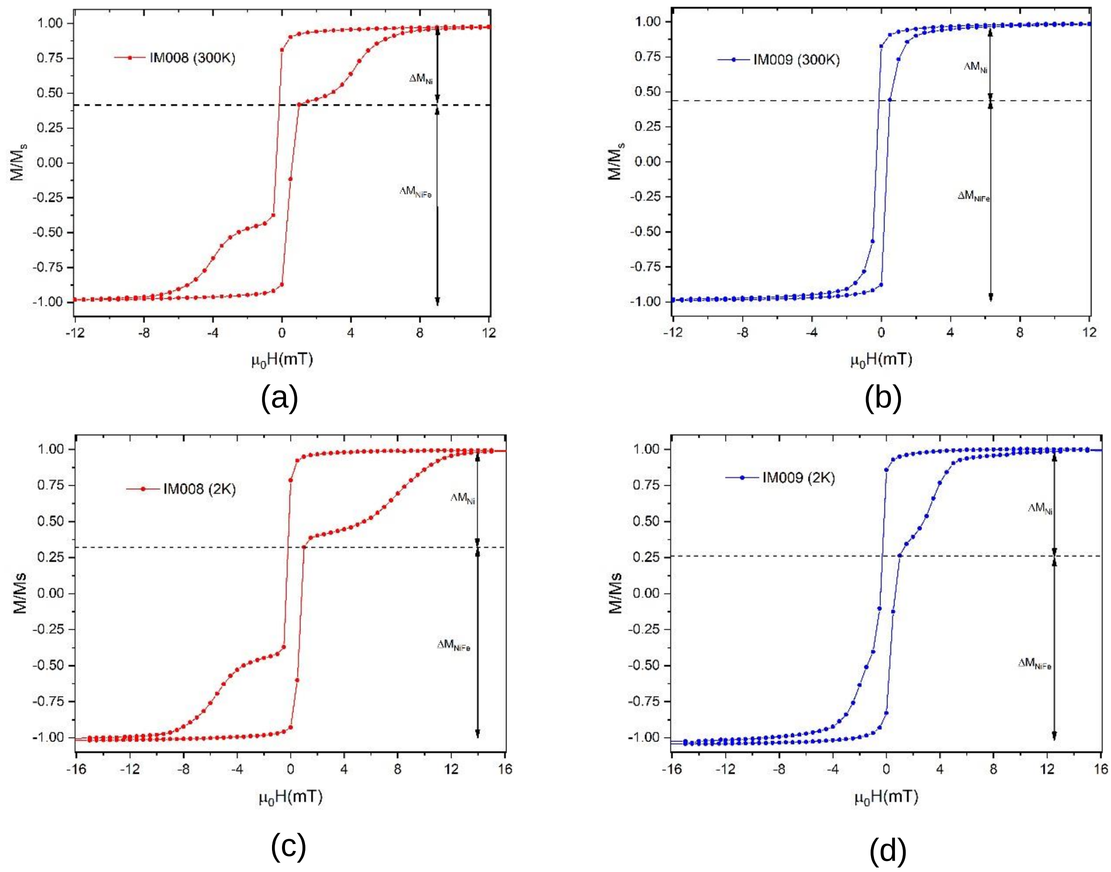

Figure 4.2: SQUID magnetic hysteresis loops for the IM008 sample at different temperatures (a) at $300K$ and (c) $2K$, and IM009 spin valve (b) $300K$ and (d) $2K$. The percentage of each layer reversal is shown for the permalloy $\Delta\mathrm{M}_{\mathrm{NiFe}}$ and nickel $\Delta\mathrm{M}_{\mathrm{Ni}}$ with the double-headed arrows inside each measurement. A different (x) scale is used in (c) and (d), since they need a higher field to saturate.

The difference between the coercivities of IM008 and IM009 samples could be due to the interface difference, which could alter each layer's structural (and thus magnetic) properties. The nickel layer was grown on the top of the Cu layer in the IM008 while it was grown on the top of Ta in the IM009 spin valve. Dieny et al. [12] attributed changing coercivity, and magnetic reversal of the exchanged biased spin valve when using two different spacers of noble metals (Ta and Cu) to a microstructural change to the permalloy layer's magnetostatic coupling. Mao et al. [172] studied the structure of pseudo spin valve and found that it showed different growth structure when using different buffer layers of Cr and Ta, and this affected the magnetoresistance of the spin valve and the coercivity of the upper layer. The microstructural growth difference might introduce some pinholes between layers which could introduce some interlayer exchange, particularly for IM009 spin valve, where the two coercivities of permalloy and nickel are very close because of the coupling [173, 174, 175]. Although they used spacer thickness suffices to decouple the ferromagnetic layers, some exchange interaction is still detectable with 4nm of Cu, as reported by Dieny et al. [173], where they observed the interaction in a structure of Ta (50nm)/ NiFe (6.2nm) / Cu (4nm)/ NiFe (4nm)/ FeMn (7nm)/ Ta (5nm).

Other SQUID measurements were performed at $2K$ for both spin valves IM008 and IM009. As shown in figures 4.2 (c) and (d), the reversal of the nickel is changing in both spin valves while the permalloy switching remained the same as at room temperature. The coercivity of the nickel changed from $4.25mT$ at $300K$ to $7.5mT$ at $2K$ in IM008, whereas for the IM009 it changed from 0.9mT to $3.4mT$ when the temperature of measurements changed from $300K$ to $2K$. On the other hand, the magnetic reversal of the permalloy steps ΔM_{NiFe} and nickel ΔM_{Ni} changed slightly, with nickel and permalloy reversals in IM008 of 33% and 67% respectively, while they are 34% and 66% for the nickel and permalloy in IM009 spin valve. The step size of the reversal is mostly agreed with the magnetisation of single layers to be 33% for the nickel and 67% for the permalloy from the net magnetic reversal. For this stage, it is not clear why temperature change alters the reversal and coercivity of nickel layers without changing the permalloy coercivity in both spin valves. In general, this is related to the thermal excitation of spin waves affect on the magnetisation of the ferromagnetic layers [173,176, 177]. Stobiecki et al. [178] found that the interlayer coupling of ferromagnetic layers of spin valves varies with temperature, where the pinholes that cause the interlayer coupling is strongly dependent with the temperature.

4.2.2 Magnetotransport measurements for the IM008 and IM009 samples

The magnetotransport properties of the pseudo spin valves IM008 and IM009 were measured using dc-four-probe measurements at room temperature. The measurements were performed in the same setup used to measure the magnetotransport properties of the single layers in chapter 3, whereby the samples were prepared as discussed in section 2.2.2. After the fabrication of the devices, the devices were mounted on the top of a piezoelectric transducer. The hybrid structures were placed in a magnetic field that swept between $-40mT$ to $+40mT$, enough to saturate the two magnetic layers in both spin valves, as shown in the SQUID data. In this chapter, all measurements were performed without applying an induced strain by the stressor ($V = 0$). Strain measurement features are discussed in detail in chapter 5. Recall here that the $0V$ does not mean the strain is equal to zero, as shown in chapter 3, and an induced strain in the films could appear due to the mounting sample, fabrication, or growth processes.

The configuration of the hybrid structure of the spin valve device on the piezoelectric transducer is shown in figure 4.3. The work presented in this chapter only takes into account the direction between the magnetic field and the current (α). It is shown in the figure that the electric current is 45^o to the long axis of the piezoelectric transducer, while the field rotates in the plane of the layers. The longitudinal and transverse resistances were measured while applying an electric current of $1mA$.

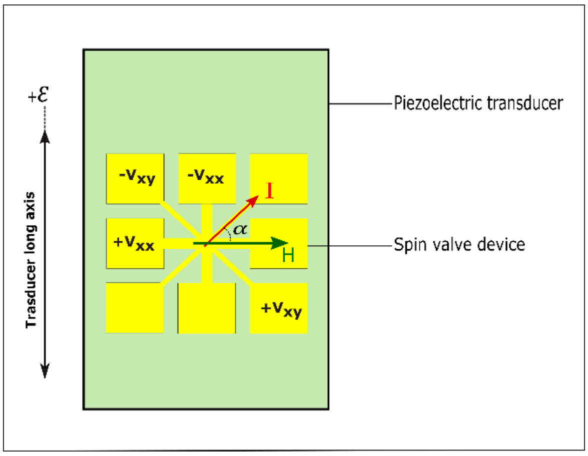

Figure 4.3: Micro-device of a spin valve film mounted on a piezoelectric transducer with current applied 45^{o} to the long axis of the transducer. A current of 1mA is applied to the device while measuring the longitudinal and transverse resistance. The angle between the magnetic field and the electric current is α.

For the IM008 spin valve, the magnetoresistance curves for longitudinal magnetotransport when the magnetic field is perpendicular $(\alpha = 90^{0})$, and parallel $(\alpha = 0^{o})$ to the current are shown in figure 4.4 (a) and (b). A typical giant magnetoresistance curve with plateau-like peaks, particularly when the field is perpendicular to the current is shown. These curves are attributed to the spin valve effect (GMR). This resistance is different from the anisotropic magnetoresistance AMR discussed in detail in chapter 3. AMR depends on the direction of the magnetisation with respect to the current (θ), following equations 1.32, and 1.33. The spin valve effect (GMR) depends on the relative magnetisation orientation of successive ferromagnetic layers in the spin valve. When the magnetic field is high enough to saturate the ferromagnetic layers to align the permalloy and nickel layers in parallel in the spin valve, the resistance is minimal (point (I) in figure 4.4 (a)), while when the layers are antiparallel aligned to each other (when the permalloy switches abruptly), the resistance reaches its maximum (point (II)). As the harder (nickel) layer starts to reverse slowly, the resistance starts to decrease until it aligns with the permalloy and the magnetic field. The resistance then remains constant as the magnetic field increases to the maximum positive field (as indicated by point (III) in figure 4.4 (a)). The arrows in the figure illustrate the orientation of the layers during the measurements. For the opposite sweep direction, the resistance peaks show a symmetrical shape, since both layers are free, with no exchange bias. For the measurement when the field is perpendicular to the electric current, the maximum GMR value is equal to 1.53%, with a magnetic field value of $1.2mT$ (see figure 4.4 (b)). The GMR is extracted from the relation:

$$GMR = \frac{\Delta R}{R} = \frac{R_{AP} - R_{PP}}{R_{PP}} \qquad (4.1)$$

where R_{AP} is the spin valve resistance when the magnetisations of ferromagnetic layers are antiparallel, and R_{PP} is the resistance when the magnetisations of the ferromagnetic layers are parallel. For accuracy, we will denote the magnetoresistance of the longitudinal resistance of the spin valves as $\Delta R/R$, as the resistance is a mixture of mostly GMR and AMR. For the direction when the magnetic field is parallel to the current, the $\Delta R/R$ is less than when the field is perpendicular to the current , where it is equal to 0.99%, and at the same field when the magnetic field is perpendicular to the electric current since the permalloy switching field is same in both directions. Figure 4.4 (b) compares between the two directions' measurements.

The maximum value of the resistance ($\Delta R/R$) represents the antiparallel configuration of the ferromagnetic layers when the permalloy switches at the low magnetic field. When the field is perpendicular to the current, the presence of a plateau until $4mT$ ascribed to the nickel layer magnetisation remains in the same magnetisation orientation (could be nickel layer easy axis direction), until it starts to reverse and the resistance decreases, representing the decrease of the antiparallel angle between layers until it reaches zero degrees at around $10.5mT$ (see figure 4.4 (a)). When the field is parallel to the current, the $\Delta R/R$ starts to decrease directly after reaching the maximum value point ($\Delta R/R_{max}$), which could be due to the hard reversal of the nickel layer, where the nickel layer starts to reverse before a complete switch of the permalloy reversing, thus the magnetoresistance curve in this direction has sharp peaks. Figure 4.5 shows the longitudinal resistance (R_{xx}) when the field is parallel to the current and the corresponding transverse resistance (R_{xy}), where it is clear that the permalloy switches firstly, similar to the switching of the permalloy described in section 3.2.2., as indicated in figure 4.5. Small red arrows show the point at the maximum values of GMR (see R_{xx} curve) and corresponding transverse resistance at the same field value when the permalloy switches (see R_{xy} curve). The peaks in R_{xy} curves show very small intensity compared to the R_{xx} (GMR),and show different direction reversal with positive and negative resistances values where the GMR shows positive resistance always. The differences between the two measurements' directions magnetoresistance ($\Delta R/R$) curve shape, particularly after the field point at the maximum magnetoresistance $H(\Delta R/R_{max})$ will be discussed in detail in chapter 5.

(a)

(b)

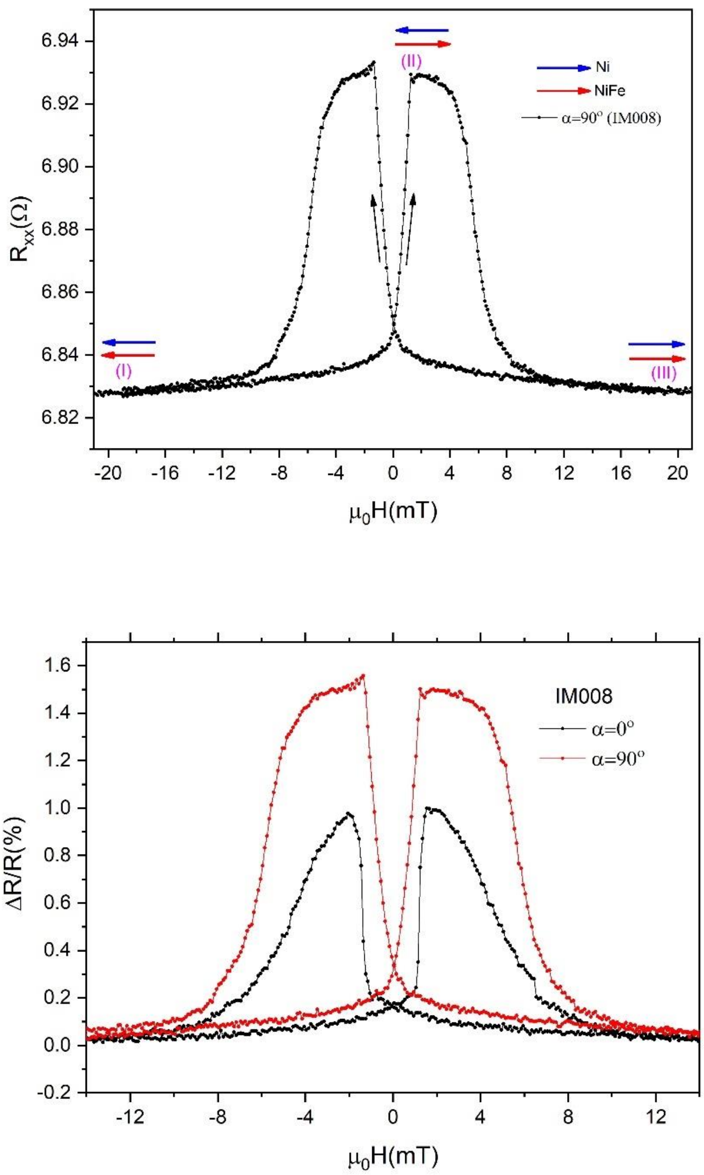

Figure 4.4: GMR curves for IM008 spin valve when the field is perpendicular $\alpha = 90^o$ (a) points (I) and (III) are where the field aligns with the permalloy and nickel layers, while (II) is when the resistance is maximum where the permalloy switches after changing the field polarity to align antiparallel to the nickel layer as shown by arrows. The black arrows represent the sweep direction. (b) compares between the GMR curves when the magnetic field is perpendicular $\alpha = 90^o$ (red curve) and parallel $\alpha = 90^o$ (black curve), with values of 1.53% and 0.99% for both directions, respectively.

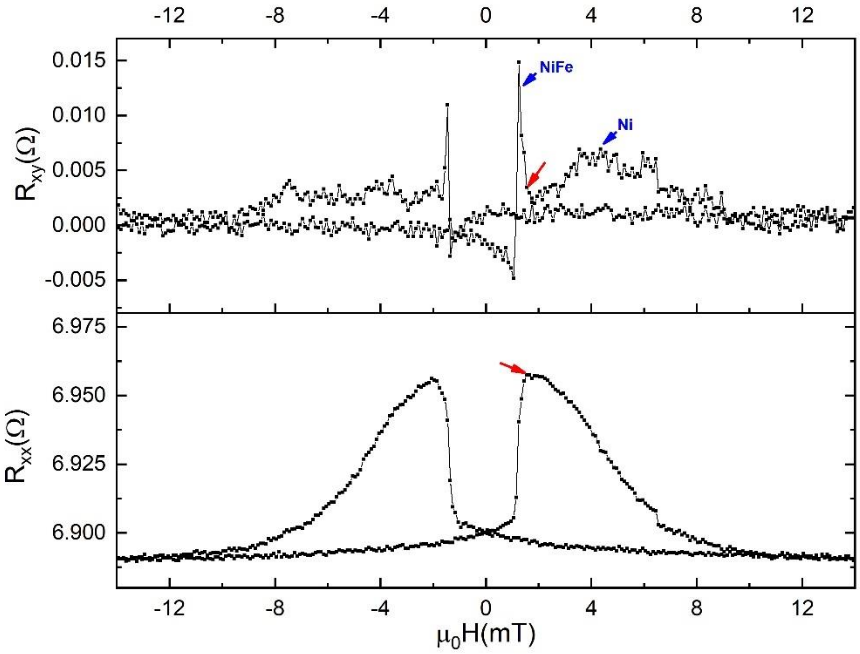

Figure 4.5: The transverse resistance R_{xy} (upper curve) when the field is parallel to the current Shows the permalloy abrupt switching following by the slow reversal of the nickel. The corresponding longitudinal resistance (lower curve) in the same direction showing the maximum resistance happened after the permalloy switching (indicated by red arrows at the same field in both resistances). The layers are indicated by names in the transverse resistance curve.

All spin valves in this chapter that showed a GMR effect, the size of which when the magnetic field is perpendicular to the current direction is bigger than when the field is parallel to the current. This difference could be attributed to different reasons. Miller et al. [179] found that for 52 spin valves it is always that $GMR_{\perp} > GMR_{\parallel}$, which they attributed to the directional dependence of the mean free path of spin-up and spin-down electrons in the two-current direction configuration. Another reason for the GMR size difference could be that the antiparallel configuration of both layers is hard to obtain due to the orientation difference at zero field, whereby each layer has different magnetisation easy axis, and hence the antiparallel alignment never exists for that direction. Moreover, the difference could be due to the early reversal of the harder material, so when the soft layer switches, the magnetisation orientation will not have the antiparallel configuration, since the harder material already starts to reverse earlier [175,180, 181].

To extract the anisotropic magnetoresistance AMR from the magnetoresistance measurements, the method demonstrated by Rijks et al. [182] is used:

$$AMR = \frac{R(P, M \parallel I) - R(P, M \perp I)}{R(P, M \parallel I)} \qquad (4.2)$$

Where $R(P, M \parallel I)$ is the magnetoresistance of the spin valve when two magnetic layers are parallel to each other, when the magnetic field is parallel to the current, and $R(P, M \perp I)$ is the magnetoresistance of the spin valve when two magnetic layers are parallel to each other when the magnetic field is perpendicular to the current. For this sample (IM008), by using the raw data of the spin valve resistance (R_{xx}) in both configuration of measurements, the parallel direction has bigger resistance, as shown in figure 4.6 (a). The value of the anisotropic magnetoresistance AMR ratio extracted from relation 4.2 for this spin valve is $(0.52 \mp 0.05)\%$. To examine this value of AMR, another magnetotransport measurement was carried out to measure the AMR by rotating a saturating magnetic field of $300mT$ around the spin valve magnetisation of both layers, using the relations:

$$R_{xy} = \Delta R \cos(2\theta_{AMR}) \qquad (4.3)$$

$$R_{xx} = R_{av} + \Delta R \cos(2\theta_{AMR}) \qquad (4.4)$$

The value of the AMR extracted from these measurements is $(0.55 \mp 0.04)\%$ and $(0.61 \mp 0.05)\%$, from the rotation measurement shown in figure 4.6 (b) and 4.6 (c) The value of the AMR extracted from the resistance difference in the sweep measurements for the direction when the magnetic field making $\alpha = +45^o$ and $\alpha = -45^o$ (see figure 4.6. (d)) to the electric current, with a value of $(0.51 \mp 0.13)\%$. All AMR values extracted for IM008 spin valve using different methods show very close values within uncertainties to the value extracted from relation 4.2.

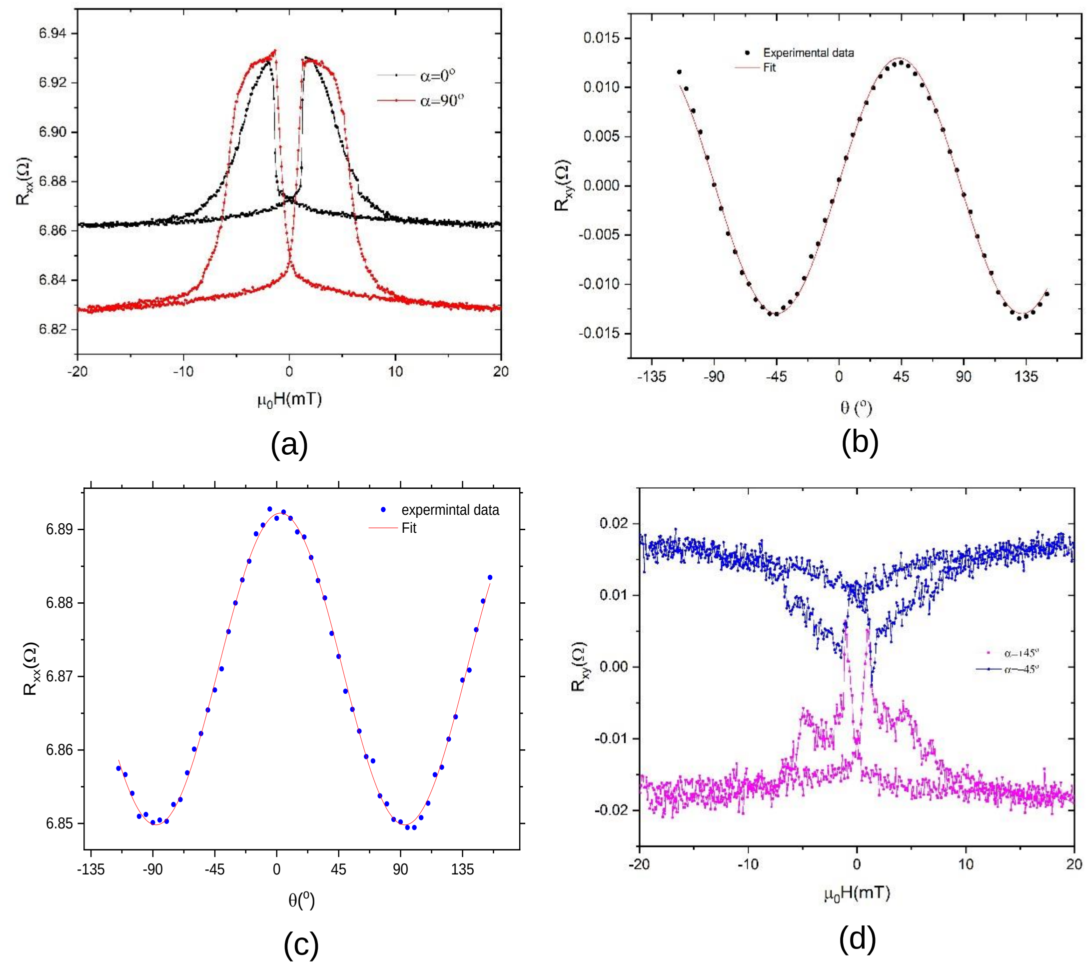

Figure 4.6: Different ways of extracting the anisotropic magnetoresistance for IM008 spin valves (a) the raw data of the GMR curves when the field is perpendicular and parallel to the field and the AMR extracted according to relation 4.2 is equal to $(0.52 \mp 0.05)\%$. (b) The R_{xy} and (c) R_{xx} resistance when the field rotates around the hybrid structure and the AMR extracted using the fit to the relation 4.3 and 4.4 are equal to $(0.55 \mp 0.04)\%$ and $(0.61 \mp 0.05)\%$, respectively, θ is the angle between the magnetisation and the current. (d) The sweep measurements for transverse resistance when $\alpha = +45^o$ and $\alpha = -45^o$and the AMR extracted is equal to $(0.51 \mp 0.13)\%$.

Both spin valves (IM008 and IM009) consist of two free ferromagnetic layers (pseudo spin valves). The GMR effect relies on the difference of coercivities between the ferromagnetic layers to enhance the antiparallel orientation since it is not an exchange biased spin valve (with an antiferromagnetic layer to pin one of the ferromagnetic layers). As shown in the magnetisation measurements (see figure 4.2 (a)), it is clear that for sample IM008 there are two distinct reversals for the NiFe and Ni layers. For the IM009 spin valve, although the magnetic reversals of the permalloy and nickel are very close, as shown in the magnetisation measurements (see figure 4.2 (b)), it shows a GMR curve as shown in figure 4.7(a) for both current direction $\alpha = 0^o$ and $\alpha = 90^o$. Since the GMR effect relies on the relative orientation of the ferromagnetic layers, the antiparallel alignment gives the maximum resistance value, which is clearly the case for the IM009 spin valve where the antiparallel alignment for a very narrow magnetic field range giving rise to the GMR. Figure 4.7 (b) shows a comparison of the $\Delta R/R$ curves when the field is perpendicular to the current in IM008 and IM009 spin valves. The main difference between this spin valve and IM008 is the spin valve stiffness [175], whereby the spin valve can hold the antiparallel magnetisation alignment of the ferromagnetic materials for a long-range magnetic field, as shown in IM008 spin valve, with a plateau peak.

For IM009 spin valve, the $\Delta R/R$ value when the magnetic field is perpendicular to the current is equal to 1.50%, while when the magnetic field is parallel to the current the value of the $\Delta R/R$ is smaller, with a value of 0.8%, consistent with the previous spin valve where the $GMR_{\perp} > GMR_{\parallel}$ (see figure 4.7 (b) for comparison). The values of the $\Delta R/R$ almost same for the same direction in both spin valve, which is due to the giant magnetoresistance depending on the orientation of the successive layer; both spin valves have the same layers, with the same low switching field for the permalloy. The peaks in IM009 spin valve are very narrow due to earlier abrupt switch of the nickel layer (unlike the slow reversal in IM008 spin valve), as can be seen in the R_{xy} curves when $\alpha = +45^o$ and $\alpha = -45^o$ (Note that for the direction of $\alpha = 0^o$ and $\alpha = 90^o$ the R_{xy} curves are not clear as other directions) in figure 4.8 (a) (the switching of both layers is indicated in the curves by blue and red arrows). After the nickel's abrupt switch, the nickel layer starts to reverse slowly until it aligns with the magnetic field direction, this reversal could be due to domains nucleation followed by domain walls propagation. The anisotropic magnetoresistance in this spin valve is in the same range of the values extracted from the IM008, giving a value of $(0.63 \mp 0.05)\%$ (the raw data of the parallel and perpendicular measurements shown in figure 4.8 (b)) extracted from equation 4.2 and $(0.58 \mp 0.08)\%$ from the transverse resistance sweep. The change in R_{xy} is smaller than that change of R_{xx}, means that AMR in $R_{xy}$and GMR in R_{xx}. Table 4.1 shows a summary for the magnetotransport and magnetisation measurements for IM008 and IM009 spin valves.

Table 4.1:Summary of magnetisation and magnetotransport of IM008, IM009 with magnetic field perpendicular and parallel to electric current (room temperature)

Spin valve	$\Delta R/R$ size (%) $\alpha = 90^o$	$\Delta R/R$ size (%) $\alpha = 0^o$	AMR size (%) (equ.4.2)	$(\mu_0 H_c)$ NiFe (mT)	$(\mu_0 H_c)$ Ni (mT)
IM008	1.53	0.99	0.52 ∓ 0.05	0.5	4.25
IM009	1.50	0.80	0.63 ∓ 0.05	0.5	0.9

Where H_C, and H_{ex} the coercivity and exchange bias fields and the saturation magnetisation respectively.

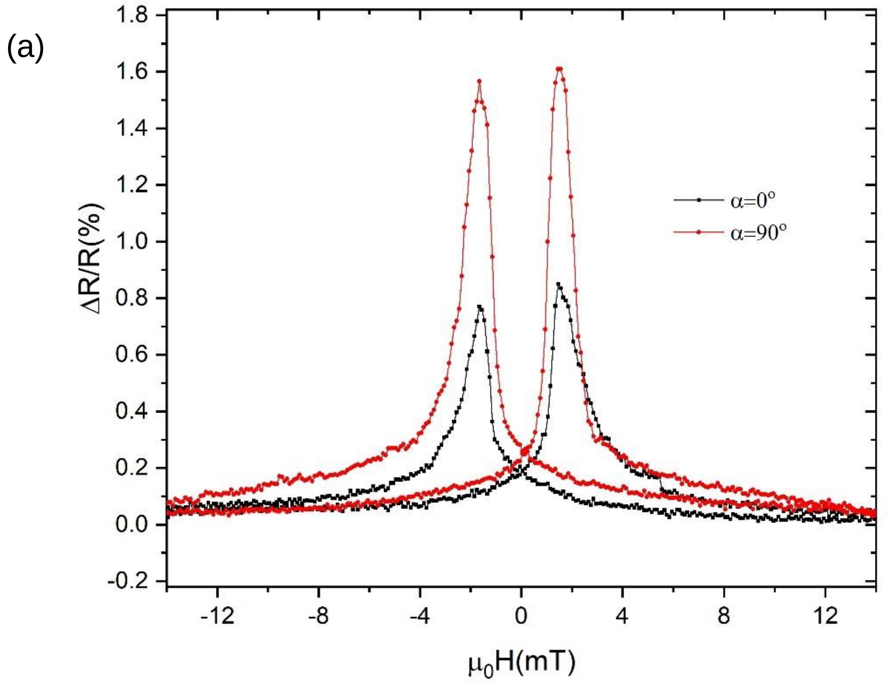

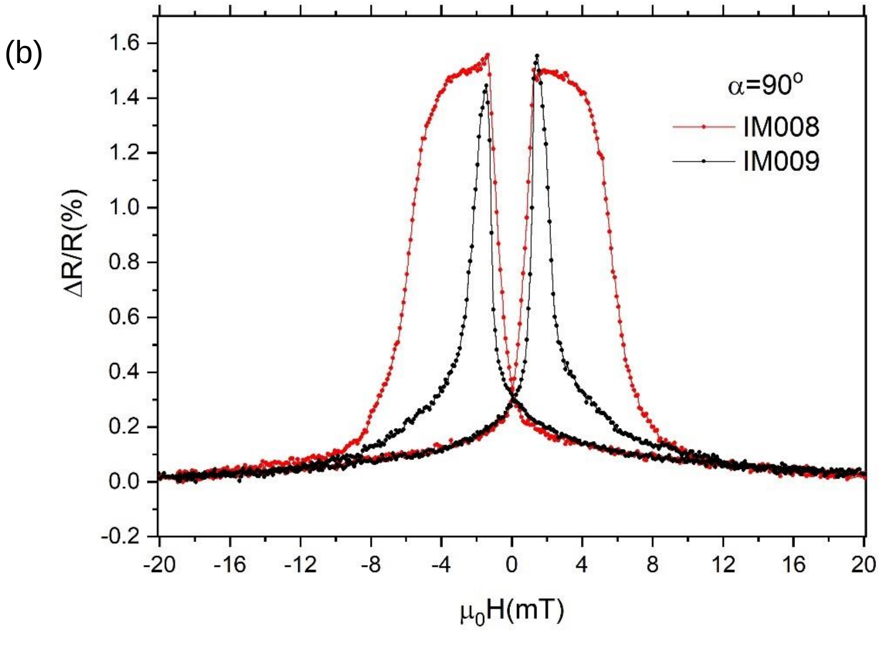

Figure 4.7: (a) the $\Delta R/R$ curves for the IM009 spin valves when the field is perpendicular (red colour) and parallel (black colour), showing values of 1.50% and 0.80% respectively. (b) Comparison between GMR curves for both IM008 and IM009 spin valves When the field is perpendicular to the current ($\alpha = 90^0$), where IM008 shows a plateau curve.

(a)

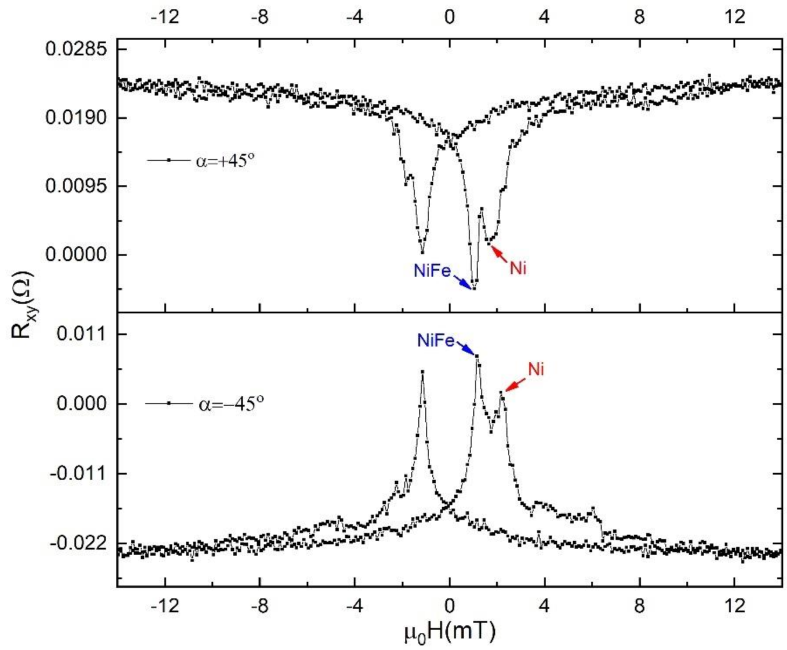

(b)

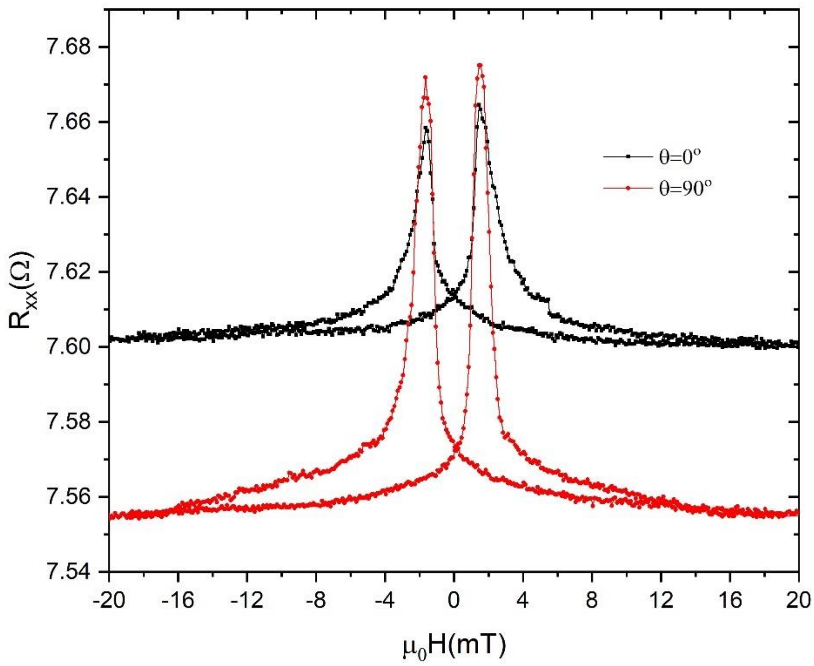

Figure 4.8: The transverse resistance of the IM009 spin valve when $\alpha = +45^{o}$ (upper curve) and $\alpha = -45^{o}$(lower curve) (a) shows the permalloy and nickel reversal where the nickel in this spin valve is switching directly after permalloy switch, manifest as a narrower GMR peak (see figure 4.7 (b)) for both directions of the magnetic field. (b) the raw data of the GMR curves when the field is perpendicular and parallel to the current, where the AMR extracted is equal to 0.63 ∓ 0.05.

4.3 Magnetisation and magnetotransport measurements for permalloy and nickel spin valves with IrMn layer

Another set of spin valve samples were grown with the introduction of an antiferromagnetic layer, to pin one of the ferromagnetic layers in the spin valve so another layer can move freely, and hence enhance the spin valve effect (GMR). During the growth process, the deposition was performed at room temperature, and an in-plane magnetic field of strength $4mT$ was used to introduce an exchange biase on one of the ferromagnetic layers (permalloy or nickel) and to induce a magnetic anisotropy in the free layer. The antiferromagnetic layer used is $\mathrm{Ir_{20}Mn_{80}}$, with a thickness of (8nm) deposited by co-sputtering of two sources Ir and Mn with different deposition rates.

4.3.1 Spin valves with Cr spacer (S548 and S549)

Another set of spin valves samples was grown with different spacer material (Cr) between the permalloy and nickel layers, with the same thickness used for the previous spin valves spacer (4nm) with same thickness for IrMn, Ni, and NiFe layers. Changing the non-magnetic spacer material yields different magnetic properties to the whole structure, and hence changes the giant magnetoresistance value and the reversal of the layers [169]. Each spacer material has a different oscillatory curve of the exchange coupling that varies with the thickness, the magnetisation orientation of the layers oscilate between ferromagnetic and antiferromagnetic coupling at zero field. [183]. The reason behind the growth of the IrMn on the top of the ferromagnetic layers is to get the best match for the spin configuration at the interface [184]. As shown in figure 4.9, at the interface, on the top of saturated ferromagnetic layer, the interfacial spins of the antiferromagnetic layer coupled ferromagnetically with the ferromagnetic spins. The ferromagnetic coupling between these layers will remain even after removing the saturating field after the deposition induces an exchange bias in the spin valve.

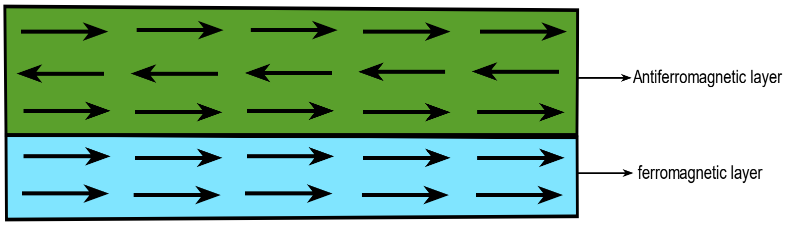

Figure 4.9: Interface between a ferromagnetic layer and an antiferromagnetic layer for perfect coupling in exchange biased bilayers

The multi-layered structures of spin valves S548 and S549 are illustrated in figure 4.10, where the order of the permalloy and nickel is swapped to study the effect of the strain on magnetotransport properties of each structure differently. The Cr is used as a buffer and capping layer, instead of Ta. Mao et al. [172] found that the insertion of the Cr layer under the permalloy in a spin valve enhances the structure of the spin valve, which enhances the antiparallel orientation between the successive ferromagnetic layers.

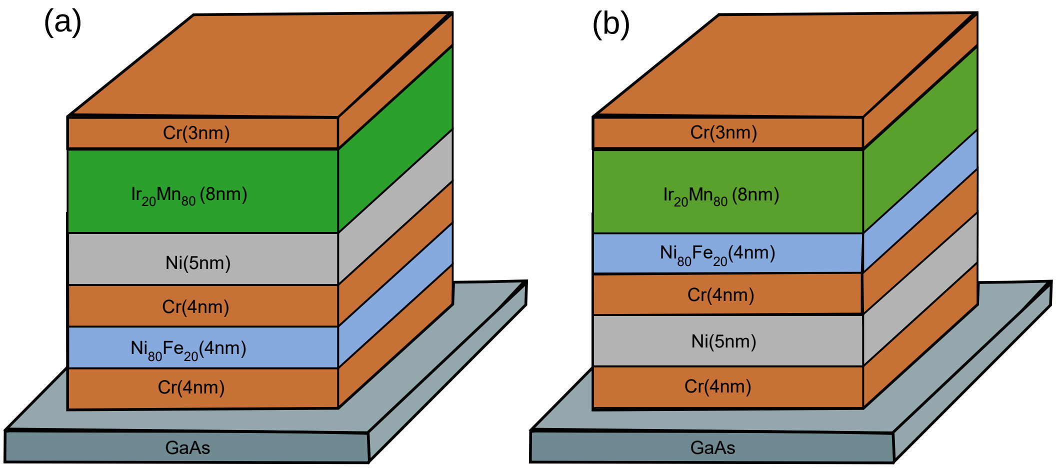

Figure 4.10: Schematic of the multilayers structure of the (a) S548 and (b) S549 spin valves films were grown using the sputtering system In these structures the IrMn layer is grown on the top of the ferromagnetic layer to get the best match at the interface. The thickness of each layer is shown on the nanometre scale.

4.3.1.1 SQUID magnetometry measurements for S548 and S549 spin valves

The magnetisation of these spin valves and the reversal of each layer were checked using SQUID magnetometry measurements. Figure 4.11 shows magnetisation curves for spin valves S548 and S549 measured at room temperature. It is obvious that for both samples, there are two distinct magnetic reversals, meaning each layer of permalloy and nickel has different coercivity. This would enhance the spin valve effect in the magnetotransport measurement, which could induce antiparallel magnetisation configuration. It can also be seen that the permalloy layer switched at a very low field value of $0.5mT$ in both spin valves, which is clear from the percentage of magnetic moments of the magnetisation of the permalloy and nickel, as discussed previously for IM008 and IM009 spin valves. The permalloy magnetic moments of reversal consist of around 65% in S548 and 72% in S549 spin valve from the whole reversal. It is not clear at this stage why the permalloy layer switched before nickel in S549 spin valve, where the permalloy was grown under the IrMn layer. Furthermore, the coercivity of nickel in S549 is more than that in S548, and this contradictory to what expecting where the nickel layer is the free layer in IM009 spin valve. One can assume that the large coercivity of the nickel in both spin valves is due to the pinning of the nickel layer with the buffer layer or IrMn. Another reason that might cause that is the IrMn/ferromagnetic layers' interface since the buffer and spacer are the same in both cases.

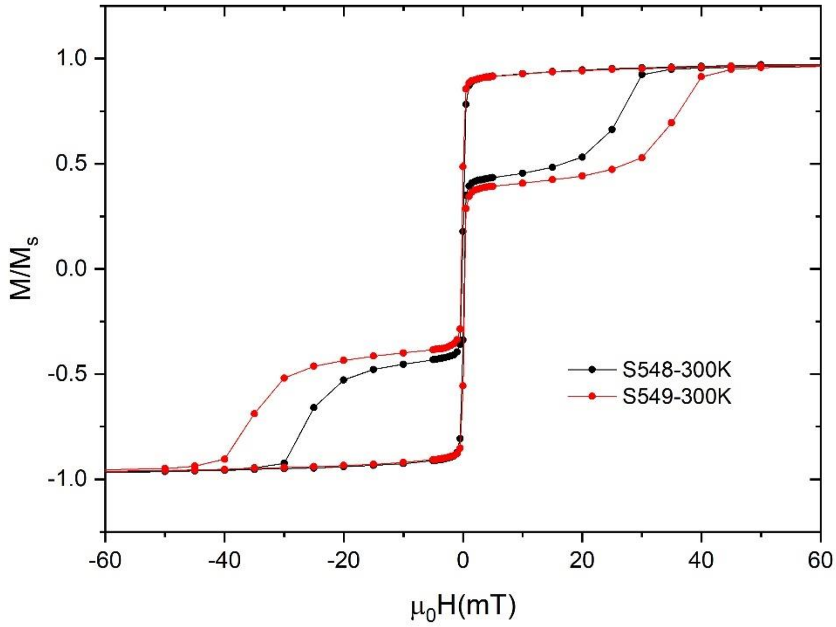

Figure 4.11: SQUID magnetic hysteresis loops for the S548 and S549 at room temperature.. The permalloy switches abruptly at 0.5mT while the nickel reverses slowly until aligned with the magnetic field. The difference in nickel coercivity could be related to the IrMn/FM interface.

Other SQUID measurements for both spin valves were carried out at different temperatures ($50K$ and $2K$) to check how magnetisation, coercivities, and exchange bias fields vary with temperature. Figure 4.12 shows the magnetisation hysteresis loops for S548 at different temperatures. At $50K$ it shows that the coercivity of the nickel layer increased more than three times from $25mT$ at room temperature to $82.5mT$ at $50K$, while for the permalloy it showed a small increase from $0.25mT$ at room temperature to $0.75mT$ at $50K$ and $1.25mT$ at $2K$. An exchange biased field for the nickel layer appears at $2K$, where asymmetric Ni layer reversal occurs, with different saturation fields for both sides of the hysteresis loop ($170mT$ on the right side of the loop, and $225mT$ on the left). This gives an exchange bias H_{ex} of $27.5mT$, calculated using the following equation:

$$H_{ex} = \frac{(H_{C2} - H_{C1})}{2} \tag{4.4}$$

where H_{C1} and H_{C2} are the switching fields of the pinned layer in both sides of the loop. The appearance of the exchange bias at low temperature could be attributed to the antiferromagnetic material blocking temperature T_B, the temperature where the net exchange bias between the antiferromagnetic and ferromagnetic is equal to zero. This temperature is usually lower than the Nèel temperature T_N, above which the antiferromagnetic material becomes a paramagnetic material. Below the T_B, the domain wall in the antiferromagnetic material aligns in such a way that the spins at the interface are aligned in parallel with the ferromagnetic material. In the case of S548, the blocking temperature is between $50K$ and $2K$. The reversal of the nickel is clearly affected by the IrMn layer, while the permalloy reversal as a free layer does not have that exchange bias effect. One can explain the increase in coercivity of the nickel layer by the temperature decreasing as the spin-wave excitation decreases. The increasing coercivity of the nickel layer as temperature decreases could be explained by the antiferromagnetic material being near the blocking temperature, the IrMn anisotropy being low, and the magnetisation reversal of the ferromagnetic dragging the antiferromagnetic spins, manifest as an increase in coercivity. By decreasing the temperature below $50K$ in case of the S548, antiferromagnetic anisotropy increased, and the interfacial spins of the IrMn pinned the nickel layer, and the IrMn spins cannot be dragged by the ferromagnetic reversal [181]. Noguès et al. [117] show that for an exchanged biased system of FeF_2/Fe, the temperature dependence of the coercivity and exchange bias is as shown in figure 4.13. It is clear that at blocking temperature, the exchange bias disappears where the coercivity of the ferromagnetic material is maximum since it is the temperature where the ferromagnetic spins can drag antiferromagnetic spins to rotate with the field, which enhances coercivity. Below the blocking temperature, the exchange bias starts to increase, since the interfacial domains between the two layers are coupled in parallel, while the AF interfacial couples firmly with the rest of the AF layer. In this case, the ferromagnetic material cannot change the antiferromagnetic spin direction during the reversal [115, 117].

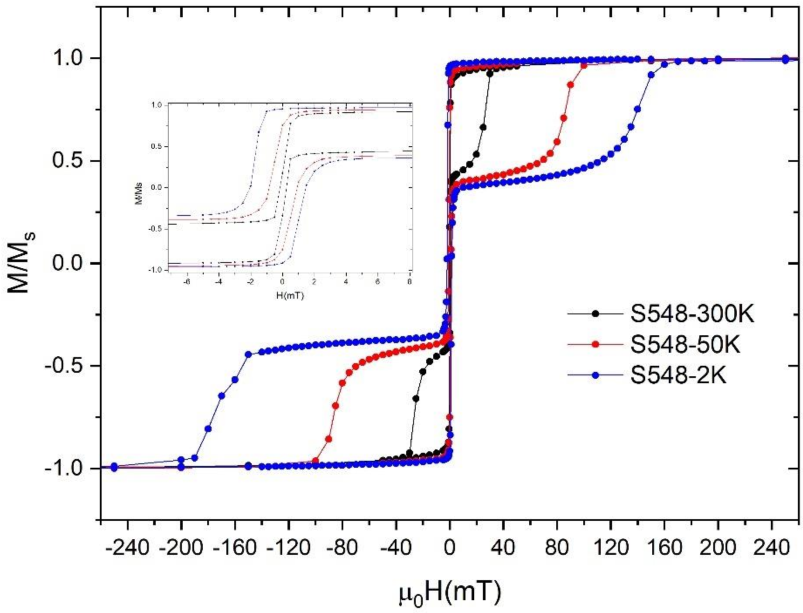

Figure 4.12: SQUID magnetometry of the S548 at temperatures of $300\mathrm{K}$, $50\mathrm{K}$, and $2\mathrm{K}$. The coercivity of the nickel changing with temperatures and the inset graph inside shows the small change of the permalloy switching field. The blocking temperature of this structure is below 50K, showing exchange bias at $2\mathrm{K}$.

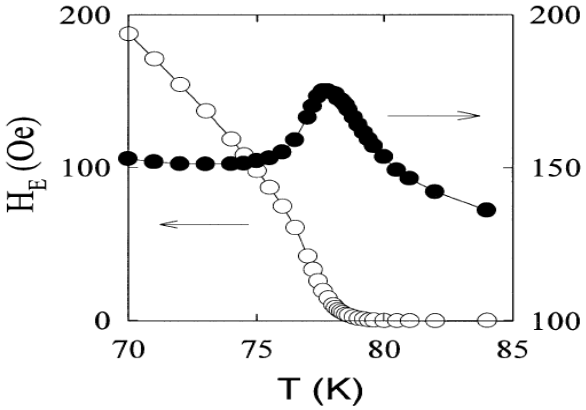

Figure 4.13: The relation between the coercivity and exchange bias and temperature in bilayers system. The exchange bias shows zero value at the blocking temperature $\mathrm{T_B}$ and an increase of the coercivity of the ferromagnetic layer at that temperature [117].

For S549 spin valve magnetisation measurements, the nickel's coercivity (considered as a free layer in this spin valve) at room temperature of $34mT$ increases to 92.5mT at $50K$ and $150mT$ at $2K$ (figure 4.14). On the other hand, the coercivity of the permalloy changes from $0.5mT$ at room temperature to

$6.1mT$ at $50K$. A small exchange bias field appeared manifest as a shift in the hysteresis loop at both sides at the permalloy magnetic moments reversal part, showing a value around $1.38mT$. One can explain this as the change to the coupling between the IrMn and the NiFe, whereby the permalloy in this spin valve grew below the IrMn. The interface coupling between the two layers is enhanced, and the spins of the permalloy are pinned by the IrMn spins, as demonstrated earlier [184,115]. As the temperature decreased to $2K$, interestingly, the exchange bias increased rapidly to reach 39mT. Figure 4.15 shows how the switching field is changing with the temperature, showing how the coercivity changing in both sides o the loop. The H_{ex} can be extracted from the curve using the 4.4 equation.

In the ascending direction, while the field increasing in the negative side, it can be seen that the permalloy spins are pinned to the IrMn spins, needs more negative field to rotate first, and switch at around $125mT$, which is attributed to the exchange bias field. For the nickel layer, the reversal already begins with the permalloy and completes the reversal to saturate at a field of around $300mT$. For the descending curve, the permalloy started to reverse earlier at a negative field, and the direction shows hard direction for the permalloy. This could be because it is in the same direction of the deposition magnetic field. One can also assume that some IrMn interfacial spins are reversed, or rotate irreversibly with the field, which changes the easy axis direction of the permalloy to lie in that direction [185]. The nickel layer is then reversed with the permalloy to saturate at a higher field of around $300mT$. The difference in the exchange bias between $50K$ and $2K$ measurements could be ascribed to the partial coupling between domain at the interface at $50K$, while the coupling was more enhanced at $2K$. A summary of the magnetic properties of the S548 and S549 spin valves are given in table 4.2.

Table 4.2: Summary of the magnetic properties of the S548 and S549 spin valves at different temperatures

Temp.	$300K$			$50K$			$2K$		
Spin valve	$(\mu_0 H_c)$ NiFe (mT)	$(\mu_0 H_c)$ Ni (mT)	$(\mu_0 H_{ex})$ (mT)	$(H_c \mu_0)$ NiFe (mT)	$(\mu_0 H_c)$ Ni (mT)	$\mu_0 Hex$ (mT)	$(\mu_0 H_c)$ NiFe (mT)	$(\mu_0 H_c)$ Ni (mT)	$\mu_0 Hex$ (mT)
S548	0.25	17.30	0	0.75	62.10	0	1.25	98.75	27.50
S549	0.5	22.5	0	6.1	72.6	1.38	125	150	39

Temperatures of $300K$, $50K$, and $2K$. H_C and H_{ex} are the coercivity and exchange bias field, respectively.

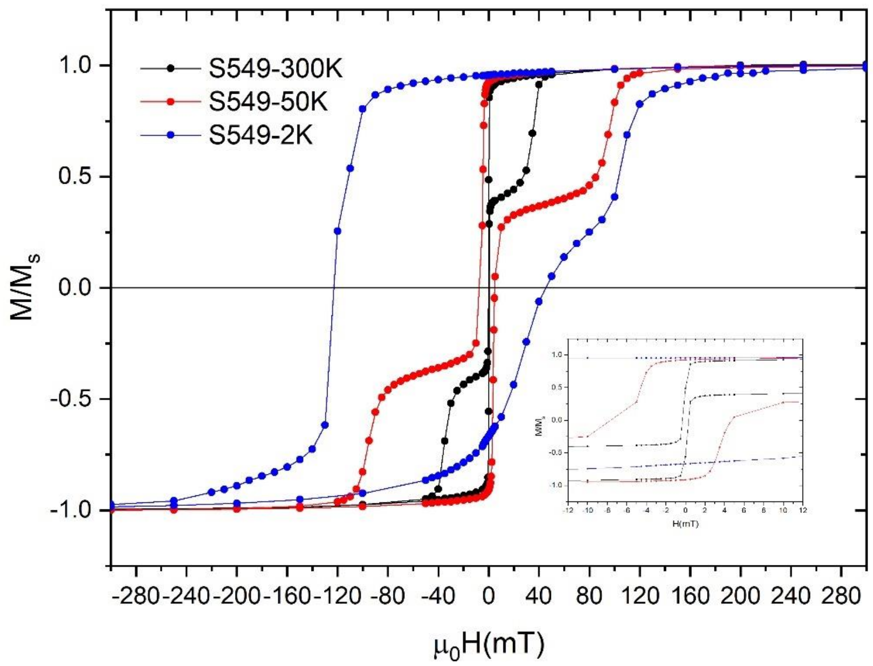

Figure 4.14: SQUID magnetometry of the S549 at temperatures of 300K, 50K, and 2K. The coercivity of the nickel and permalloy changing with temperature. The exchange bias appeared for the permalloy layer at 50K and 2K. The inset graph shows the permalloy switching at low field.

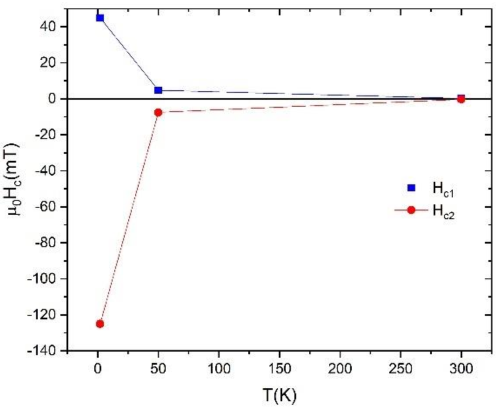

Figure 4.15: The variation of H_c of S549 pin valve sample with the temperature where H_{C1} and H_{C2} are the switching fields of the permalloy in both sides of the loop. The H_{ex}can be extracted from equation 4.4.

4.3.1.2 Magnetotransport measurements for S548 and S549 spin valves

Samples S548 and S549 were fabricated and then mounted onto a piezoelectric transducer (as discussed in section 2.2.2) to prepare the samples to study the strain effect on the magnetotransport properties. Figure 4.16 (a) shows the magnetotransport measurements for the S548 spin valve for the longitudinal resistance for the measurements, when the field is along $\alpha = 0^o$and 90^0 to the current. The magnetoresistance curve for this spin valve shows two anisotropic magnetoresistance curves, which depend on the direction between the field and the current. Here the magnetoresistance curves do not show any GMR effect even with two distinct features of reversal and wide coercivity for the nickel layer, as shown by the SQUID measurements in figure 4.12. This could be due to the interface between the magnetic layers and the Cr spacer. The GMR could also be very small compared to the AMR, and it is difficult to determine in the resistance curves since the AMR is dominant.

The longitudinal resistance measurements show non-symmetric curves (the difference in features between the ascending and descending curves), which could be related to the superposition of the AMR and GMR small value. Another reason for this could be ascribed to the IrMn contribution to the anisotropic resistance. Marti et al. [186] demonstrated that the IrMn moments does not rotate back to the initial state upon the reversal of the ferromagnetic layer (NiFe), hence gives asymmetric resistance curve for the field rotation measurements. Figure 4.16(b) shows the transverse resistance of the S548 spin valve when the field making angles of $\alpha = +45^{o}$ and -45^{0} to the current, it shows very symmetric curves for ascending and descending curves. At the maximum applied field of $-40mT$ at point (I), the resistance curve starts to increase or decrease (depending on the field direction relative to the current), as an indication that one or both layers started to reverse at high negative field gradually. At point (II), the permalloy switches at a field of $0.8mT$, as shown by the sharp reversal in the magnetisation measurements, then the resistance curve completes to the same direction of increasing or decreasing until it changes direction at point (III). Changing the resistance at point (III) could be ascribed to the nickel layer reversal. As the magnetic field swept to $+40mT$, the two layers aligned at the same direction with the magnetic field at point (IV). Sweeping the field in the opposite direction gives symmetric curve for both measurements' directions. The spacer type could be the main reason for the small size of the GMR and for the AMR dominance in the magnetoresistance measurements. The early reversal of one layer (most likely the nickel layer, since it shows a slow reversal) might also be another reason for decreasing the GMR size.

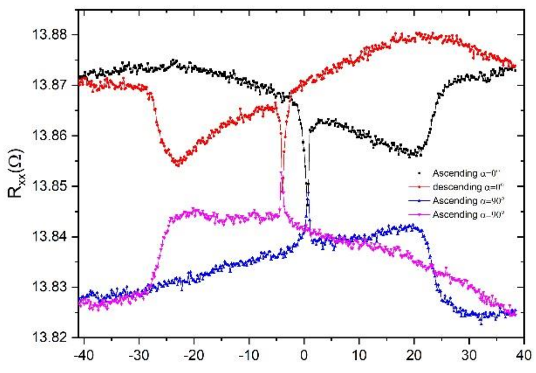

(a)

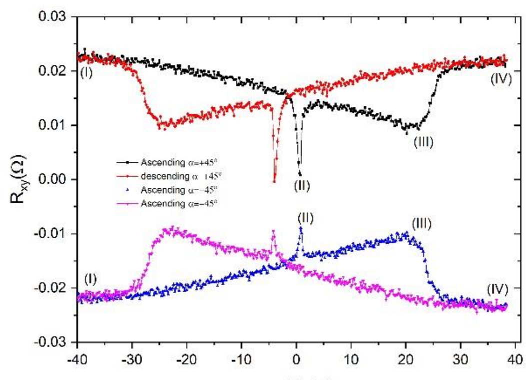

(b)

Figure 4.16: (a) The longitudinal resistance of the S548 for $\alpha = 0^{o}$ and 90^{0}measurements show that the magnetoresistance curves are dominated by the AMR, with no clear GMR peaks. For the same direction measurements, the curves are not symmetric for ascending and descending field direction, which could be related to a superposition of the AMR with a small value of GMR. (b) The transverse resistance of the S548 when the angle is between the field and the current are $\alpha = +45^{o}$and -45^{0}. The letters in the graph are described in the text.

Rotational transport measurements were performed for the S548 spin valve, to check the anisotropic magnetoresistance change with changing the direction between the magnetic field and the current at different magnetic field values ($7mT, 10mT, 20mT, 25mT, 40mT, \text{and } 300mT$). The magnetic field was rotated by 250^o around the electric current direction with a resolution of 5^o, and rotated back to check if there any hysteresis in the magnetoresistance curve. Figure 4.17 (a-f) shows the transverse resistance for different magnetic field values. The magnetoresistance properties were extracted using equation 4.3.

The values of ΔR increase with increasing magnetic field (shown in the figures). From the sweep and SQUID measurements for S548, it is clear that the permalloy switches at a low field while the nickel layer is rotating until it aligns with the permalloy at around $30mT$. It can be seen that, for both $7mT$ and $300mT$, there is no hysteresis between the two rotation curves. This can be explained as follows: for the $300mT$, the permalloy and nickel magnetisations are aligned and saturated with the magnetic field direction, which means all domains from both magnetic layers are aligned, even though the nickel spins are coupled strongly with IrMn spins. In both directions (1) and (2) of the measurements, the field overcomes the coupling of the spins at the IrMn/Ni interface, and that shows zero hysteresis between both directions. At $7mT$, the rotation in both directions does not show hysteresis between the two curves, which could be due to the rotation of the permalloy layer domains and some rotation of nickel spins, which does not affect any spins coupled with the IrMn, hence no irreversible rotation is seen in both directions of the field. One can expect a GMR contribution in this case as the permalloy rotate only, but the GMR size might be very small compared to AMR.

For field values between $300mT$ and $7mT$, a hysteresis between the two curves' directions appears, which could be attributed to the interface between the Ni and IrMn, where the domains reversal between the two layers is irreversible. For the two values of $20mT$and $25mT$, the hysteresis between the two measurements is around $15mT$, possibly because of the nickel layer magnetisation around the kink, manifest in resistance sweep data (point III in figure 4.16(b)), which could be near the nickel switching. This means the field is rotating the nickel spin along with coupled IrMn domains at the interface, which could show irreversible rotation from the IrMn spins. The difference in ΔAMR between $300mT$ and $40mT$ measurements could be related to the coupling between the nickel and IrMn layers' interface, where the nickel spins might not be fully saturated at $40mT$, as shown in the magnetisation and magnetotransport measurements. Although some hysteresis is still evident for the field value $40mT,$ that value is enough to make closed loops for sweep magnetoresistance. The curves for R_{xx} at different magnetic field values are shown in figure 4.18, showing the same behaviour of the R_{xy}curves with more hysteresis at $20mT$ and $25mT$. The values of the ΔR shown in the inset of each plot shown larger values compared to the similar field for R_{xy}. This difference could be ascribed to the geometry of the central area of the micro-device used in these measurements (see figure 2.5), where the longitudinal measurement does not measure a perfect square of material and hence a slight difference in the AMR value in the longitudinal and transverse measurements [187].

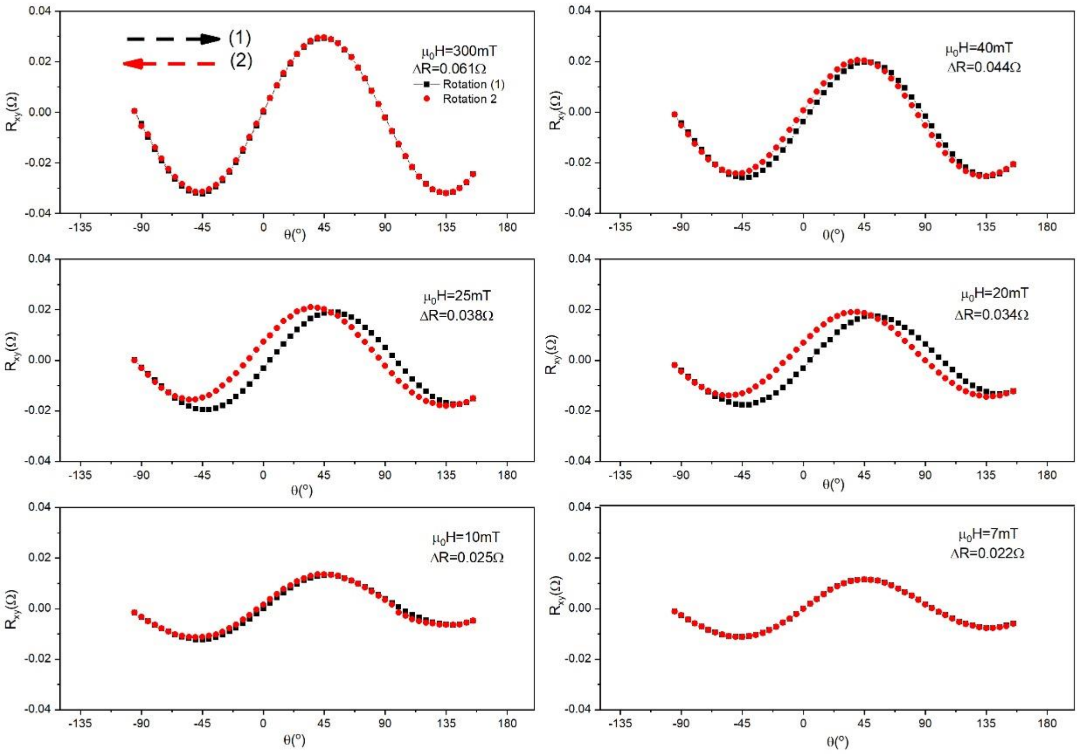

Figure 4.17: Rotational transverse resistance for the S548 spin valve applying different fields values $(7\mathrm{mT}, 10\mathrm{mT}, 20\mathrm{mT}, 25\mathrm{mT}, 40\mathrm{mT}\text{ and }300\mathrm{mT})$ when the magnetic field rotates by 250^{o}. (1) and (2) represent the magnetic field direction (rotated oppositely).

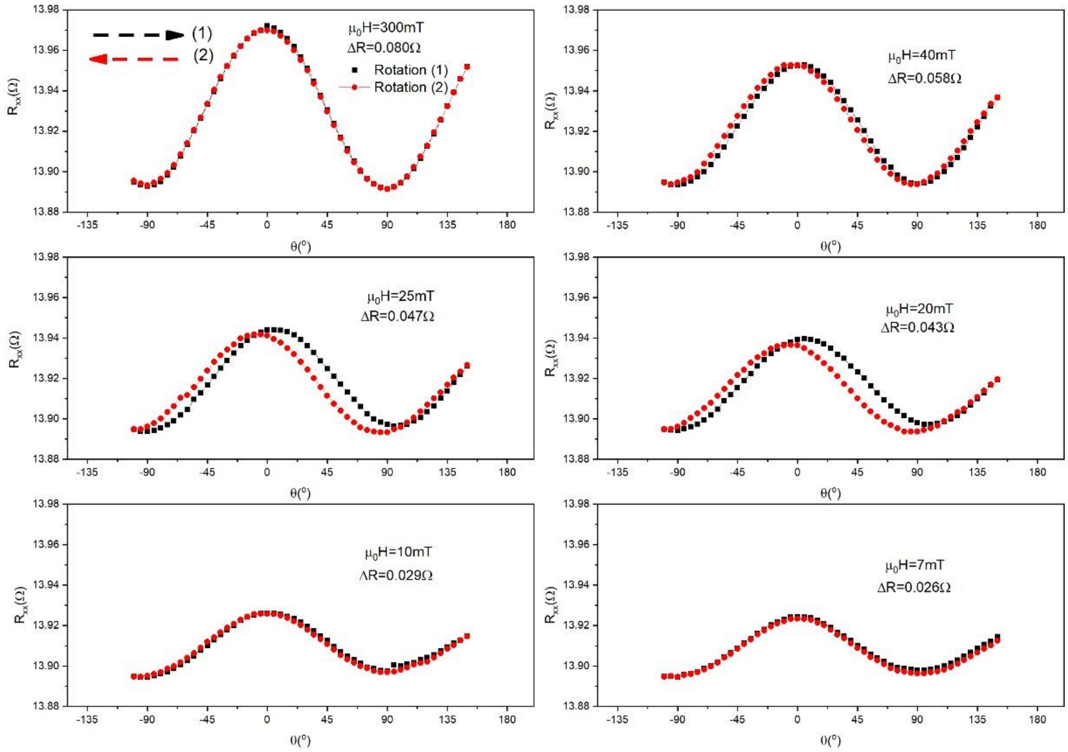

Figure 4.18: Rotational longitudinal resistance for the S548 spin valve applying different fields values $(7\mathrm{mT}, 10\mathrm{mT}, 20\mathrm{mT}, 25\mathrm{mT}, 40\mathrm{mT}\text{ and }300\mathrm{mT})$ when the magnetic field rotates by 250^{o}. (1) and (2) represent the magnetic field direction (rotated oppositely).

For the S549 spin valve, it shows the same magnetoresistance curve shape where the permalloy switches at the same magnetic field for the S548 spin valve. Figure 4.19 (a) and (b) shows the longitudinal and transverse resistance for S549 spin valve. Although the nickel layer in this spin valve reversal needs a higher field to saturate than that in S548 (see figure 4.19 (c)), the magnetotransport curves show close reversal curves in all directions and both spin valves show the same curves' shapes with same peaks intensities. For this spin valve, the magnetoresistance curves show anisotropic magnetoresistance curves as well, and there is no clear GMR effect on this sample.

For S548 and S549 spin valves do not show any significant GMR effect, which could be due to the spacer layer. Dieny et al. [188] investigated permalloy based spin valve using different spacers and found that using noble metals like

Cu enhanced the GMR since the electrons can be transmitted through the interlayer, while for metals like Cr, the electron spin flow is suppressed and the GMR is decreased. The thickness of the spacer used here is $4nm$, and the giant magnetoresistance value is oscillating with the spacer thickness, which could mean that the optimal Cr thickness for the permalloy and nickel layers is less or more than 4nm, as demonstrated by Parkin [169].

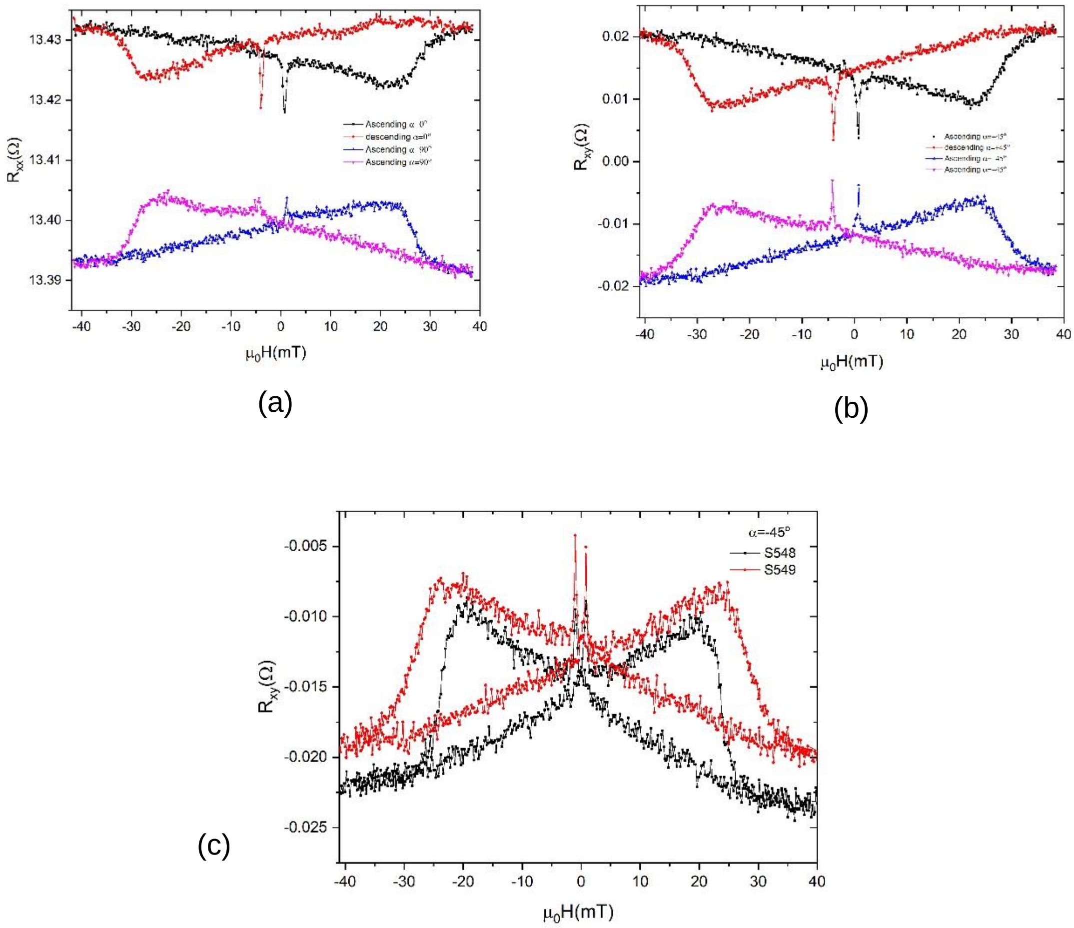

Figure 4.19: (a) the longitudinal resistance of the S549 for $\alpha = 0^{o}$and 90^{0}, showing magnetoresistance dominated by AMR and no GMR. (b) the transverse resistance of the S549 when the angle between the field and the current are $\alpha = +45^{o}$and -45^{0}. (c) comparison between transverse resistance for the measurements when $\alpha = +45^{o}$in S548 and S549 spin valves, showing the same amplitude and shape, and shows that the spin valve S549 needs a higher magnetic field to saturate, because of the different interface between the IrMn and the ferromagnetic layers in each spin valve.

4.4 Conclusion

The magnetisation and magnetotransport properties for a set of spin valves were studied in this chapter. SQUID magnetometry and DC four-probe measurements were used to study the reversal of the layers that consists of the multi-layered structures. This chapter mainly studied the reversal of each spin valve separately at $0V$ without inducing strain using the piezoelectric transducers. Same micro-device shapes for all spin valves were used for transport measurements, after mounting each device onto piezoelectric transducer, as discussed in detail in chapter 2, whereas for the measurements performed by the SQUID, films of this spin valves were used without any fabrication. Two sets of spin valves were studied, pseudo spin valve (with no antiferromagnetic layer), and spin valve with IrMn layer. Two spacers were used in these spin valves. Samples all consist of permalloy and nickel with the same thickness as used in work presented in chapter 3.

All spin valves with Cu spacer show typical giant magnetoresistance curves, while all samples grown with Cr spacer show magnetoresistance curves dominated by anisotropic magnetoresistance. IM008 and IM009 pseudo spin valves grown with Cu spacer show two different reversals of the permalloy and nickel. The nickel layer shows a slow reversal in IM008 after the abrupt switching of the permalloy. On the other hand, in IM009 spin valve, the nickel shows abrupt switching and then reverses slowly. The permalloy coercivity in both samples is equal to $0.5mT$, while the coercivity of the nickel layer varies in these spin valves. The contrast in the nickel coercivity enhances the GMR effect in both spin valve with a value of around 1.50% for both samples. The GMR peaks are different, since the coercivity of the nickel varies, with IM008 showing a GMR plateau peak, while IM009 shows a very sharp peak. The difference between these spin valves is the nickel coercivity, which is related to the interface and the microstructure of each layer. The nickel interface varies among the spin valves since it grew on top of different layers (Ta and Cu) [172]. Another reason for the narrow nickel switching in IM009 might be the inter-layer coupling between the permalloy and nickel, which introduced pinholes between the layers [173, 174, 175]. For all spin valves that show GMR effect, $\mathrm{GMR}_{\perp} > \mathrm{GMR}_{\parallel}$, which could be attributed to different reasons. One of these reasons concerns the directional dependence of the mean free path of spin-up and spin-down electrons in the two-current direction configuration [179].

For the last set of the spin valves with IrMn layer, a Cr spacer was grown in the S548 and S549 spin valves, which did not show any apparent GMR effect. Two configurations were used for these spin valves, with the permalloy and nickel layers swapped between free and pinned positions. The use of Cr enhances the coercivity of the nickel layer with a saturation field between $35mT$ and $45mT$. No exchange bias is shown for all IrMn spin valves at room temperature. Due to the enhancement of the interface at low temperature, both S548 and S549 show exchange bias field at low-temperature measurements, related to reaching the IrMn blocking temperature [117].

To conclude, in the optimisation of building multilayers with different ferromagnetic materials and enhanced magnetoresistance value, it is critical to find different material coercivities to enhance the antiparallel alignment of the magnetisation. Using the antiferromagnetic layer to pin one of the spin valves helps to increase the field range over which the anti-parallel configuration can be observed since the ferromagnetic spins are coupled by the AFM. The type of spacer and optimal thickness plays a crucial role in the GMR effect since this phenomenon is dependent on the spin scattering at the interfaces. The GMR effect opens many possibilities, having originated in the field of high-density storage technology in read-head hard disks, enabling the study of many phenomena related to electron spins.

Chapter 5: Investigation of the strain manipulation of magnetic reversal and magnetoresistance properties of permalloy and nickel spin valves

5.1 Introduction

The manipulation of magnetisation in ferromagnetic films plays a significant role in the development of novel spintronics devices, particularly for information storage and logical operations. The ability to control the magnetisation of material using an electric field can facilitate the development of new devices with lower power consumption and efficient processing. This can be performed by means of the inverse magnetostrictive effect in hybrid multiferroic structures, whereby a voltage-induced strain modifies the magnetic anisotropy energy [88,65]. Chapter 4 presented the magnetotransport and magnetisation reversal mechanism of a set of spin valves mounted on piezoelectric transducers, but with $0V$ applied to the transducers. This chapter studies the magnetotransport properties and magnetisation reversal in the same spin valves, this time with a range of voltages applied to the piezoelectric transducers in order to induce a uniaxial strain in the plane of the spin valves.

The same samples are used in this chapter as in the previous one, including pseudo spin valves with two free magnetic layers (Cu spacer), and spin valves with IrMn layer (Cr spacer). The pseudo spin valves IM008 and IM009 show large changes in magnetotransport characteristics arising from modifications of the magnetisation reversal of the individual layers in response to the strain, manifest as changes in the features related to giant magnetoresistance (GMR) and anisotropic magnetoresistance (AMR). Moreover, tuning the strain in the spin valves changes other magnetic features in the magnetotransport measurements, the coercivity, reversal process, and switching field of individual layers. On the other hand, the spin valves set with IrMn show a response for only the permalloy layer for S548 sample, while the S549 does not show any response to the strain for both layers.

This chapter comprises two main parts. First, it discusses the strain effect on pseudo spin valves samples, where different directions of the magnetic field with respect to the long axis of the piezoelectric transducer are mainly used to compare between the strain effects on different magnetotransport measurement features, with IM008 and IM009 spin valves. Second, it studies the strain effect on the spin valves with IrMn layer, S548 and S549 samples. The strain effect on magnetotransport properties; GMR, AMR, switching field, magnetoresistance features, and magnetisation reversal of magnetic layers are discussed in detail. Comparisons between spin valves in each set are carried out to understand the magnetic reversal of each magnetic layer in each spin valve at different strain values.

5.2 Strain control of magnetic reversal and magnetoresistance of pseudo spin valves

In this section, two spin valves with free permalloy and nickel layer are examined under varying strain by tuning the voltage applied to the transducer. IM008 with the structure of Ta/NiFe/Cu/Ni/Ta and IM009 consists of Ta/Ni/Cu/NiFe/Ta. Measurements were conducted for different directions of the magnetic field with respect to the hybrid transducer/spin valve device.

5.2.1 IM008 spin valve

All spin valves in this chapter were fabricated and glued onto piezoelectric transducers using the method discussed in section 2.2.1, where an epoxy used to affix the devices to the stressor, left to cure for 24 hours at room temperature. The hybrid structure (shown in figure 5.1) was placed in a magnetic field that can rotate by 360^o in-plane of the device to measure the magnetoresistance using the four-point magnetoresistance measurements. The measurements were performed at different strain values by tuning the voltage on the piezoelectric transducer. The values of the strain-induced in the spin-valve film were measured by sweeping the voltages up and down between $-30V$ and $+50V$, with a step of $+1V$ for the upsweep and $-1V$ for the downsweep, as explained in section 2.1.2. Using the phenomenon when an elastic deformation affects metals, the electric resistance changes accordingly to strain [189]. A magnetic field of $300mT$ is applied in this measurement to make sure that both magnetic layers are saturated with the field, and any change in resistance value is attributed to the strain values induced in the spin valve film. The longitudinal resistance values at different voltages were collected, then the strain was calculated from this data (as discussed in section 2.2.3), as shown by a hysteric loop of the strain-voltage in figure 5.2. A zero-strain value with respect to the strain at $0V$ is induced in the IM008 spin valve when $+17V$ (for the sweep up direction used for magnetotransport measurements) is applied to the transducer. In this case, all voltages less than $+17V$ (negative strain values) represent compressive strain values, while all voltages larger than +17V (positive strain values) are considered as tensile strain values. The Poisson ratio values for all layers are stated in table 5.1, where the value of the Poisson ratio for the spin valve is the average of all layers' ratios. The strain loop for IM008 stack shows similar values and features to the loop for the permalloy single layer sample S476, as shown in figure 3.5.

Table 5.1: Poisson's ratio for the layers consists of IM008 spin valve.

Material	Poisson’s ratio
GaAs	0.32 [190]
Ta	0.35 [191]
NiFe	0.33 [192]
Cu	0.34 [193]
Ni	0.33 [192]

For the magnetoresistance measurements, three directions of the magnetic field with respect to the long axis of the piezoelectric transducer were conducted ($\varphi = 0^o,\ +45^o,$ and 90^o). The direction of the electric current with respect to the magnetic field is also changed in each field direction $\alpha = 0^o$, and 90^o. In all measurements, the effect of strain on magnetotransport properties of the spin valve and the magnetisation reversal will be discussed in detail. For all magnetotransport measurements, the field swept between $-40mT$ and $+40mT$ which was enough to saturate both permalloy and nickel layers in the IM008 spin valve. The voltage sweep direction always starts from $-30V$ to $+50V$, or $+80V$ in some cases. The measurements show that the strain affects the magnetic reversal of both layers of the spin valve where the permalloy and nickel layers show different magnetostrictive properties with different magnetostriction sign. Hence that manifests in the whole magnetic reversal and the magnetic properties of the whole spin valve.

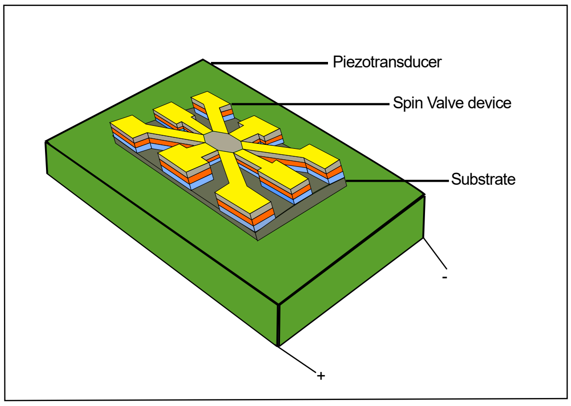

Figure 5.1: Schematic of the hybrid device comprising the spin valve device glued onto the piezoelectric transducer using the technique discussed in section 2.2.1. Tuning the bias values and sign induces different strain values and types (compressive or tensile) in the spin valve device.

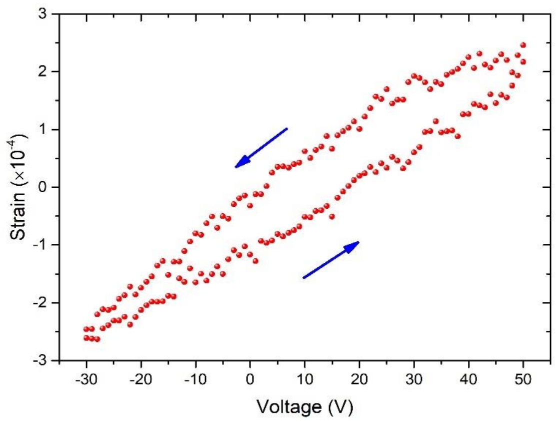

Figure 5.2: Hysteric strain-voltage loop for IM008 sample. The voltage bias across the piezoelectric transducer swept up and down between $-30V$ and $+50V$. The strain extracted from the longitudinal resistance R_{xx}, as discussed in section 2.2.3. The zero-strain value for the sweep up direction is obtained by applying a voltage of $+17V$ through the transducer (the sweep up direction is used for all transport measurements).

5.2.1.1 Magnetic field perpendicular to the long axis of the transducer ($\boldsymbol{\varphi = 90^o}$).

The first measurement configuration is when the magnetic field is perpendicular to the transducer's long axis ($\varphi = 90^o$). For this configuration, different electric current directions were applied with respect to the magnetic field: $\alpha = 0^o$, and 90^o. The measurement configurations are shown in figure 5.3. (a) and (b). The $\Delta R/R$ curves at different voltages applied to the piezoelectric transducer, when the field is perpendicular to the transducer, for $\alpha = 90^o$ and $\alpha = 0^o$ (different electric current direction with respect to the field while the long axis of the transducer is perpendicular to the field) are shown in Figure 5.4 (a) and (b). The $\Delta R/R$ values were calculated as discussed in chapter 4, using the longitudinal resistance R_{xx} curves and substituting in equation 4.1. As mentioned in chapter 4, the longitudinal resistance is a mixture of mostly giant magnetoresistance (GMR) and anisotropic magnetoresistance (AMR). The $\Delta R/R$ will be used in this chapter as an indication to the magnetoresistance in the spin valves. All values of the compressive and tensile strain values are shown in the inset beside the corresponding voltages, except for $+80V$, where no measurement was performed to determine the strain value due to the risk of cracking the device due to being subjected to high strain value for multiple iterations. These $\Delta R/R$ curves show different maximum values and shapes in both current directions with changing voltages from $-30V$ to $+80V$. For the perpendicular current direction ($\alpha = 90^o$), the maximum $\Delta R/R$ increased from 1.30% (all maximum of the $\Delta R/R$ in this chapter are calculated from the average of the maximum $\Delta R/R$ of the ascending and descending curve parts) when a voltage of $-30V$ (a compressive strain of value 2.46×10^{-4}) is applied to the transducer, while it increased to 1.49% when the voltage changed to $+80V$ (tensile strain). The maximum value of the $\Delta R/R$ for $+80V$ curve could be at any point at the peak as the peak is more like a plateau. For the measurement when the magnetic field is parallel to the current ($\alpha = 0^o$), the $\Delta R/R$ value increased from 0.93% for $-30V$, to reach 1.24% when the voltage ramped up to $+80V$.

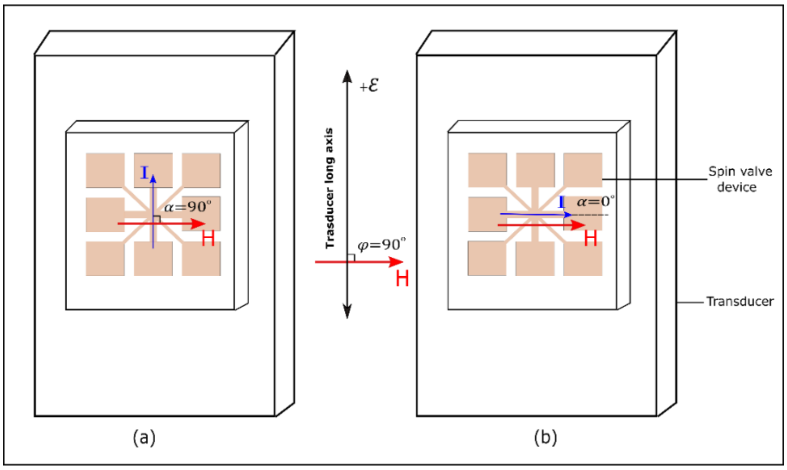

Figure 5.3: The measurements configuration for the IM008 spin valve when the magnetic field is perpendicular to the long axis of the piezoelectric transducer ($\varphi = 90^o$), where (a) the magnetic field is perpendicular to the current $\alpha = 90^o$, and (b) the magnetic field is parallel to the current $\alpha = 0^o$.

To understand the strain effect on IM008 spin valve magnetoresistance properties, the magnetic reversal of each magnetic layer of the spin valve must be studied for each strain value individually, by comparing the transverse R_{xy} and longitudinal R_{xx} ($\Delta R/R$) magnetoresistance. Figure 5.6 (a) and (b) (using the same scale for all curves) show the R_{xy} curves for IM008 spin valve when the magnetic field is perpendicular to the long axis of the transducer ($\varphi = 90^o$) at different voltages ($+30V$ is not included since it gives similar features to the $+50V$) for $\alpha = 90^o$and $\alpha = 0^o$ directions, respectively. For the whole range of the voltages applied between $-30V$ and $+80V$, the R_{xy} curves show different features (discussed in next sections), indicating different magnetic reversals behaviours for each layer with changing strain for both measurement directions.

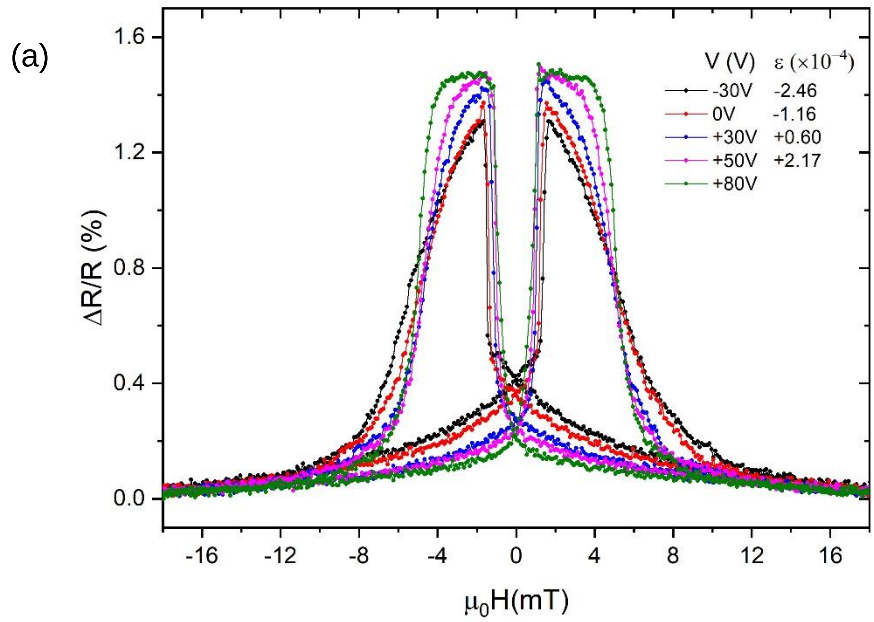

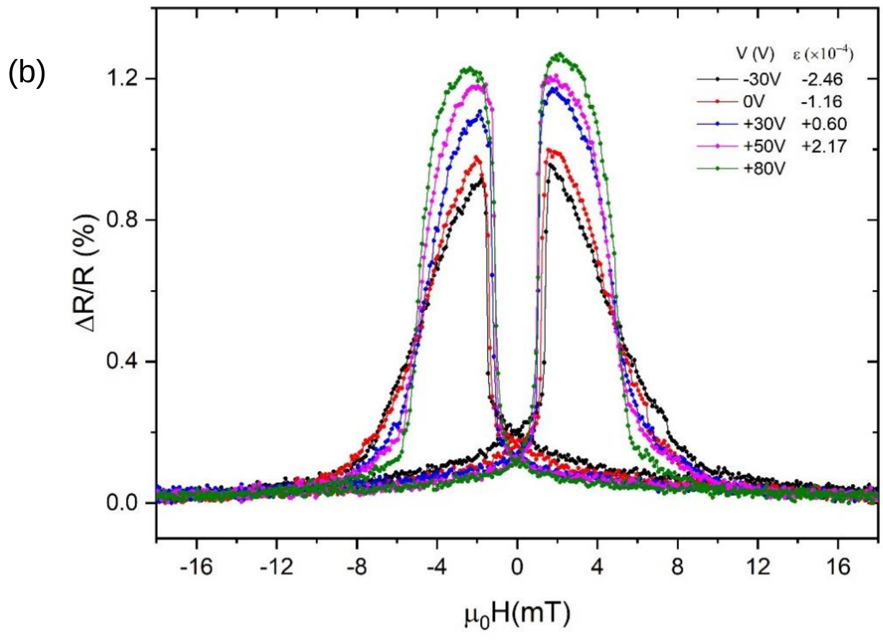

Figure 5.4: The $\Delta R/R$ curves of the IM008 spin valve when the magnetic field is perpendicular to the long axis of the transducer $\varphi = 90^o$; (a) when the field makes an angle of $\alpha = 90^o$ with the current, and (b) for $\alpha = 0^o$. Both directions show changes in the $\Delta R/R$ values and shapes, depending on the value and type of strain applied to the spin valve. As discussed, there is no corresponding strain value for $+80V$.

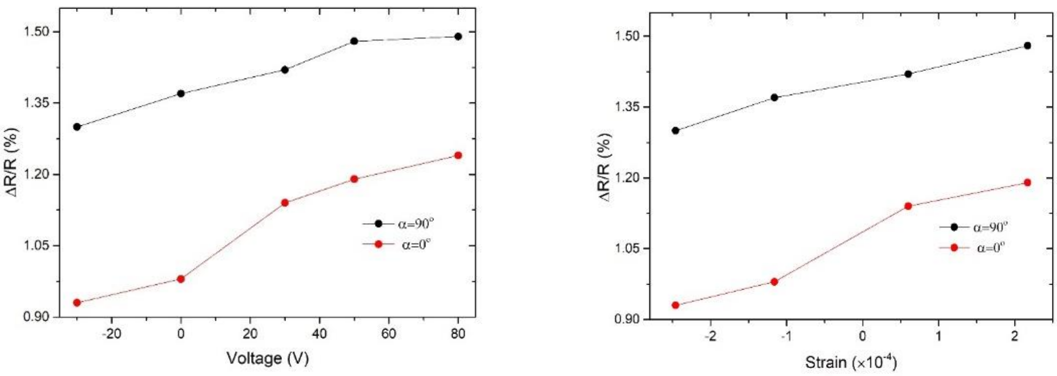

(a) (b)

Figure 5.5: The dependence of the $\Delta R/R$ values on the (a) voltages applied to the transducer and (b) the corresponding strain values when the magnetic field is perpendicular to the piezoelectric for IM008 spin valve (the lines between points are for the reader to follow). Note that there is no corresponding strain value for $+80V$ value.

5.2.1.1.1 Strain control magnetic reversal of the permalloy layer $\varphi = 90^o$

Permalloy layer in IM008 spin valve exhibits the same magnetostrictive properties (positive magnetostriction) as the permalloy single layer sample S476 discussed in chapter 3 where the strain controls the magnetisation direction of the layer. To study that, focussing in the permalloy reversal for $\alpha = 90^o$ measurements, the reversal of the permalloy occurs at lower fields as represents by region (1) (represents the reversal feature of the permalloy in the sweep up direction) for voltages $-30V$ and $+80V$ in figure 5.6 (a), followed by the nickel reversal, as also shown by the SQUID magnetisation measurements in section 4.2.1. The permalloy reversal shows changes with varying voltage values through the transducer. For $-30V$ (compressive strain), an abrupt switch is seen at the field value of $1.25mT$, while it changed to $1.15mT$ when the voltage ramped up to $0V$. This switching of the permalloy might be related to a soft magnetisation direction as the magnetisation switches abruptly. When the voltage increased to $+50V$ and $+80V$, it is challenging to determine the switch field, since the permalloy reversal shows slower reversal (which could be due to domains coherent rotation or domain walls movements) rather than abrupt and this could be a hard direction of the permalloy magnetisation. For the measurement when the current direction is parallel to the field ($\alpha = 0^o$) shows the same behaviour reversal for the permalloy at low field values and varies with the strain, see the difference between $-30V$ and $+80V$ curves as indicated by region (1) in figure 5.6 (b). Figure 5.7 shows the corresponding R_{xy} curves for different voltages measurements for the permalloy sample (S476) (discussed in chapter 3) when the magnetic field is perpendicular to the transducer with $\alpha = 90^o$. Comparing region (1) related to permalloy layer reversal in IM008 spin valve in figure 5.6 (a) and (b) with the magnetoresistance curves in figure 5.7 for the permalloy sample show consistency for the changing curves with the voltages. As discussed in chapter 3, this changing in magnetoresistance is ascribed to the changing of the magnetisation direction of the permalloy as the strain-induced anisotropy changing the permalloy free energy. The permalloy layer in IM008 shows the same magnetostrictive properties as the permalloy single layer sample S476, and hence, responds the same to the strain. One can conclude for permalloy layer in IM008 spin valve since the permalloy sample has positive magnetostriction constant, the magnetisation easy axis prefers to lie along the long axis of the transducer when a tensile strain applied to the permalloy layer. Conversely, applying a compressive strain to the permalloy layer changes the magnetisation direction by 90^o, whereby the magnetisation favours lying along the short axis of the stressor.

5.2.1.1.2 Strain control magnetic reversal of the nickel layer $\varphi = 90^o$

For the IM008 spin valve, the reversal of both layers, permalloy and nickel, are critical for the $\Delta R/R$ value and shape. In chapter 3, the nickel sample S475 did not show any response to the strain, and the sample showed zero magnetostriction value for that thickness and interface. The permalloy layer in all spin-valves was planned to be the strain sensing layer, to control the magnetoresistance and magnetic properties of the spin valves, while the nickel layer serves as a reference layer in all spin valves. However, the magnetoresistance features related to the nickel layer reversal change with changing strain induced in the spin valve as indicated by region (2) (represents the reversal feature of the nickel in the sweep up direction) in figure 5.6 (a) and (b) for $-30V$ and $+80V$, and it shows negative magnetostriction in IM008 spin valve. To investigate that, focusing on the measurements for $\alpha = 90^o$ shown in figure 5.6 (a), when applying $-30V$ or $0V$ (compressive strain) to the transducer (i.e. see region (2) in figure 5.6 (a)), the reversal of the nickel shows a very slow reversal which could be attributed to a slow rotation or nucleation of magnetic domains. The blue arrows at $7.5mT$ for the compressive strain values indicate that the nickel layer still reversing, as shown by the magnetoresistance feature at that field value, unlike the magnetoresistance for the tensile strain at the same field. For the tensile strain ($+30V, +50V \text{ and } +80V$), the reversal of the nickel shows a different shape (i.e. see region (2) for $+80V$ measurement in figure 5.6 (a)), with more flat peaks for the nickel reversal, which could be attributed to slow nucleation of domains, until it switches abruptly when the domain walls move quickly at around $6mT$, and it does not show any increase in resistance after that field. For the measurements when the magnetic field is along the current direction ($\alpha = 0^o$), as shown in figure 5.7 (b), the compressive strain exhibits an earlier reversal for the nickel magnetisation, where the magnetoresistance peaks of the nickel are superimposed with the permalloy peaks (see area (2) for $-30V$), and it is hard to distinguish between them. The change in magnetoresistance takes a wide range of the field to complete the whole reversal (noting that there might be a hard axis along the field). Conversely, for the tensile strain, the resistance feature related to the nickel started to increase at a higher field value around $5mT$, which occurred for a very short range of the field (could be easy magnetisation axis) as indicated by region (2) for $+80V$ measurement in figure 5.6 (b).

(a)

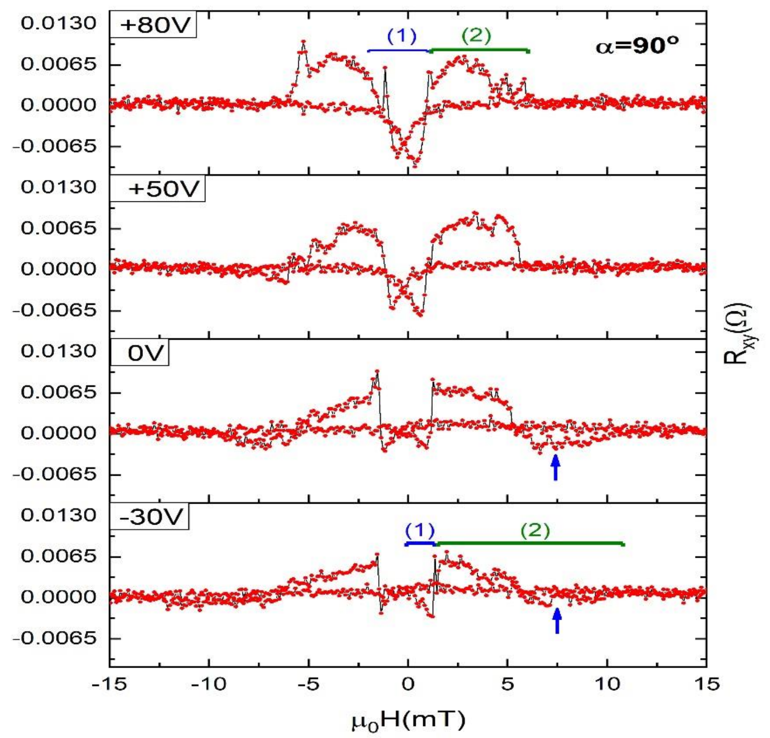

(b)

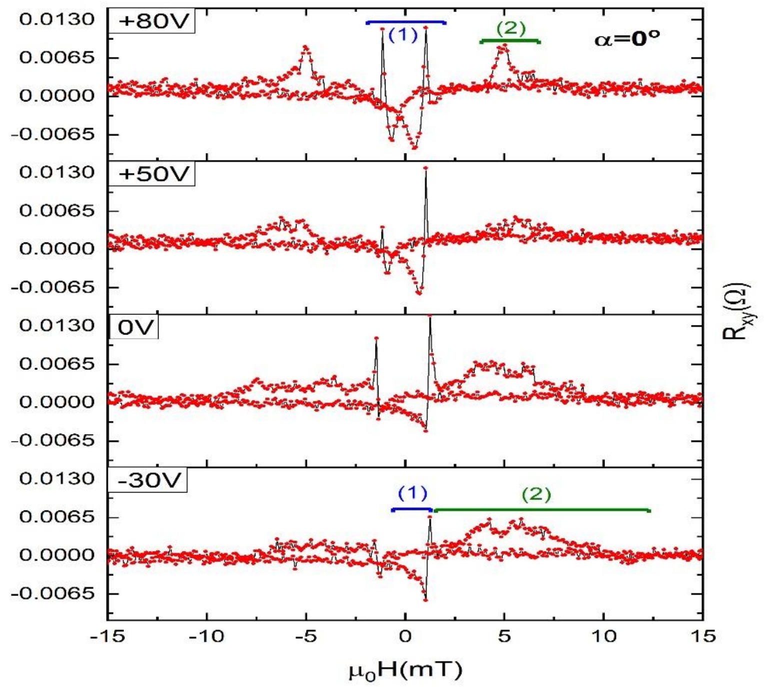

Figure 5.6: The R_{xy} curves of the IM008 spin valve for the measurements when the magnetic field is perpendicular to the transducer $\varphi = 90^{o}$ at different voltages for (a) $\alpha = 90^{o}$ and (b) $\alpha = 0^{o}$ measurements. The blue arrows in (a) show the reversal of the nickel features, which has different reversal from the tensile strain. Regions indicated by (1) and (2) represent the permalloy and nickel reversals for the sweep up measurement.

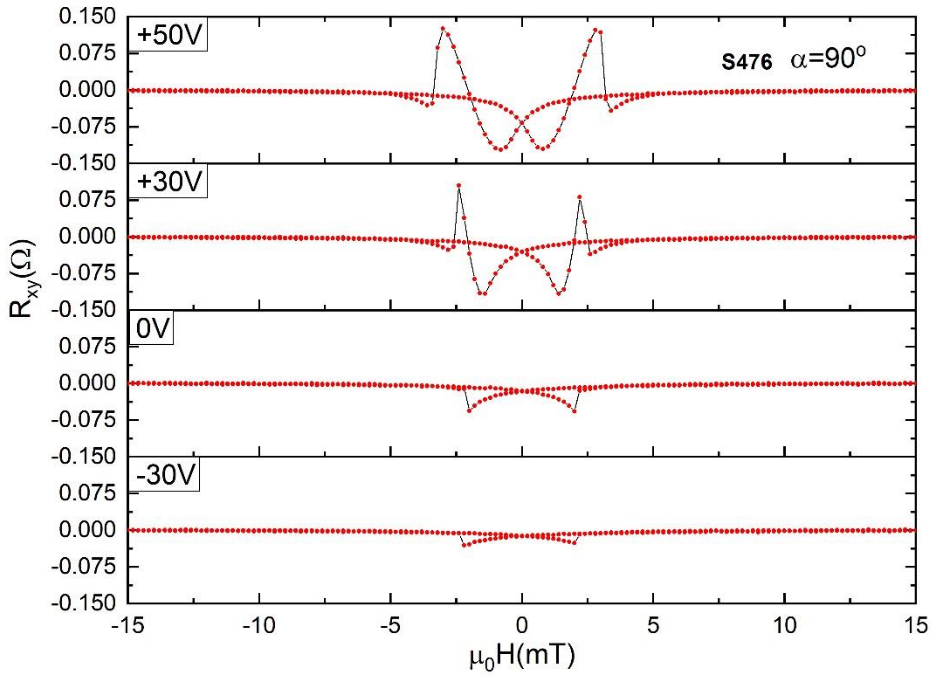

Figure 5.7: R_{xy} curves for the S476 sample (permalloy single layer sample) for the measurements when the magnetic field is perpendicular to the transducer $\varphi = 90^o$ at different voltages for $\alpha = 90^o$. For the compressive strain values ($-30V$ and $0V$) the permalloy is magnetically softer along the field direction, while it is harder for the same direction when applying tensile strain values ($+30$ and $+50V$).

From the nickel transverse resistance peaks (region 2) in figure 5.6 (a) and (b), one can assume that the nickel layer is magnetically harder along the field direction when a compressive strain is applied to the spin valve, while it is softer along the field when the tensile strain is applied. The effect of the strain on the nickel magnetisation easy axis direction is the opposite effect to the permalloy layer. The reason behind this could be ascribed to the negative value of the magnetostriction constant λ_s of the nickel [194, 195, 196], which is equal to -34×10^{-6} for bulk material [197, 198, 51]. The nickel layer in IM008 spin valve shows negative magnetostrictive properties same as that shown for the bulk form, and it responds to the strain oppositely to that shown for positive magnetostriction for the permalloy layer. The magnetostriction sign affects the magnetisation direction differently. For example, for positive magnetostriction (i.e. permalloy in this study), the magnetisation favoured lying along the strain direction. Conversely, the magnetisation prefers to lie perpendicular to the strain direction for the negative magnetostriction (i.e. for the tensile strain, the magnetisation prefers to lie along the compressive strain direction and perpendicular to the tensile strain direction) [199-2]. Wiler et al. [80] demonstrated that changing the polarity of the voltage applied through the piezoelectric transducer changes the magnetisation easy axis of the nickel by 90^o. Hu and Nan [200] also proved that applying an electric field to the nickel can cause a gradual or an abrupt orientation in-plane or out-of-plane orientation of its easy axis. The nickel layer in IM008 shows magnetostrictive behaviour different than the single layer for S475 sample, and that could be ascribed to the interface difference in the spin valve in the presence of the copper layer as a buffer for the nickel layer. The interfaces could affect the magnetic and magnetostrictive properties of the nickel, as demonstrated by Waser [201]. The growth quality and texture could be affected by changing the substrate type, which could affect the magnetostriction properties of the material grown on the substrate [202].

5.2.1.1.3 Strain control magnetoresistance features of IM008 spin valve ($\boldsymbol{\varphi = 90^o}$)

The main aim of this section is to investigate different features of the permalloy and nickel layer from magnetoresistance curves to understand the effect of the strain in the whole reversal of the spin valve. The relation between the size of the $\Delta R/R$ with the voltages and strain values are shown in figure 5.5 (a) and (b), when $\alpha = 0^o$, and $\alpha = 90^o$ respectively. It is clear from these measurements that the $\Delta R/R$ ratio for the current direction $\alpha = 90^o$ is larger than that for $\alpha = 0^o$ measurements for all voltages applied to the transducer. The difference in the $\Delta R/R$ values between these two directions is ascribed to the difference in the mean free path between the spin-up and spin-down electrons in the two current orientation, as discussed in chapter 4 [179]. A qualitative model is assumed to understand the effect of the strain on the magnetoresistance properties of the whole reversal of the spin valve. The magnetisation orientations for both layers when no magnetic field is applied are assumed as follows. When a compressive strain is applied to the spin valve, the magnetisation orientation of the permalloy M_{NiFe} prefers to lie along the short axis of the piezoelectric transducer. For the nickel, the magnetisation

M_{Ni} favours the direction of the long axis, as displayed in figure 5.8 (a). On the other hand, for the tensile strain, for both layers, the magnetisation easy axis changes by 90^o from the direction when applying a compressive strain, as shown in figure 5.8 (b).

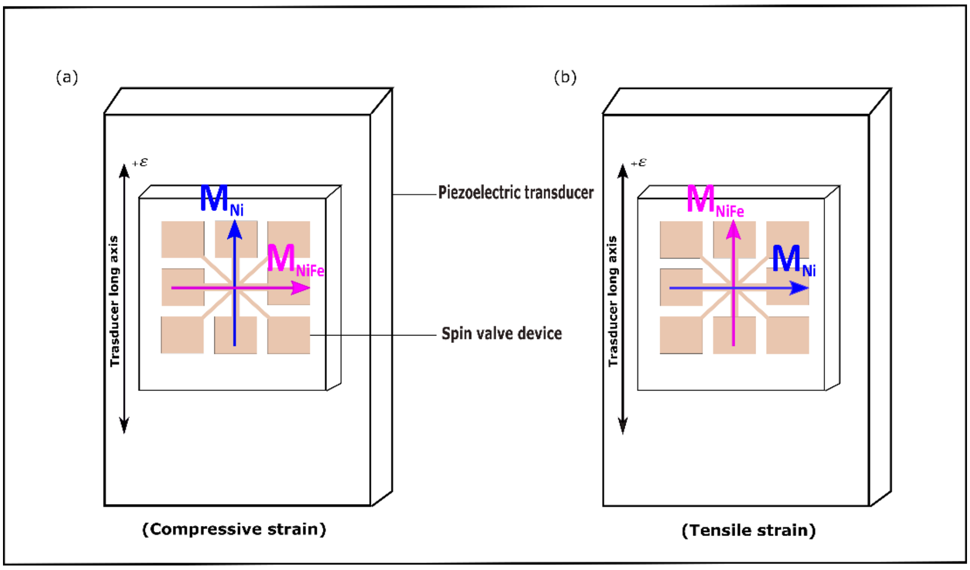

Figure 5.8: The magnetisation orientation of the easy axes of the permalloy (M_{NiFe}) and nickel (M_{Ni}) layers when applying (a) compressive strain and (b) tensile strain values to spin valve stack, with no magnetic field applied.

Starting with $-30V$ (compressive strain), comparing the R_{xy} and R_{xx} ($\Delta R/R$) curves in figure 5.9. (a) for this voltage, it can be seen that sweeping the field from the maximum value at negative field direction ($-40mT$) saturates both layers' magnetisations along the field direction, hence the $\Delta R/R$ is minimal, since the angle between their magnetisations is zero. When the magnetic field changes to the positive direction, at low positive value, the permalloy layer switches abruptly, while the nickel layer reversal shows a superposition with the permalloy peak reversal, as an indication that the nickel magnetisation starts to reverse at an early field (see the resistance curve before point (1) in $\Delta R/R$ and R_{xy} curves), which could be at low negative field since the nickel is magnetically harder in the field direction. However, by comparing R_{xy} curve and $\Delta R/R$ curve for the sweep up field, the $\Delta R/R$ curve shows a gradual increase before the zero-field (point (1)) (as an indication for the earlier reversal of the nickel layer) while R_{xy} show almost no change till the permalloy start to reverse at a very small negative field. The difference between R_{xy} and $\Delta R/R$ curves before zero-field could be ascribed to the size difference of the AMR between the permalloy and nickel layers. As shown in chapter 3 that the ΔR for the permalloy sample (S476) is equal to 0.4Ω (see figure 3.2) while it is equal to 0.05Ω (see figure 3.28) for the nickel sample (S475). Hence, in IM008 spin valve, the permalloy anisotropic magnetoresistance might show dominant behaviour compared to the nickel layer and might be the reason for the R_{xy} different behaviour (before point (1) in figure 3.9 (a)) to the $\Delta R/R$. At point (2) in figure 5.9 (a), when the permalloy switches completely with the field direction, the nickel layer is already making an angle with the negative field direction. For the nickel, it is hard to determine the magnetisation easy axis angle with respect to the field at the moment when the permalloy switches completely with the field. As the nickel prefers to align perpendicular to the field at zero field, it is difficult to say if the nickel follows the single domain model reversal; instead, it breaks into domains with the fraction pointing in the different direction of the field increases as the field increases. The $\Delta R/R$ value, in this case, is equal to 1.30%, which shows less value than other voltages measurements. As mentioned in section 1.2.4.2 that the magnetoresistance ratio depends on the orientation of adjacent magnetic layers in the spin valve following equation:

$$\frac{\Delta R(\psi)}{R} = (\frac{\Delta R}{R})_{GMR} \frac{(1-cos\psi)}{2} \tag{5.1}$$

where ψ is the angle between the orientation of the magnetisation of the two successive layers gives the maximum value when the alignment is antiparallel with $\psi = 180^{o}$. The strain affects the angle ψ as it controls the magnetisation alignment of layers and hence controls the $\Delta R/R$ value.

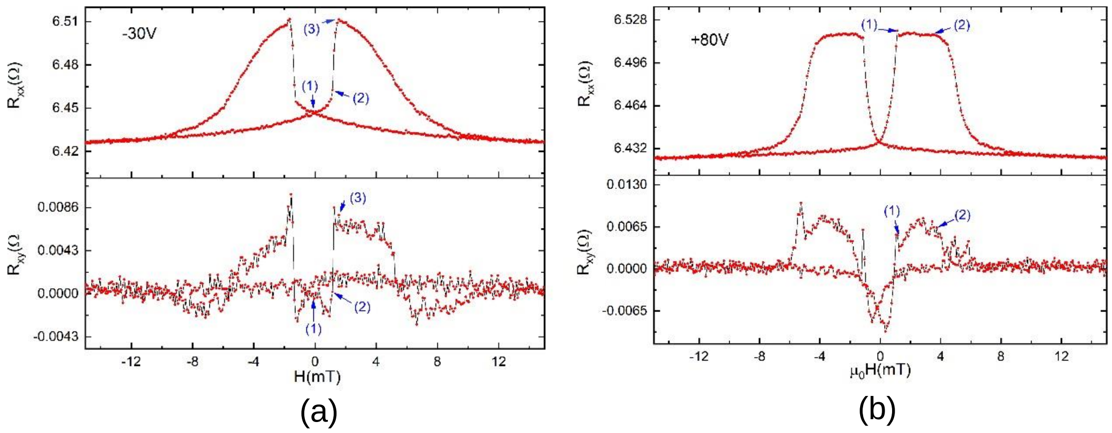

Figure 5.9: Comparison between R_{xy} and R_{xx} curves for IM008 spin valve when the field is perpendicular to the transducer $\varphi = 90^o$ with $\alpha = 90^o$ when applying different voltages to the transducer: (a) $-30V$, and (b) $+80V$. Numbers shown in figures are explained in the text.

The peaks' shape of the $\Delta R/R$ curve also depends on the strain values and types, as can be seen in figure 5.9 (a) and (b). For the compressive strain, the peaks' top of the $\Delta R/R$ is very narrow, while it becomes broader as the tensile strain increases to reach the maximum for the maximum voltage value of $+80V$. At higher compressive strain value $(-30V)$, after the magnetoresistance value reaches its maximum ($\Delta R/R_{max}$) at point (3) in figure 5.9 (a), it starts to decrease directly, indicating that the antiparallel configuration of permalloy and nickel layers does not hold for long-range of the magnetic field (spin valve stiffness). That depends on the magnetisation orientation of the two layers since the GMR value depends on the angle between the magnetisation on the successive magnetic layers. For compressive strain, when the permalloy switches to the positive direction, the nickel layer has already started to reverse, since the magnetisation easy direction is perpendicular to the field direction. The value of the $\Delta R/R$ then starts to decrease directly after the permalloy coercive field, where the curve subsequently shows a constant slope, indicating gradual changing in the nickel magnetisation direction with respect to the permalloy magnetisation, until it aligns with the permalloy orientation. The $0V$ measurement (a compressive strain of -1.16×10^{-4}) shows the same reversal as $-30V$ while the $\Delta R/R$ maximum value increased and hence the angle (ψ) between the magnetisation of the layers increases.

For the positive voltages (tensile strain), focussing in $+80V$ measurement (see R_{xy} and R_{xx} curves for this voltage in figure 5.9 (b)). In this case, the magnetisation of the permalloy prefers to lie along the long axis of the piezoelectric transducer. At the low field, the permalloy reverses gradually until it switches to align with the positive magnetic field direction. On the other hand, the nickel layer at this voltage favoured the field direction (along the short axis of the transducer). When the permalloy switches completely at point (1) in figure 5.9 (b), the nickel layer could still be lying in the opposite direction to the permalloy magnetisation. In this case, the $\Delta R/R$ value is increased to reach the value of 1.49% since the giant magnetoresistance value depends on the magnetisation orientation angle (ψ) between the two magnetic layers, which in turn depends on the value and type of strain. At high tensile strain, the stiffness of the IM008 spin valve increases, whereby the spin valve can hold the antiparallel alignment of the magnetisation of the layers for a wider range of magnetic field. The $\Delta R/R$ peaks become wider like plateaus for the tensile strain values and reach the maximum for $+80V$, whereby the antiparallel alignment configuration lasts until around $4mT$, see point (2) in figure 5.9 (b) in both curves. This can be seen from the $\Delta R/R$ curve, where no change in the value at the top (between point (1) and point (2)) indicates that the angle between the magnetisations of both layers remains unchanged for that field range. On the other hand, for $\alpha = 0^o$ (see figure 5.6 (b)), the transverse resistance for the Ni layer does not show any change after the permalloy reversal, indicating that there is no change in the Ni reversal until the magnetic field value of $4mT$. In both current directions, for the tensile strain, the $\Delta R/R$ value decreases rapidly as an indication of an abrupt switch (fast reversal) of the nickel until the field value of around $6mT$, then it completes to reverse gradually until it aligns with the permalloy magnetisations.

From the $\Delta R/R$ curves, it is clear that the magnetoresistance at the remnant state $\Delta R/R_{rem}$ (the magnetoresistance value at $H = 0mT$) changes with strain, as seen in figure 5.4 (a) and (b) for both directions ($\alpha = 90^o$ and $\alpha = 0^o$). In both measurement directions, increasing the compressive strain increases the $\Delta R/R_{rem}$ value, while it decreases with increasing the tensile strain values. Figure 5.10 shows the variation of $\Delta R/R_{rem}$ of the IM008 spin valve with the voltage values, where the $\Delta R/R_{rem}$ of values, 0.41% and 0.20% are obtained when a voltage of $-30V$ is applied to the transducer for $\alpha = 90^o$ and $\alpha = 0^o$ measurements, respectively. While for the $+80V$, it gives the minimum $\Delta R/R_{rem}$ with values of $0.24.\%$ and 0.12% for both current directions. This could be attributed mainly to the strain effect on the nickel layer, where for compressive strain values it is magnetically harder for the direction with the field. The $\Delta R/R$ curve value shows a gradual decrease at remanence due to the nickel layer early reversal. Conversely, when a tensile strain is applied, the nickel layer magnetisation prefers to lie along the field direction, and hence the $\Delta R/R$ curves show less $\Delta R/R_{rem}$ for $+80V$ for both current directions. Other studies assumed that changing the magnetisation orientation of one layer in the spin valve structure could change the remnant resistance of the $\Delta R/R$ at zero field [203, 181].

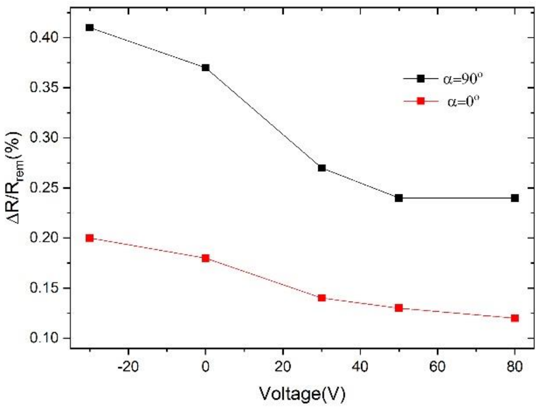

Figure 5.10: The variation of the $\Delta R/R_{rem}$ with the voltages in IM008 spin valve when the magnetic field is perpendicular to the long axis of the transducer for $\alpha = 90^o$ and $\alpha = 0^o$ configuration measurements.

5.2.1.2 Magnetic field parallel to the long axis of the transducer ($\boldsymbol{\varphi = 0^o}$).

In this measurement, the field is rotated by 90^o from the previous measurements, where the field is along the long axis of the piezoelectric transducer ($\varphi = 0^o$). Two current directions are also applied for this direction, $\alpha = 0^o$ and $\alpha = 90^o$, as can be seen in figure 5.11 (a) and (b), respectively. Figure 5.12 (a) and (b) shows the $\Delta R/R$ curves for both current directions. It can be seen that the $\Delta R/R$ values and curves changed with strain, giving the opposite effect to that obtained from the measurements when the field is perpendicular to the transducer (section 5.2.1.1). When the magnetic field is perpendicular to the current $\alpha = 90^o$, for $-30V$ (a compressive strain of -2.46×10^{-4}), the maximum $\Delta R/R$ value is 1.53%, while it decreases to 1.24% when the voltage is $+50V$ (tensile strain of $+2.17 \times 10^{-4}$) (figure 5.13 (a)). When the magnetic field is parallel to the current $\alpha = 0^o$, the maximum $\Delta R/R$ value of 1.28% is given when a voltage of $-30V$ is applied to the stressor, while the a value of 1.04% is obtained when the voltage is changed to $+50V$ (figure 5.12 (b)). The variation of the $\Delta R/R$ values with voltage and strain values are shown in figures 5.13(a) and (b). The opposite effect is observed for $\Delta R/R$ size to the measurements when the field is perpendicular to the long axis of the piezoelectric transducer (section 5.2.1). Rizwan et al. [69-70] found that $\Delta R/R$ values and curve shapes depend on the strain direction with respect to the stack magnetisation initial direction relative to the magnetic field applied during the measurements. Figure 5.14 shows a comparison between the two measurements directions when the field is perpendicular and parallel to the long axis of the transducer with the current direction is always along the long axis of the transducer.

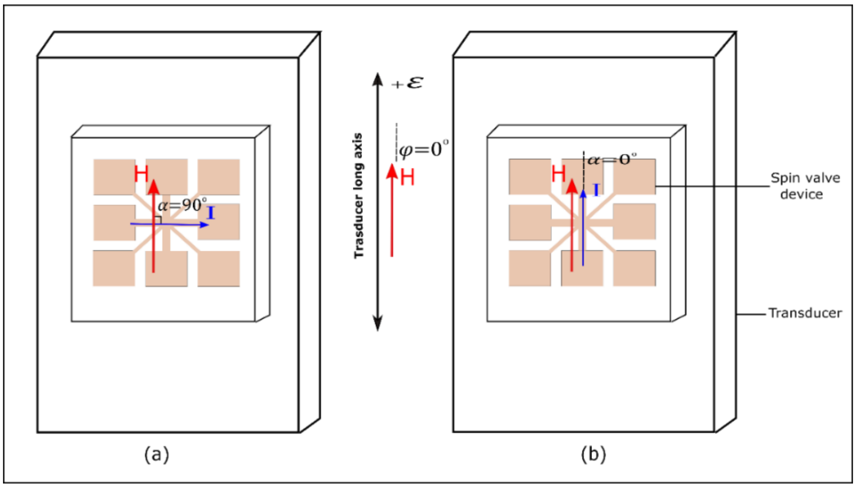

Figure 5.11: The measurements configuration when the magnetic field is parallel to the long axis of the piezoelectric transducer ($\varphi = 0^o$) for IM008 spin valve, where (a) the magnetic field is perpendicular to the current $\alpha = 90^o$, and (b) the magnetic field is parallel to the transducer $\alpha = 0^o$.

5.2.1.2.1 Strain control magnetic reversal of the permalloy layer $\varphi = 0^o$

The permalloy magnetisation easy direction rotates by 90^o from the previous position in section 5.2.2.1. The magnetisation easy axis lies along the field direction when applying a tensile strain while it is perpendicular to the field when a compressive strain is applied. The reversal of the permalloy layer in IM008 spin valve is shown by region (1) (represents the reversal feature of the permalloy in the sweep up direction) in figure 5.15 (a) for $-30V$ and $+50V$ with a hard axis reversal for $-30V$ and easy axis reversal along the field for $+50V$. Figure 5.16 shows the corresponding R_{xy} for the single-layer sample (S476) when the magnetic field is parallel to the long axis of the transducer for $\alpha = 90^o$. The magnetoresistance feature and hence the magnetic reversal of the permalloy in the single-layer sample shows consistency with the permalloy layer reversal in IM008 indicated by region (1) in figure 5.16 (a). One can assume that the reversal shows a hard magnetic axis for the compressive strain values since the strain is perpendicular to the field, while for the tensile strain, the axis along the field is magnetically easier for the permalloy magnetisation.

5.2.1.2.2 Strain control magnetic reversal of the nickel layer $\varphi = 0^o$

The nickel layer easy axis in this configuration lies along the field direction when applying compressive strain while it is perpendicular to the field when applying a tensile strain. The magnetoresistance curves related to the nickel layer reversal when the current direction is $\alpha = 90^o$, shows different reversal behaviours of the nickel by changing voltage from $-30V$ to $+50V$, as indicated by region (2) (represents the reversal feature of the nickel in the sweep up direction) in figure 5.15 (a). For $-30V$, the reversal shows fast reversal as shown by small magnetoresistance feature while it is wider and slower for $+50V$. The magnetisation directions for permalloy and nickel layers follow the same model assumed in figure 5.8 (a) and (b) when no magnetic field is applied.

(a)

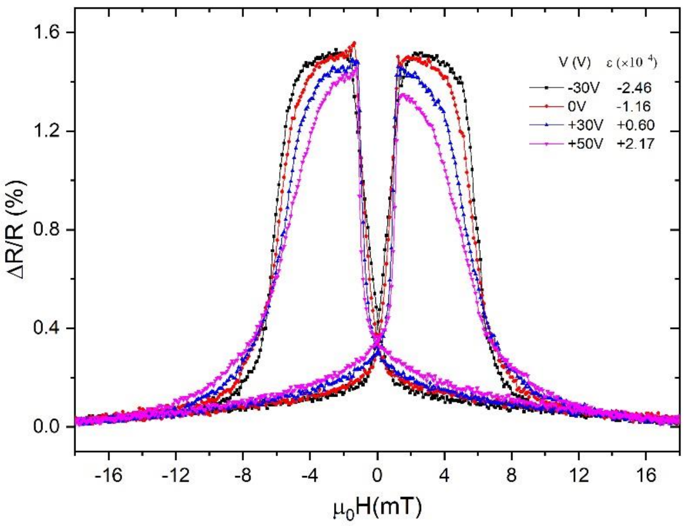

(b)

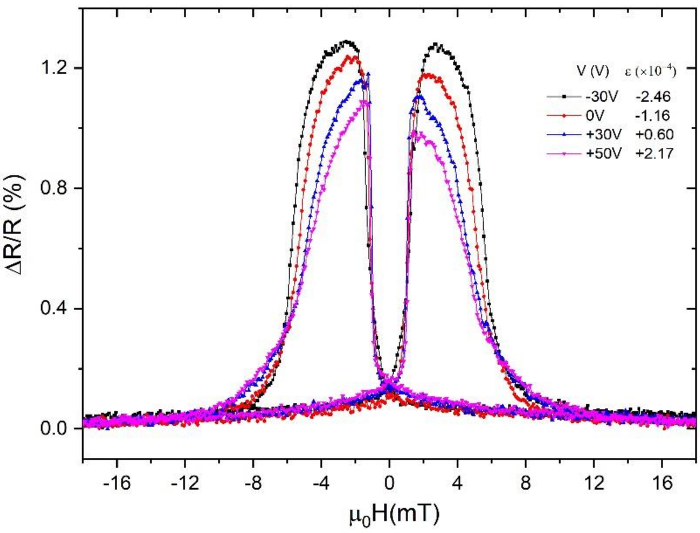

Figure 5.12: The $\Delta R/R$ curves of the IM008 spin valve when the magnetic field is parallel to the long axis of the transducer ($\varphi = 0^o$), (a) when the field makes an angle of $\alpha = 90^o$ with the current, and (b) for $\alpha = 0^o$.

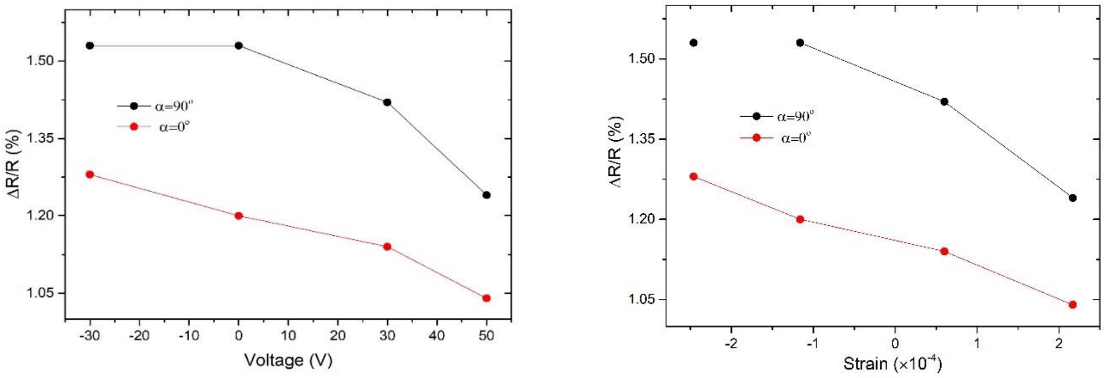

(a) (b)

Figure 5.13: The dependence of the $\Delta R/R$ values on (a) voltages applied to the transducer, and (b) the corresponding strain values when the magnetic field is parallel to the transducer ($\varphi = 0^o$) for IM008 spin valve for $\alpha = 90^o$ and $\alpha = 0^o$.

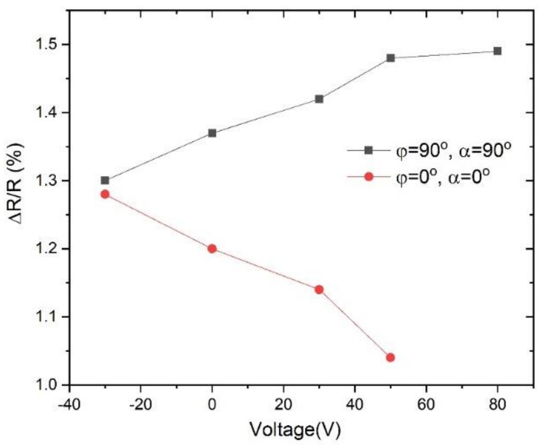

Figure 5.14: A comparison between the $\Delta R/R$ value of the IM008 spin valve when the long axis of the transducer is parallel and perpendicular to the field.

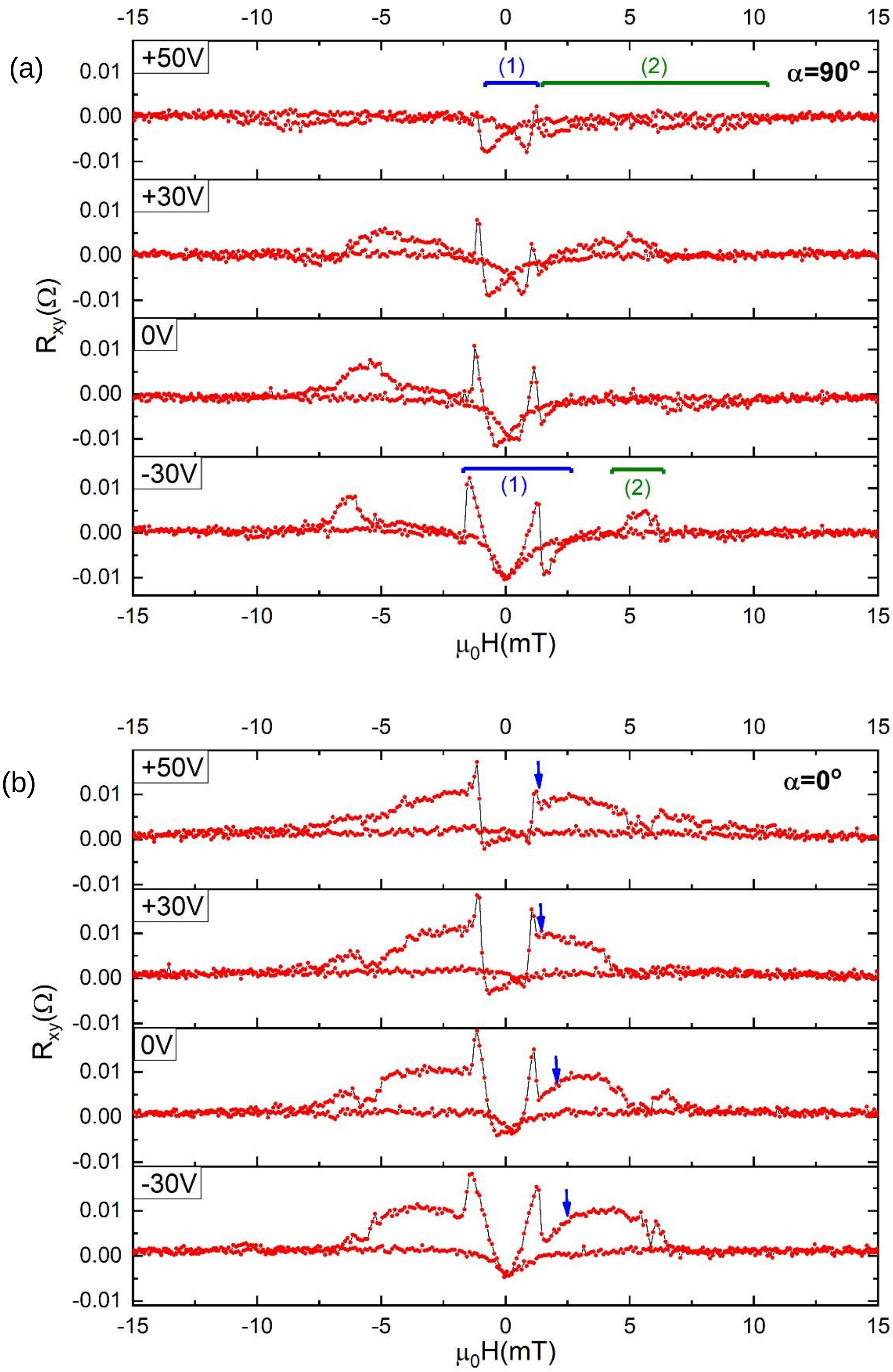

Figure 5.15: R_{xy} curves of the IM008 spin valve for the measurements when the magnetic field is parallel to the transducer ($\varphi = 0^o$) at different voltages for (a) $\alpha = 90^o$, and (b) $\alpha = 0^o$ measurements. The blue arrows in (b) indicate the $H(\Delta R/R_{max})$ points, while areas indicated by (1) and (2) in (a) represent the permalloy and nickel reversals for the sweep up measurement.

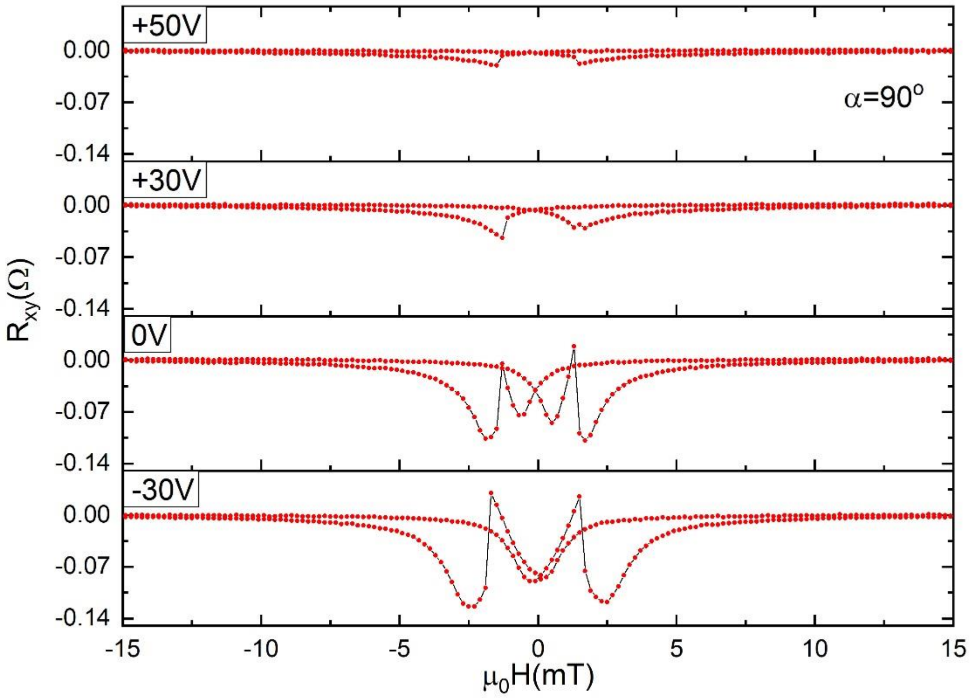

Figure 5.16: R_{xy} curves of the permalloy single layer S476 for the measurements when the magnetic field is parallel to the transducer ($\varphi = 0^o$) at different voltages for $\alpha = 90^o$. For the compressive strain values ($-30V$ and $0V$), the permalloy is magnetically harder along the field direction, while it is softer for the same direction when applying tensile strain values ($+30$ and $+50V$).

5.2.1.2.3 Strain control magnetoresistance features of IM008 spin valve ($\boldsymbol{\varphi = 0^o}$)

To understand the $\Delta R/R$ changing with the strain for this direction, the R_{xy} curves for both layers in the spin valve should be discussed along with $\Delta R/R$ curves. When a voltage of $-30V$ is applied for $\alpha = 90^o$ direction (see figure 5.15 (a)), it shows a distinct reversal of both layers, which means that after the switching of the permalloy, the nickel layer starts to reverse at a higher field (around $5mT$). In this case, the alignment of the two magnetic layers is oriented antiparallel after the permalloy switch and the $\Delta R/R$ reaches the maximum value of 1.53%. For this strain value, the peak shows more plateau-like shape, since the spin valve can hold the antiparallel alignment for a wider field range. This could be ascribed to domains nucleation of the nickel at that field range until the domains grow quickly (or might domain walls move abruptly) in the field range between $4mT$ and $8mT$, then the magnetisation completes to reverse gradually until it aligns with the permalloy layer.

When a voltage of $+50V$ (tensile strain) is applied to the transducer, the $\Delta R/R$ value decreases, as the nickel layer magnetisation starts to reverse earlier (nickel's hard axis along the field direction); hence the perfect alignment never exists in this case, which manifests as a decrease in the $\Delta R/R$ value compared to $-30V$ to reach 1.29 gives an indication that the angle (ψ) between the two layers'magnetisation is smaller than that of $+50V$. The gradual decrease in $\Delta R/R$ after $H(\Delta R/R_{max})$ point is attributed to the slow reversal of the nickel layer as the angle between the two layers decreased gradually, which might be due to the slow nucleation or rotation of the magnetic domains. The measurements when $\alpha = 0^o$ show a more complicated reversal, with the blue arrows in all graphs (see figure 5.15 (b)) showing the corresponding point of $H\left(\Delta R/R_{max}\right)$). For all voltages, the reversal of both layers is superimposed with each other, and that could be another reason for smaller $\Delta R/R$ in this direction.

5.2.1.3 Magnetic field $+45^{\mathbf{o}}$ with respect to the long axis of the transducer ($\boldsymbol{\varphi} = \mathbf{45^o}$)

In this measurement's configuration, the magnetic field is aligned along $+45^o$ to the long axis of the piezoelectric transducer ($\varphi = 45^o$). Here the magnetic field is rotated by $+45^o$ from the perpendicular direction, whereby the strain (compressive or tensile) is competing with the magnetic field since the strain always makes angles of $+45^o$ or -45^o with the field, depending on the strain type. The main aim of this measurement is to check how the $\Delta R/R$ values and curves will be effected with the magnetic field along $+45^o$ or -45^o to the tensile or compressive strain, respectively. The measurements were performed for different electric current directions ($\alpha = 0^o, +45^o, -45^o$, and 90^o). The measurements of $\alpha = +45^o$ with the configuration shown in figure 5.17 (a) is discussed in detail. The $\Delta R/R$ curves for $\alpha = +45^o$ measurements at different voltages are shown in figure 5.17 (b). It is clear that the $\Delta R/R$ curves and size change with changing voltage values (strain). The minimum value of $\Delta R/R$ with a value of 0.97%, acquired when a voltage of $-30V$ (compressive strain) is applied to the transducer, while the maximum value of 1.27% is obtained when a voltage of $+30V$ (tensile strain) is applied to the transducer. In the previous measurements (when the field is perpendicular and parallel to the long axis of the piezoelectric transducer), the values of the $\Delta R/R$ have the same tendency of decreasing or increasing in the whole range of the voltages measurements. Interestingly, in this configuration, when a voltage of $+50V$ is applied, the $\Delta R/R$ size is decreased to 1.19%.

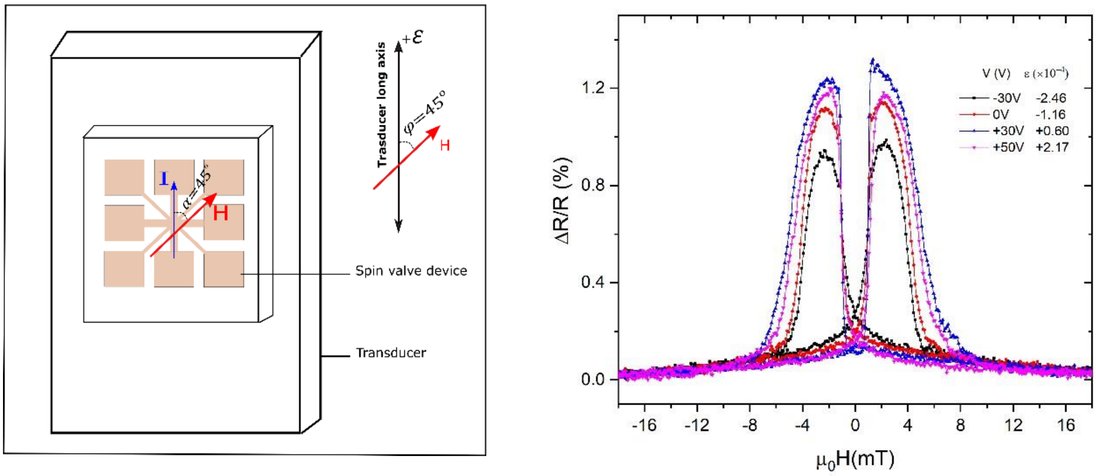

(a) (b)

Figure 5.17: (a) The configuration of the IM008 for the measurement when the magnetic field is making an angle of 45^o to the long axis of the piezoelectric transducer and $\alpha = +45^o$. (b) the $\Delta R/R$ curves at different voltages for IM008 spin valve for this configuration measurement.

5.2.1.3.1 Strain control magnetic reversal of permalloy and nickel layers $\boldsymbol{\alpha = +45^o}$

The transverse magnetoresistance measurements for the IM008 spin valve for this measurement at different voltages are shown in figure 5.18. The magnetoresistance features of the spin valve show changes with tuning strain as an indication of the change in the magnetisation reversal of the spin valve layers. The first reversal indicated by region (1) (represents the reversal feature of the permalloy in the sweep up direction) shows very few changes which related to the permalloy reversal, while nickel features indicated by region (2) show the main changes in the measurement. To understand the permalloy layer reversal, figure 5.19 (a) and (b) show the R_{xx} and R_{xy} of the permalloy single layer sample S476 (discussed in section 3.2.2.4) with the same configuration measurements of IM008 spin valve. The longitudinal resistance measurement in 5.19 (a) shows that the resistance curves direction changes when the strain changes from compressive to tensile strain. On the other hand, the peaks in transverse resistance curves of sample S476 (see figure 5.19 (b)) show a consistency with the peaks shown in the transverse resistance at the low field for the IM008 spin valve (see figure 5.18, region (1)). As discussed in section 3.2.2.4, for this measurement configuration, the change in transverse resistance reversal direction is ascribed to the changing of magnetisation easy axis direction when changing the strain from compressive to tensile strain values. The reversal for measurements when the voltage is equal to $-30V$ (the maximum value of the compressive strain) and $+50$ (the maximum value of the tensile strain) show that greater magnetic field values are needed for saturation since the magnetisation of the permalloy favours the long and short axes of the piezoelectric transducer, $+45^o$ or -45^o to the field direction for these voltages. One can conclude that the permalloy in IM008 shows the same behaviour as permalloy sample S476 for this direction measurement, and hence it shows different reversal directions for different strain types. For the nickel layer, from the R_{xy} curves of $-30V$ and $+50V$ measurements as indicated by region (2) (represents the reversal feature of the nickel in the sweep up direction) in figure 5.18, the nickel reversal shows two different directions reversal as shown by the magnetoresistance features changing direction when the strain changes from $-30V$ to $+50V$. Hence, One can assume that when a compressive strain applied, the magnetisation favours lying along the long axis of the transducer, while for the tensile strain values, it favours the short axis of the transducer. In this case, the two layers have different direction reversals, whereby both easy axes of these layers are $+45^o$ or -45^o from the field direction.

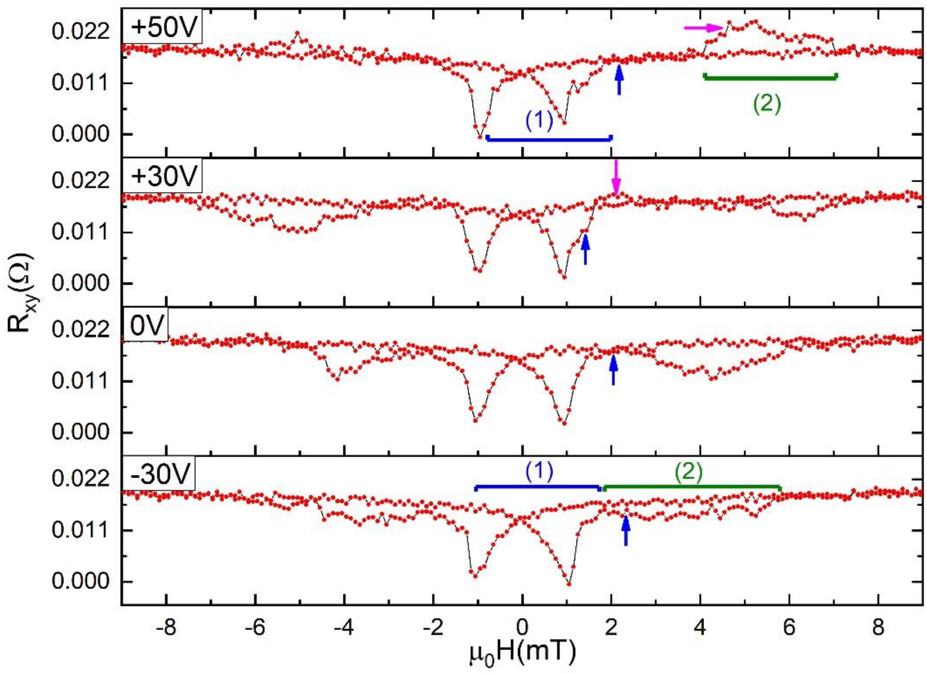

Figure 5.18: The transverse magnetoresistance curves $R_{xy}$of the IM008 spin valve for the measurements when the magnetic field is making an angle of 45^o to the long axis of the transducer at different voltages for $\alpha = +45^o$ measurements. The blue arrows show the corresponding point for $H(\Delta R/R_{max})$, showing that the field for $+30V$ is small compared to other voltages, and the $\Delta R/R_{max}$ for this voltage is obtained before the permalloy reversal is completed. The pink arrows show the different behaviour of the nickel reversal for tensile strain values. Regions indicated by (1) and (2) represent the permalloy and nickel reversals for the sweep up measurement.

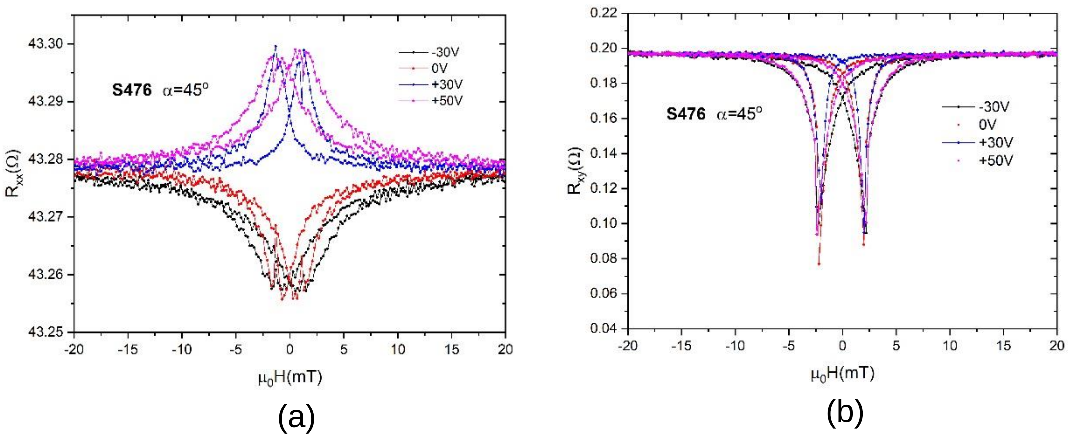

Figure 5.19: (a) R_{xx} and (b) R_{xy} curves of the permalloy single layer sample S476 for the measurements when the magnetic field is 45^o to the transducer at different voltages for $\alpha = +45^o$. The R_{xx} shows that the reversal direction of the permalloy changes when the strain changes from compressive values to tensile values, while the R_{xy} features show the same features shown in figure 5.18 for IM008 spin valve R_{xy} curves at low field values.

5.2.1.3.2 Strain control magnetoresistance features of IM008 spin valve $\varphi = +45^o$

The reversal of the whole spin valve at $-30V$ shows two superimposed reversals of the permalloy and nickel as can be seen that by the blue arrows at $H(\Delta R/R_{max})$ in figure 5.18. This could be ascribed to the hard reversal of the permalloy, as can be seen in the longitudinal resistance of the permalloy single layer sample in figure 5.19 (a), which shows a very hard reversal that needs more field to saturate. On the other hand, the nickel layer has hard magnetisation reversal in the opposite direction; hence their reversals are never in perfect antiparallel alignment, and the $\Delta R/R$ value is small and equal to 0.97 as the angle between their magnetisations is less than 180^o. For the $0V$, both layers have less hard direction, as can be seen for permalloy single film data (S476), and the nickel layer reversal shows late reversal compared to $-30V$ (see the R_{xy} feature after the blue arrow); hence the orientation angle between the two layers is increased, and the $\Delta R/R$ value increased for this voltage to reach 1.13%. For the tensile strain ($+30V$), the permalloy changes the reversal direction, as shown by the data for the single-layer sample, see figure 5.19 (a). The nickel layer might also change the reversal direction, and the resistance curve shows a different R_{xy} curve feature direction for the nickel layer peaks, as shown by a pink arrow in figure 5.18. This could be attributed to the changing direction of the nickel's easy axis, and hence the reversal direction. The $\Delta R/R$ value is increased to reach the value of 1.27%, as a manifestation of the increased angle between the magnetisations of the two layers for this voltage. In this case, the $\Delta R/R_{max}$ point occurs at less magnetic field $H(\Delta R/R_{max})$ compared to all other voltages (see the blue arrow at the permalloy peak in $\Delta R/R$ curve), even before the permalloy completes the reversal, which might be related to the complicated reversal of the nickel layer at this voltage. For $+50V$, the transverse resistance shows one clear peak for the nickel reversal with a different shape (shown by a pink arrow) compared to other voltages, and the $\Delta R/R$ decreases for this voltage to reach 1.19%. For the tensile strain (both voltages $+30V$ and $+50V$), it is difficult to understand the reversal of the nickel layer, and it could be attributed to more complicated reversal related to domain nucleation with complicated growth direction, whereby it is more challenging to determine the direction of the reversal of the magnetisation from just the spin valve transverse resistance measurement data. Another reason for this could be attributed to intrinsic anisotropies that could appear in the spin valve layers with a certain angle that raised at any stage of the sample preparation (growth, fabrication, and mounting the sample onto the piezoelectric transducer). These anisotropies could compete with the induced magnetoelastic anisotropy in the spin valve by the transducer and with the magnetic field. Furthermore, magnetic domain wall pinning could manipulate the propagation of the domains in a certain direction [204].

5.2.1.3.3 Investigation of the strain effect at different current directions $\boldsymbol{\varphi = +45^o}$

Other measurements for this direction when the magnetic field is $+45^o$ to the transducer were conducted, by changing the current direction along $\alpha = 0^o$, $-45^o \text{and } 90^o$ with respect to the field. Figure 5.20 (a) and (b) show a comparison of how the $\Delta R/R$ values change with the voltages and strain values between all current directions when the field is making $+45^o$ to the transducer. For $\alpha = 0^o \text{and } 90^o$, the curves show more voltage points measurements performed for these directions. In all measurements, the maximum value of the $\Delta R/R$ is when a voltage of $+30V$ is applied to the transducer, followed by a decrease for $+40V$ and $+50V$. The $\Delta R/R$ size changes are very small for all tensile strains compared to the change between the compressive strain values as an indication of the angle between the magnetisations of the layers is bigger for the compressive strain rather than tensile values. The tensile strain shows difficult behaviour to follow from these measurements, and it needs more investigation techniques like FMR or XMCD to have a clear idea about the nickel reversal under different strain values and types. Figure 5.20 (a) and (b) also proves that the GMR ratio is always larger for $\alpha = 90^o$ than for $\alpha = -45^o, 0^o$ and $+45^o$. This is attributed to the angular dependence of the mean free path between the spin up and down electrons in the current directions, as discussed in chapter 4.

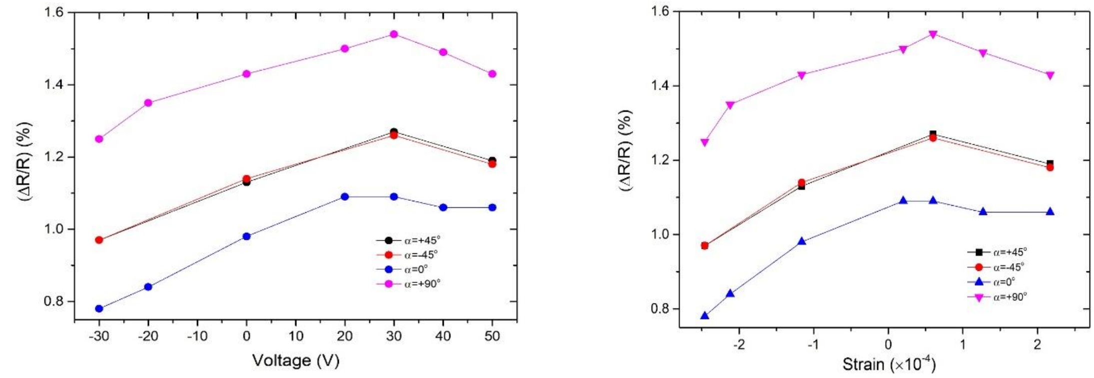

(a) (b)

Figure 5.20: The dependence of the $\Delta R/R$ values on the (a) voltages applied to the transducer and (b) the corresponding strain values when the magnetic field is making an angle of 45^o to the piezoelectric transducer for IM008 spin valve with the current direction along $\alpha = 0^o, -45^o, +45^o, \text{and } 90^o$.

5.2.2 IM009 spin valve

In this spin valve, the order of magnetic layers is exchanged, with the nickel layer on the bottom of the spin valve with a structure of (GaAs/Ta/Ni/Cu/NiFe/Ta), as shown previously in figure 4.1 (b). Figure 5.21 shows the relation between the voltage applied to the transducer and the strain-induced into the IM009 sample. It shows a different curve than that shown previously for S476 and IM008. The curve shows no hysteresis between the two sweeps measurements, which could be related to the strain relaxation on the epoxy layer. The values of the strain are almost in the same range of the strain applied in the IM008 sample. As the growth sequence is different in both spin valves, which could have different impacts and this could be ascribed to different reasons, including the intrinsic uniaxial strain value induced in the sample during the cure of the device process affecting the value of the free energy of the device. Other reasons could be related to the growth and interface in each sample. Fabrication process might have some effect on introducing an intrinsic uniaxial anisotropy in the spin valve devices. Hence, the intrinsic strain competes differently in each spin valves with the magnetoelastic anisotropy induced by the transducer. The same Poisson ratio is used for this sample, as discussed in section 5.2.1 for the IM008 spin valve since they both have the same layers.

As discussed in chapter 4, at $0V$ magnetic reversal of IM008 and IM009 spin valves is quite different since each layer of the nickel and permalloy has different coercivities and magnetic reversals. Hence, when applying strain in this chapter, the response of each layer could affect the whole magnetic reversal of each spin valve differently. For instance, the variation of $\Delta R/R$ in IM009 spin valve is greater than that in IM008 spin valve when the voltage changed between $-30V$ and $+50V$. Furthermore, the shapes of the $\Delta R/R$ curves and coercivities of the layers are changing differently in the two spin valves. In the next sections, the strain effect will be studied in two directions of the field with respect to the transducer $\varphi = 0^{o}$ and $\varphi = 90^{o}$ where the compressive and tensile strain will be discussed in detail.

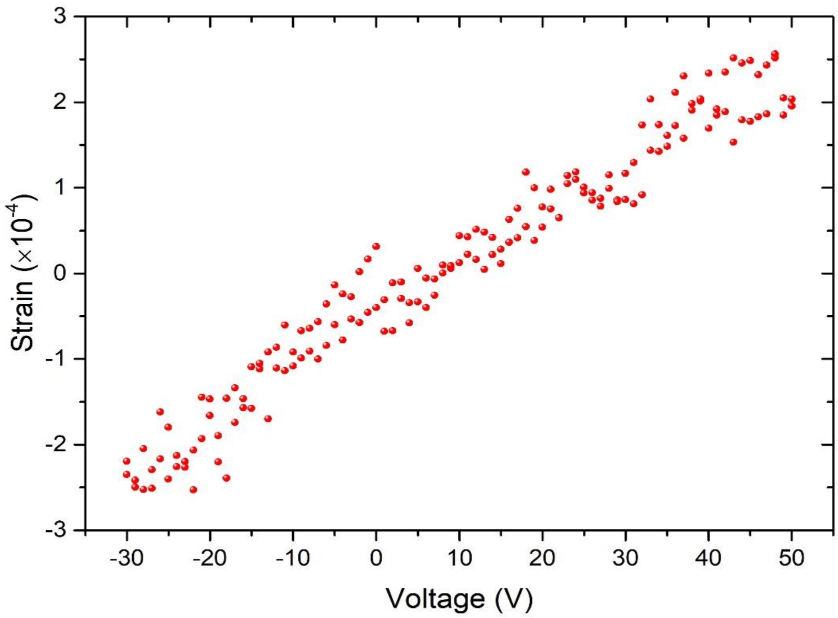

Figure 5.21: Hysteric strain-voltage loop for IM009 spin valve. The voltage bias across the piezoelectric transducer swept up and down between $-30V$ and $+50V$. The strain was extracted from the longitudinal resistance Rxx, as discussed in section 2.2.3. The zero strain value for the sweep up direction was acquired by applying a voltage of $+8V$ through the transducer.

5.2.2.1 Magnetic field perpendicular to the long axis of the transducer ($\boldsymbol{\varphi = 90^o}$)

The magnetic field is applied perpendicular to the long axis of the piezoelectric transducer ($\varphi = 90^{\boldsymbol{o}}$), and the electric current is applied along different directions with respect to the magnetic field ($\alpha = 90^o$ and 0^o), with the same configuration in section 5.2.1 (figure 5.3 (a) and (b)). The $\Delta R/R$ curves, are shown in figure 5.22, where (a) and (b) are the measurements for the configuration of $\alpha = 90^o$ and 0^o, respectively. For these measurements, more voltage values were applied for IM009, reflected in more points in the graphs. As discussed in chapter 4, the $\Delta R/R$ curves of IM009 are different from those of IM008 at $0V$. Where IM009 have narrower peaks and different reversal behaviour for the permalloy and nickel since they have different interface layers orders. Figure 5.23 (a) and (b) show the change in $\Delta R/R$ values with respect to the voltages and strain values in both magnetic field directions with respect to the current $\alpha = 90^o$ and $\alpha = 0^o$. When the field is perpendicular to the current ($\alpha = 90^o$), the $\Delta R/R$ values change with tuning voltages through the transducer, giving the maximum value of 1.85% when the voltage is equal to $+50V$ (a tensile strain of 2.04×10^{-4}) and a minimum value of 1.32% when the voltage is $-30V$ (a compressive strain of -2.35×10^{-4}), with very close $\Delta R/R$ values for other compressive strain values. On the other hand, for the parallel direction ($\alpha = 0^o$), the maximum value is equal to 1.40% for $+50V$ measurement, and minimum for $-20V$ (a compressive strain of -1.69×10^{-4}), with a value of 0.77%. It can be seen that the $\Delta R/R$ values for $\alpha = 90^o$are always larger than those for $\alpha = 0^o$, as mentioned previously for IM008 spin valve. In general, all compressive strain values give similarly $\Delta R/R$ values, while tensile strain values have larger variations. This spin valve has a larger $\Delta R/R$ ratio values than that in IM008 even with less voltage, where for $+80V$, the $\Delta R/R$ value is 1.49% for IM008, and 1.85% for IM009 when applying less voltage ($+50V$) for the same measurement direction ($\varphi = 90^o,$ and $\alpha = 90^o$).

The tensile strain has broader peak tops compared to the compressive curves. Furthermore, for the compressive strain values, the $\Delta R/R$ curve shows high remnant resistance values at zero field ($\Delta R/R_{rem}$) in both current directions, as can be seen clearly in figure 5.22 (a) and (b) at $H = 0mT$ as indicated by the pink arrow. Figure 5.24 (a) shows the relation between $\Delta R/R_{rem}$ and voltages in both current directions. The maximum value of 0.72% is given for $-30V$ (compressive strain), and the minimum value of 0.26% is for $+50V$ (tensile strain) for the measurement direction $\alpha = 90^o$. One of the features affected by tuning the strain in IM009 spin valve is $H(\Delta R/R_{max})$, which is equal to $1.90mT$ when a voltage of $+50V$ is applied, while it is minimum with a value of $1.40mT$ when a voltage of $-30V$ is applied to the actuator for $\alpha = 90^o$ measurement. Figure 5.24 (b) shows the relationship between the $H(\Delta R/R_{max})$ and the voltage applied to the transducer.

(a)

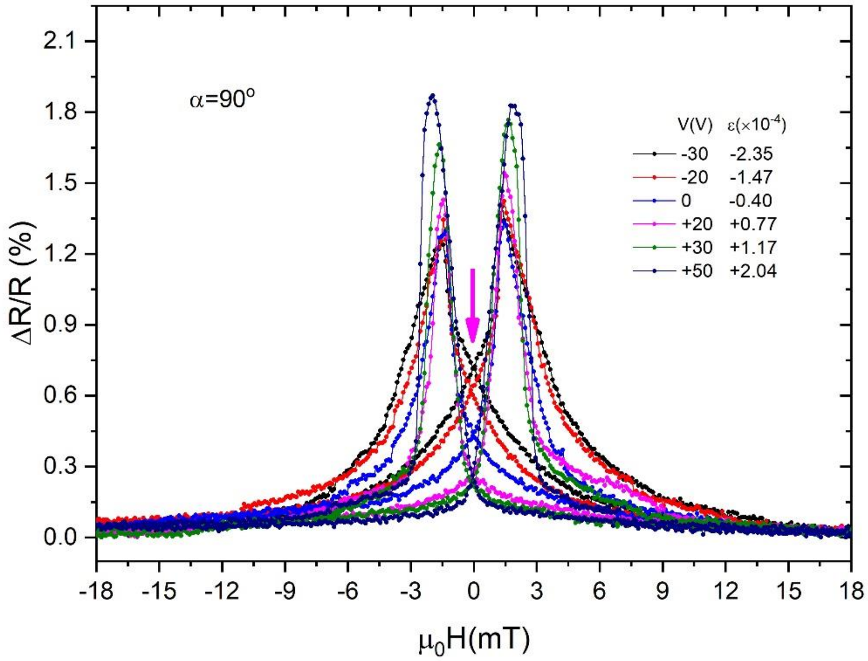

(b)

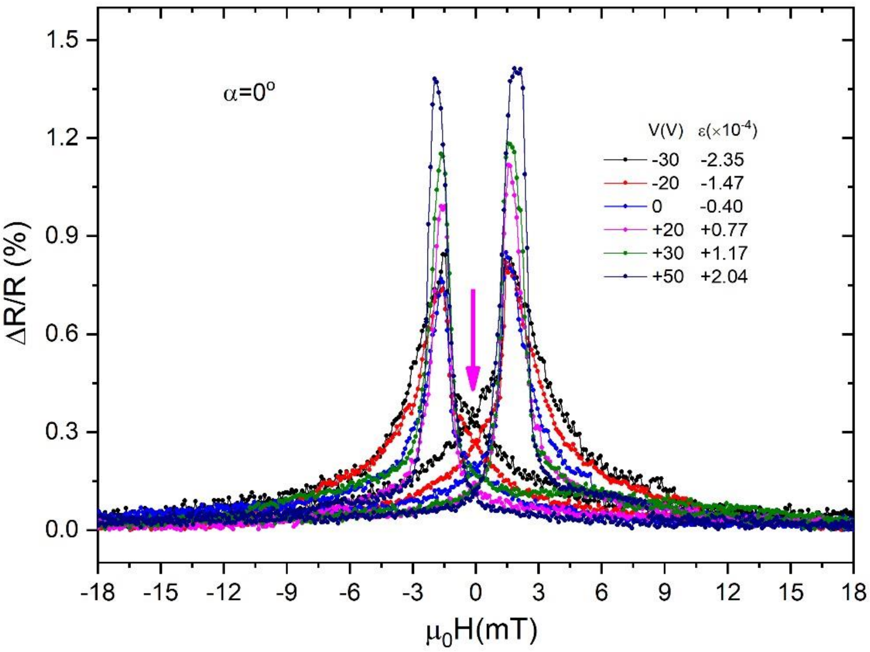

Figure 5.22: The $\Delta R/R$ curves of the IM009 spin valve when the magnetic field is perpendicular to the long axis of the transducer ($\varphi = 90^o$), (a) when the field makes an angle of $\alpha = 90^o$with the current, (b) for $\alpha = 0^o$. The pink arrows represent $\Delta R/R_{rem}$ point in both figures.

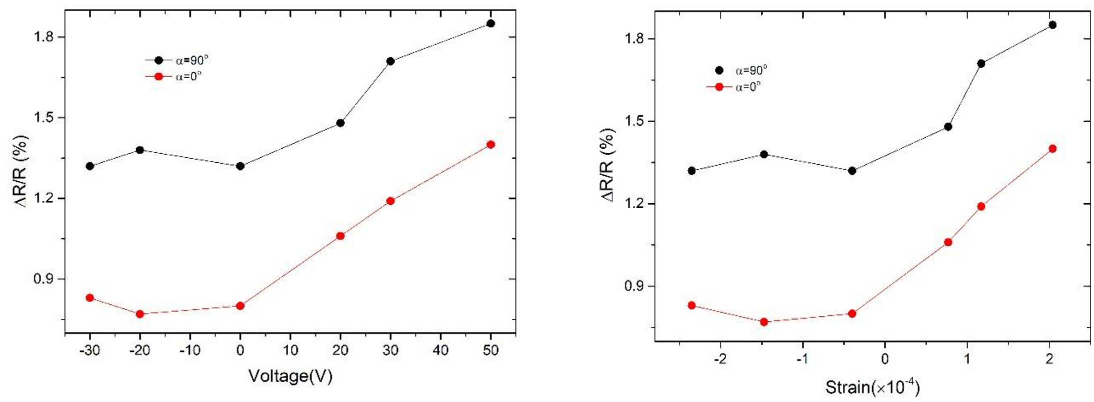

(a) (b)

Figure 5.23: The dependence of the $\Delta R/R$ value on the (a) voltages applied to the transducer and (b) the corresponding strain values when the magnetic field is perpendicular to the long axis of the piezoelectric transducer ($\varphi = 90^o$) for IM009 spin valve for $\alpha = 90^o$ and 0^o measurements.

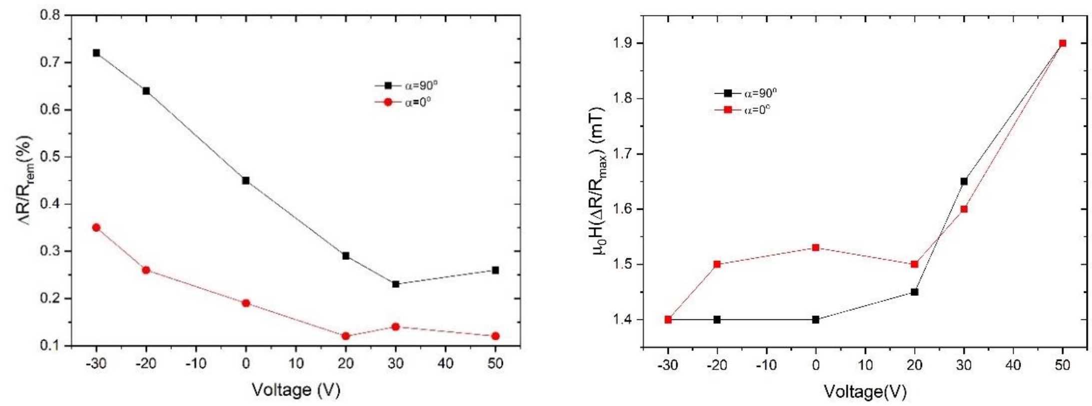

(a) (b)

Figure 5.24: The variation of the (a) $\Delta R/R_{rem}$ and (b) $H(\Delta R/R_{max})$ with the voltages in IM009 spin valve when the magnetic field is perpendicular to the long axis of the transducer ($\varphi = 90^o$) for $\alpha = 90^o$ and $\alpha = 0^o$.

5.2.2.1.1 Compressive strain effect on magnetoresistance features $\varphi = 90^o$

In general, for this sample, the R_{xy} shows complicated reversal for both layers. As discussed in chapter 4, from the magnetisation measurement, the permalloy moments switch before the nickel layer moments. In magnetoresistance measurements, the peaks are different than those of IM008 spin valve, but the trends observed when applying strain are similar to IM008. From figure 5.25, the blue arrows represent the $H(\Delta R/R_{max})$ point for all voltages and hence one can assume that the reversal peaks after that is related to nickel layer while the one before is for the permalloy for the sweep up direction measurement. The features related to the nickel layer became narrower and sharper as the voltage changed from $-30V$ to $+50V$ while that for the permalloy become broader with the same voltages change. Hence, for the permalloy, it shows a hard magnetic direction along field direction when applying a tensile strain while it is easier along the field direction when a compressive strain is applied to the spin valve. In contrast, nickel show hard magnetisation direction along the field direction when applying a compressive strain, while applying a tensile strain makes the nickel magnetisation easier along the field.

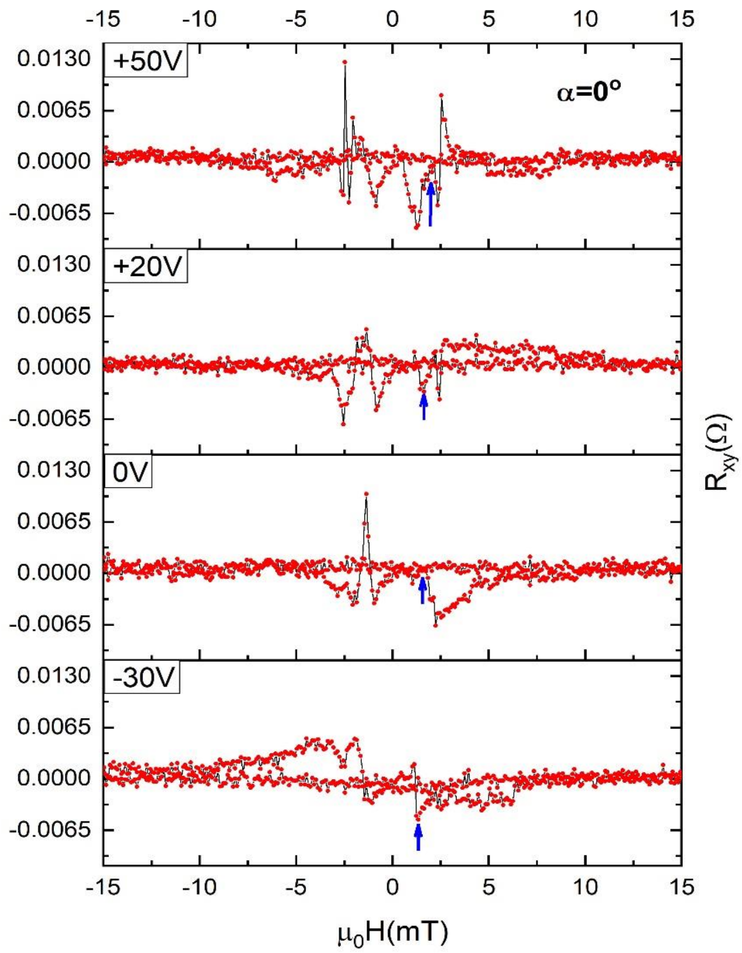

Figure 5.25: The transverse magnetoresistance curves R_{xy} for the IM009 spin valve for the measurements when the magnetic field is perpendicular to the long axis of the transducer ($\varphi = 90^o$) for $\alpha = 0^o$ measurements at different voltages. The blue arrows show the $H(\Delta R/R_{max})$ point for all measurement.

For verification, certain voltages are compared to investigate the difference between each voltage measurement. The R_{xx} and R_{xy} curves when a voltage of $-30V$ is applied to the transducer are shown in figure 5.26 (a) for $\alpha = 0^o$. It can be seen that the transverse resistance shows an abrupt switch at $1.15mT$, which is related to the permalloy layer. The small blue arrows represent the points of $H(\Delta R/R_{max})$ in R_{xx} curve and the corresponding field point in R_{xy} at $1.40mT$. The permalloy reversal shows complicated peaks, and it is difficult to determine the switching field to compare with the single-layer sample S476, while for the nickel, a broad slow reversal can be seen after the blue arrow. As the magnetic field value exceeds the $H(\Delta R/R_{max})$, the R_{xx} decreases gradually with almost constant slope curve until $5mT$, and then changes to exhibit more slow reversal until it aligns with permalloy magnetisation at around $10mT$. This gradual decrease in $\Delta R/R$ curve means that the angle between the permalloy and nickel magnetisation decreases gradually. Consequently, it can be concluded that at this voltage ($-30V$), the magnetisation of permalloy is easier along the field direction, while it is magnetically harder for the nickel layer along that direction. The IM009 sample follows the same model assumed for magnetisation orientation of the nickel and permalloy for IM008 sample when no magnetic field is applied, as shown in figure 5.8 (a) and (b) for the compressive and tensile strain values, respectively. As shown by the transverse magnetoresistance, it is difficult to distinguish between the permalloy and nickel layer reversal where both are superimposed, particularly at lower field values. The smaller $\Delta R/R$ value of 0.83% at this voltage could be attributed to the early reversal of the nickel magnetisation, which already starts to reverse and make an angle with the negative direction of the field when the permalloy is switched to the positive direction of the field. As discussed for the IM008 spin valve sample, that the nickel AMR is very small compared to the AMR of the permalloy and hence the magnetoresistance curve R_{xy} is dominated by the permalloy reversal.

The gradual increase of the $\Delta R/R$ curve before $H(\Delta R/R_{max})$ point and high remnant resistance of 0.35% for this voltage could be ascribed to the early reversal of the nickel's magnetisation until the $\Delta R/R$ value jumped abruptly to the $\Delta R/R_{max}$ due to the abrupt switch of the permalloy magnetisation as mentioned before at $1.15mT$. Almost the same $\Delta R/R$ values and curve shapes are shown for $-20V$ and $0V$ measurements as for $-30V$ measurement, with a decrease in remnant resistance $\Delta R/R_{rem}$ where the nickel becomes less magnetically harder in the field direction since the compressive strain is decreasing.

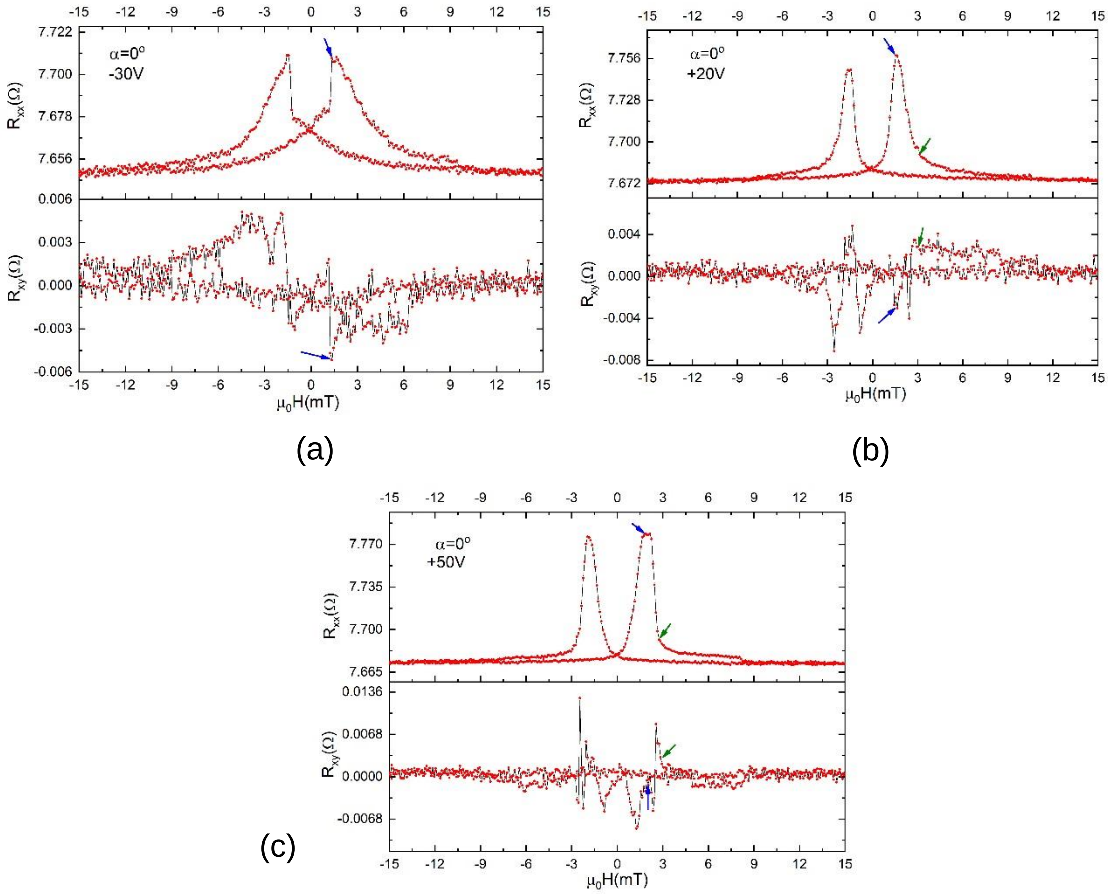

Figure 5.26: Comparison between R_{xy} and R_{xx} curves for IM009 spin valve when the field is perpendicular to the magnetic field ($\varphi = 90^o$), with the configuration of $\alpha = 0^o$ measurements applying different voltages to the transducer (a) $-30V$, (b) $+20V$, (c) $+50V$. The blue arrows show the $H(\Delta R/R_{max})$, while the green arrows indicate the end of abrupt nickel switch.

5.2.2.1.2 Tensile strain effect on magnetoresistance features $\varphi = 90^o$

In contrast to the previous measurement for the compressive strain, the tensile strain shows an opposite effect to that measurement where both layers magnetisation easy axis changed by 90^o from the previous position. For instance, the resistance curves for the $+20V$ (smallest tensile strain measurement with a value of 0.77×10^{-4} is shown in figure 5.23 (b). In this voltage, the reversal of both magnetic layers is changed, since the direction of the strain is changed, showing that the reversal of the permalloy becomes clearer, as can be seen in the first peak after the field changing direction for the sweep up measurement at a lower field in the transverse measurements. The $H(\Delta R/R_{max})$ is equal to $1.55mT$, as indicated in the longitudinal and transverse resistance by the blue arrow. The corresponding point in the R_{xy} curve shows that the peaks of the two layers are superimposed or could be due to the permalloy is not saturated yet, and hence for both layers, magnetisation still cannot be perfectly antiparallel aligned at the switching field of the permalloy. The $\Delta R/R$ value is equal to 1.06%, which is greater than that of $-30V$, hence that indicating the angle (ψ) between the magnetisations of the two layers is bigger than that of $-30V$ measurement at $H(\Delta R/R_{max})$. The $\Delta R/R$ shows small remanence in this case equal to 0.12%, as the nickel layer magnetisation prefers to lie along the short axis (field direction). The gradual increase in the $\Delta R/R$ before $H(\Delta R/R_{max})$ could be related to the permalloy, since it becomes harder in the direction of the field and does not show any abrupt increase in the $\Delta R/R$ value as the $-30V$ curve. As indicated by the region between the blue and green arrows in the transverse resistance, the reversal of the nickel shows an abrupt switch in that field range and the $\Delta R/R$ curve decreases rapidly at the same field range between these two arrows until it starts to reverse gradually after the green arrow ($\sim 3.15mT$). This slow reversal could be attributed to domain nucleation followed by domain wall movement, or it could be related to the slow rotation of domains.

For the measurements when the voltage is equal to $+50V$, the R_{xy} and R_{xx} are shown in figure 5.26 (c). In this voltage measurement, the permalloy reversal is distinguishable from the nickel layer reversal, and it shows a gradual reverse for the permalloy with no abrupt switch, see the reversal before the blue arrow. As mentioned in chapter 3, the permalloy sample S476 reversal is very hard in this direction, with a tensile strain perpendicular to the field, exhibiting a prolonged reversal. The $H\left(\Delta R/R_{max}\right)$ is equal to $1.90mT$, as shown in the R_{xx} curve by the blue arrow and the corresponding point is shown with the same arrow in the R_{xy} curve after the reversal of the permalloy magnetisation. The nickel layer reversal starts after the permalloy completed the reversal and saturated with the positive field, which means that the magnetisation alignment angle between the two-layers is approximately 180^o, manifest as an increase in the $\Delta R/R$ value to reach the value of 1.40% (note that GMR value in $\alpha = 0^o$ direction is less than that for $\alpha = 90^o$). The nickel layer starts to reverse abruptly, since its magnetisation easy axis in the same direction of the magnetic field, see the peaks between the green and blue arrows. The $\Delta R/R$ curve (R_{xx}) shows a significant decrease in the field range between the $H(\Delta R/R_{max})$ and $2.75mT$ (also shown by the green arrows in both curves), and this abrupt switch is the reason behind narrower peaks compared to those for the IM008 sample. Then the nickel completes a slow reversal, which could be due to some nucleation of the domains followed by domains expansion and domain walls movement until it aligns with the permalloy magnetisation. The $H(\Delta R/R_{max})$ changing with the strain in both current direction is related to the permalloy switching field, which increases as the magnetisation becomes harder along the field direction to reach the maximum of $1.90mT$ for $+50V$ as shown in figure 5.26. This is consistent with the single-layer permalloy S476 sample result discussed in section 3.2.2.3, where the permalloy switching field changes from $0.8mT$ to $0.14mT$ when changing the voltages from $-30V$ to $+50V$, see figure 3.15. Liu et al. [66] and Cavaco et al. [205] demonstrated that the strain modulates the coercivity of the free layer in a spin valve system when the strain changes the magnetisation orientation, to reach the maximum value of the coercivity for the harder axis along the field direction.

Figure 5.27 (a) shows a comparison between the change in the $\Delta R/R$ values for IM008 and IM009 spin valves with the voltages when the magnetic field is perpendicular to the long axis of the transducer ($\varphi = 90^o$) and $\alpha = 90^o$. It shows that the change in IM009 spin valve magnetoresistance is more than that for IM008, indicating that strain affects the magnetisation orientation in IM009 more than that in IM008. On the other hand, figure 5.27 (b) shows the strain effect on the $\Delta R/R_{rem}$ in the direction of the same measurement when the field is perpendicular to the transducer for IM008 and IM009 spin valves. It shows the $\Delta R/R_{rem}$ in IM009 responds significantly to the strain, changing by 300% when changing the voltage from $-30V$ to $+50V$, while it changes by 100% when changes from $-30V$ to $+80V$ for IM008. In general, the difference between the two spin valves could be related to the order of the layers. In IM009 the nickel grew at the bottom of the spin valve, which means that the nickel layer is close to the piezoelectric transducer and could show more response to the strain than the permalloy layer as the effect in IM009 magnetoresistance features are more than that in IM008. As discussed previously from the SQUID measurement, at $0V$, the magnetisation hysteresis loops show different reversals for both spin valves and that ascribed to the different interfaces for each layer in both spin valves. Hence, the interface could play different roles when applying strain in magnetotransport measurement.

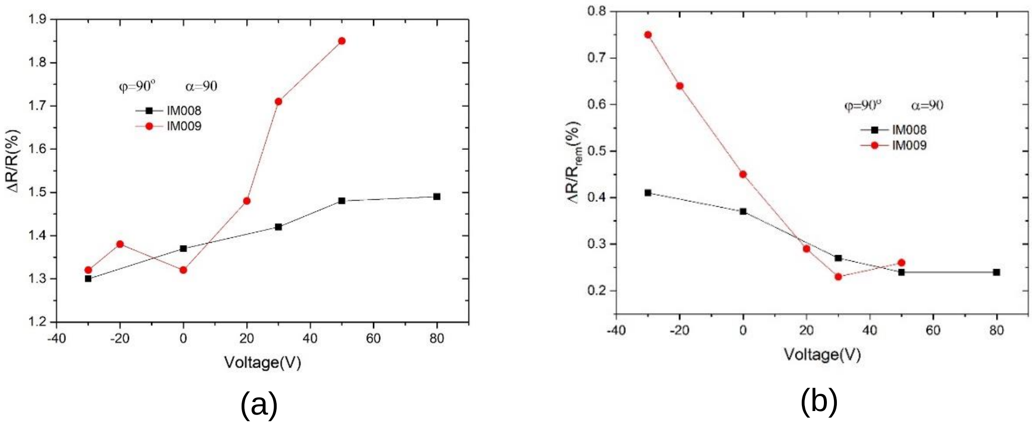

Figure 5.27: A comparison between (a) $\Delta R/R$ ratio, and (b) $\Delta R/R_{rem}$ at different voltages for IM008 and IM009 spin valves for the measurements when the magnetic field is perpendicular to the long axis of the transducer.

5.2.2.2 Magnetic field parallel to the long axis of the transducer ($\varphi = 0^o$)

In this measurement, the magnetic field is aligned along the long axis of the piezoelectric transducer ($\varphi = 0^o$), and the current is also applied in two directions: $\alpha = 90^o$ and $\alpha = 0^o$. The illustration of the measurements' configuration is the same, as shown in figure 5.12 (a) and (b). The $\Delta R/R$ curves for this direction measurement are shown in 5.28 (a) and (b) for the two current directions. Figure 5.29 (a) and (b) shows the $\Delta R/R$ values changing with the voltage and strain when the magnetic field is along the long axis of the piezoelectric transducer. For $\alpha = 90^o$, the $\Delta R/R$ value changes with the strain, and gives the maximum value of 1.83% when a compressive strain of -2.35×10^{-4} $(-30V)$ is applied into the IM009 stack, while it is a minimum value of 1.30% when a tensile strain of $+2.04 \times 10^{-4}$ $(+50V)$ is applied in the spin valve. On the other hand, for the $\alpha = 0^o$ measurement, the $\Delta R/R$ values changed with the same trend as the $\alpha = 90^o$ direction with smaller values of $\Delta R/R$ with 1.58% for the $-30V$ and 0.74% for $+50V$. The curves of the $\Delta R/R$ also show different features between the tensile and compressive strain, as shown in figure 5.28 (a) and (b), with a very wide base reversal for the tensile strain compared to the compressive values. The peaks' tops are also wider for the compressive strain values and narrower for the tensile strain. The remanence of resistance when the field equals zero $(\Delta R/R_{rem})$ shows very high values for the tensile strain values, reaching 0.90% in case of $\alpha = 90^o$, and it decreases gradually as the tensile strain decreases, while it shows low values for all compressive strain values to reach 0.25% when a $-30V$ is applied to the transducer. Figure 5.30 (a) shows the variation of the $\Delta R/R_{rem}$ with the voltages applied to the transducer in both current directions measurements.

As can be seen in figure 5.30 (b), the $H(\Delta R/R_{max})$ also changes with the strain, giving the maximum values when a voltage of $-30V$ is applied to the transducer (compressive strain), with a value of $1.85mT$ and $1.80mT$ for $\alpha = 90^o$and $\alpha = 0^o$ measurements directions, respectively. On the other hand, applying a voltage of $+50V$ (tensile strain) decreases the $H(\Delta R/R_{max})$ to reach the values of $1.40mT$ and $1.35mT$ for both current directions. In general, all features of the magnetoresistance for this measurement direction $\varphi = 0^o$ gives the opposite behaviour to the measurement when the long axis is perpendicular to the field $\varphi = 90^o$. Giang et al. [68] found that changing the strain direction by 90^o to the magnetic layers stack changes the $H(\Delta R/R_{max})$ values to the opposite effect for each direction.

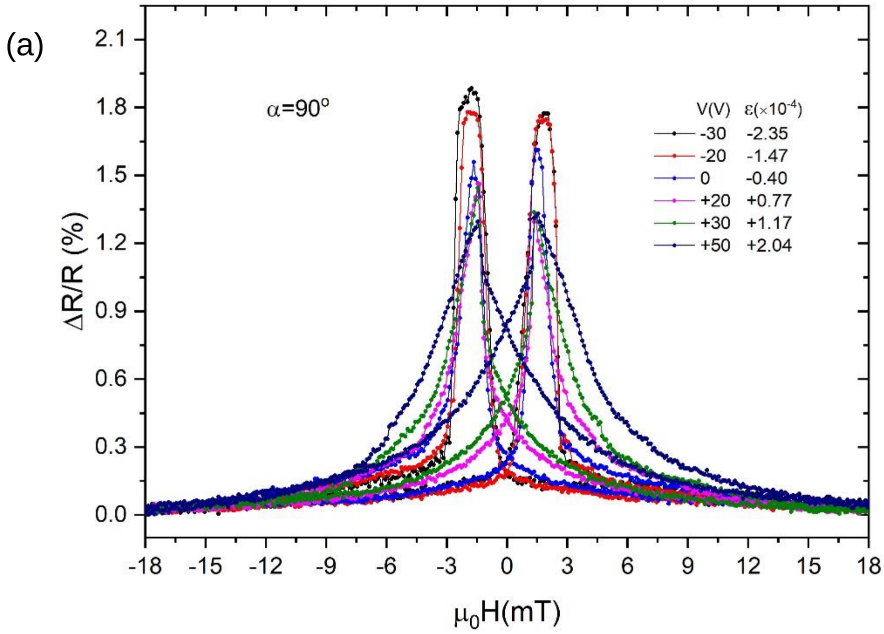

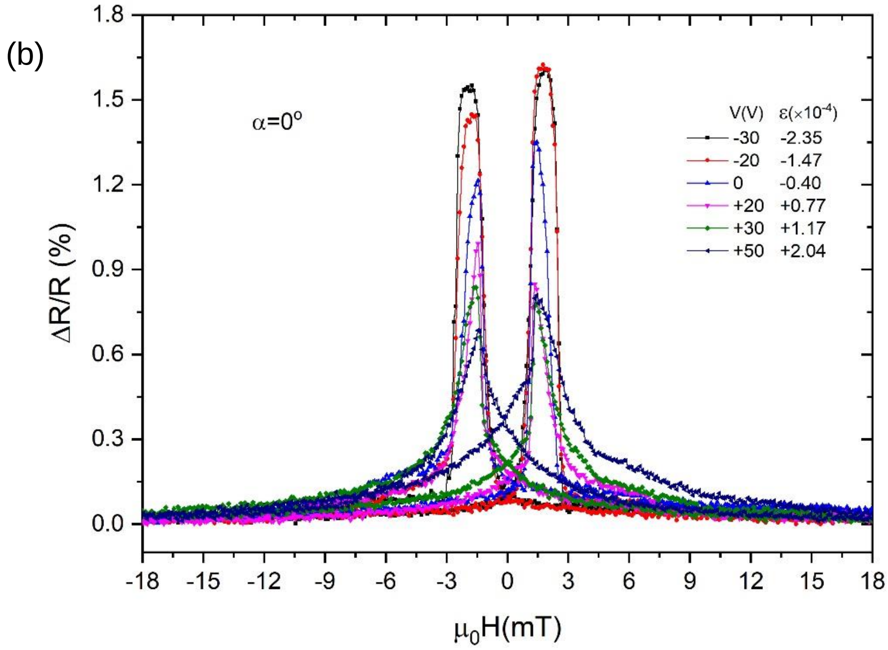

Figure 5.28: The $\Delta R/R$ curves for the IM009 spin valve when the magnetic field is parallel to the long axis of the transducer ($\varphi = 0^o$), (a) when the field makes an angle of $\alpha = 90^o$ with the current and (b) for $\alpha = 0^o$. Both directions show a change in the $\Delta R/R$ values and shapes, depending on the value and type of strain applied to the spin valve.

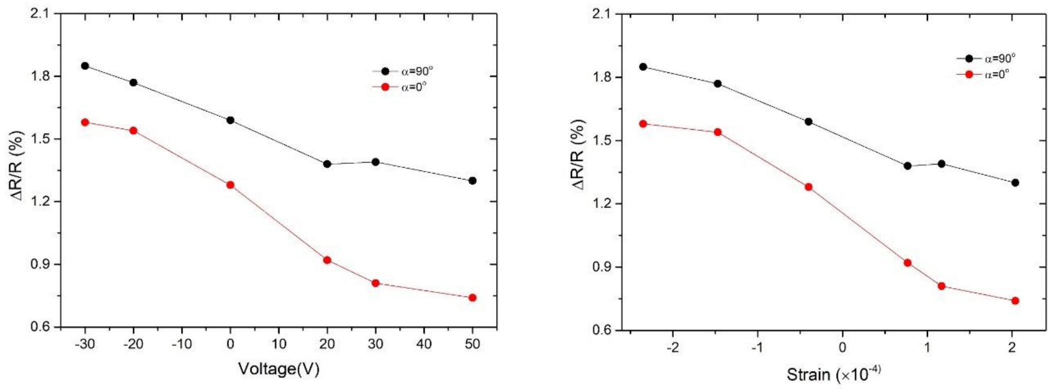

(a) (b)

Figure 5.29: The dependence of the $\Delta R/R$ values on (a) voltages applied to the transducer and (b) the corresponding strain values when the magnetic field is parallel to the transducer for IM009 spin valve.

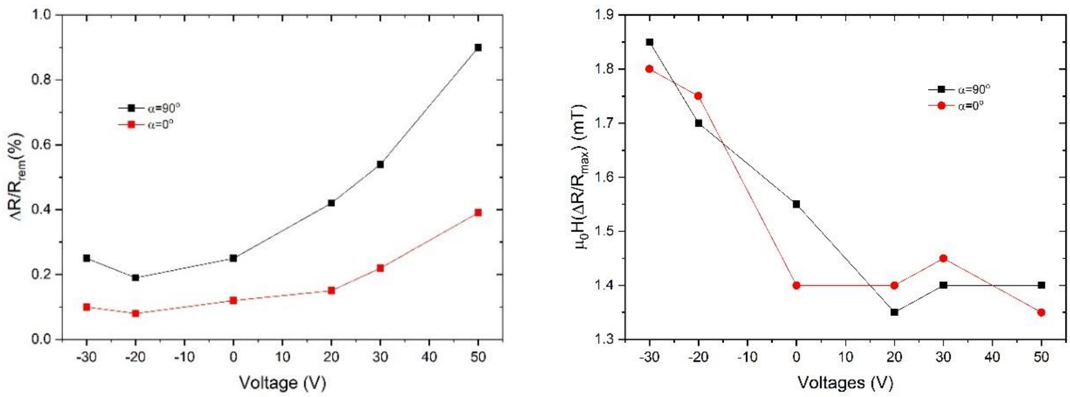

(a) (b)

Figure 5.30: The variation of the (a) $(\Delta R/R)_{rem}$ and (b) $H(\Delta R/R_{max})$ with the voltages in IM009 spin valve when the magnetic field is parallel to the long axis of the transducer for $\alpha = 90^o$ and $\alpha = 0^o$.

5.2.2.2.1 compressive strain effect on magnetoresistance features $\boldsymbol{\varphi = 0^o}$

To study the effect of these features, focussing on certain voltages for $\alpha = 90^o$, figure 5.31 (a) shows the R_{xx} ($\Delta R/R$) and R_{xy} magnetoresistance curves when a voltage of $-30V$ applied to the transducer. Applying compressive strain in this direction makes the magnetisation of the permalloy perpendicular to the field while it is parallel to the field for the nickel layer. Since the permalloy magnetisation favoured the short axis perpendicular to the magnetic field direction, its reversal occurs slowly without a clear switching as shown by the peaks before the blue arrow (represents $H(\Delta R/R_{max})$) in both R_{xy} and R_{xx} curves) for the sweep up measurement. For the nickel layer, it starts to reverse directly after the reversal of the permalloy layer, which means that the magnetisation alignment angle between the two-layers is $\psi = 180^{o}$. The nickel layer magnetisation then switches abruptly (see the transverse resistance) in the field range between the $H(\Delta R/R_{max})$ and the field of $2.95mT$ (see the green arrows in both curves), while it exhibits a rapid decrease in the $\Delta R/R$ value, as shown in the R_{xx} curve manifests as a high negative slope curve. The nickel magnetisation completes reversing until it lies along the positive field direction. The remnant resistance $\Delta R/R_{rem}$ shows a very low value of 0.25% for this voltage, as the nickel is reversing after the complete reversal of the permalloy and saturates with the field direction.

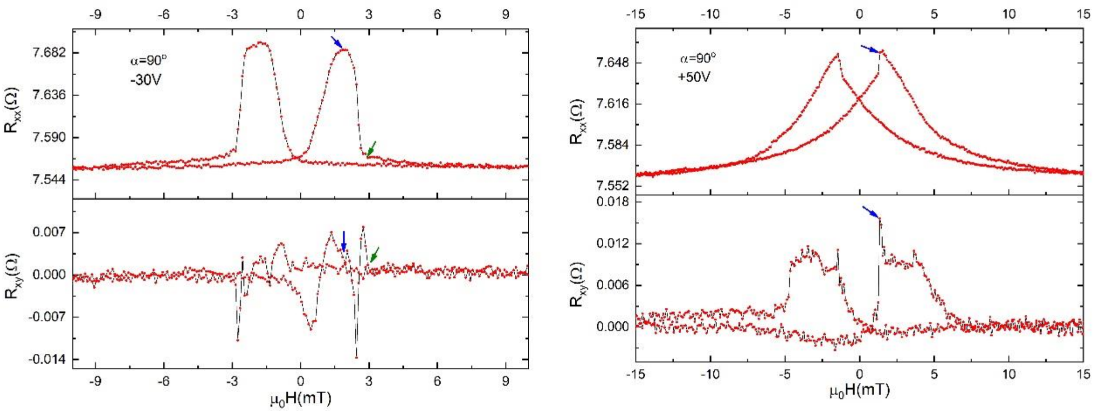

(a) (b)

Figure 5.31: Comparison between the R_{xy} and R_{xx} magnetoresistance for IM009 spin valve when the field is parallel to the magnetic field with the electric current direction $\alpha = 90^{o}$, when applying different voltages to the transducer, (a) $-30V$, and (b) $+50V$.

5.2.2.2.2 Tensile strain effect on magnetoresistance features $\varphi = 0^{o}$

In this case, the permalloy moments prefer to lie along the field direction, while nickel is harder in this direction. When a voltage of $+50V$ is applied to the transducer (see the resistances curves of R_{xy} and R_{xx} in figure 5.31 (b)), the reversal is changed, and it can be seen that the peak of the permalloy is changed, and it is difficult to distinguish between the permalloy and nickel reversal. When the reversal of the permalloy occurs at $1.40mT$ (shown by the blue arrow in figure 5.31 (b)), the nickel layer magnetisation is already starting to reverse at the earlier field, (see the broad reversal in R_{xy} after the blue arrow ($H(\Delta R/R_{max})$ point), which gives smaller $\Delta R/R$ compared to the compressive strain with a value of 1.30%.The nickel layer completes reversing away from the negative field direction, as seen in both curves (R_{xy} and R_{xx}), until it aligns with the permalloy direction. The slow reversal could be ascribed to the slow growth of domains, or it might be a slow rotation. The high remanence in the $\Delta R/R$ curve with a value of 0.90% is related to the misalignment between the permalloy and nickel magnetisations directions, due to the hard reversal of the nickel at that direction, while the abrupt increase of the $\Delta R/R$ prior to the $H(\Delta R/R_{max})$ is related to the permalloy switch. The variation of $H(\Delta R/R_{max})$ for this measurement is attributed to the switching field of the permalloy with the strain as discussed before in the previous section. For this direction in S476 sample (see figure 3.16), the switching field changes from $1.8mT$ to $0.8mT$ when the voltages changed from $-30V$ to $+50V$.

Figure 5.32 shows the difference between the two measurements direction for how $\Delta R/R$ varies with the voltage for IM009 when the field is parallel ($\varphi = 0^o$) and perpendicular ($\varphi = 90^o$) to the long axis of the transducer and the current always along the short axis of the transducer. The $\Delta R/R$ variation with the strain is the opposite to each other as the uniaxial anisotropy induced by the stressor affects differently and depends on the strain direction with respect to the field. On the other hand, a comparison between the strain effect on $\Delta R/R$ change when the field along the long axis of the transducer ($\varphi = 0^o$) for both spin valve IM008 and IM009 with the current direction $\alpha = 0^o$ in figure 5.33 shows that the $\Delta R/R$ varies more in IM009. That could be ascribed to the different response of the layers to the strain as the order of the layers changed between the two spin valves and shows that the nickel might respond more to the strain.

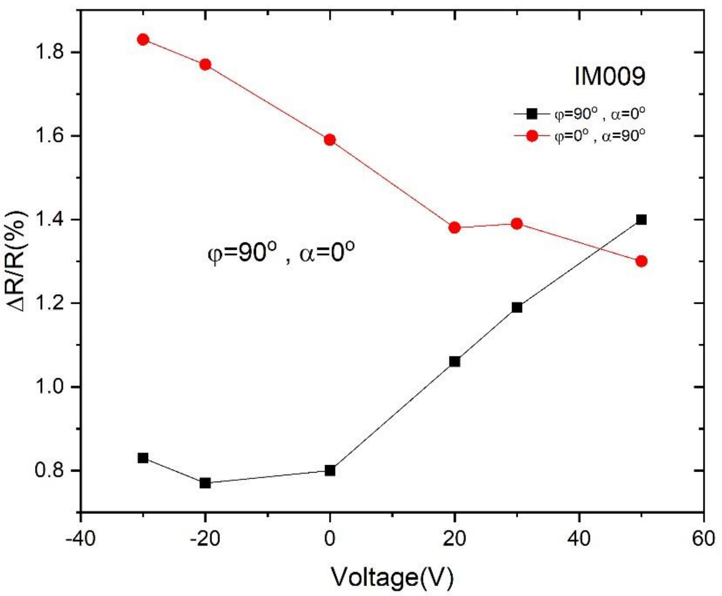

Figure 5.32: A comparison of the voltage varying (strain) on $\Delta R/R$ between the two measurements directions of IM009 sample when the magnetic field is perpendicular and parallel to the field and the electric current always applying along the short axis.

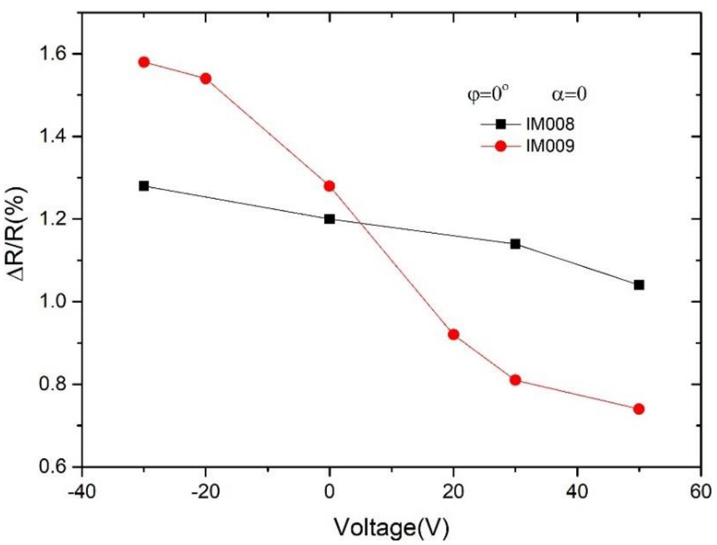

Figure 5.33: A comparison between the $\Delta R/R$ ratio at different voltages for IM008 and IM009 spin valve for the measurements when the magnetic field is parallel to the long axis of the transducer.

5.3 Investigating the effect of the strain on the spin valve with an antiferromagnetic layer

For these spin valves, as discussed in chapter 4, a layer of IrMn was incorporated in S548 and S549 samples, to introduce an exchange bias in the stack to enhance the possibilities of obtaining the antiparallel alignment of the magnetisations of the successive magnetic layers. For these spin valves, the magnetoresistance curves show a clear anisotropic magnetoresistance curve with a wide coercivity, as discussed in chapter 4. This section presents strain measurements carried out for these spin valves to examine how the strain affects magnetoresistance properties, and if that would enhance the giant magnetoresistance of the spin valve by affecting the magnetisation reversal of the layers consisted these spin valves. The strain could also affect other magnetic properties of the spin valves, such as coercivities, exchange bias, or the interaction of these layers through the spacer thickness. The magnetotransport measurements were performed by tuning the strain values between $-30V$ and $+50V$ for different magnetic field directions.

5.3.1 S548 spin valve

As shown in figure 4.10, the structure of this spin valve consists of Cr/NiFe/Cr/Ni/IrMn/Cr, where the permalloy is the free layer of the spin valve designed to be the sensing layer for the strain to control the whole spin valve magnetoresistance properties. As discussed previously, strain affects the permalloy single layer sample S476, and the permalloy layer in the multilayered structure in IM008 and IM009 samples. On the other hand, the nickel layer did not show any change for the single-layer sample in S475, whereas it responds to the strain in the pseudo samples, as discussed in section 5.2. In this spin valve, both layers have different interfaces with different spacers and capping layer. Moreover, the existence of the IrMn could affect the strain impact in the pinned magnetic layer, since it is pinned partially, as discussed in chapter 4. However, the permalloy layer responds to the strain while the nickel shows no response to the strain. The measurements were performed in different directions of the magnetic field with respect to the long axis of the transducer and the electric current. The next section discusses these measurements.

5.3.1.1 Magnetic field parallel and perpendicular to the long axis of the transducer

The transport measurements when the magnetic field is perpendicular and parallel to the piezoelectric transducer were performed to investigate the effect of strain on S548 spin valve magnetoresistance. Different directions of the field with respect to the electric current were carried out, with two directions of the electric current ($\alpha = +45^o$ and -45^o), showing the main changes when strain applied, with the configurations shown in figure 5.34 (a) and (b) where a range of voltages between $-30V$ and $+50V$ is applied. The peaks of the magnetoresistance of this spin valve show the same features as when $0V$ is applied, as presented in chapter 4. The resistances show anisotropic magnetoresistance and no sign of giant magnetoresistance effect. Figure 5.35 (a) shows the transverse resistance of the S548 spin valve at different voltages. The strain affects the first peak on the spin valve reversal as indicated by the pink arrows. As explained in chapter 4, this peak is related to the permalloy, as also proved by the SQUID measurements. The strain changes the maximum values of the resistance (peak intensity) of the permalloy layer for the measurements when the field is perpendicular to the long axis of the transducer ($\varphi = 90^o$) and $\alpha = -45^o$. Figure 5.35 (b) shows zoomed permalloy peaks to see how the permalloy peaks changing with the strain.

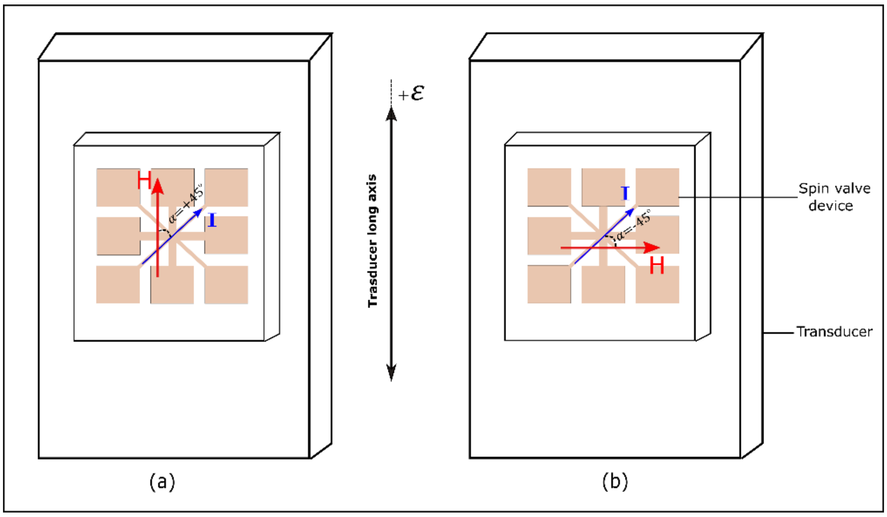

Figure 5.34: The measurements configuration of S548 spin valve when the magnetic field is (a) perpendicular ($\varphi = 90^o$) and (b) parallel ($\varphi = 0^o$) to the long axis of the piezoelectric transducer, where the current directions are $\alpha = +45^o$, and $\alpha = -45^o$ respectively.

One can assume that the intensity change of the permalloy layer in S548 spin valve with the voltages following the same behaviour of the permalloy sample S476 (see figure 3.6). the peaks intensity decreases when the voltage change from $-30V$ to $+50V$ as an indication of the strain changing magnetisation direction of the permalloy. Hence, one can assume that the permalloy layer in S548 spin valve might show a hard axis along the field direction when a tensile strain (i.e.$+50V$) is applied, and a soft magnetic axis along the field when a compressive strain is applied to the spin valve (i.e. $-30V$) for this measurement configuration. On the other hand, figure 5.35 (b) shows that the switching field of the permalloy also changes with the strain. Figure 5.36 shows the relation between the switching field and the voltage applied to the transducer, and this change is the opposite to the change in the permalloy single layer sample (S476) shown in figure 3.16. This could involve the interface playing a crucial role in changing this trend, where the Cr changes the microstructure of the whole spin valve, affecting all properties of the spin valve, including the magnetic reversal [206, 207]. The reversal of the nickel remains unchanged for the whole range of the voltage applied to the transducer, see the magnetoresistance feature between the permalloy peak and the saturation field. Although the same nickel layer thickness is used for IM008 and IM009 that show magnetostrictive properties, the nickel in S548 might show zero magnetostriction; the interfaces are different and hence that could alter the magnetic and magnetostrictive properties of the nickel layer manifest as zero magnetostriction. On the other hand, the strain applied to the sample is weak to overcome the partial coupling between the nickel layer and IrMn layer.

On the other hand, when the field is parallel to the long axis of the transducer $\varphi = 0^o$, and the field is $\alpha = +45^o$ to the electric current, the peaks related to the permalloy are affected by the strain. For the $-30V$ (compressive strain), giving the maximum magnetoresistance value for this peak, whereas applying a voltage of $+50V$ (tensile strain) gives the minimum value of the resistance consistent with the permalloy single layer sample for this direction measurement. The whole reversal is shown in figure 5.37 (a), while a magnification of the figure for the permalloy layer change is presented in figure 5.37 (b). This direction also shows that permalloy could have the easy axis of the magnetisation along the field when applying tensile strain to the spin valve, while it shows hard axis along the field direction for the compressive strain value. The nickel layer also shows no response to the strain for this direction measurement.

(a)

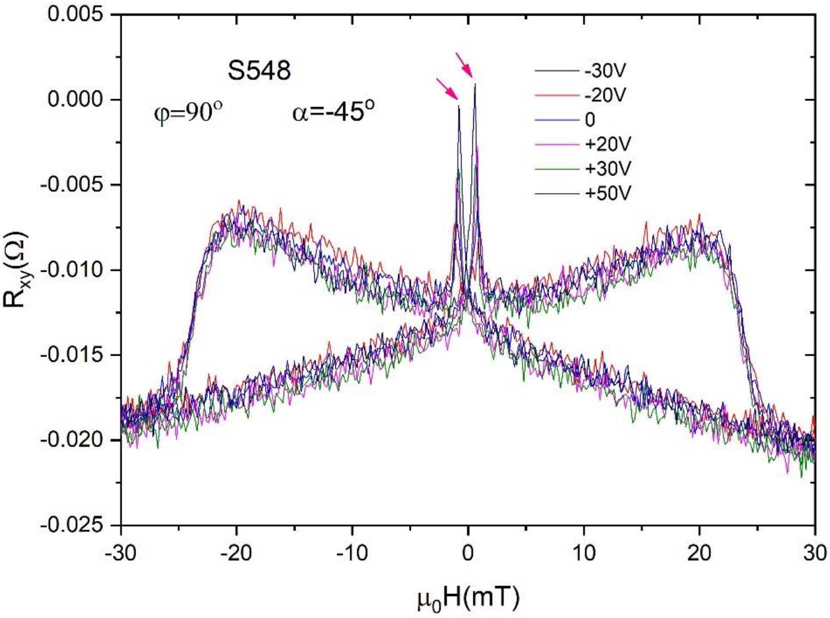

(b)

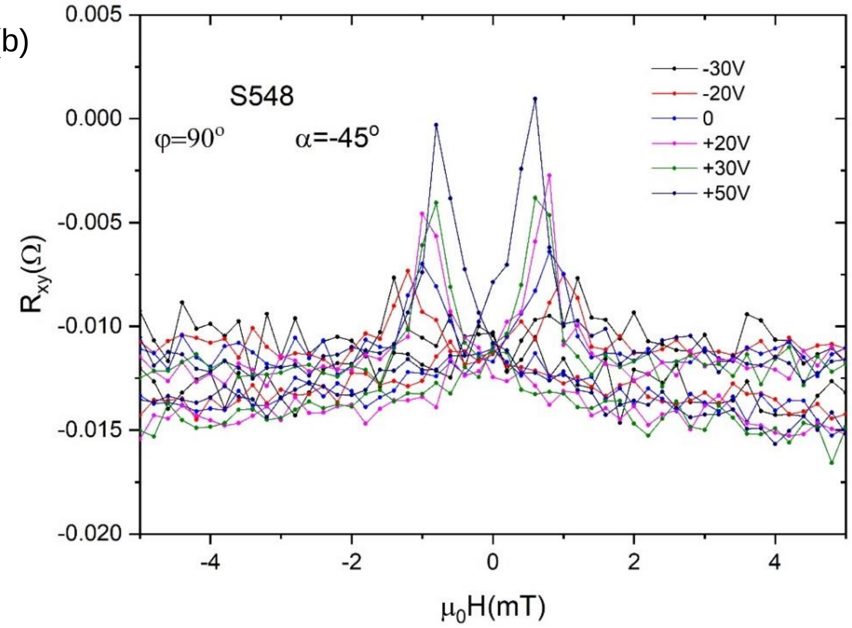

Figure 5.35: (a) The $R_{xy}$of the S548 spin valve at different voltages when the magnetic field is perpendicular to the long axis of the transducer and $\alpha = -45^o$, and (b) zoomed curves for the R_{xy} of the permalloy peaks for the same measurement. The intensities of the peaks change with the voltages, indicating the change in the magnetisation direction of the permalloy. The switching field shows a change with the field, as shown in the following figure.

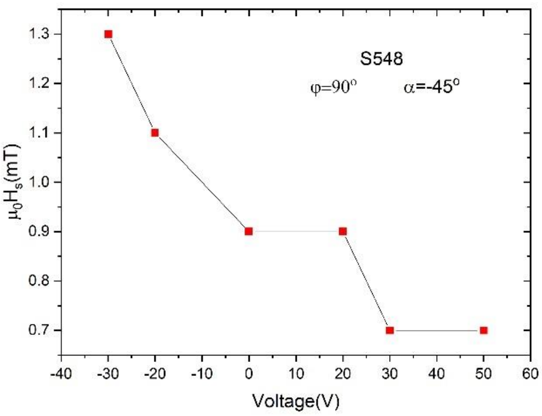

Figure 5.36: Variation of the switching field of the permalloy layer with the voltage in S548.

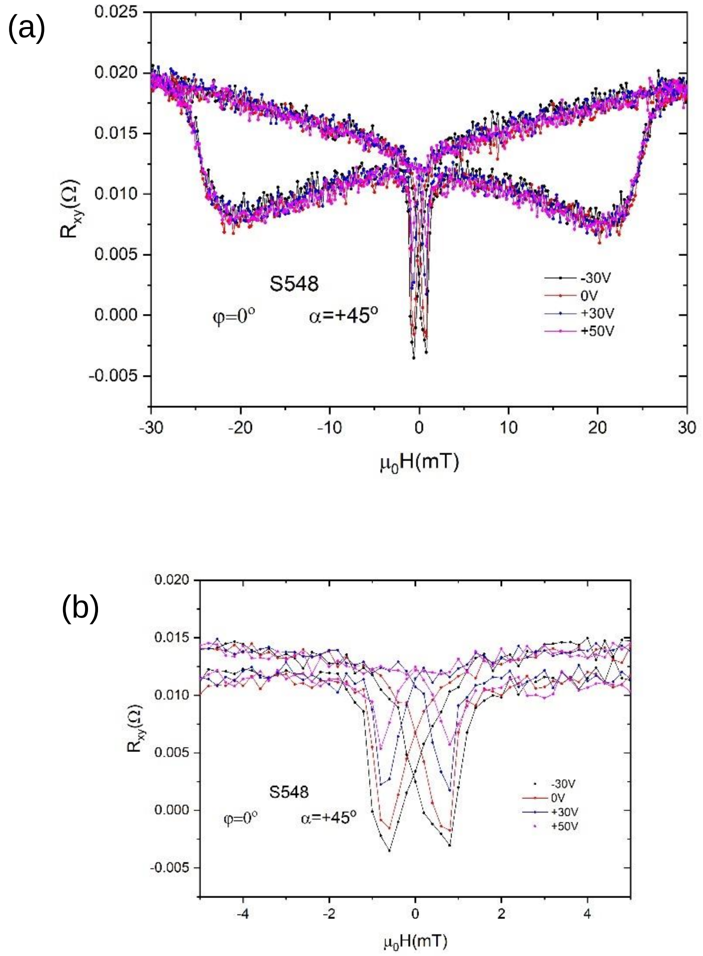

Figure 5.37: (a) The R_{xy} of the S548 spin valve at different voltages when the magnetic field is parallel to the long axis of the transducer and $\alpha = +45^o$, and (b) a zoomed scale for the R_{xy} for the permalloy peaks for the same measurement.

5.3.1.2 Magnetic field $+45^{o}$ along the long axis of the transducer $\varphi = +45^{o}$

When the field is aligned along $+45^{o}$ with the current making an angle of $\alpha = 0^{o}$, for the measurement configuration displayed in figure 5.38, the transverse measurement for this direction shows a response to the strain. It is challenging to determine the effect of the strain in this direction (see figure 5.39 (a)); however, the peaks direction change show similar behaviour to that shown for permalloy sample S476 (section 3.2.2.4) and permalloy layer in IM008 spin valve (section 5.2.2.3) for the same measurement direction ($\varphi = +45^{o}$). As discussed for the permalloy in these samples, the magnetisation easy axis favours lying along the short axis for the compressive strain and along the long axis for the tensile strain. Consequently, the reversal shows different directions, depending on the type of strain applied to the sample and the field direction. Figure 5.39 (a) shows how R_{xy} curves of S548 spin valve change when the voltages of $-30V$ and $+50V$ are applied, with the peak direction changing as an indication of the change on the permalloy layer reversal direction for $\varphi = 45^{o}$ and $\alpha = 0^{o}$ measurements. For the nickel layer, it is difficult to see any change for different voltage values in the whole voltage range. The corresponding longitudinal resistance R_{xx} curves at different voltages show a clear anisotropic resistance, as shown in figure 5.39 (b). For all curves at different voltages values, it is challenging to see any changes in these peaks, where they show asymmetric shapes for ascending and descending sides, as discussed in chapter 4. There is no sign for the GMR value, which could be negligible with respect to the AMR value, and it is difficult to determine in these curves.

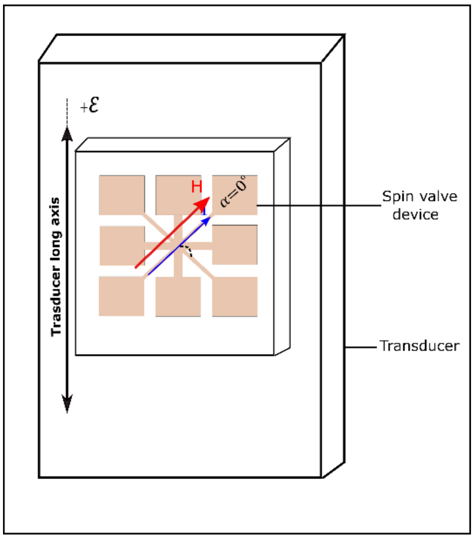

Figure 5.38: Measurement configuration when the field is aligned along $+45^{o}$, with the current direction $\alpha = 0^{o}$.

For all measurements directions for S548 spin valve, the change in the permalloy reversal is consistent with the S476 sample and with permalloy in IM008 and IM009. The nickel layer does not respond to any change with the strain, which could be due to one of two reasons: the nickel magnetisation coupling with the IrMn is strong enough to hold the nickel's magnetisation from any change under strain; or the nickel could be showing zero magnetostriction [48] in this structure, as seen in the nickel's single layer sample S475. For this sample, the strain did not enhance the GMR value, even with existing different magnetisation alignments between the magnetic layers, which could be ascribed to the Cr layer as discussed in chapter 4 [188].

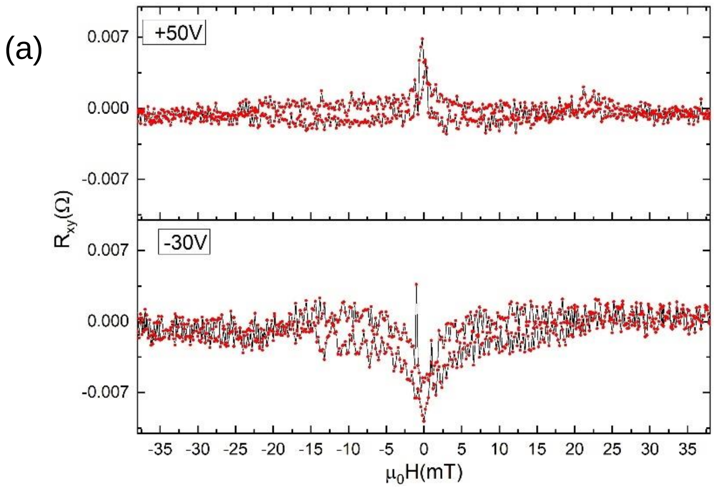

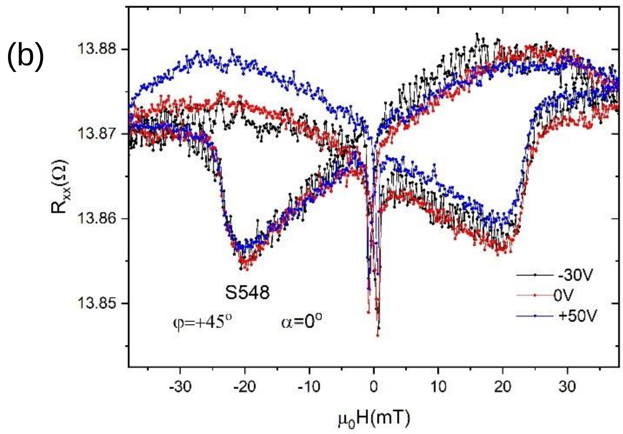

Figure 5.39: (a) R_{xy} and (b) R_{xx} for the S548 spin valve when the magnetic field is $+45^o$ along the long axis of the transducer, and $\alpha = 0^o$ with the electric current. The transverse resistance shows different permalloy peak directions as a manifestation of the magnetisation changing direction, while the longitudinal resistance shows anisotropic magnetoresistance with asymmetric curves, which could be a sign of a small GMR effect.

5.3.2 S549 spin valve

This sample consists of a structure of Cr/Ni/Cr/NiFe/IrMn/Cr, where the permalloy layer grew under the antiferromagnetic layer, and the nickel is the free layer of the spin valve. Here both layers do not show any response to the strain in the spin valve. Figure 5.40 (a) and (b) show the transverse resistance for the spin valve When the magnetic field is perpendicular to the piezoelectric transducer ($\varphi = 90^o$) for $\alpha = +45^o$ and when the field making $\varphi = 45^o$ for $\alpha = 0^o$, there is no sign for any change of the resistance curves for both layers, permalloy and nickel. Hence, the magnetic reversal for both layers in this spin valve does not respond to the strain in all measurements directions. It is clear for this spin valve that the permalloy could be coupled by the IrMn layer, and hence the strain is weak to overcome the coupling and change the direction of the magnetisation. On the other hand, although the nickel layer is the free layer in this spin valve, the strain does not affect its magnetostriction properties. It might show zero magnetostriction in this system similar to that shown in nickel single layer sample S475.

(a)

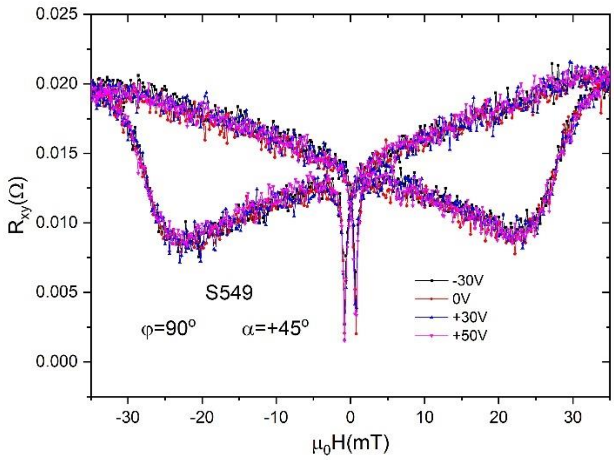

(b)

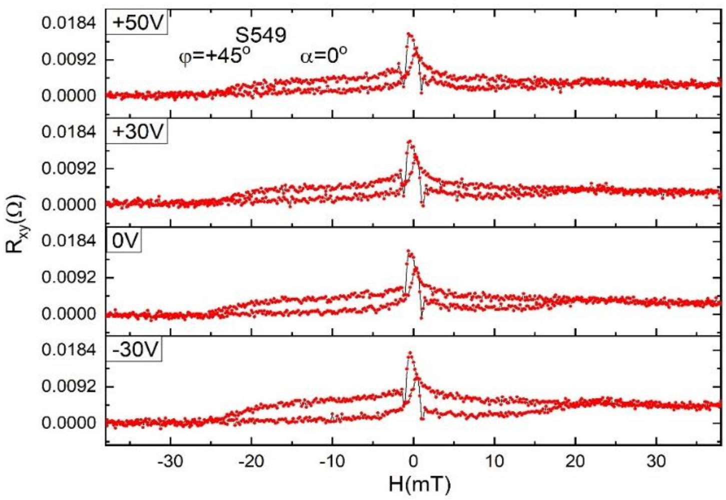

Figure 5.40: The R_{xy} for the S549 spin valve when the magnetic field is along different directions of the long axis of the transducer (a) $\varphi = 90^o$ and $\varphi = 45^o$.

5.4 Conclusion

The strain effect on the magnetotransport measurements of two sets of spin valves was examined in this chapter. The magnetostriction properties of each spin valve were studied using a hybrid structure of piezoelectric transducer/spin valve, whereby the spin valve films were fabricated as micro-devices and then mounted onto the transducer. DC four-probe measurement was then used to study the strain effect on the magnetoresistance properties of the spin valves by placing the hybrid structure in a magnetic field, rotatable by 360^o in the plane of the spin valve device. The voltages through the transducer were tuned between $-30V$ and $+50V$ (in some cases $+80V$) for each direction while measuring the transverse and longitudinal resistance to study the changes in curves' features to understand the strain effect on each layer reversal and magnetoresistance properties.

Magnetoelastic measurements were carried out for IM008 and IM009 to measure the exact strain applied to the spin valve films. It was found that for strain applied to the films in the range of $\times 10^{-4}$. The difference between the two spin valves could be attributed to the formation of an intrinsic strain during any process before the measurements. For the transport measurements, IM008 spin valve showed different magnetoresistance behaviour with changing strain, whereby the $\Delta R/R$ (consists both GMR and AMR) value changed with the strain to reach the maximum of 1.53% when the magnetic field was parallel to the long axis of the transducer while giving a minimum value of 0.93% when the field was parallel to the transducer. The shape of the magnetoresistance curves $\Delta R/R$ also affected by the strain direction with respect to the magnetisation easy axes of permalloy and nickel and the magnetic field. For instance, the curves could show sharp peaks or plateau-like peaks (spin valve stiffness) depends on the strain value and directions. The changes of the magnetotransport measurements attributed to the magnetostrictive properties of the permalloy and nickel layers were both layers showed a change in the magnetic reversal. The magnetostriction of both layers has a different sign (positive for the permalloy and negative for the nickel), showing opposite responses to the type of strain.

On the other hand, IM009 spin valve shows a clear dependence on the strain, with higher $\Delta R/R$ value than the IM008 spin valve. The maximum $\Delta R/R$ ratio was obtained for $\varphi = 90^o$ and $\alpha = 90^o$ measurements, with a value of 1.85%. The $H(\Delta R/R_{\ max})$ and $\Delta R/R_{\ rem}$ show very clear change with the strain, with the former increasing to the maximum value when the easy axis of the permalloy is perpendicular to the field; and the latter reaching its maximum value for each measurement direction when the nickel magnetisation is perpendicular to the field direction. The difference between the IM008 and IM009 spin valves could be ascribed to the growth sequence as the strain affects the two layers differently. The interface could be another reason for different strain response to each layer. This difference leads to different reversal processes for each layer.

The other set of spin valves consisting of IrMn layer show different behaviour with the changing strain. Both samples show clear anisotropic magnetoresistance, and changing the strain does not enhance the GMR effect where the AMR is dominant. S548 shows a response to the strain manifest as a change in the permalloy peaks and switching field related to the magnetisation direction change with changing strain, while the nickel layer remained unchanged for the whole range of applied voltages. This could be related to the nickel coupling with IrMn, or it has zero magnetostriction. In contrast, S549 spin valve does not respond completely to the strain, with the nickel showing zero magnetostriction and the permalloy being pinned partially to the IrMn layer.

To sum up, the magnetic properties of the multilayered structure could be changed by using different layers with different magnetostrictive properties, which could give a different response to the strain and hence control the whole properties of the spin valve. Using different spacers, growth sequences, and different coupling (i.e. exchange bias coupling) could alter the spin valve response to the strain-induced through the tuning voltages in the transducer. Controlling the magnetisation of spin valves by inducing sizable anisotropy using an electric field can facilitate the development of a new method for low-power storage and logic devices.

Chapter 6: Investigation of the Strain Effect on the Static and Dynamic Magnetic Properties of Permalloy and Nickel Layers in Pseudo Spin Valves Using Ferromagnetic Resonance

6.1 Introduction

Ferromagnetic resonance (FMR) technique is an effective way to measure the static and dynamic properties of ferromagnetic thin films and multilayers [155, 208, 209, 210]]. In this chapter, the static and dynamic properties of IM008 (PZT/Ta/NiFe/Cu/Ni/Ta) and IM009 (PZT/Ta/Ni/Cu/NiFe/Ta) spin valves are investigated under different uniaxial strain conditions using FMR technique. It was shown in chapter 5 that the magnetic properties of these samples showed a dependence on the strain. On the other hand, other spin valves with IrMn layer were not measured by the FMR technique because they show less or no response to the strain in chapter 5. As discussed in chapters 4 and 5, IM008 and IM009 spin valves show different magnetic behaviour to each other, the permalloy and nickel have different properties due to the different growth order, which was examined by the magnetisation measurements (SQUID) and magnetotransport measurements. However, sometimes it is difficult to determine the response of each layer in the spin valves from these measurements. FMR measurement gives information for each layer separately, since they have different saturation magnetizations, magnetic anisotropies, and dynamic properties, which manifest as different resonance peaks for each layer in multilayer samples [211]. All FMR spectra show a clear resonance peak for the permalloy layer, while nickel shows a very small intensity peak, and it is hard to examine in most experiments. Permalloy shows magnetostrictive properties, agreeing with the observations in chapter 3 and 5.

This chapter firstly studies the strain effect on the magnetic anisotropies and saturation magnetization of the magnetic layers in both IM008 and IM009 spin valves, starting with the $0V$ for both samples, to compare between the spin valves and to determine which layers cause the resonance peaks. This is followed by the study of changing the voltage on the transducer for each spin valve separately. The dynamic properties of each spin valve are discussed at the end of this chapter.

6.2 Experimental setup of the FMR measurements

All measurements in this chapter were carried out using modulated FMR at the University of York, performed by Dr Stuart Cavill. Both samples were prepared at the University of Nottingham, as discussed in chapter 2. The unpatterned films of the spin valve were mounted onto two separate piezoelectric transducers. The strain transferred to the films could be different from that transferred to the transport devices of the same samples in chapter 5, and films' anisotropies might slightly be different than anisotropies introduced in devices during fabrication and mounting on the transducer. Hence the strain values extracted from the strain calibration measurements in chapter 5 cannot be used in this chapter. Instead, the voltages applied values to the transducer are used, and the strain type can be determined regarding the trend of the measurements.

Figure 6.1 (a) illustrates the configuration of the measurement of the hybrid structure of the thin film and the piezoelectric transducer, where φ is the in-plane angle between the long axis of the transducer and the dc-magnetic field. The microwave field is perpendicular to the dc-field when $\varphi = 0^o$. For extracting magnetic and dynamic properties of the spin valves, the derivative of S_{21} spectra (FMR spectra) were recorded as a function of the in-plane angles between the applied magnetic field and the main axis of the piezoelectric transducer. The positive and negative angles are to show the rotation direction from both sides of $\varphi = 0^o$, to reach $\varphi = +80^o$ and $\varphi = -80^o$, completing a rotation angle of $160\,^o$. The resonance field H_{res} (the field value at the resonance condition) and linewidth ΔH (the magnitude of the difference between the maxima and minima of the resonance peak) are extracted from the derivative of S_{21} spectrum by fitting it to the first derivative of Lorentzian function. The measurements were performed as a function of angle in order to extract the magnetic anisotropies, saturation magnetization, and dynamic properties of magnetic layers in the spin valves [157, 212, 213, 214]. Figure 6.1

(b) shows an example of the FMR spectrum with the theoretical fit, while the H_{res} and ΔH are indicated in the graph. As discussed in chapter 2, the solid red line is the first derivative of the asymmetric Lorentzian function giving by the equation [157,158]:

$$\frac{d(+\chi' \sin(\epsilon)+\chi'' \cos(\epsilon))}{dH} = A\left[-\frac{2(H-H_{res})\Delta H cos(\epsilon)}{[\Delta H^2(H-H_{res})^2]^2} - \frac{[\Delta H^2-(H-H_{res})^2]\sin(\epsilon)}{[\Delta H^2(H-H_{res})^2]^2}\right] + \mathrm{B} \qquad (6.1)$$

where $\chi'$and χ'' are the real and imaginary components of the AC susceptibility, respectively, A and B are constants, H is the external dc-magnetic field and ϵ is the mixing angle between the dispersive and absorptive components of the distorted FMR line shape. For the static magnetic properties, rotation measurements for IM008 sample were performed at fixed microwave frequencies of $8GHz$ and $14GHz$, while IM009 sample measured at $8GHz$. On the other hand, for both samples, to extract the damping parameters, a range of frequencies between $5GHz$ and $15GHz$ is applied for one direction only when the field is parallel to the long axis of the transducer ($\varphi = 0^o$).

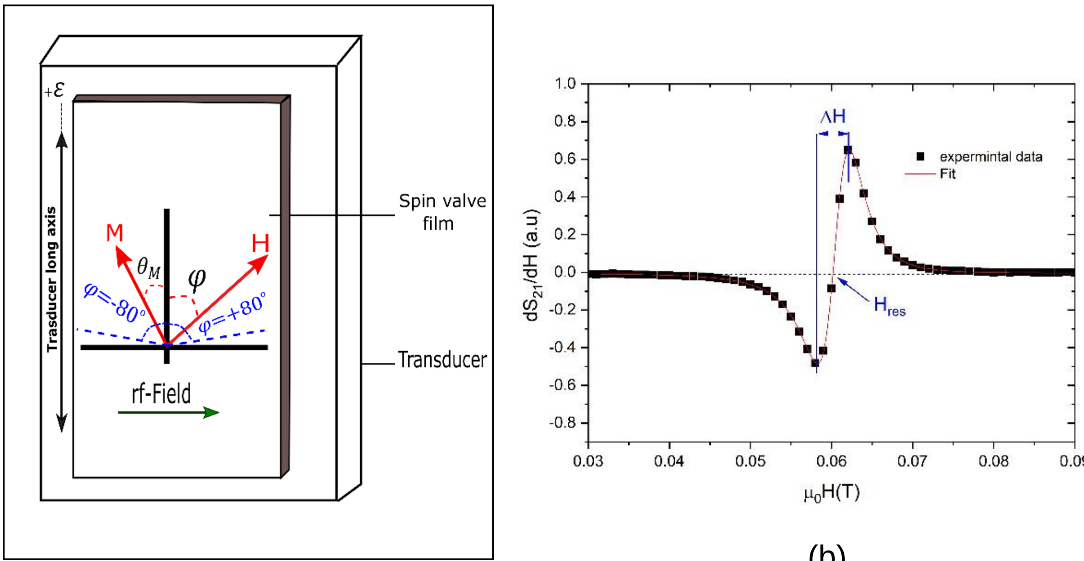

(a) (b)

Figure 6.1: (a) Schematic representation of the hybrid structure of the spin valve film and the piezoelectric transducer for the FMR measurements, where φ and θ_M are the angles between the magnetic field (H) and magnetisation (M) with respect to the transducer long axis, respectively. The field rotates around the hybrid structure to complete 160^o between $\varphi = +80^o$ and $\varphi = -80^o$. The rf-field is perpendicular to the applied field at $\varphi = 0^o$. (b) The derivative of S_{21} spectrum with the fit (red line) to the first derivative of the Lorentzian function, where $H_{res}$and ΔH parameters are indicated in the graph.

6.3 Investigation of the static magnetic properties of IM008 and IM009 spin valves at $0V$

Before investigating the strain effect on magnetic properties, it is worth discussing the main features of the FMR spectra of the spin valves at $0V$ to distinguish the resonance features of each layer. Figure 6.2 shows the FMR spectra for the measurements at a microwave frequency of $8GHz$ for the IM008 and IM009 samples for the direction of $\varphi = 0^o$, with $0V$ applied to the actuator. Both samples show one clear resonance peak at a similar resonance field. It is difficult to determine which layer is causing this peak from the first look since no reference measurements have been performed for a single layer of permalloy (S476) and nickel (S475) samples. Further analysis is needed to determine which layer shows clearer resonance behaviour, manifest as strong peaks in the absorption line. It is not clear for this stage why just one clear resonance peak appeared in the spin valves measurements, and this needs more investigation.

However, there is another feature at a higher applied field in FMR spectra for both samples' measurements that might be related to one of the spin valve layer's resonance. As discussed in chapter 4, for the magnetisation and transport measurements for both samples at $0V$ (as shown in figures 4.2 and 4.2), both permalloy and nickel layers show different reversal field and no static exchange coupling between the layers and hence the two layers might have different H_{res} values. Figure 6.2 shows the spectra of IM008 and IM009, where a small feature at the higher field, as shown in the inset and indicated by red and black arrows for both samples. This feature could be related to one of the magnetic layers resonance, where the amplitude of the resonance is very small compared to the another layer (with the clear peak). Heinrich et al. [215] assumed that for the magnetic bilayer system, there is a dynamic coupling between the layers, and they suggested that is related to the spin transport between the magnetic layers through the nonmagnetic spacer layer. One layer acts as a spin pump while the second one considered as a spin sink. When the two layers have different H_{res}, one of them ($F1$) has a large precessional amplitude (spin pump) while the second layer ($F2$) has a small precessional amplitude (spin sink) which causing non-local damping for the layer ($F1$). As this phenomenon arises from pumped spin current, it depends on the interfacial structures of the spacer/ferromagnetic [216, 217]. For this chapter, the smaller (second) peak is difficult to reconcile with the theoretical model, since the peak has small intensity and is not easy to fit. Hence, most of this chapter focuses on the clear resonance peak. All spectra of IM008 and IM009 samples show asymmetry in the signal, which could be attributed to the coupling between the film and the coplanar waveguide (CPW)[158, 212].

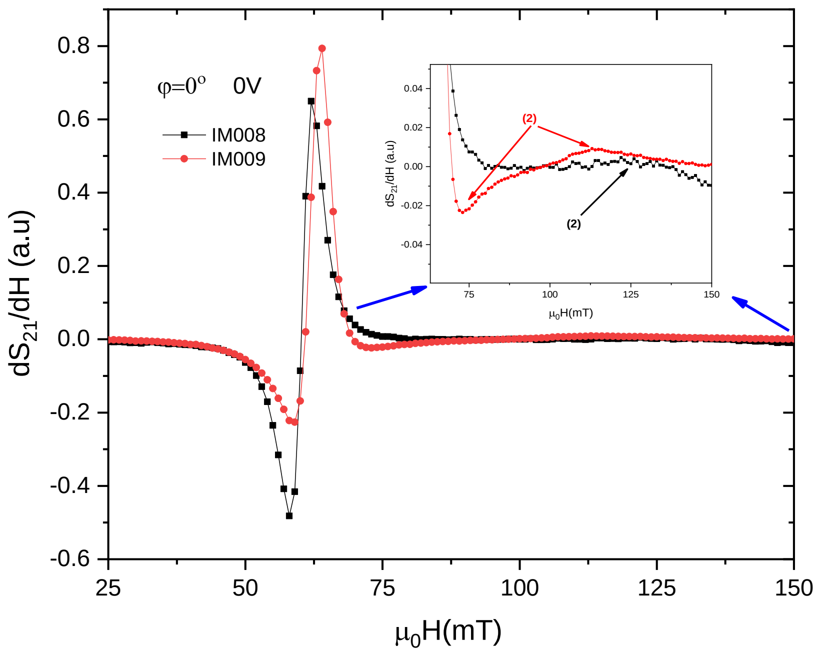

Figure 6.2: The spectra of IM008 and IM009 samples at $8GHz$ and $0V$, showing one clear resonance peak at the same field for both spin valves. The inset indicates the zoomed line between the two blue arrows, and the second feature (2) is indicated by black (IM008) and red (IM009) arrows for each spin valve.

The in-plane rotation measurements for both samples were performed at $0V$ with a microwave frequency of $8GHz$. Figure 6.3 (a) and (b) shows the spectra for in-plane rotation for the hybrid structure in the magnetic field for IM008 and IM009 spin valves. It can be seen that the intensity of the peaks decreases as the field rotates away from the direction of $\varphi = 0^o$. This could be related to the rf- field direction with respect to the magnetisation. At $\varphi = 0^o$, its direction is perpendicular to the direction of the dc-applied field (and hence the magnetisation), thus when the angle between them starts to decrease as the field's angle rotation increases until it reaches $\varphi = \mp 80^o$, the magnetisation is approximately parallel to the rf-field, hence the intensity of the FMR spectrum decreases [158]. For all angles, the FMR spectra show one clear resonance peak, with an H_{res} value of around $60mT$. Using a different scale in figure 6.4 (a) and (b) to show the difference between the $\varphi = 0^o$ and $\varphi = -80^o$ spectra measurements for IM008 and IM009, respectively, the H_{res} for both samples increases for $\varphi = \mp 80^o$, where the peak shifts to a higher field value. At first glance, it is apparent that the change in H_{res} in IM008 is greater than that in IM009, as discussed in detail later.

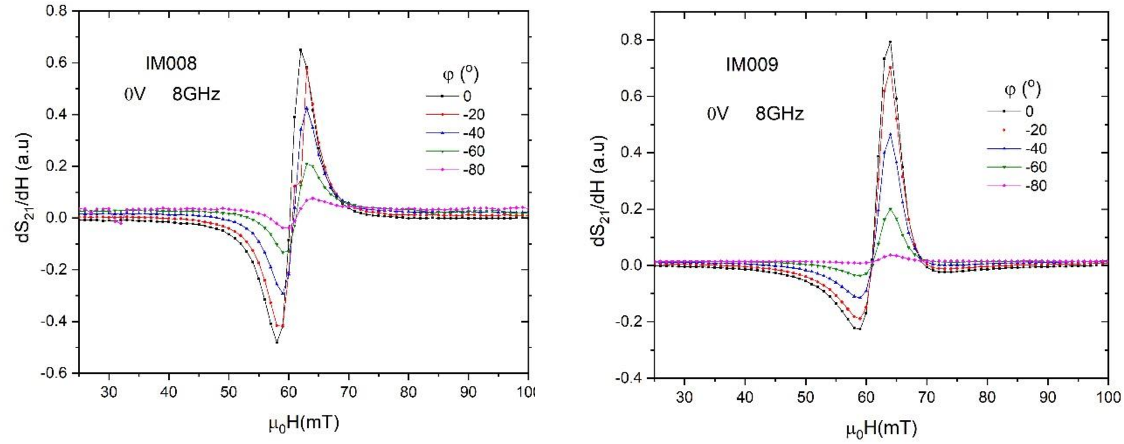

(a) (b)

Figure 6.3: FMR spectra for (a) IM008 and (b) IM009 spin valve rotation measurements between $\varphi = 0^o$ and $\varphi = -80^o$. These measurements were carried out at $0V$ and $8GHz$ microwave frequency. The results for rotation between $\varphi = 0^o$ and $\varphi = +80^o$ are not shown, but they show the same trend. The intensity of the spectra decrease is attributed to the rf-field direction with respect to the magnetisation, as discussed.

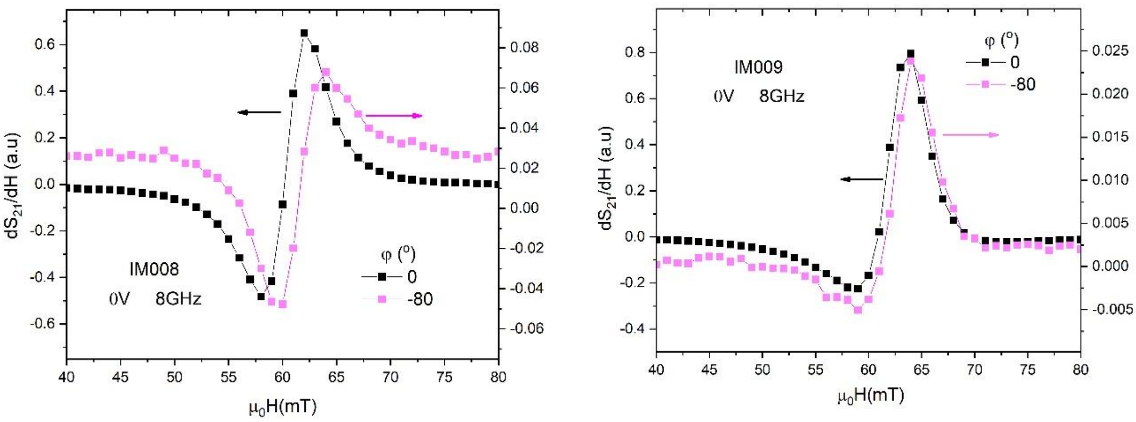

(a) (b)

Figure 6.4: Different scale of the FMR spectra for (a) IM008 and (b) IM009 spin valve rotation measurements for $\varphi = 0^o$ and $\varphi = -80^o$ to show the difference in H_{res} value.

To have a clear idea about the H_{res} dependence of the in-plane rotation of the field, figure 6.5 shows the H_{res} curves at $0V$ for IM008 and IM009 spin valves. Given the limitation in the rotation angle measurements, one can say that curves show a sinusoidal shape with two-fold symmetry form. The curve of H_{res} of IM008 shows a large phase shift from $\varphi = 0^o$ with the value of 24^o, while the H_{res} curve for IM009 shows very small phase difference with -4^o. In the H_{res} curve, the angle of the magnetic field (magnetisation) that gives the minimum (maximum) value of H_{res} represents the easy (hard) direction of the magnetisation [218]. For IM008 the easy axis is along $\varphi = +24^o$, while the hard axis is around $\varphi = -56^o$. For IM009, the data show the easy axis around $\varphi = -4^o$, and a hard axis at a certain value of $\varphi > +80^o$.

To extract the magnetic anisotropy K_u and the saturation magnetisation M_s of the magnetic layer that shows a clear resonance peak, the angular dependence of the H_{res} curves are fitted using the following equation (as discussed in section 2.5.1) [213, 219, 220, 221]:

$$H_{res} = \frac{\omega^2}{4\pi M_s \gamma^2} - H_u \cos\left(2\varphi - \beta\right) \tag{6.2}$$

where H_u is the uniaxial anisotropy field, β is the phase shift from $\varphi = 0^o$, and γ is the gyromagnetic ratio, ω is the microwave angular frequency equal to $2\pi f$, and M_s is the saturation magnetisation. The simulated curves are represented by solid blue lines in figure 6.5 for samples IM008 and IM009, whereas dots represent the experimental data. The fitting shows that this layer has a uniaxial anisotropy field $\mu_0 H_u = 0.32 \mp 0.06mT$ in IM008 spin valve, and $\mu_0 H_u = 0.18 \mp 0.01mT$ for the same layer in IM009. On the other hand, the saturation magnetisation is obtained from the fitting with a value of $M_s = (968 \mp 30) \times 10^3 A/m$ for IM008, while $M_s = (932 \mp 10) \times 10^3 A/m$ for IM009, using the permalloy $\gamma = 1.84 \times 10^{11} s^{-1} T^{-1}$ [222, 223]. From the saturation magnetisation values in both spin valves, one can say that the resonance peaks in the FMR spectra are related to the permalloy layer. For the single-layer sample of the permalloy (S476), the $M_s = (1030 \mp 20) \times 10^3 A/m$, measured using SQUID magnetometry (see section 3.2.3), showing a similar range of values of the M_s of the permalloy layers in the spin valve samples from this measurement. One the other hand, nickel has $M_s = 509 \times 10^3 A/m$ [51], which is very different compared to the permalloy, giving evidence of that peak being related to the permalloy. The difference in M_s values between the permalloy layers in all samples for single layer and spin valves could be attributed to the different interfaces in the samples [224]. Similar FMR measurements found that the M_s for the permalloy thin film with a thickness of $6nm$ is equal to $905 \times 10^3 A/m$ at room temperature measurements [223].

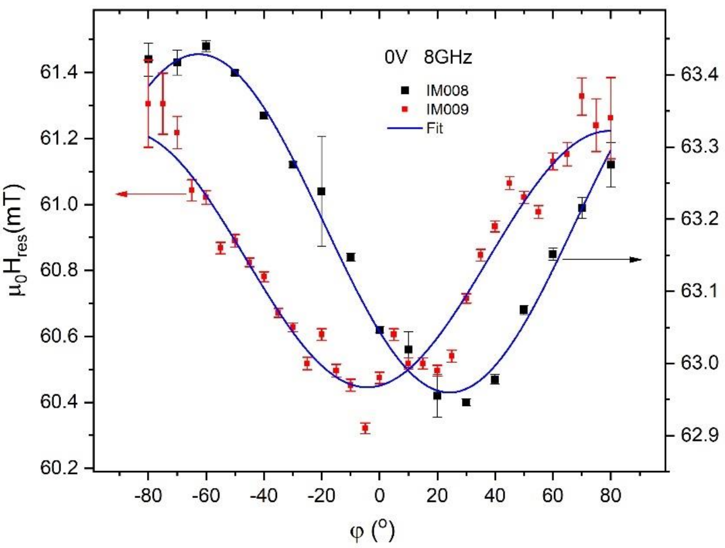

Figure 6.5: In-plane rotation dependence of H_{res} of permalloy layer in IM008 and IM009 spin valves samples, applying $0V$ to the transducer at $8GHz$ frequency. Dots represent the experimental data, and the solid line is the fit to equation 6.2.

To extract the magnetic anisotropies K_u constant for permalloy layer, the equation discussed in section 1.2.2.3 is used:

$$H_u = \frac{2K_u}{M} \tag{6.3}$$

This gives $K_u = 155 \mp 30J/m^3$ for the permalloy layer in IM008, and $K_u = 84 \mp 5J/m^3$ for the same layer in the IM009 spin valve. The difference between the two samples, as discussed previously, could be related to the interface, since samples have a different growth order of layers [224]. Here, for $0V$, the magnetic anisotropies in both samples are induced by strain, which could be introduced while mounting samples into the transducer. As discussed previously, the $0V$ does not mean 0 strain, as shown by the strain calibration in chapter 5 for the spin valve samples, where a compressive strain was demonstrated for spin valve devices used in magnetotransport measurements. In this measurement, a film was mounted on the piezoelectric transducer instead of devices for both spin valves, which means that at $0V$ the strain value or type could be different, which could be determined when discussing different voltages in the following sections.

6.4 Study of the strain effect on the permalloy layer static magnetic properties in IM008 and IM009 spin valves

6.4.1 The strain effect on static properties of permalloy in IM008 at $8GHz$

For IM008, two voltages were applied $+25V$ and $+50V$. The FMR spectra for $\varphi = 0^o$, and -80^o at different voltages are shown in figures 6.6 (a) and (b) respectively. For $\varphi = 0^o$, it can be seen that increasing the voltage from $0V$ to $+50V$ causes the H_{res} of the permalloy shift to the lower field, while for $\varphi = -80^o$ the H_{res} increases when the voltage increases. Focusing on $+50V$ rotation measurements, as shown in figure 6.6 (c), the H_{res} increases when the field rotates from $\varphi = 0^o$ to both directions of $\varphi = \mp 80^o$. The H_{res}increases from $60.6mT$ for $\varphi = 0^o$ to reach $61.4mT$ for $\varphi = -80^o$ when a $0V$ is applied, while it changes from $59.2mT$ to $62.7mT$ for $+50V$ for the same angle changes.

To understand the angular dependence of the resonance field at different voltages for the permalloy in IM008, the H_{res} curves are shown in figure 6.7 with the theoretical simulation. It can be seen that the variation of H_{res} with angle is increasing with increasing voltages. This indicates that the uniaxial field is increased by increasing the strain, and hence the magnetic anisotropy increases by increasing the strain. Using equation 6.2, the uniaxial field increases from $0.32 \mp 0.06mT$ for $0V$ to reach $1.0 \mp 0.1mT$ and $1.9 \mp 0.1mT$ for $+25V$ and $+50V$ (respectively). The saturation magnetisation M_s for the permalloy shows the same values as for $0V$ with $M_s = (966 \mp 15) \times 10^3 A/m$ for $+25V$ and $M_s = (969 \mp 10) \times 10^3 A/m$ for $+50V$. It is worth mentioning that $0V$ gives the same strain type, as all voltages give the same curve shape with the easy axis around $\varphi = 0^o$. This could be attributed to a tensile strain, as shown for the positive voltages in magnetotransport measurements since the easy direction is aligned along the long axis of the transducer.

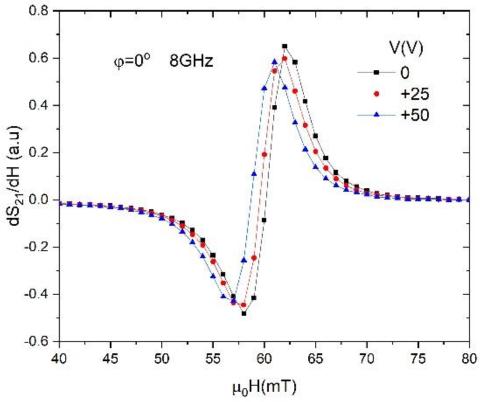

(a)

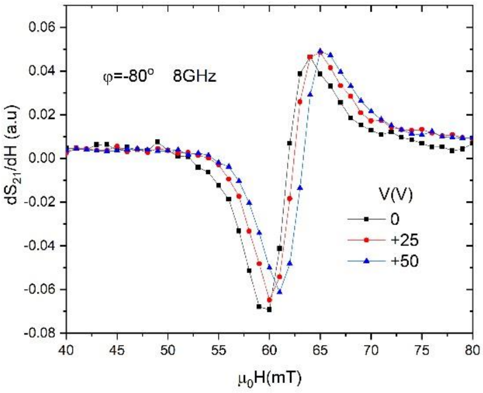

(b)

(c)

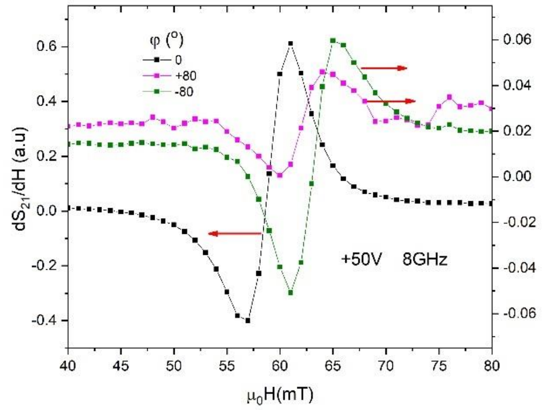

Figure 6.6: Different voltages measurements spectra for the permalloy in IM008 spin valve measured at 8GHz frequency when (a) $\varphi = 0^o$ and (b) $\varphi = -80^o$. The H_{res} value shifts to the left or right, depending on the direction of the magnetic field (magnetisation) with respect to the strain. (c) The spectra for the permalloy when a voltage of $+50V$ is applied at different directions $\varphi = 0^o$, -80^o, and $+80^o$. The difference between H_{res} of $-80^o$and $+80^o$ is discussed in the text.

The magnetic anisotropies change with voltage, as shown in figure 6.8 (a), increasing from $K_u = 155 \mp 30 J/m^3$ for $0V$ to $K_u = 920 \mp 50 J/m^3$for $+50V$. The phase shift also decreases from $\beta = 24^o$ for $0V$ to reach $\beta = 6^o$ for $+50V$, as shown in figure 6.8 (b). Figure 6.8 (a) and (b) could be connected, as when the magnetic anisotropies increase, the phase shift decreases. This could be ascribed to another induced anisotropy during the growth or mounting the film into the transducer, whereby this anisotropy competes with the magnetic anisotropy (magnetoelastic anisotropy) induced by the transducer. As the strain increases, the phase shift decreases due to the dominance of the magnetoelastic anisotropy. This agrees with the previous results of the strain controls the permalloy single layer sample and the permalloy in spin valves samples, where applying a tensile strain aligned the easy axis of the permalloy along this direction, since the permalloy has positive magnetostriction.

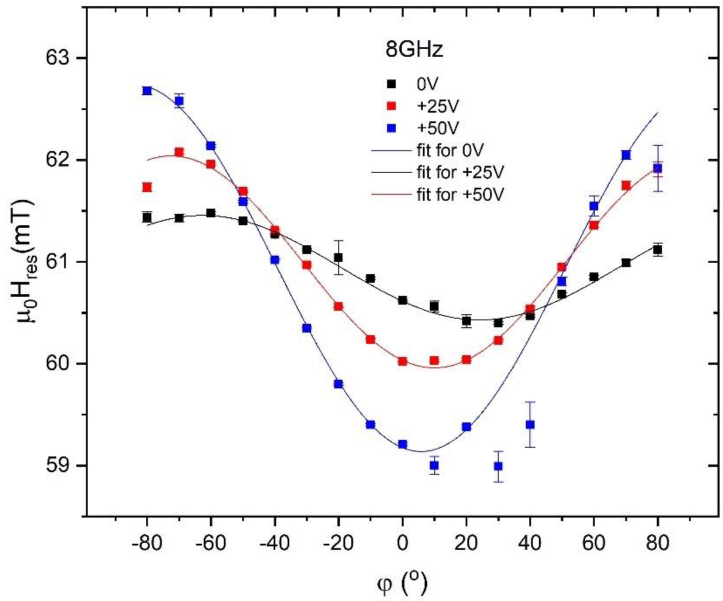

Figure 6.7: In-plane dependence of H_{res} of the permalloy layer in IM008 spin valve applying different voltages ($0V, +25V, +50V$) to the transducer at $8GHz$ frequency. Dots represent the experimental data and the solid line is the fit to equation 6.2.

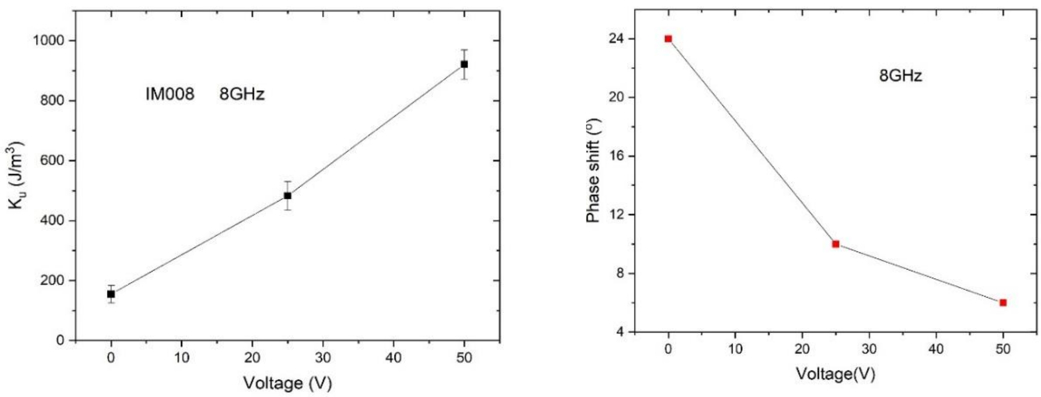

(a) (b)

Figure 6.8: (a) Magnetic anisotropies (K_u) of the permalloy layer in IM008 spin valve as a function of voltages ($0V, +25V, +50V$) applied to the transducer. The magnetic anisotropy (magnetoelastic anisotropy) increases with increasing strain induced in the spin valve. (b) The phase shift (β) of the easy axis of the permalloy from the long axis of the transducer decreases with increasing the voltage, as an indication of the dominance of the anisotropy induced by the actuator.

6.4.2 The strain effect on static properties of permalloy layer in IM008 at $14GHz$

For IM008, another microwave frequency measurement ($14GHz$) was carried out to check if there any difference in the static magnetic properties of the permalloy in IM008, and if that would show a clear peak for the nickel layer. Figure 6.9 shows the in-plane dependences of the H_{res} on magnetic field direction at different voltages: $0V$, $+25V$, and $+50V$. For all FMR spectra in all directions, similar line shape can be seen as for the 8GHz measurements, with no clear resonance for the nickel layer. For the permalloy layer, the M_s is equal to $(1000 \mp 50) \times 10^3 A/m$ for this frequency measurement, compared to $(970 \mp 30) \times 10^3$ for the $8GHz$ measurement when $0V$ is applied. These values agree within experimental uncertainty. The uniaxial anisotropy induced by the transducer and the phase shift of H_{res} curves have similar values obtained from $8GHz$ measurement. However, there are some differences, mostly within the uncertainty values, as shown by a comparison between the $8GHz$ and $14GHz$ measurements of anisotropies and the H_{res} curves phase shift, shown in figure 6.10 (a) and (b). A summary of all magnetic parameters of the permalloy in IM008 spin valve is presented in table 6.1.

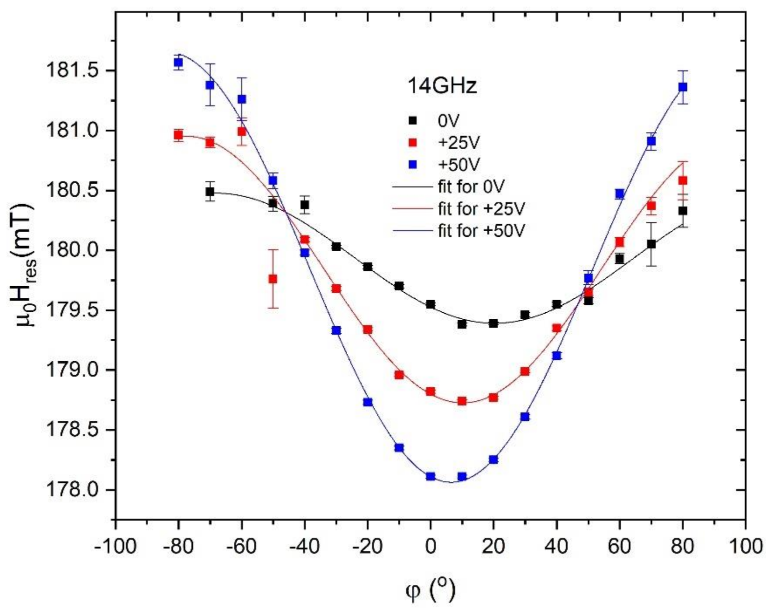

Figure 6.9: In-plane dependence of H_{res} of permalloy layer in IM008 spin valve applying different voltages ($0V, +25V, +50V$) to the transducer at $14GHz$ frequency. Dots represent the experimental data, and the solid line is the fit to equation 6.2.

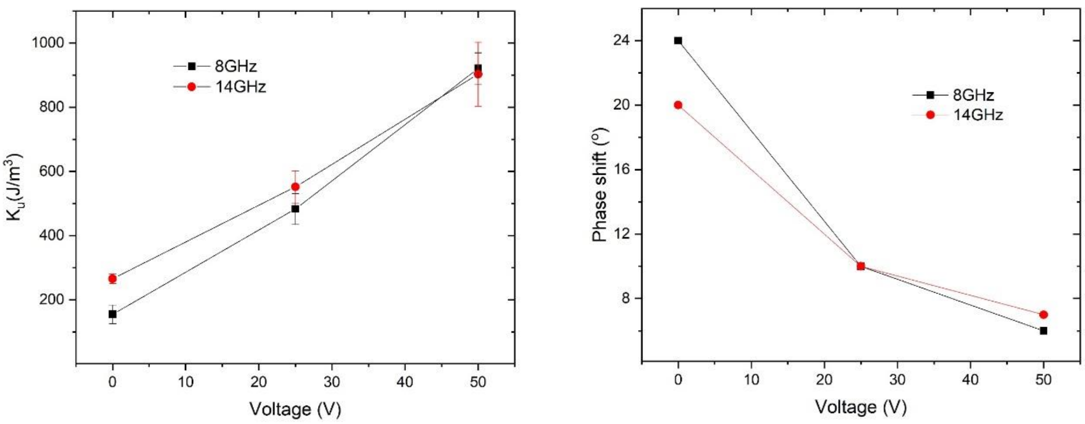

(a) (b)

Figure 6.10: Comparison between $8GHz$ and $14GHz$ measurements of (a) magnetic anisotropies of the permalloy layer in IM008 spin valve when different voltages are applied to the transducer, and (b) the phase shift of the easy axis from $\varphi = 0^o$.

Table 6.1: Summary of the static magnetic properties (Uniaxial field H_u, magnetic anisotropy K_u, saturation magnetisation M_s, and the easy axis shift β from $\varphi = 0$) of the permalloy in IM008 spin valve when applying two different frequencies ($8GHz$ and $14GHz$).

Frequency (GHz)	**Voltage (V)**	$\mu_0 H_u$ (mT)	K_u (J/m^3)	$M_s \times 10^3 A/m$	β (°)
	0	0.32 ∓ 0.06	155 ∓ 30	968 ∓ 30	24
8	25	1.0 ∓ 0.1	480 ∓ 50	966 ∓ 15	10
	$50V$	1.9 ∓ 0.1	920 ∓ 50	969 ∓ 10	6
	0	0.53 ∓ 0.03	266 ∓ 15	1000 ∓ 20	20
14	25	1.1 ∓ 0.1	550 ∓ 50	1002 ∓ 50	10
	$50V$	1.8 ∓ 0.2	900 ∓ 100	1000 ∓ 10	7

6.4.3 The strain effect on static properties of permalloy layer in IM009 at $8GHz$

For IM009 sample, two voltages were applied to the actuator, $-25V$ and $+50V$, along with $0V$. Figure 6.11 shows the in-plane H_{res} dependence of the field rotation of the permalloy layer in IM009 at different voltages. It can be seen from these curves that the different voltages (strain) affect the permalloy layer differently. For $0V$ and $+50V$ (tensile strain) it shows the same behaviour with the easy direction aligned around $\varphi = 0^o$, while applying $-25V$ (compressive strain) makes that direction magnetically harder. On the other hand, rotating the field by $\varphi = +80^o$or -80^o makes these directions magnetically harder for $0V$ and $+50V$, and easier for $-25V$. Figure 6.12 shows the FMR spectra at (a) $\varphi = 0^o$, (b) -80^o, and (c) $+80^o$ when applying different voltages values (note that the $+25V$ measurement is just applied for the $\varphi = 0^o$direction). It can be seen that H_{res} has the smallest value when applying $+50V$ compared to other voltages for $\varphi = 0^o$ direction measurement, as shown in 6.12 (a), with the largest value for $\varphi = -80^o$ and $+80^o$ shown in 6.12 (b) and (c) (respectively). One the other hand, for $-25V$ measurements, H_{res} has the opposite effect compared to $+50V$ measurements. This is attributable to the magnetostriction of the permalloy, whereby the magnetizations align along the long axis when a tensile strain is applied ($0V$ and $+50V$), aligned perpendicular to the long axis when applying a compressive strain ($-25V$).

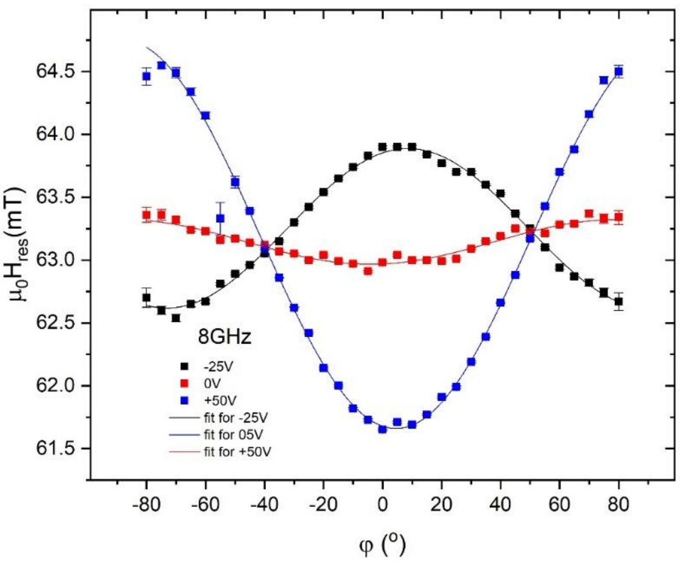

Figure 6.11: The in-plane dependence of H_{res} of permalloy layer in IM009 spin valve applying different voltages ($-25V, 0V, +50V$) to the transducer at $8GHz$ frequency. Dots represent the experimental data, and the solid line is the fit to equation 6.2.

The phase differences of the H_{res}curves of the permalloy in this sample are very small compared to the IM008 sample, which could be related to the quality of the sample (no extra or tiny induced anisotropy during the growth or glueing of the film into the transducer). The largest phase shift is $\beta = 8^o$ when a voltage of $-25V$ applied, while the smallest is equal to $\beta = -4^o$, and $\beta = +4^o$ for $0V$ and $+50V$ measurements, respectively. It is obvious that the intensity of the curves varies by changing voltages, which is attributable to uniaxial anisotropy changing with changing strain. The magnetic anisotropies are equal to $K_u = -585 \mp 10J/m^3$ when a voltage of $-25V$ is applied to the transducer, and $K_u = 700 \mp 10J/m^3$ when the voltage is ramped up to $+50V$.

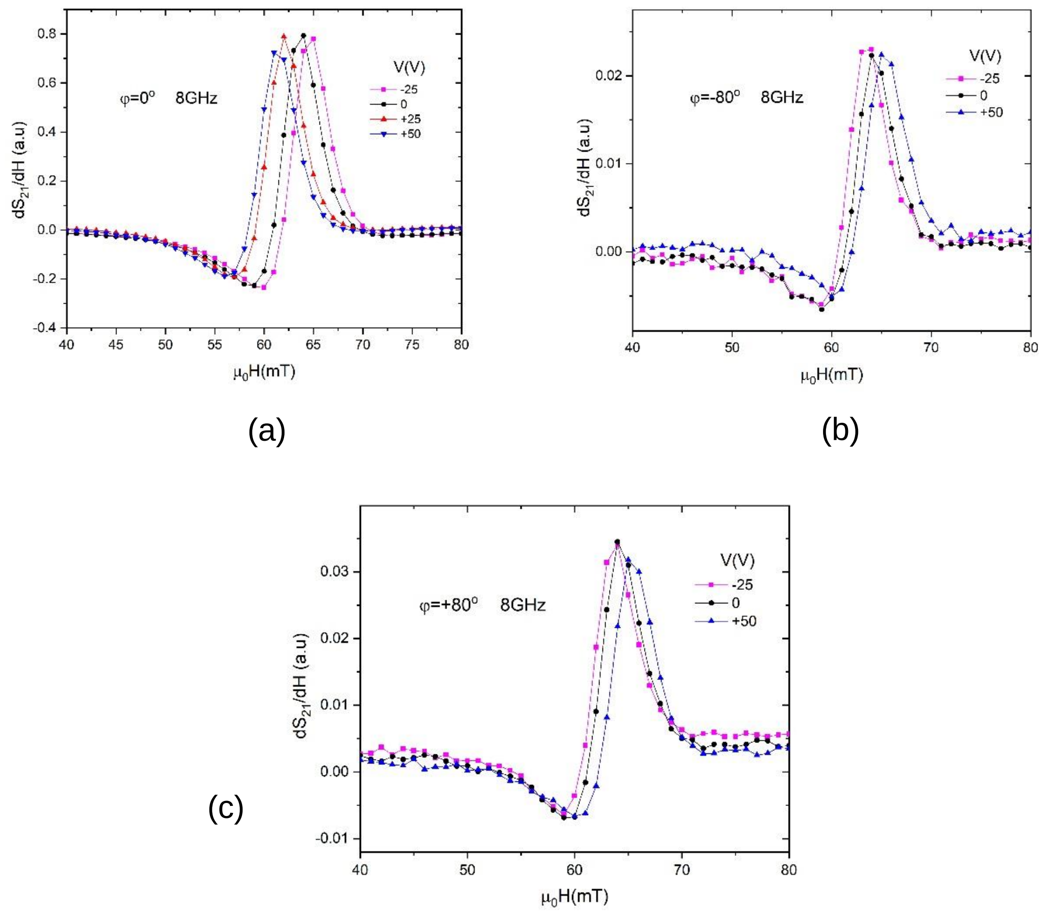

Figure 6.12: Different voltages measurements spectra for the permalloy in IM009 spin valve measured at $8GHz$ frequency when (a) $\varphi = 0^o$, (b) $\varphi = -80^o$, and (c) $\varphi = +80^o$. The H_{res} value shifts to the left or right, depending on the direction of the magnetic field (magnetisation) with respect to the strain.

Figure 6.13 shows the magnetic anisotropy dependence on the applied voltage. The magnetic anisotropy when $-25V$ is applied to the transducer is negative since a compressive strain is applied in this case. The M_s at different voltages for the permalloy in this spin valve is same as when $0V$ is applied. A summary of the magnetic parameters extracted for the permalloy is stated in table 6.2, along with the same data of permalloy in IM008 at $8GHZ$ frequency. Comparing the values of magnetic anisotropies and uniaxial field of the permalloy at $0V$ and $+50V$ (the only voltages in common for the two samples) in both spin valves, IM008 and IM009 show that the anisotropies and the uniaxial field have lower values for the permalloy in IM009 sample. This could be due to the growth order of the layers; in the IM008 sample, the permalloy is the bottom layer, near to the actuator, while it is at the top in the IM009 spin valve.

Table 6.2: Comparison between the static magnetic properties (Uniaxial field H_u, magnetic anisotropy K_u, saturation magnetisation M_s, and the easy axis shift β from ($\varphi = 0$) of the permalloy in IM008 and IM009 spin valves at $8GHz$ frequency.

Spin Valve	Voltage (V)	$\mu_0 H_u$ (mT)	K_u (J/m^3)	$M_s \times 10^3 A/m$	β (°)
$IM008$	0	0.32 ∓ 0.06	155 ∓ 30	970 ∓ 30	24
	25	1.0 ∓ 0.1	485 ∓ 50	965 ∓ 15	10
	$50V$	1.9 ∓ 0.1	920 ∓ 50	970 ∓ 10	6
$IM009$	-25	-0.63 ∓ 0.01	-590 ∓ 10	930 ∓ 30	8
	0	0.18 ∓ 0.01	84 ∓ 5	930 ∓ 10	-4
	$50V$	1.5 ∓ 0.01	700 ∓ 10	935 ∓ 60	4

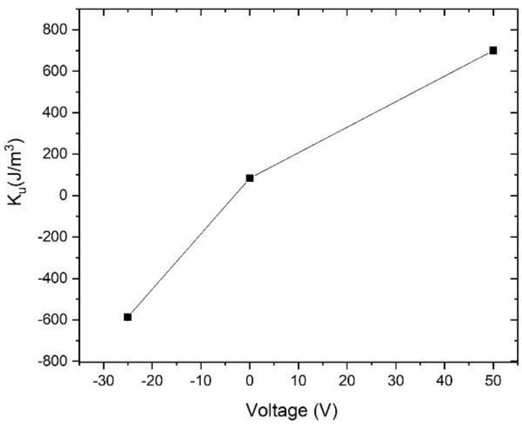

Figure 6.13: Magnetic anisotropies of the permalloy layer in IM009 spin valve as a function of voltages ($-25V, 0V, +50V$) applied to the transducer. The magnetic anisotropy (magnetoelastic anisotropy) increases with increasing strain induced in the spin valve. The error bars are very small compared to the size of the points.

Figure 6.14 compares the anisotropy constants that extracted for the permalloy layer in IM008 and IM009 spin valves (from this chapter), with the permalloy single layer sample (S476) (from chapter 3). The data for S476 sample extracted from two measurement directions, as discussed in detail in section 3.2.3. As explained before in chapter 3, the anisotropies are not extracted from all voltages between $-30V$ and $+50V$, rather for $\varphi = 90^o$ measurements, the voltages between $+50V$ and $+20V$ are used in the calculations while for $\varphi = 0^o$ the voltages used are between $-30V$ and $-5V$. Hence no continuous values for anisotropies for the whole voltage range between $-30V$ and $+50V$ for the single layer sample. Consequently, positive voltages are used from $\varphi = 90^o$ measurement, while negative voltages from $\varphi = 0^o$ measurement with no $0V$ in both measurements. As can be seen that the anisotropy values for the permalloy in IM008 spin valve and S476, there is a little difference in the values for positive voltage but still in the same range, with values of $920 \mp 50 J/m^3$ and $1020 \mp 40 J/m^3$, for $+50V$, respectively. On the other hand, for the IM009, the value of anisotropy of the permalloy at $+50V$ is $700 \mp 10 J/m^3$, which is different than the permalloy in S476 and IM009 samples. The difference between all samples could be related to the interface difference. As discussed previously in this chapter, IM009 sample shows the lowest anisotropy between these samples, and that might be related to the sample quality with less induced anisotropy during the growth. The decreasing in the anisotropy values with reducing voltages follow the same trend for all samples and nearly with the same slope. For the negative values, the values from S476 single layer sample and IM009 spin valve (no data for IM008) are not agreed, and that also could be related to the interface difference. The applicability of the single domain model for determining the anisotropy constant for S476 sample could be another reason for this difference slightly.

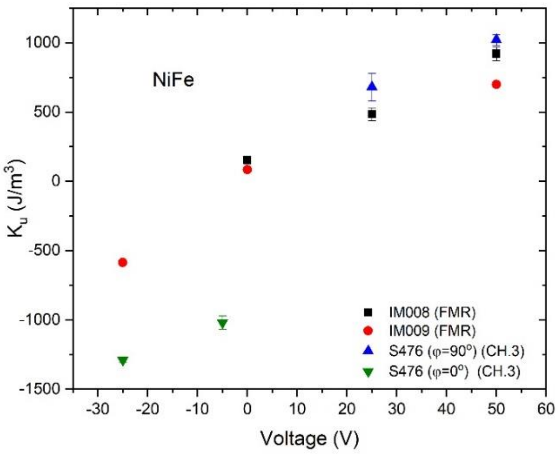

Figure 6.14: Comparison between the anisotropies of the permalloy from S476 single layer sample, and the permalloy in IM008 and IM009 spin valves (note that that data of S476 is from chapter 3, and no anisotropy value at $0V$ for S476 sample).

6.5 An investigation of the static magnetic properties of nickel layer in IM009 spin valve

As discussed previously, for both samples, the resonance peak of the nickel is not sufficiently clear to extract the quantitative parameters of the magnetic properties. However, for the IM009 spin valve, when a voltage of $+50V$ is applied to the transducer, one can see a feature show some consistent changes around the field of $120mT$ in the FMR spectra of the different in-plane rotation measurements, which could be related to the nickel layer. To investigate this feature, zoomed FMR spectra at different directions are shown in figure 6.15 (note that the angles shown are from 0^o to $+45^o$, just to show the trend of changes, and not all angles are included). The in-plane change is opposite to the change in the permalloy layer when a voltage of $+50V$ is applied (the red arrows in figure 6.15 indicate the beginning and the end of the change as a function of field rotation). The field value H at the maximum intensity of the point of that feature is determined from each spectrum for each measurement of angles between $\varphi = +80^o$ and $\varphi = -80^o$. An assumption was made, and that values of H are considered as H_{res} for the nickel layer and plotted as a function of the in-plane rotation of the applied field, as shown in figure 6.16.

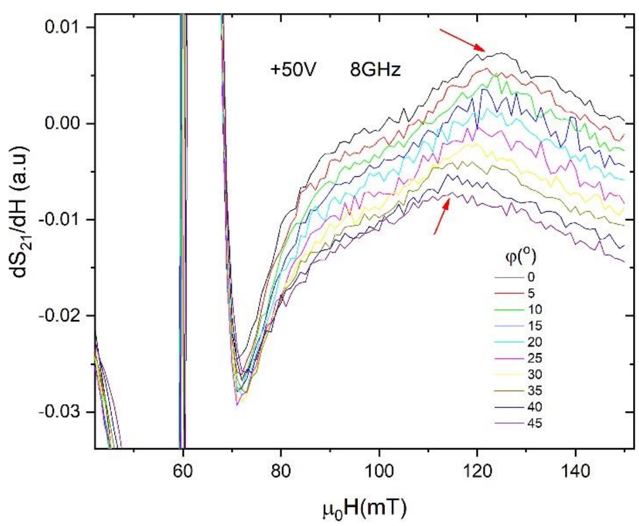

Figure 6.15: Zoomed FMR spectra of the IM009 spin valve at $+50V$ showing a small feature (possibly related to the nickel layer) changing with the rotation of the field (change indicated by red arrows). The maximum of the feature was determined for all directions and assumed to be equal to the H_{res}. These values were plotted in figure 6.15 as a function of the in-plane field.

At $\varphi = 0^o$. The curve shows a hard magnetic axis for this layer (nickel) and the opposite to the permalloy curve when applying the same voltage. On the other hand, for $\varphi = +80^o$ and $\varphi = -80^o$, the curve shows softer directions. A comparison between the curves of the permalloy and nickel layers' resonance field of the IM009 spin valve is shown in figure 6.16. This agrees with the previous result of the effect of strain on magnetotransport measurements of nickel and permalloy in IM008 and IM009 spin valves; these layers have different magnetostriction signs, and hence different magnetisation easy axis direction when strain is applied.

The nickel curve of H_{res} is fitted to the equation 6.2 to give $\mu_0 H_u = 10.2 \mp 1.2mT$, which is very large compared to the permalloy. Weiller et al. [80] found that applying a voltage of $+20V$ to an actuator induced a uniaxial field in a nickel polycrystalline film of the of value $4.4mT$. Another measurement carried out by Brandlmaier [225] found that applying $+90V$ to a polycrystalline nickel sample, is inducing uniaxial field with a value around $17mT$. Comparing the values from these studies with the value extracted in this study shows the same range of the uniaxial field. The saturation magnetization extracted for the nickel layer is equal to $(470 \mp 10) \times 10^3 A/m$, which is in the range of the nickel saturation magnetization (as explained previously), with a value of $M_s = 509 \times 10^3 A/m$ found by Neugebauer et al. [222], although it does not agree within experimental uncertainty. The gyromagnetic ratio used for the nickel is $1.94 \times 10^{11} s^{-1} T^{-1}$ [226].

Figure 6.17 (a) and (b) show the second feature (related to the nickel layer) in FMR spectra of IM009 spin valve at different directions when applying $0V$ and $-25V$, respectively. For $0V$, It is difficult to discern any trend for the nickel resonance feature change with directions, as shown by the red arrow in the figure, whereby all peaks are at the same field represent H_{res}. For $-25V$, there is a small change in the feature as can be seen by the small shift in the H_{res} feature from high field to low field, as shown in figure 6.17 (b). The H_{res} values are extracted in the same way performed for $+50V$ and plotted in figure 6.17 (c) along with the data of $+50V$. As can be seen, the angular dependence of H_{res} at $-25V$ shows the opposite effect to the $+50V$ as expected that the compressive strain affected oppositely to the tensile strain. The data between

$\mp 45^o$ and $\mp 80^o$ angles are not shown in the curve since the FMR spectra for this direction is very flat at this feature. However, the $M_s = (470 \mp 10) \times 10^3 A/m$ is extracted which agree with $+50V$ measurement, while $\mu_0 H_u = 4.0 \mp 3.5mT$ with a high uncertainty value. From the measurements of $-25V$ and $+50V$, one can assume that the nickel has negative magnetostriction opposite to the magnetostriction effect in the permalloy sample, as shown in figure 6.11.

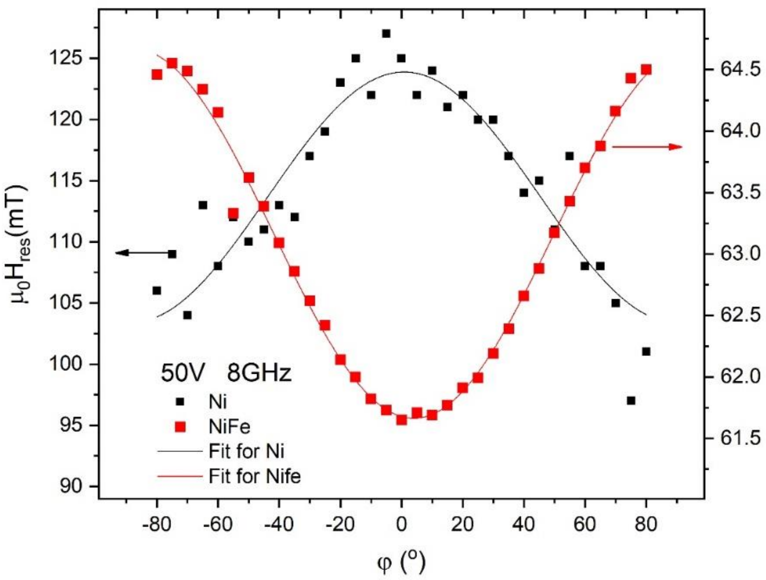

Figure 6.16: The in-plane dependence of H_{res} of the nickel layer in IM009 spin valve at $+50V$, where H_{res} values extracted as discussed in the text (black dots). The red dots are the H_{res} curve for the permalloy layer at the same voltage and frequency. The solid lines represent the fit to equation 6.2.

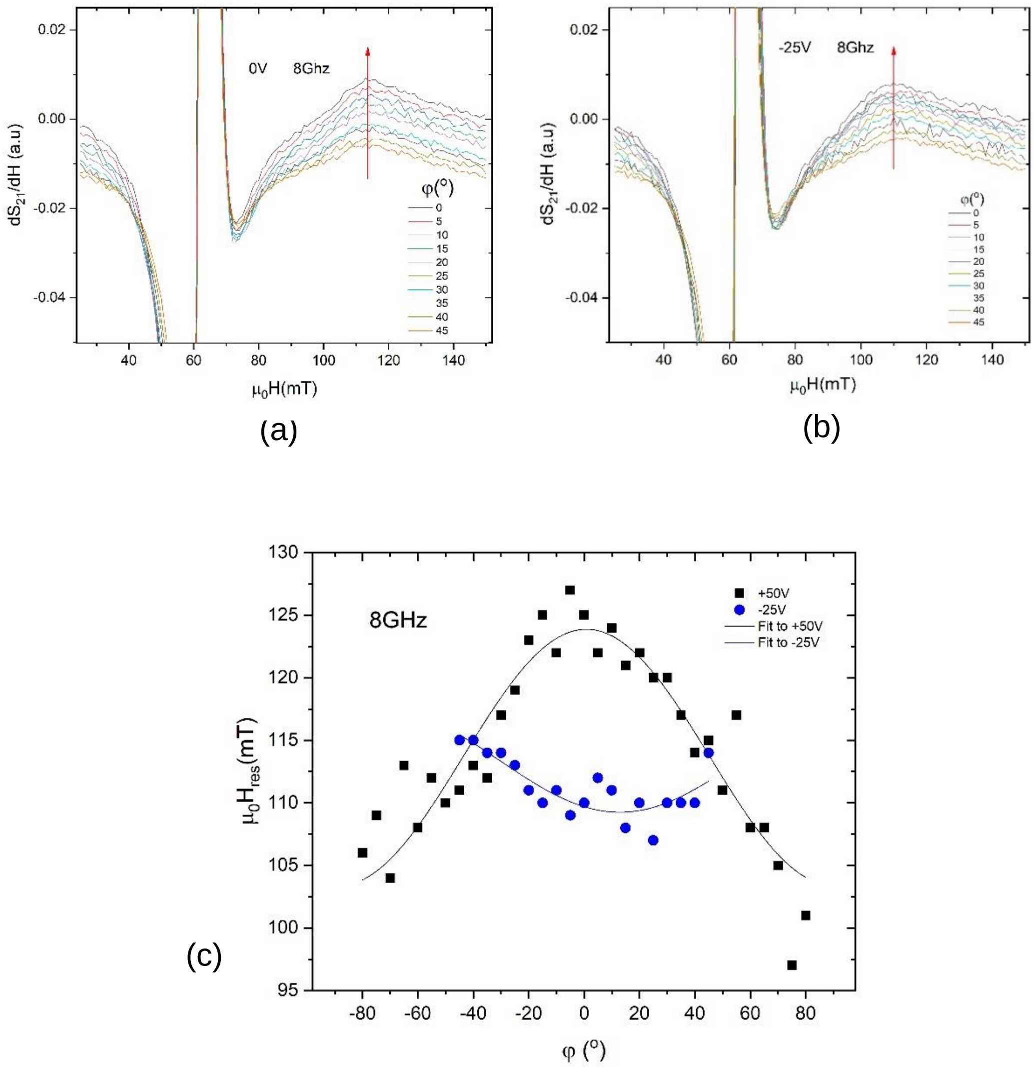

Figure 6.17: Zoomed FMR spectra of the second feature of IM009 spin valve at (a) $0V$ and (b) $-25V$, whith small shift in peaks' maximum (H_{res}) related to the nickel for -25, while no difference in $0V$ spectra. (c) comparison between The in-plane dependence of H_{res} of the nickel layer in IM009 spin valve at $+50V$ and $-25V$, shows the opposite effect between the two voltages.

6.6 Study of the strain effect of dynamic properties of the permalloy layer in IM008 and IM009 spin valve samples

Since no data can be extracted for the nickel dynamic properties, this section studies only the permalloy layer dynamic properties in IM008 and IM009, and how the strain could affect those properties. To study the dynamic properties of the permalloy, the linewidth values as a function of the microwave frequency were extracted by fitting the FMR spectrum, as discussed in 6.2. (see figure 6.1 (b)), where a range of frequencies was applied between $6GHz$ and $15GHz$ for both spin valves at $0V$. Figure 6.18 shows the FMR spectra of the IM008 spin valve sample at different frequencies between $13GHz$ and $15GHz$ for $\varphi = 0^o$ direction and $0V$ (black coloured spectra). The linewidth as a function of frequency for the permalloy layer in both spin valves is shown in figure 6.19 (a) and (b). Figures in 6.19 shows that the linewidth depends linearly with the microwave frequencies and hence this data can be fit to the equation 1.51 that discussed before in chapter 1:

$$\Delta H(f) = \Delta H_o + \frac{2\pi\alpha f}{\gamma} \tag{6.4}$$

where ΔH_o is the extrinsic damping that depends on magnetic inhomogeneities of the sample, its value increases with increasing defects in the sample, while the second term is dependent on the frequency with α is the Gilbert damping. For Gilbert damping, the permalloy layer in IM009 shows a value of 0.012 ∓ 0.001, which is the same within the experimental uncertainty of the permalloy layer in IM008, with a value of 0.010 ∓ 0.002. Permalloy of $4nm$ thickness with different interfaces of Ta and Cu has been found to have a value of $\alpha = 0.01$ [227]. On the other hand, the extrinsic damping shows different values for the two samples, being equal to $0.46 \mp 0.08mT$ for the permalloy layer in IM008, and smaller for the permalloy layer in IM009, with a value of $0.31 \mp 0.06mT$. This could be attributed to the growth quality of the IM009 sample, as mentioned previously. In general, these values are small for both samples, and that gives an indication that both spin valves have good structure quality.

A voltage of $+50V$ is applied to IM008 sample in the same direction using the same range of frequencies to compare with $0V$ measurements, see the spectra of the $+50V$ with the red colour in figure 6.18 where the H_{res} values of all spectra of $+50V$ measurements shift to the left of $0V$ spectra. The extracted linewidth values at each frequency are shown in figure 6.19 (c), along with the linear fit. The Gilbert damping shows the same value to that measurement at $0V$ for the same sample, with a value of 0.010 ∓ 0.001. On the other hand, the extrinsic damping shows an increase when the voltage ramped to $+50V$ to reach $0.73 \mp 0.04mT$. As will discuss later that the extrinsic contributions to the linewidth broadening could be introduced in the film due to many reasons. Parkes et al. [212] found that extrinsic damping is dependent on strain induced in the film, which could be due to the varying of the strain across the thin film, and which could introduce magnetic properties inhomogeneity.

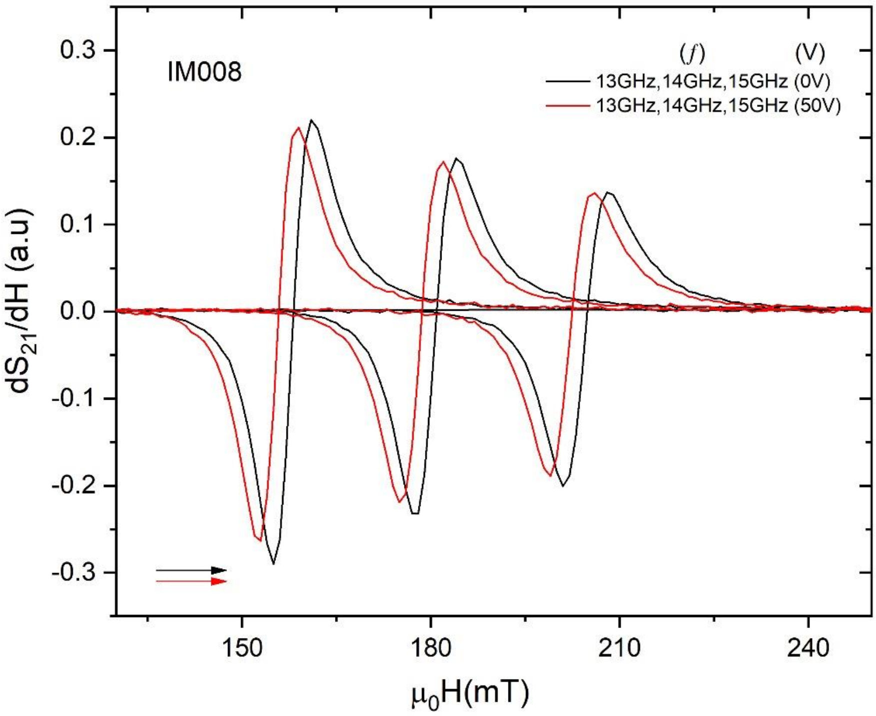

Figure 6.18: Comparison between spectra of $0V$ (black colour) and $+50V$ (red colour) measurements for a range of frequencies between $13GHz$ and $15GHz$ where the H_{res} values of $+50V$ measurements shift to the left. The two arrows at the bottom indicate the direction of frequency starting from ($13GHz$).

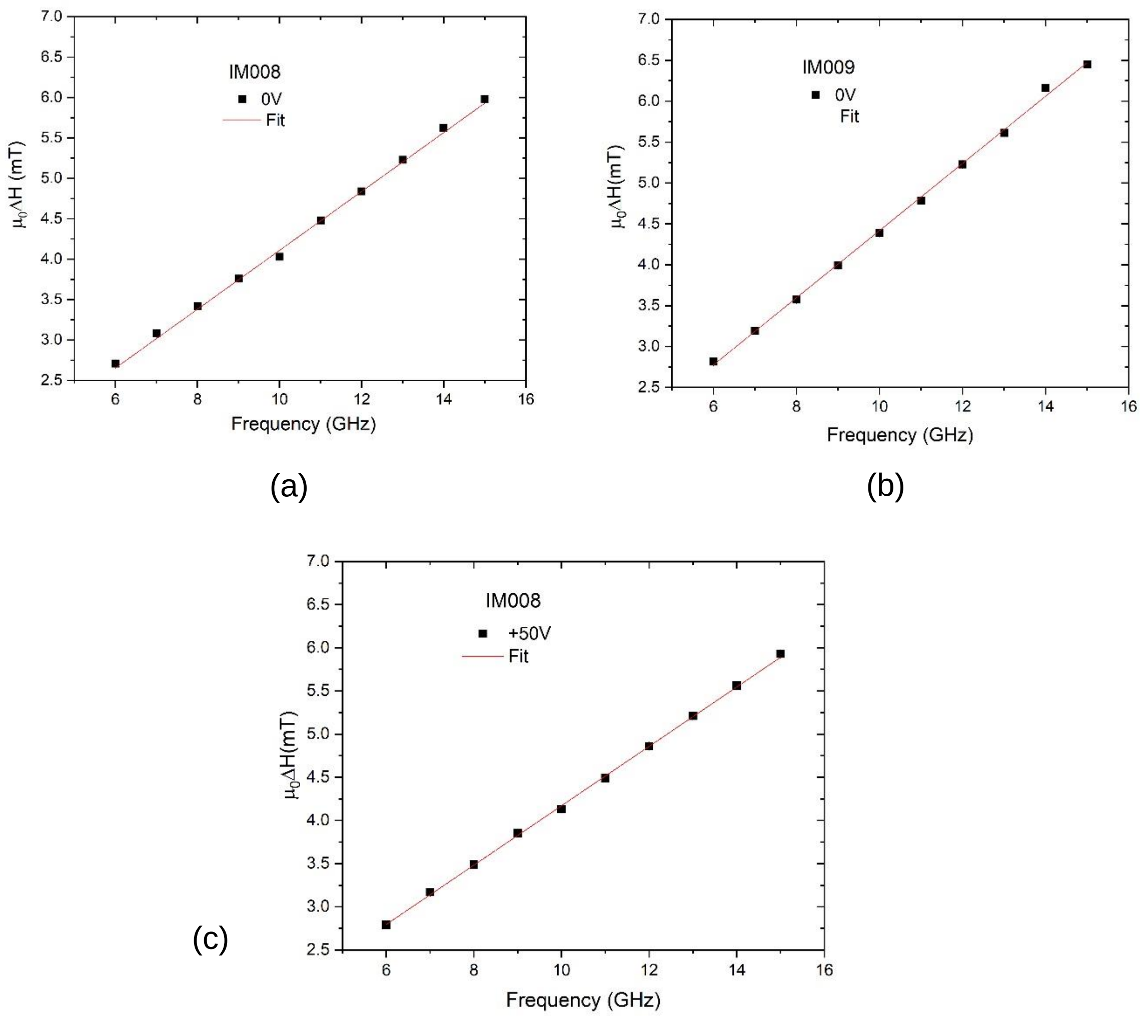

Figure 6.19: The linear fit of the linewidth values for the permalloy layer as a function of frequency for (a) IM008 at $0V$, (b) IM009 at $0V$, and (c) IM008 at $+50V$. The line is fitted to equation 6.3 to extract the Gilbert damping and extrinsic damping values.

The ΔH shows an in-plane angular dependence of the magnetic field as shown in figures 6.20 (a) and (b) for the permalloy layer in IM008 and IM009 samples at 8GHz frequency and different voltages applied. The curves of the ΔH show different curve shape than that shown for the in-plane dependence of the H_{res}. As shown in equation 6.3 that there are two contributions to the linewidth, extrinsic (ΔH_o) and intrinsic representing by the second term ($\frac{2\pi\alpha f}{\gamma}$) in the equation. The linear fit using the equation enables to find the intrinsic Gilbert damping, while the zero-microwave frequency offset determines the extrinsic contribution. To understand the angular dependence of the ΔH, recall the equation 1.56 that discussed in section 1.2.6.1 giving different contributions of the linewidth broadening as follows:

$$\Delta H = \Delta H^{Gilb} + \Delta H^{mosaic} + \Delta H^{inhom} + \Delta H^{2mag} \tag{6.5}$$

where the first term represents the intrinsic part of the linewidth while others represent the extrinsic contributions. The second term represents the mosaicity term which is due to the variation of the magnetic properties of the thin film sample over a large scale of regions within the film. The third term of the linewidth broadening is inhomogeneity which due to the fluctuation of the magnitude and direction of the effective internal magnetic field in the film. The fourth term is the Two magnon scattering (TMS), and it measures the scattering rate between the uniform magnon ($k = 0$) and the degenerate magnon ($k \neq 0$) and depends on the in-plane defect of the film. This term can affect the in-plane measurement of the linewidth since it relies on structural features and defects. In the linewidth measurement as a function of frequency, the TMS term manifests as nonlinear curve (knee) instead of linear relation which is not in this study and that could exclude the TMS from the in-plane dependence of the ΔH [228, 229, 230, 231]. Another measurement could be useful also to determine if the TMS has any contribution by performing out of plane measurement since the TMS is an in-plane feature, and it is inactive for the perpendicular measurement [232]. The mosaicity term also depends on the in-plane and out of plane measurements while the inhomogeneity term depends on the demagnetisation field [227, 231,233, 234]. Another reason that might cause an angular dependence of the linewidth in spin valves is the spin pumping which arises from the layers different alignments and their precession's magnitude [235, 236]. Baker et al. [149] found that in the spin valve of structure $Co_{50}Fe_{50}$/Cr/$Ni_{81}Fe_{19}$, the angular dependence of the linewidth is related to the anisotropic spin pumping of the $Ni_{81}Fe_{19}$ correlated to the in-plane damping variation of $Co_{50}Fe_{50}$ layer. They attributed that to the anisotropic torque exerted by the pumped current from the permalloy layer through Cr (they used different Cr thickness to control the static magnetic alignment between layers) to $Co_{50}Fe_{50}$ layer. The spin pumping can cause an angular dependence in the linewidth of multi-layered systems. This phenomenon can be studied by measuring the increase in the damping through the change in the FMR linewidth. Inverse Spin Hall effect is another technique that can be used to study the spin pumping through the normal metal [237]. Another measurement could be conducted is the x-ray magnetic circular dichroism (XMCD) for precession measurement for specific layers [149].

Further investigation needed to carry out to understand the in-plane dependence of the linewidth. For instance: Conducting measurement of sweeping frequencies at different voltages and different directions and compares that with $\varphi = 0^o$ measurement (measurements for $\varphi = 0^o$ shown in figures 6.19). Out of plane measurements could be useful also to compare that with the in-plane measurement, which could give a clear idea about which term is contributing to the angular dependence of ΔH, mainly useful to determine TMS contribution.

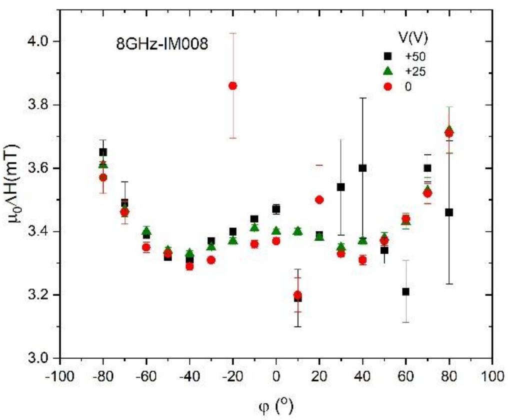

(a)

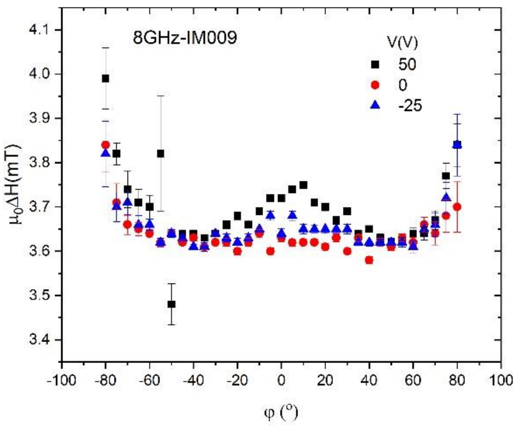

(b)

Figure 6.20: The in-plane dependence of ΔH of the permalloy in (a) IM008 and (b) IM009 spin valves at different voltages (the same voltages explained in the previous sections).

6.7 Conclusion

The strain effect on static and dynamic magnetic properties of pseudo spin valves was investigated in this chapter using ferromagnetic resonance technique. The IM008 and IM009 spin valves films were mounted onto the top of the piezoelectric transducers, and different measurements were conducted by rotating the magnetic field by 160^o around the hybrid structure, mainly at one frequency of $8GHz$ for both samples, while $14GHz$ was also applied for IM008 to check for any differences in the permalloy properties, or to show any response for the nickel layer. For the purpose of studying the dynamic properties of the spin valves, a range of frequencies between $6GHz$ and $15GHz$ were applied at $\varphi = 0^o$. The effects of the voltage (strain) in the FMR measurements were studied and compared between samples.

For the permalloy layer in both spin valves, the resonance field values were controlled by the voltage, which is due to the strain-induced anisotropies in the permalloy layer. The anisotropy values extracted from the angular dependence of H_{res}, for permalloy in IM008, the anisotropy changes from $155 \mp 30J/m^3$**,** when $0V$ is applied to the transducer, to $920 \mp 50J/m^3$**,** when the voltage increases to $+50V$. On the other hand, for the same layer in IM009, the magnetic anisotropy increases from $-585 \mp 10J/m^3$ to $700 \mp 10J/m^3$ when the voltage changes from $-25V$ to $+50V$. The change in the magnetic anisotropy is ascribed to the magnetostriction properties of the permalloy, whereby the strain controls the magnetisation direction; since it has positive magnetostriction, its magnetisation aligns with the strain direction. For the M_s of the permalloy, the measurements of both samples show a value for the M_s in the range of measurement performed to the single-layer S476 measured using the SQUID (chapter 3), with values of $M_s = (968 \mp 30) \times 10^3 A/m$ and $M_s = (932 \mp 10) \times 10^3 A/m$ for the IM008 and IM009 samples at $0V$, respectively.

The FMR spectra for both samples show one clear resonance related to the permalloy, while the nickel peaks were not clear, and it is difficult to extract the static properties of nickel. This could be ascribed to the dynamic exchange between the permalloy and nickel layers which related to the spin pumping between the two layers through the copper where the permalloy act as a spin sink causing non-local damping for the nickel layer. However, at $+50V$ for IM009, a consistent change in the absorption line as a second feature appeared, and an assumption was made to calculate the static properties of the nickel. This strain measurement gives a uniaxial field of $\mu_0 H_u = 10.2 \mp 1.2 J/m^3$ and $M_s = (469 + 10) \times 10^3 A/m$ for the nickel layer, which is comparable to other studies [51,224]. For $-25V$ measurement, the angular dependence of the H_{res} is extracted from the data of angles between 0 and ∓ 45, and gives $\mu_0 H_u = 4.0 \mp 3.5 J/m^3$ and $M_s = (470 + 10) \times 10^3 A/m$. The results from $-25V$ and $+50V$ proved that nickel has negative magnetostriction opposite in sign to the permalloy layer.

For the dynamic properties, the permalloy shows a Gilbert damping of 0.010 ∓ 0.002 for IM008 and 0.012 ∓ 0.001 for IM009, while the extrinsic damping shows that the quality of IM009 is better than IM008, since it has less extrinsic damping value. The Gilbert damping is independent of strain, while the extrinsic damping shows some dependence, which may indicate that the strain might vary inhomogeneously across the film. Further investigation needed to study the angular dependence of the linewidth to determine the broadening reason as discussed the terms in equation 6.5. For instance, out of plane measurement could be useful to determine if it is the broadening caused by the two magnons scattering effect. Another measurement could be useful also, measuring the line width by conducting measurement at different frequencies for different directions and compare that with $0V$ and $\varphi = 0^o$ measurement. Other techniques could be used to examine if the angular dependence is related to spin pumping phenomenon by using, i.e. inverse Spin Hall effect and XMCD.

Chapter 7: Conclusion and Outlook

This thesis investigated strain-induced anisotropy in the permalloy and nickel single layers and spin valves using a hybrid structure of piezoelectric transducer/ spin valve (single layer). This was motivated by the great interest in the technological application of spintronics with low power consumption. The experiments used films and devices of three sets of samples grown in a sputter magnetron system. The study of all samples was carried out using magnetotransport measurements, SQUID, ferromagnetic resonance, and computational calculation. Photolithography technique was used to fabricate microdevices from all samples for the magnetotransport measurements. The strain was induced in the magnetic layers by applying a voltage across the piezoelectric transducer.

The strain effect on the single-layer samples was investigated in chapter 3, using magnetotransport measurements. Permalloy sample Ta/$Ni_{80}Fe_{20}$/Ta (S476) showed a clear response to the strain, manifested as a change in magnetoresistance curves as the voltage was varying across the actuator. Varying the voltages between $-30V$ and $+50V$ across the transducer tunes the strain in the permalloy layer between -1.76×10^{-4} (compressive strain) and $+1.76 \times 10^{-4}$ (tensile strain), respectively. The magnetoresistance ratio varied significantly with varying strain-induced anisotropy. For example, it changed from 0.09% to 0.90% when the voltage across the transducer was ramped up from $-30V$ to $+50V$ for the measurements when the magnetic field was perpendicular to the long axis of the transducer ($\varphi = 90^o$). The magnetisation hysteresis loops were extracted from the magnetoresistance curves, showing a clear change in the reversal loops with the strain. For instance, for $\varphi = 90^o$ measurment, the magnetisation prefers to lie along the field direction when applying a compressive strain, and thus the magnetisation hysteresis loops exhibit easy reversal for this direction. On the other hand, applying a tensile strain on this configuration changed the direction of the magnetisation to align perpendicular to the field and show hard hysteresis loop. The strain-induced magnetic anisotropy in permalloy sample affected the magnetisation orientation to rotate by 90^o when changing the strain between the maximum values of tensile and compressive strain.

The switching field of the permalloy varied between $0.8mT$ and $1.8mT$ when the voltages change between $-30V$ and $+50V$, respectively, for the measurement when the magnetic field is parallel to the transducer ($\varphi = 0^o$). The normalised remanent magnetisation (Mr/Ms) of the permalloy sample also tuned with the voltage, where it changed from 0.99 (easy axis) to 0.49 (hard axis), when the voltage changed from $+50V$ to $-30V$, respectively. The coherent rotation model was applied to extract magnetic anisotropies from a certain region in the magnetisation hysteresis loop, as other regions did not follow the single model rotation, exhibiting more complicated reversal of domain nucleation and domain walls movements. For the calculated curves, the magnetic anisotropy varied as a function of voltages. For the measurement direction when $\varphi = 90^o$, the anisotropy values changed between $K_s = 1020 \mp 40 J/m^3$ and $K_s = 640 \mp 120 J/m^3$ for the voltages of $+50V$ and $+20V$, respectively, while for the direction of $\varphi = 0^o$, the anisotropy values changed between $K_s = -1370 \mp 20 J/m^3$ for $-30V$ and $K_s = -1020 \mp 50 J/m^3$ for $-5V$. The magnetoelastic anisotropy constants B_1 were extracted from the linear fit of anisotropies versus strain curves, with values of $B_1 = (3.8 \mp 0.3) \times 10^6 J/m^3$ and $B_1 = (2.9 \mp 0.2) \times 10^6 J/m^3$ for $\varphi = 0^o$ and $\varphi = 90^o$, respectively. The saturation magnetisation of the permalloy was measured using SQUID magnetometry with $M_s = (1030 \mp 20) \times 10^3 A/m$, and magnetic anisotropy of $K_s = 320 \mp 10 J/m^3$ which might be introduced in the sample during the growth process.

Although the permalloy $Ni_{80}Fe_{20}$ has zero magnetostriction in bulk form, this sample showed quite large value compared to the values reported by other studies, even for low-thickness films. The magnetostriction of S476 could be enhanced due to the surface term at low thicknesses, as suggested by the Néel model [49]. Another reason for the magnetostriction of S476 is that the sputtering target gave different stoichiometry rather than 80:20 ratio, and it was found that the magnetic properties of this sample are close to the values of a previous investigation [53], with the stoichiometry of $\mathrm{Ni_{61.9}Fe_{39.1}}$.

For the nickel (Ni) sample Ta/S475/Ta with a thickness of $5nm$, the magnetotransport measurements did not show any response to the strain in all measurements directions. The zero magnetostriction value of this sample is comparable to that achieved by Bochi et al. [48] where the magnetostriction at the thickness of $8nm$ showed zero magnetostriction, and at this thickness the sign of magnetostriction inverted between positive (for films with more than $8nm$ thickness) and negative (for films with less than $8nm$ thickness).

Both samples show different magnetostriction values compared to the bulk value, which could be further investigated by growing two sets of samples for the permalloy and nickel to study the effects of thickness variation on magnetostriction. The reversal of the permalloy sample S476 at different strain values could be studied using magneto-optical Kerr effect (*MOKE*) imaging technique, to study the formation of the magnetic domains at different induced strain values using the same microdevices deployed in transport measurements. This could allow understanding of why the reversal is different before and after the switching field, particularly at the hard reversal.

Studying the magnetisation reversal and magnetoresistance properties of all spin valves at $0V$ is presented in chapter 4. Magnetisation reversal for all spin valves was measured using SQUID magnetometry, which showed two distinct reversals for the permalloy and nickel layer (except for IM009), with a very narrow switch for both layers. For IM008 (PZT/Ta/NiFe/Cu/Ni/Ta) and IM009 (PZT/Ta/Ni/Cu/NiFe/Ta) pseudo spin valves, the coercivities of the permalloy show similar values at $300K$ with a value of $H_c = 0.5mT$ in both spin valves, while the nickel shows different values with $H_c = 4.25mT$ for IM008 and narrow reversal with $H_c = 0.9mT$ for IM009 spin valves. Both pseudo spin valves show clear giant magnetoresistance (GMR) with very close values of 1.5%, with broader peaks for IM008 (as the coercivity of nickel is greater than in IM009).

On the other hand, for S548 (PZT/Cr/NiFe/Cr/Ni/IrMn/Cr) and S549 (PZT/Cr/Ni/Cr/NiFe/IrMn/Cr), the magnetisation reversal hysteresis showed similar coercivities for the permalloy of $\mu_0 H_c = 0.25mT$ and $\mu_0 H_c = 0.5mT$ in S548 and S549 samples at RT, respectively. On the other hand, nickel showed a difference in coercivity, with values of $17.3mT$ and $22.5mT$ in these spin valves. Although the use of Cr spacer in these spin valves enhances the coercivity of the nickel layer, the magnetoresistance showed a clear anisotropic magnetoresistance effect (AMR) and no GMR in these spin valves. This could be ascribed to the Cr layer suppressing the electron spin flowing between layers, hence affecting the GMR.

Despite using IrMn layer in these spin valves, the reversal of both spin valves did not show any exchange bias H_{ex} at RT. Two low-temperature measurements of $50K$ and $2K$ were conducted using SQUID for $50K$. S548 did not show any sign of exchange bias, while S549 showed a small value of $H_{ex} = 1.38mT$. On the other hand, for $2K$ measurements, both samples showed H_{ex} at this temperature, with values of $27.5mT$ and $39mT$ for S548 and S549, respectively. In both spin valves, the blocking temperature is at low temperature, and it varies between the two samples, as manifested by the appearance of exchange bias. The rotational magnetoresistance measurements of S548 at $20mT$ and $25mT$ proved that the Ni is pinned partially to the IrMn, due to the nickel reversing with the domains of IrMn at the interface.

Chapter 5 investigated the strain-induced magnetic anisotropy effect in magnetisation reversal and the magnetoresistance of all spin valves grown in this study using magnetotransport measurements. This chapter was divided into two parts, exploring the strain effect on pseudo spin valves, and the spin valves with IrMn layer. For the pseudo spin valves, both layers show response to the strain whereby the GMR changes as a function of voltages applied to the transducer, which varied between the two spin valves. The different magnetostriction signs of both layers contributed differently on spin valve magnetic properties. The magnetoresistance ratio changed between 0.93% and 1.53% in IM008, while it changed between 0.77% and 1.85% in IM009. The strain effect on permalloy showed the same effect to the permalloy in single layer sample S476, which showed positive magnetostriction. On the other hand, the nickel layer showed the opposite effect to the permalloy with negative magnetostriction, which has the same sign as the nickel magnetostriction in bulk form. The magnetisations orientation of both layers at zero magnetic field are aligned perpendicular to each other. For instance, applying a tensile strain to the spin valve aligns the permalloy magnetisation along the long axis of the transducer, while it is perpendicular to that direction for the nickel layer.

Each layer's magnetostriction responds differently to the strain, and thus contributes more to a certain change in the curve. For instance, the change in

$H(\Delta R/R_{max})$ between $1.4mT$ and $1.9mT$ when varying voltages between $-30V$ and $+50V$ in IM009 spin valve for $\varphi = 90^o$ could be related to the varying of the permalloy switching field with the voltages. On the other hand, the change of $\Delta R/R_{rem}$ in IM009 spin valve between 0.25% to 0.90% for IM009 when changing the voltage from $-30V$ to $+50V$ for $\varphi = 0^o$ could be ascribed more to the nickel magnetisation direction, which changed from easy to hard axis direction with respect to the field when changing between those voltages.

The IM009 spin valve response was greater than IM008, as most of the magnetoresistance features varied more with varying voltages. This could be attributed to the higher magnetostriction of the nickel layer in IM009, and to the order of the layers, as the nickel was close to the transducer in this spin valve. Nickel reversal showed more complicated reversal, particularly in IM009, and it is difficult to predict the reversal direction as it could have a complicated reversal of domain nucleation or domain walls movement. The difference in the layers' magnetostriction could be facilitated in certain applications, for instance, changing $H(\Delta R/R_{max})$ (related to the changing switching field of permalloy layer) as a function of voltage could be used in logic gates to control domain wall propagation on racetrack memories, as demonstrated in a previous study [88].

The second part of chapter 5 investigated the strain effect on spin valves with incorporated IrMn layer. These spin valves showed less response to the strain effect, with no enhancement of the GMR effect. For S548 spin valve with permalloy at the bottom of the spin valve (free layer), the spin valve magnetoresistance curve showed a change in the permalloy peaks intensity similar to the effect in permalloy layers in other samples. The switching field of the permalloy varies between $1.3mT$ and $0.7mT$ when varying voltages between $-30V$ and $+50V$ for $\varphi = 90^o$ measurement direction. The nickel layer in this sample showed no response to the strain, which could be ascribed to two reasons: the nickel showed zero magnetostriction in this layer, as in the S475 sample, or that could be the attributed to pinning to the IrMn layer, which could be stronger than the strain-induced anisotropy. On the other hand, for S549 spin valve, with the nickel at the bottom (free layer), both layers in this spin valve did not show any response to the strain. The permalloy in this spin valve is pinned partially to the IrMn layer, which could be the reason for showing no change with varying voltage, while the nickel showed zero magnetostriction in this structure, as in the S548 sample.

In chapter 6, a modulated ferromagnetic resonance (FMR) was used to investigate the strain effect on static and dynamic magnetic properties of the IM008 and IM009 spin valves. Both samples showed in-plane angular dependence of the resonance field H_{res}, which controlled by the strain value and type. The measurements for the permalloy showed positive magnetostriction affirming the finding from chapters 3 and 5. For IM008 spin valve, the value of the anisotropies extracted for the permalloy was changed from $155 \mp 30 J/m^3$ when $0V$ is applied to the transducer to $920 \mp 50 J/m^3$ when the voltage increases to $+50V$, with a microwave frequency of $8GHz$. For IM009, the permalloy anisotropies showed smaller values with $84 \mp 5 J/m^3$ when $0V$ was applied, and increased to $700 \mp 10 J/m^3$ when the voltage was ramped to $+50V$ at the former frequency. A comparison of these values of anisotropies extracted for the permalloy for both spin valves with the anisotropy of the permalloy single layer sample S476, showed that values of anisotropies in IM009 are smaller than those in S476 and IM008 samples, which could be attributed to the interface difference and to the quality of IM009 sample.

The M_s for the permalloy layer in both spin valves showed values of $970 \mp 30 J/m^3$ and $930 \mp 30 J/m^3$ in IM008 and IM009, respectively. The FMR spectra for IM008 showed only one clear resonance feature wich is related to the permalloy, which could be ascribed to the dynamic exchange between the permalloy and nickel layers. This is related to the spin pumping between the two layers through the spacer, whereby the permalloy acts as a spin sink, causing non-local damping for the nickel layer. However, small peaks related to the nickel appeared in IM009 spectra for $-25V$ and $+50V$ measurements. The angular dependence of H_{res} was extracted and plotted as a function of voltage and gave $M_s = (470 \mp 10) \times 10^3 A/m$ for $-25V$, and $\mu_0 H_u = 10.2 \mp 1.2 mT$ for $+50V$, while it gave $M_s = (470 + 10) \times 10^3 A/m$, and $\mu_0 H_u = 4.0 \mp 3.5 mT$ for $+25V$. The magnetostriction of nickel in IM009 measured by FMR possessed negative magnetostriction, agreeing with the results of nickel from magnetotransport measurements of IM008 and IM009 spin valves presented in chapter 5.

For the dynamic properties for both IM008 and IM009 samples, the Gilbert damping constant of the permalloy layer was found to be 0.010 ∓ 0.002 for IM008 and 0.012 ∓ 0.001 for IM009. The line broadening due to extrinsic damping increased with the strain for the permalloy layer from $0.46 \mp 0.08mT$ for $0V$ to $0.73 \mp 0.04mT$ for $+50V$, which may indicate that the strain might vary inhomogeneously across the film. Although the linewidth showed a linear relation with the microwave frequency, it displayed in-plane angular dependence. Different factors could cause this, including mosaicity, two magnon scattering, and spin pumping. This needs more investigation with more measurements (TMS), for instance exploring the effects of sweeping the frequency at different voltages and different in-plane directions, out of plane measurements to check TMS contribution, spin hall effect, and XMCD measurements.

As discussed in chapters 5 and 6, the spin valves micro-devices respond to the strain as their magnetisation and magnetoresistance changed as a function of voltages applied to the actuator. The study presented in this thesis could be extended by conducting another experiment using IM008 and IM009 pseudo spin valves. Study of the domain wall motion in nanowires in the presence of strain could be achieved by fabricating nanowires of the spin valves using electron beam lithography (EBL). A possible study could involve fabricating spin valves nanowires with varies widths of $50nm$, $100nm$, $200nm$, and $300nm$, and then to mount these wires onto the piezoelectric transducer. The competition between magnetostatic and strain-induced anisotropy could be studied as a function of the voltage applied the transducer while using GMR to detect the domain wall propagation and nucleation, using magnetotransport measurement. The domain wall propagation and switching fields could be measured as a function of voltages.

Figure 7.1 (a) shows the proposed hybrid structure of piezoelectric transducer/spin valve nanowire with a length of $25\mu m$, where the thickness represents the thicknesses of the IM008 and IM009 spin valves. The pad is for domain wall nucleation, which injects the domains into the wire, while a tapered end prevents the formation of domain walls in that region. Figure 7.1 (b) shows a part of the nanowire design with the contacts for transport measurement. This study could also be further extended to study the domains and domain walls formation and dynamics as a function of strain applied to the transducer using an imaging technique like XMCD PEEM.

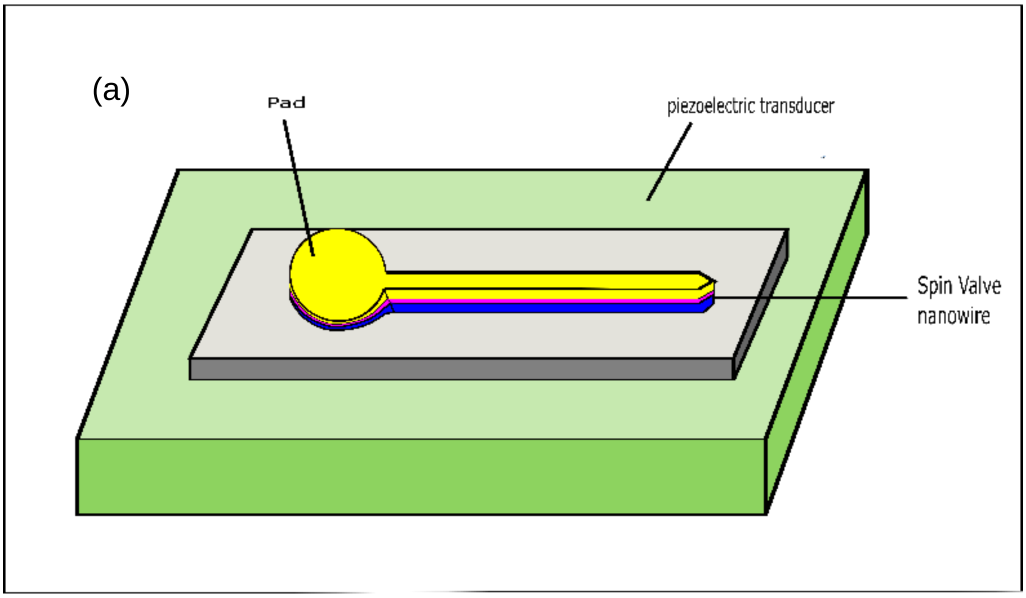

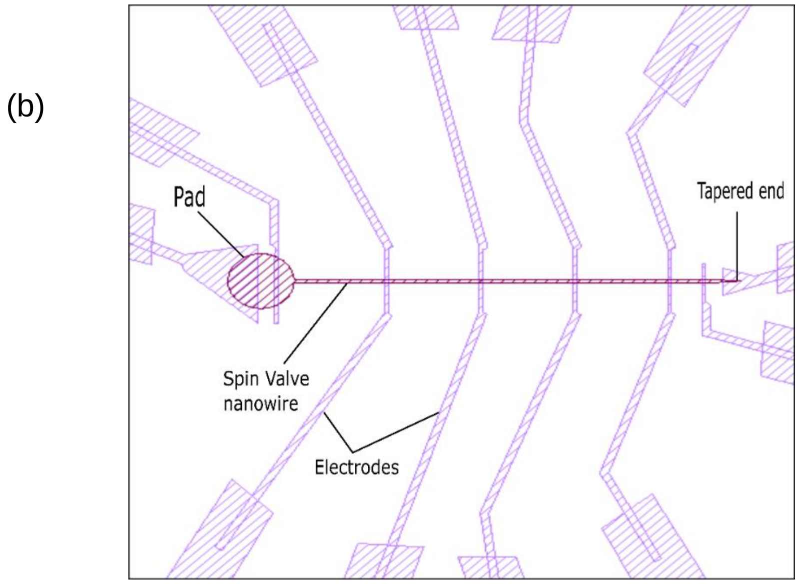

Figure 7.1: (a) Schematic of the proposed hybrid structure of the piezoelectric transducer/ spin valve nanowire. (b) Part of the design of the nanowire with the electrodes for studying the strain effect on domains wall motion in spin valve nanowires using magnetotransport measurements.

References

[1] Thomson, W. On the electro-dynamic qualities of metals: Effects of magnetisation on the electric conductivity of nickel and of iron. *Proceedings of the Royal Society of London*, (8), pp.546-550, 1857.

[2] McGuire, T. and Potter, R.L. Anisotropic magnetoresistance in ferromagnetic 3d alloys. *IEEE Transactions on Magnetics*, *11*(4), pp.1018-1038, 1975.

[3] Piramanayagam, S.N. and Chong, T.C. eds. *Developments in data storage: materials perspective*. John Wiley & Sons, 2011.

[4] Bhatti, S., Sbiaa, R., Hirohata, A., Ohno, H., Fukami, S. and Piramanayagam, S.N. Spintronics based random access memory: a review. *Materials Today*, *20*(9), pp.530-548, 2017.

[5] Baibich, M.N., Broto, J.M., Fert, A., Van Dau, F.N., Petroff, F., Etienne, P., Creuzet, G., Friederich, A. and Chazelas, J. Giant magnetoresistance of (001) Fe/(001) Cr magnetic superlattices. *Physical review letters*, *61*(21), p.2472, 1988.

[6] Binasch, G., Grünberg, P., Saurenbach, F. and Zinn, W. Enhanced magnetoresistance in layered magnetic structures with antiferromagnetic interlayer exchange. *Physical review B*, *39*(7), p.4828, 1989.

[7] Mott, N.F., The electrical conductivity of transition metals. *Proceedings of the Royal Society of London. Series A-Mathematical and Physical Sciences*, *153*(880), pp.699-717, 1936.

[8] Thompson, S.M. The discovery, development and future of GMR: The Nobel Prize 2007. *Journal of Physics D: Applied Physics*, *41*(9), p.093001, 2008.

[9] Parkin, S.S.P., Li, Z.G. and Smith, D.J. Giant magnetoresistance in antiferromagnetic Co/Cu multilayers. *Applied Physics Letters*, *58*(23), pp.2710-2712 1991.

[10] Parkin, S.S.P. Magnetotransport in transition metal multilayered structures. *Matematisk Fysiske Meddelelser-Kongelige Danske Videnskabernes Selskab*, *45*, pp.113-132, 1997.

[11] Parkin, S.S.P., Bhadra, R. and Roche, K.P. Oscillatory magnetic exchange coupling through thin copper layers. *Physical Review Letters*, *66*(16), p.2152, 1991.

[12] Dieny, B., Speriosu, V.S., Parkin, S.S., Gurney, B.A., Wilhoit, D.R. and Mauri, D. Giant magnetoresistive in soft ferromagnetic multilayers. *Physical Review B*, *43*(1), p.1297, 1991.

[13] Shinjo, T. and Yamamoto, H. Large magnetoresistance of field-induced giant ferrimagnetic multilayers. *Journal of the Physical Society of Japan*, *59*(9), pp.3061-3064, 1990.

[14] Coey, J.M. *Magnetism and magnetic materials*. Cambridge university press, 2010.

[15] Fert, A. Nobel Lecture: Origin, development, and future of spintronics. *Reviews of modern physics*, *80*(4), p.1517, 2008.

[16] Li, G., Sun, S., Wilson, R.J., White, R.L., Pourmand, N. and Wang, S.X. Spin valve sensors for ultrasensitive detection of superparamagnetic nanoparticles for biological applications. *Sensors and Actuators A: Physical*, *126*(1), pp.98-106, 2006.

[17] Weiss, R., Mattheis, R. and Reiss, G. Advanced giant magnetoresistance technology for measurement applications. *Measurement Science and Technology*, *24*(8), p.082001, 2013.

[18] Julliere, M. Tunneling between ferromagnetic films. *Physics letters A*, *54*(3), pp.225-226, 1975.

[19] Moodera, J.S., Kinder, L.R., Wong, T.M. and Meservey, R. Large magnetoresistance at room temperature in ferromagnetic thin film tunnel junctions. *Physical review letters*, *74*(16), p.3273, 1995.

[20] Miyazaki, T. and Tezuka, N. Giant magnetic tunneling effect in Fe/Al2O3/Fe junction. *Journal of magnetism and magnetic materials*, *139*(3), pp.L231-L234, 1995.

[21] Parkin, S.S., Kaiser, C., Panchula, A., Rice, P.M., Hughes, B., Samant, M. and Yang, S.H. Giant tunnelling magnetoresistance at room temperature with MgO (100) tunnel barriers. *Nature materials*, *3*(12), pp.862-867, 2004.

[22] Yuasa, S., Nagahama, T., Fukushima, A., Suzuki, Y. and Ando, K. Giant room-temperature magnetoresistance in single-crystal Fe/MgO/Fe magnetic tunnel junctions. *Nature materials*, *3*(12), pp.868-871, 2004.

[23] Lee, Y.M., Hayakawa, J., Ikeda, S., Matsukura, F. and Ohno, H. Effect of electrode composition on the tunnel magnetoresistance of pseudo-spin-valve magnetic tunnel junction with a MgO tunnel barrier. *Applied physics letters*, *90*(21), p.212507, 2007.

[24] Kasap, S. *Springer handbook of electronic and photonic materials*. Springer Science & Business Media, 2006.

[25] Berger, L. Emission of spin waves by a magnetic multilayer traversed by a current. *Physical Review B*, *54*(13), p.9353, 1996.

[26] Slonczewski, J.C. Current-driven excitation of magnetic multilayers. *Journal of Magnetism and Magnetic Materials*, *159*(1), p.L1, 1996.

[27] Katine, J.A., Albert, F.J., Buhrman, R.A., Myers, E.B. and Ralph, D.C. Current-driven magnetisation reversal and spin-wave excitations in Co/Cu/Co pillars. *Physical review letters*, *84*(14), p.3149, 2000.

[28] Jourdan, M. Revival of Heusler compounds for spintronics. *Materials Today*, *8*(17), pp.362-363, 2014.

[29] Diao, Z., Panchula, A., Ding, Y., Pakala, M., Wang, S., Li, Z., Apalkov, D., Nagai, H., Driskill-Smith, A., Wang, L.C. and Chen, E. Spin transfer switching in dual MgO magnetic tunnel junctions. *Applied Physics Letters*, *90*(13), p.132508, 2007.

[30] Sbiaa, R., Meng, H. and Piramanayagam, S.N. Materials with perpendicular magnetic anisotropy for magnetic random access memory. *physica status solidi (RRL)–Rapid Research Letters*, *5*(12), pp.413-419, 2011.

[31] Garcia, V., Bibes, M., Bocher, L., Valencia, S., Kronast, F., Crassous, A., Moya, X., Enouz-Vedrenne, S., Gloter, A., Imhoff, D. and Deranlot, C. Ferroelectric control of spin polarisation. *Science*, *327*(5969), pp.1106-1110, 2010.

[32] Chu, Y.H., Martin, L.W., Holcomb, M.B., Gajek, M., Han, S.J., He, Q., Balke, N., Yang, C.H., Lee, D., Hu, W. and Zhan, Q. Electric-field control of local ferromagnetism using a magnetoelectric multiferroic. *Nature materials*, *7*(6), pp.478-482, 2008.

[33] Hu, J.M., Li, Z., Chen, L.Q. and Nan, C.W. High-density magnetoresistive random access memory operating at ultralow voltage at room temperature. *Nature communications*, *2*(1), pp.1-8, 2011.

[34] Sixtus, K.J. and Tonks, L. Propagation of large Barkhausen discontinuities. *Physical Review*, *37*(8), p.930, 1931.

[35] Sixtus, K.J. and Tonks, L. Propagation of large Barkhausen discontinuities. II. *Physical Review*, *42*(3), p.419, 1932.

[36] Parkin, S.S., Hayashi, M. and Thomas, L. Magnetic domain-wall racetrack memory. *Science*, *320*(5873), pp.190-194, 2008.

[37] Rushforth, A.W., De Ranieri, E., Zemen, J., Wunderlich, J., Edmonds, K.W., King, C.S., Ahmad, E., Campion, R.P., Foxon, C.T., Gallagher, B.L. and Výborný, K. Voltage control of magnetocrystalline anisotropy in ferromagnetic-semiconductor-piezoelectric hybrid structures. *Physical Review B*, *78*(8), p.085314, 2008.

[38] Geprägs, S., Brandlmaier, A., Opel, M., Gross, R. and Goennenwein, S.T.B. Electric field controlled manipulation of the magnetization in Ni/BaTiO 3 hybrid structures. *Applied Physics Letters*, *96*(14), p.142509, 2010.

[39] Ostler, T.A., Cuadrado, R., Chantrell, R.W., Rushforth, A.W. and Cavill, S.A. Strain induced vortex core switching in planar magnetostrictive nanostructures. *Physical review letters*, *115*(6), p.067202, 2015.

[40] Maruyama, T., Shiota, Y., Nozaki, T., Ohta, K., Toda, N., Mizuguchi, M., Tulapurkar, A.A., Shinjo, T., Shiraishi, M., Mizukami, S. and Ando, Y. Large voltage-induced magnetic anisotropy change in a few atomic layers of iron. *Nature nanotechnology*, *4*(3), pp.158-161, 2009.

[41] Zhang, H., Richter, M., Koepernik, K., Opahle, I., Tasnádi, F. and Eschrig, H. Electric-field control of surface magnetic anisotropy: a density functional approach. *New Journal of Physics*, *11*(4), p.043007, 2009.

[42] Stolichnov, I., Riester, S.W.E., Trodahl, H.J., Setter, N., Rushforth, A.W., Edmonds, K.W., Campion, R.P., Foxon, C.T., Gallagher, B.L. and Jungwirth, T. Non-volatile ferroelectric control of ferromagnetism in (Ga, Mn) As. *Nature materials*, *7*(6), pp.464-467, 2008.

[43] Chu, Y.H., Martin, L.W., Holcomb, M.B., Gajek, M., Han, S.J., He, Q., Balke, N., Yang, C.H., Lee, D., Hu, W. and Zhan, Q. Electric-field control of local ferromagnetism using a magnetoelectric multiferroic. *Nature materials*, *7*(6), pp.478-482, 2008.

[44] Laukhin, V., Skumryev, V., Martí, X., Hrabovsky, D., Sánchez, F., García-Cuenca, M.V., Ferrater, C., Varela, M., Lüders, U., Bobo, J.F. and Fontcuberta, J. Electric-field control of exchange bias in multiferroic epitaxial heterostructures. *Physical review letters*, *97*(22), p.227201, 2006.

[45] Borisov, P., Hochstrat, A., Chen, X., Kleemann, W. and Binek, C. Magnetoelectric switching of exchange bias. *Physical Review Letters*, *94*(11), p.117203, 2005.

[46] He, X., Wang, Y., Wu, N., Caruso, A.N., Vescovo, E., Belashchenko, K.D., Dowben, P.A. and Binek, C. Robust isothermal electric control of exchange bias at room temperature. *Nature materials*, *9*(7), pp.579-585, 2010.

[47] Kim, Y.K. and Silva, T.J. Magnetostriction characteristics of ultrathin permalloy films. *Applied physics letters*, *68*(20), pp.2885-2886, 1996.

[48] Bochi, G., Ballentine, C.A., Inglefield, H.E., Thompson, C.V. and O'handley, R.C. Evidence for strong surface magnetoelastic

anisotropy in epitaxial Cu/Ni/Cu (001) sandwiches. *Physical Review B*, *53*(4), p.R1729, 1996.

[49] Vaz, C.A. Electric field control of magnetism in multiferroic heterostructures. *Journal of Physics: Condensed Matter*, *24*(33), p.333201, 2012.

[50] Cullity, B.D. and Graham, C.D. *Introduction to magnetic materials*. John Wiley & Sons, 2011.

[51] Neugebauer, C.A., Saturation magnetisation of nickel films of thickness less than 100 A. *Physical Review*, *116*(6), p.1441, 1959.

[52] Parkes, D.E. *Strain control of ferromagnetic thin films and devices* (Doctoral dissertation, University of Nottingham), 2016.

[53] Bonin, R., Schneider, M.L., Silva, T.J. and Nibarger, J.P. Dependence of magnetisation dynamics on magnetostriction in NiFe alloys. *Journal of applied physics*, *98*(12), p.123904, 2005.

[54] Dean, J., Bryan, M.T., Morley, N.A., Hrkac, G., Javed, A., Gibbs, M.R.J. and Allwood, D.A. Numerical study of the effective magnetocrystalline anisotropy and magnetostriction in polycrystalline FeGa films. *Journal of Applied Physics*, *110*(4), p.043902, 2011.

[55] O'handley, R.C. *Modern magnetic materials: principles and applications*. Wiley, 2000.

[56] Steinle-Neumann, G., Stixrude, L. and Cohen, R.E. First-principles elastic constants for the hcp transition metals Fe, Co, and Re at high pressure. *Physical Review B*, *60*(2), p.791, 1999.

[57] Clark, A.E., Hathaway, K.B., Wun-Fogle, M., Restorff, J.B., Lograsso, T.A., Keppens, V.M., Petculescu, G. and Taylor, R.A. Extraordinary magnetoelasticity and lattice softening in bcc Fe-Ga alloys. *Journal of Applied Physics*, *93*(10), pp.8621-8623, 2003.

[58] Einspruch, N.G. and Claiborne, L.T. Elastic Constants of a (73.8% Ni-26.2% Fe) Ferromagnetic Alloy. *Journal of Applied Physics*, *35*(1), pp.175-175, 1964.

[59] Priya, S., Islam, R., Dong, S. and Viehland, D. Recent advancements in magnetoelectric particulate and laminate composites. *Journal of Electroceramics*, *19*(1), pp.149-166, 2007.

[60] Zheng, H., Wang, J., Lofland, S.E., Ma, Z., Mohaddes-Ardabili, L., Zhao, T., Salamanca-Riba, L., Shinde, S.R., Ogale, S.B., Bai, F. and Viehland, D. Multiferroic batio3-cofe2o4 nanostructures. *Science*, *303*(5658), pp.661-663, 2004.

[61] Kim, S.K., Lee, J.W., Shin, S.C., Song, H.W., Lee, C.H. and No, K. Voltage control of a magnetisation easy axis in piezoelectric/ferromagnetic hybrid films. *Journal of magnetism and magnetic materials*, *267*(1), pp.127-132, 2003.

[62] Vaz, C.A., Hoffman, J., Posadas, A.B. and Ahn, C.H. Magnetic anisotropy modulation of magnetite in Fe 3 O 4/BaTiO 3 (100) epitaxial structures. *Applied Physics Letters*, *94*(2), p.022504, 2009.

[63] Zhu, G., Wong, K.L., Zhao, J., Amiri, P.K., Zhu, J., Krivorotov, I. and Wang, K.L. Quantitative analysis of electric field induced change in anisotropy field in Co60Fe20B20/(011) xPb (Mg1/3Nb2/3) O3-(1− x) PbTiO3 (x∼ 0.68) heterostructures. *Applied Physics Letters*, *101*(20), p.202404, 2012.

[64] Guo, Q., Xu, X.G., Zhang, Q.Q., Liu, Q., Wu, Y.J., Zhou, Z.Q., Zhu, W.M., Wu, Y., Miao, J. and Jiang, Y., Strain-controlled giant magnetoresistance of a spin valve grown on a flexible substrate. *RSC advances*, *6*(91), pp.88090-88095, 2016.

[65] Cavill, S.A., Parkes, D.E., Miguel, J., Dhesi, S.S., Edmonds, K.W., Campion, R.P. and Rushforth, A.W., Electrical control of magnetic reversal processes in magnetostrictive structures. *Applied Physics Letters*, *102*(3), p.032405, 2013.

[66] Liu, M., Li, S., Obi, O., Lou, J., Rand, S. and Sun, N.X. Electric field modulation of magnetoresistance in multiferroic heterostructures for ultralow power electronics. *Applied Physics Letters*, *98*(22), p.222509, 2011.

[67] Brandlmaier, A., Geprägs, S., Woltersdorf, G., Gross, R. and Goennenwein, S.T.B. Nonvolatile, reversible electric-field controlled

switching of remanent magnetisation in multifunctional ferromagnetic/ferroelectric hybrids. *Journal of Applied Physics*, *110*(4), p.043913, 2011.

[68] Giang, D.H., Thuc, V.N. and Duc, N.H. Electric field-induced magnetoresistance in spin-valve/piezoelectric multiferroic laminates for low-power spintronics. *Journal of magnetism and magnetic materials*, *324*(13), pp.2019-2023, 2012.

[69] Rizwan, S., Liu, H.F., Han, X.F., Zhang, S., Zhao, Y.G. and Zhang, S. March. Electric-field control of giant magnetoresistance in spin-valves. In *Spin* (Vol. 2, No. 01, p. 1250006). World Scientific Publishing Company, 2012.

[70] Rizwan, S., Zhang, S., Yu, T., Zhao, Y.G. and Han, X.F., Piezoelectric enhancement of giant magnetoresistance in spin-valves with different magnetic anisotropies. *Journal of Applied Physics*, *113*(2), p.023911, 2013.

[71] Zhao, W., Huang, W., Liu, C., Hou, C., Chen, Z., Yin, Y. and Li, X. Electric-Field-Controlled Nonvolatile Magnetisation Rotation and Magnetoresistance Effect in Co/Cu/Ni Spin Valves on Piezoelectric Substrates. *ACS applied materials & interfaces*, *10*(25), pp.21390-21397, 2018.

[72] Allibe, J., Fusil, S., Bouzehouane, K., Daumont, C., Sando, D., Jacquet, E., Deranlot, C., Bibes, M. and Barthelemy, A. Room temperature electrical manipulation of giant magnetoresistance in spin valves exchange-biased with BiFeO3. *Nano letters*, *12*(3), pp.1141-1145, 2012.

[73] Heron, J.T., Bosse, J.L., He, Q., Gao, Y., Trassin, M., Ye, L., Clarkson, J.D., Wang, C., Liu, J., Salahuddin, S. and Ralph, D.C. Deterministic switching of ferromagnetism at room temperature using an electric field. Nature, 516(7531), pp.370-373, 2014.

[74] Lou, J., Liu, M., Reed, D., Ren, Y. and Sun, N.X. Giant Electric Field Tuning of Magnetism in Novel Multiferroic FeGaB/Lead Zinc Niobate–Lead Titanate (PZN-PT) Heterostructures. *Advanced Materials*, *21*(46), pp.4711-4715, 2009.

[75] Hu, J.M., Nan, T., Sun, N.X. and Chen, L.Q., Multiferroic magnetoelectric nanostructures for novel device applications. *MRS Bulletin*, *40*(9), pp.728-735, 2015.

[76] Liu, L., Zhan, Q., Yang, H., Li, H., Zhang, S., Liu, Y., Wang, B., Tan, X. and Li, R.W. Magnetostrictive GMR spin valves with composite FeGa/FeCo free layers. *AIP Advances*, *6*(3), p.035206, 2016.

[77] Kwon, J.H., Kwak, W.Y., Choi, H.Y., Kim, G.H. and Cho, B.K. Effects of repetitive bending on the magnetoresistance of a flexible spin-valve. *Journal of Applied Physics*, *117*(17), p.17E120, 2015.

[78] Pattnaik, D.P., Beardsley, R.P., Love, C., Cavill, S.A., Edmonds, K.W. and Rushforth, A.W. Multilevel information storage using magnetoelastic layer stacks. *Scientific reports*, *9*(1), pp.1-6, 2019.

[79] Lou, J., Liu, M., Reed, D., Ren, Y. and Sun, N.X. Giant Electric Field Tuning of Magnetism in Novel Multiferroic FeGaB/Lead Zinc Niobate–Lead Titanate (PZN-PT) Heterostructures. *Advanced Materials*, *21*(46), pp.4711-4715, 2009.

[80] Weiler, M., Brandlmaier, A., Geprägs, S., Althammer, M., Opel, M., Bihler, C., Huebl, H., Brandt, M.S., Gross, R. and Goennenwein, S.T.B. Voltage controlled inversion of magnetic anisotropy in a ferromagnetic thin film at room temperature. *New Journal of Physics*, *11*(1), p.013021, 2009.

[81] Shastry, S., Srinivasan, G., Bichurin, M.I., Petrov, V.M. and Tatarenko, A.S. Microwave magnetoelectric effects in single crystal bilayers of yttrium iron garnet and lead magnesium niobate-lead titanate. *Physical Review B*, *70*(6), p.064416, 2004.

[82] Fetisov, Y.K. and Srinivasan, G. Electric field tuning characteristics of a ferrite-piezoelectric microwave resonator. *Applied physics letters*, *88*(14), p.143503, 2006.

[83] Lonappan, A. Novel method of detecting cholesterol using microwaves. *Microwave and Optical Technology Letters*, *54*(5), pp.1212-1215, 2012.

[84] Lahtinen, T.H., Tuomi, J.O. and van Dijken, S. Pattern transfer and electric-field-induced magnetic domain formation in multiferroic heterostructures. *Advanced Materials*, *23*(28), pp.3187-3191, 2011.

[85] De Ranieri, E., Roy, P.E., Fang, D., Vehsthedt, E.K., Irvine, A.C., Heiss, D., Casiraghi, A., Campion, R.P., Gallagher, B.L., Jungwirth, T. and Wunderlich, J. Piezoelectric control of the mobility of a domain wall driven by adiabatic and non-adiabatic torques. *Nature materials*, *12*(9), pp.808-814, 2013.

[86] Chung, T.K., Keller, S. and Carman, G.P. Electric-field-induced reversible magnetic single-domain evolution in a magnetoelectric thin film. *Applied Physics Letters*, *94*(13), p.132501, 2009.

[87] Parkes, D.E., Cavill, S.A., Hindmarch, A.T., Wadley, P., McGee, F., Staddon, C.R., Edmonds, K.W., Campion, R.P., Gallagher, B.L. and Rushforth, A.W. Non-volatile voltage control of magnetisation and magnetic domain walls in magnetostrictive epitaxial thin films. *Applied Physics Letters*, *101*(7), p.072402, 2012.

[88] Lei, N., Devolder, T., Agnus, G., Aubert, P., Daniel, L., Kim, J.V., Zhao, W., Trypiniotis, T., Cowburn, R.P., Chappert, C. and Ravelosona, D. Strain-controlled magnetic domain wall propagation in hybrid piezoelectric/ferromagnetic structures. *Nature communications*, *4*(1), pp.1-7, 2013.

[89] Kittel, C. *Introduction to solid state physics* (Vol. 8). New York: Wiley, 1976.

[90] Tian, C.S., Qian, D., Wu, D., He, R.H., Wu, Y.Z., Tang, W.X., Yin, L.F., Shi, Y.S., Dong, G.S., Jin, X.F. and Jiang, X.M. Body-centered-cubic Ni and its magnetic properties. *Physical review letters*, *94*(13), p.137210, 2005.

[91] Yin, L.F., Wei, D.H., Lei, N., Zhou, L.H., Tian, C.S., Dong, G.S., Jin, X.F., Guo, L.P., Jia, Q.J. and Wu, R.Q. Magnetocrystalline anisotropy in permalloy revisited. *Physical review letters*, *97*(6), p.067203, 2006.

[92] Slater, J.C. Atomic shielding constants. *Physical Review*, *36*(1), p.57, 1930.

[93] Goldman, A. *Handbook of modern ferromagnetic materials* (Vol. 505). Springer Science & Business Media, 2012.

[94] Slater, J.C. Ferromagnetism and the band theory. *Reviews of Modern Physics*, *25*(1), p.199, 1953.

[95] Allan. H. Morrish.The Physical principal of Magnetism. IEEE Press, second edition, 2001.

[96] Chikazumi, S. and Graham, C.D. *Physics of Ferromagnetism 2e* (No. 94). Oxford University Press on Demand, 2009.

[97] Stöhr, J. and Siegmann, H.C. *Magnetism: from fundamentals to nanoscale dynamics* (Vol. 152). Springer Science & Business Media, 2007.

[98] Getzlaff, M. *Fundamentals of magnetism*. Springer Science & Business Media, 2007.

[99] Bozorth, R.M. Directional ferromagnetic properties of metals. *Journal of Applied Physics*, *8*(9), pp.575-588, 1937.

[100] Sander, D., 1999. The correlation between mechanical stress and magnetic anisotropy in ultrathin films. *Reports on Progress in Physics*, *62*(5), p.809.

[101] Brandlmaier, A., Geprägs, S., Weiler, M., Boger, A., Opel, M., Huebl, H., Bihler, C., Brandt, M.S., Botters, B., Grundler, D. and Gross, R. In situ manipulation of magnetic anisotropy in magnetite thin films. *Physical Review B*, *77*(10), p.104445, 2008.

[102] Draaisma, H.J.G. and De Jonge, W.J.M. Surface and volume anisotropy from dipole-dipole interactions in ultrathin ferromagnetic films. *Journal of applied physics*, *64*(7), pp.3610-3613, 1988.

[103] Hubert, A. and Schäfer, R. *Magnetic domains: the analysis of magnetic microstructures*. Springer Science & Business Media, 2008.

[104] Prutton, M. *Thin ferromagnetic films*. Butterworth, 1st ed., 1964.

[105] Tannous, C. and Gieraltowski, J. The Stoner–Wohlfarth model of ferromagnetism. *European journal of physics*, *29*(3), p.475, 2008.

[106] Smit, J. Magnetoresistance of ferromagnetic metals and alloys at low temperatures. *Physica*, *17*(6), pp.612-627, 1951.

[107] De Lacheisserie, E.D.T., Gignoux, D. and Schlenker, M. eds. *Magnetism* (Vol. 1). Springer Science & Business Media, 2005.

[108] Campbell, I.A., Fert, A. and Jaoul, O. The spontaneous resistivity anisotropy in Ni-based alloys. *Journal of Physics C: Solid State Physics*, *3*(1S), p.S95, 1970.

[109] Malozemoff, A.P. Anisotropic magnetoresistance of amorphous and concentrated polycrystalline iron alloys. *Physical Review B*, *32*(9), p.6080, 1985.

[110] Tang, D.D. and Lee, Y.J. *Magnetic memory: fundamentals and technology*. Cambridge University Press, 2010.

[111] Wang, K.Y., Edmonds, K.W., Campion, R.P., Zhao, L.X., Foxon, C.T. and Gallagher, B.L. Anisotropic magnetoresistance and magnetic anisotropy in high-quality (Ga, Mn) As films. *Physical Review B*, *72*(8), p.085201, 2005.

[112] Van den Berg, H.A.M., Coehoorn, R., Gijs, M.A.M., Grünberg, P., Rasing, T. and Röll, K. *Magnetic multilayers and giant magnetoresistance: fundamentals and industrial applications* (Vol. 37). Springer Science & Business Media, 2013.

[113] Mott, N.F. and Stevens, K.W.H. The band structure of the transition metals. *Philosophical magazine*, *2*(23), pp.1364-1386, 1957

[114] Meiklejohn, W.H. and Bean, C.P. New magnetic anisotropy. *Physical review*, *102*(5), p.1413. 1956.

[115] Ali, M., Marrows, C.H., Al-Jawad, M., Hickey, B.J., Misra, A., Nowak, U. and Usadel, K.D. Antiferromagnetic layer thickness dependence of the IrMn/Co exchange-bias system. *Physical review B*, *68*(21), p.214420, 2003.

[116] Radu, F. and Zabel, H. Exchange bias effect of ferro-/antiferromagnetic heterostructures. In *Magnetic heterostructures* (pp. 97-184). Springer, Berlin, Heidelberg, 2008.

[117] Nogués, J. and Schuller, I.K., Exchange bias. *Journal of Magnetism and Magnetic Materials*, *192*(2), pp.203-232, 1999.

[118] Eckert, J.C., Stern, N.P., Snowden, D.S., Sparks, P.D. and Carey, M.J. Properties of thin IrMn in exchange biased multilayers. *Journal of applied physics*, *93*(10), pp.6608-6610, 2003.

[119] Xi, H., White, R.M., Gao, Z. and Mao, S. Antiferromagnetic thickness dependence of blocking temperature in exchange coupled polycrystalline ferromagnet/antiferromagnet bilayers. *Journal of applied physics*, *92*(8), pp.4828-4830, 2002.

[120] Tshitoyan, V., Ciccarelli, C., Mihai, A.P., Ali, M., Irvine, A.C., Moore, T.A., Jungwirth, T. and Ferguson, A.J. Electrical manipulation of ferromagnetic NiFe by antiferromagnetic IrMn. *Physical Review B*, *92*(21), p.214406, 2015.

[121] Carey, M.J. and Berkowitz, A.E. Exchange anisotropy in coupled films of Ni81Fe19 with NiO and Co x Ni1− x O. *Applied physics letters*, *60*(24), pp.3060-3062, 1992.

[122] Lai, C.H., Bailey, W.E., White, R.L. and Anthony, T.C. Exchange anisotropy in NiFe/Fe-doped NiO bilayers. *Journal of applied physics*, *81*(8), pp.4990-4992, 1997.

[123] Lai, C.H., Matsuyama, H., White, R.L., Anthony, T.C. and Bush, G.G. Exploration of magnetisation reversal and coercivity of epitaxial NiO {111}/NiFe films. *Journal of applied physics*, *79*(8), pp.6389-6391, 1996.

[124] Devasahayam, A.J. and Kryder, M.H. A study of the NiFe/NiMn exchange couple. *IEEE Transactions on Magnetics*, *32*(5), pp.4654-4656, 1996.

[125] Landau, L.A.L.E. and Lifshitz, E. On the theory of the dispersion of magnetic permeability in ferromagnetic bodies. In *Perspectives in Theoretical Physics* (pp. 51-65). Pergamon, 1992.

[126] Bland, A. and Bland, J.A.C. *Ultrathin Magnetic Structures II: Measurement Techniques and Novel Magnetic Properties* (Vol. 2). Springer Science & Business Media, 1994.

[127] Landau, L.D., Bell, J.S., Kearsley, M.J., Pitaevskii, L.P., Lifshitz, E.M. and Sykes, J.B. *Electrodynamics of continuous media* (Vol. 8). Elsevier, 2013.

[128] Lakshmanan, M. The fascinating world of the Landau–Lifshitz–Gilbert equation: an overview. *Philosophical Transactions of the Royal Society A: Mathematical, Physical and Engineering Sciences*, *369*(1939), pp.1280-1300, 2011.

[129] Gilbert, T.L. A Lagrangian formulation of the gyromagnetic equation of the magnetisation field. *Phys. Rev.*, *100*, p.1243, 1955.

[130] Farle, M. Ferromagnetic resonance of ultrathin metallic layers. *Reports on progress in physics*, *61*(7), p.755, 1998.

[131] Heinrich, B. and Cochran, J.F. Ultrathin metallic magnetic films: magnetic anisotropies and exchange interactions. *Advances in Physics*, *42*(5), pp.523-639, 1993.

[132] Smit, J. and Beljers, H.G., Philips res. *Rep*, *10*(113), p.92, 1955.

[133] Smit, J. and Beljers, H.J. Ferromagnetic resonance absorbtion in BaFe12O19, a highly anisotropic crystall. *Philips Res. Rep*, *10*, pp.113-130, 1955.

[134] Puszkarski, H. and Kasperski, M. On the interpretation of the angular dependence of the main FMR/SWR line in ferromagnetic thin films. *Acta Physica Polonica-Series A General Physics*, *121*(5), p.1165, 2012.

[135] Suhl, H. Ferromagnetic resonance in nickel ferrite between one and two kilomegacycles. *Physical Review*, *97*(2), p.555, 1955.

[136] Bland, J.A.C. and Heinrich, B. eds. *Ultrathin Magnetic Structures I: An Introduction to the Electronic, Magnetic and Structural Properties* (Vol. 1). Springer Science & Business Media, 2006.

[137] Heinrich, B., Urban, R. and Woltersdorf, G. Magnetic relaxation in metallic films: Single and multilayer structures. *Journal of applied physics*, *91*(10), pp.7523-7525, 2002.

[138] Heinrich, B., Fraitová, D. and Kamberský, V. The Influence of s-d Exchange on Relaxation of Magnons in Metals. *physica status solidi (b)*, *23*(2), pp.501-507, 1967.

[139] Luo, C., Zhang, D., Wang, Y., Huang, H., Zhai, Y. and Zhai, H. Angular dependence of ferromagnetic resonance in Tb-doped Ni80Fe20 thin films. *Journal of Alloys and Compounds*, *598*, pp.57-60, 2014.

[140] Hurben, M.J. and Patton, C.E. Theory of two magnon scattering microwave relaxation and ferromagnetic resonance linewidth in magnetic thin films. *Journal of applied physics*, *83*(8), pp.4344-4365, 1998.

[141] McMichael, R.D., Stiles, M.D., Chen, P.J. and Egelhoff Jr, W.F. Ferromagnetic resonance linewidth in thin films coupled to NiO. *Journal of applied physics*, *83*(11), pp.7037-7039, 1998.

[142] Woltersdorf, G. and Heinrich, B. Two-magnon scattering in a self-assembled nanoscale network of misfit dislocations. *Physical Review B*, *69*(18), p.184417, 2004.

[143] Mendes, J.B.S., Vilela-Leao, L.H., Rezende, S.M. and Azevedo, A., 2010. Possible interplay between intrinsic and extrinsic ferromagnetic damping mechanisms. *IEEE transactions on magnetics*, *46*(6), pp.2293-2296.

[144] Liu, X., Zhang, W., Carter, M.J. and Xiao, G. Ferromagnetic resonance and damping properties of CoFeB thin films as free layers in MgO-based magnetic tunnel junctions. *Journal of Applied Physics*, *110*(3), p.033910, 2011.

[145] Slonczewski, J.C. Current-driven excitation of magnetic multilayers. *Journal of Magnetism and Magnetic Materials*, *159*(1), p.L1, 1996.

[146] Heinrich, B., Woltersdorf, G., Urban, R. and Simanek, E. Role of spin current in magnetic relaxations of metallic multilayer films. *Journal of magnetism and magnetic materials*, *258*, pp.376-381, 2003.

[147] Stiles, M.D. and Zangwill, A. Anatomy of spin-transfer torque. *Physical Review B*, *66*(1), p.014407, 2002.

[148] Tserkovnyak, Y., Brataas, A. and Bauer, G.E. Enhanced Gilbert damping in thin ferromagnetic films. *Physical review letters*, *88*(11), p.117601, 2002.

[149] Baker, A.A., Figueroa, A.I., Love, C.J., Cavill, S.A., Hesjedal, T. and Van Der Laan, G. Anisotropic absorption of pure spin currents. *Physical review letters*, *116*(4), p.047201, 2016.

[150] Taniguchi, T. and Imamura, H. Enhancement of the Gilbert damping constant due to spin pumping in noncollinear ferromagnet/nonmagnet/ferromagnet trilayer systems. *Physical Review B*, *76*(9), p.092402, 2007.

[151] Scherbakov, A.V., Danilov, A.P., Godejohann, F., Linnik, T.L., Glavin, B.A., Shelukhin, L.A., Pattnaik, D.P., Wang, M., Rushforth, A.W., Yakovlev, D.R. and Akimov, A.V. Optical excitation of single-and multimode magnetisation precession in Fe-Ga nanolayers. *Physical Review Applied*, *11*(3), p.031003, 2019.

[152] Shepley, P.M., Rushforth, A.W., Wang, M., Burnell, G. and Moore, T.A. Modification of perpendicular magnetic anisotropy and domain wall velocity in Pt/Co/Pt by voltage-induced strain. *Scientific reports*, *5*(1), pp.1-5, 2015.

[153] Piezomechanik GmbH. Low voltage co-fired multilayer stacks, rings and chips for actuation, Germany, 2010.

[154] McElfresh, M. Fundamentals of magnetism and magnetic measurements featuring Quantum Design’s magnetic property measurement system. *Quantum Design*, *11578*, p.132, 1994.

[155] Kalarickal, S.S., Krivosik, P., Wu, M., Patton, C.E., Schneider, M.L., Kabos, P., Silva, T.J. and Nibarger, J.P., 2006. Ferromagnetic resonance linewidth in metallic thin films: Comparison of measurement methods. *Journal of Applied Physics*, *99*(9), p.093909, 2006.

[156] Montoya, E., McKinnon, T., Zamani, A., Girt, E. and Heinrich, B. Broadband ferromagnetic resonance system and methods for ultrathin magnetic films. *Journal of magnetism and magnetic materials*, *356*, pp.12-20, 2014

[157] Love, C. *Correlating Magnetic Damping and Microstructure in" Half Metal" Thin Films* (Doctoral dissertation, University of York), 2018.

[158] Woltersdorf, G. *Spin-pumping and two-magnon scattering in magnetic multilayers* (Doctoral dissertation, Sinon Fraser University), 2004.

[159] Klokholm, E. and Aboaf, J.A. The saturation magnetostriction of permalloy films. *Journal of Applied Physics*, *52*(3), pp.2474-2476, 1981.

[160] Song, O., Ballentine, C.A. and O'handley, R.C. Giant surface magnetostriction in polycrystalline Ni and NiFe films. *Applied physics letters*, *64*(19), pp.2593-2595, 1994.

[161] Liu, Y.F., Cai, J.W. and Sun, L, Large enhancement of anisotropic magnetoresistance and thermal stability in Ta/NiFe/Ta trilayers with interfacial Pt addition. *Applied Physics Letters*, *96*(9), p.092509, 2010.

[162] Bozorth, R.M., The permalloy problem. *Reviews of Modern Physics*, *25*(1), p.42, 1953.

[163] Gao, Y., Hu, J., Shu, L. and Nan, C.W. Strain-mediated voltage control of magnetism in multiferroic Ni77Fe23/Pb (Mg1/3Nb2/3) 0.7 Ti0. 3O3 heterostructure. *Applied Physics Letters*, *104*(14), p.142908, 2014.

[164] Stoner, E.C. and Wohlfarth, E.P. A mechanism of magnetic hysteresis in heterogeneous alloys. *Philosophical Transactions of the Royal Society of London. Series A, Mathematical and Physical Sciences*, *240*(826), pp.599-642., 1948.

[165] Hashim, I. and Atwater, H.A. In situ magnetic and structural analysis of epitaxial Ni80Fe20 thin films for spin-valve heterostructures. *Journal of Applied Physics*, *75*(10), pp.6516-6518, 1994.

[166] Sharma, P. and Gupta, A., 2005. Effect of preparation condition on the soft magnetic properties of FeCuNbSiB thin films. *Journal of magnetism and magnetic materials*, *288*, pp.347-353, 2005.

[167] Ueno, M. and Tanoue, S. Magnetic properties of ion-beam sputter deposited NiFe ultrathin films. *Journal of Vacuum Science & Technology A: Vacuum, Surfaces, and Films*, *13*(4), pp.2194-2198, 1995.

[168] Vaz, C.A.F., Bland, J.A.C. and Lauhoff, G. Magnetism in ultrathin film structures. *Reports on Progress in Physics*, *71*(5), p.056501, 2008.

[169] Parkin, S.S.P., 1997. Magnetotransport in transition metal multilayered structures. Matematisk Fysiske Meddelelser-Kongelige Danske Videnskabernes Selskab, 45, pp.113-132.

[170] Hirota, E., Hirota, E., Sakakima, H., Inomata, K. and Inomata, K., *Giant magneto-resistance devices* (Vol. 40). Springer Science & Business Media, 2002.

[171] Gritsenko, C., Dzhun, I., Volochaev, M., Gorshenkov, M., Babaytsev, G., Chechenin, N., Sokolov, A., Tretiakov, O.A. and Rodionova, V. Temperature-dependent magnetization reversal in exchange bias NiFe/IrMn/NiFe structures. *Journal of Magnetism and Magnetic Materials*, *482*, pp.370-375, 2019.

[172] Mao, M., Cerjan, C., Law, B., Grabner, F., Miloslavsky, L. and Chien, C. Enhanced spin-valve giant magneto-resistance in non-exchange biased sandwich films. *IEEE transactions on magnetics*, *36*(5), pp.2866-2868, 2000.

[173] Dieny, B., Speriosu, V.S., Metin, S., Parkin, S.S., Gurney, B.A., Baumgart, P. and Wilhoit, D.R., 1991. Magnetotransport properties of magnetically soft spin-valve structures. *Journal of Applied Physics*, *69*(8), pp.4774-4779, 1991.

[174] Thiyagarajah, N., Lin, L. and Bae, S. Effects of NiFe/Co insertion at the [Pd/Co] and Cu interface on the magnetic and GMR properties in perpendicularly magnetized [Pd/Co]/Cu/[Co/Pd] pseudo spin-valves. *IEEE transactions on magnetics*, *46*(4), pp.968-973, 2009.

[175] Tripathy, D., Adeyeye, A.O. and Shannigrahi, S. Effect of spacer layer thickness on the magnetic and magnetotransport properties of Fe 3 O 4⁄ Cu⁄ Ni 80 Fe 20 spin valve structures. *Physical Review B*, *75*(1), p.012403, 2007.

[176] Chaiken, A., Tritt, T.M., Gillespie, D.J., Krebs, J.J., Lubitz, P., Harford, M.Z. and Prinz, G.A., Temperature dependence of magnetoresistance in Fe-Cr-Fe sandwiches. *Journal of applied physics*, *69*(8), pp.4798-4800, 1991.

[177] Teixeira, J.M., Ventura, J.O., Fermento, R.P., Araujo, J.P., Sousa, J.B., Freitas, S.C. and Freitas, P.J. Interlayer coupling and

magnetoresistance of MnIr-based spin valves: Dependencies on deposition rate, spacer thickness, and temperature. *IEEE transactions on magnetics*, *43*(7), pp.3143-3145, 2007.

[178] Stobiecki, F., Stobiecki, T., Ocker, B., Maass, W., Powroznik, W., Paja, A., Loch, C. and Roll, K. Temperature Dependence of Magnetisation Reversal and GMR in Spin Valve Structures. *ACTA PHYSICA POLONICA SERIES A*, *97*(3), pp.523-526, 2000.

[179] Miller, B.H., Stojković, B.P. and Dahlberg, E.D. Universal relationship between giant magnetoresistance and anisotropic magnetoresistance in spin valve multilayers. *Physics Letters A*, *256*(4), pp.294-298, 1999.

[180] Lottis, D., Fert, A., Morel, R., Pereira, L.G., Jacquet, J.C., Galtier, P., Coutellier, J.M. and Valet, T. Magnetoresistance in rf-sputtered (NiFe/Cu/Co/Cu) spin-valve multilayers. *Journal of applied physics*, *73*(10), pp.5515-5517, 1993.

[181] Lohndorf, M., Duenas, T.A., Ludwig, A., Ruhrig, M., Wecker, J., Burgler, D., Grunberg, P. and Quandt, E. Strain sensors based on magnetostrictive GMR/TMR structures. *IEEE transactions on magnetics*, *38*(5), pp.2826-2828, 2002.

[182] Rijks, T.G., Coehoorn, R., De Jong, M.J.M. and De Jonge, W.J.M. Semiclassical calculations of the anisotropic magnetoresistance of NiFe-based thin films, wires, and multilayers. *Physical Review B*, *51*(1), p.283, 1995.

[183] Tsymbal, E.Y. and Pettifor, D.G. Perspectives of giant magnetoresistance. In *Solid state physics* (Vol. 56, pp. 113-237). Academic Press, 2001.

[184] Van Driel, J., De Boer, F.R., Lenssen, K.M. and Coehoorn, R. Exchange biasing by Ir 19 Mn 81: Dependence on temperature, microstructure and antiferromagnetic layer thickness. *Journal of Applied Physics*, *88*(2), pp.975-982, 2000.

[185] Stiles, M.D. and McMichael, R.D. Coercivity in exchange-bias bilayers. *Physical review B*, *63*(6), p.064405, 2001.

[186] Martí, X., Park, B.G., Wunderlich, J., Reichlová, H., Kurosaki, Y., Yamada, M., Yamamoto, H., Nishide, A., Hayakawa, J., Takahashi, H. and Jungwirth, T. Electrical measurement of antiferromagnetic moments in exchange-coupled IrMn/NiFe stacks. *Physical review letters*, *108*(1), p.017201, 2012.

[187] Howells, B. *Studies of spin-orbit coupling phenomena in magnetic semiconductors* (Doctoral dissertation, University of Nottingham), 2015.

[188] Dieny, B., Speriosu, V.S., Gurney, B.A., Parkin, S.S.P., Wilhoit, D.R., Roche, K.P., Metin, S., Peterson, D.T. and Nadimi, S. Spin-valve effect in soft ferromagnetic sandwiches. *Journal of Magnetism and Magnetic Materials*, *93*(2), pp.101-104, 1991.

[189] Kuczynski, G.C. Effect of elastic strain on the electrical resistance of metals. *Physical review*, *94*(1), p.61. 1954.

[190] B.F. Usher, D. Zhou, S.C. Goh, T. Warminski and X.P. Huang. Poisson's ratio of GaAs. *IEEE*, 290-293, 1999.

[191] Škoro, G.P., Bennett, J.R.J., Edgecock, T.R., Gray, S.A., McFarland, A.J., Booth, C.N., Rodgers, K.J. and Back, J.J. Dynamic Young's moduli of tungsten and tantalum at high temperature and stress. *Journal of Nuclear Materials*, *409*(1), pp.40-46,2011.

[192] Gibbs, M.R. ed. *Modern trends in magnetostriction study and application* (Vol. 5). Springer Science & Business Media, 2012.

[193] Freund, L.B. and Suresh, S. *Thin film materials: stress, defect formation and surface evolution*. Cambridge university press, 2004.

[194] Tkach, A., Kehlberger, A., Büttner, F., Jakob, G., Eisebitt, S. and Kläui, M. Electric field modification of magnetotransport in Ni thin films on (011) PMN-PT piezosubstrates. *Applied Physics Letters*, *106*(6), p.062404, 2015.

[195] Sablik, M.J. and Jiles, D.C. Coupled magnetoelastic theory of magnetic and magnetostrictive hysteresis. *IEEE transactions on magnetics*, *29*(4), pp.2113-2123, 1993

[196] Park, Y., Lee, E.J. and Kouh, T. Field-Dependent Resonant Behavior of Thin Nickel Film-Coated Microcantilever. *Micromachines*, *8*(4), p.109, 2017

[197] Berger, L. Magnetostriction in Nickel Alloys. *Physical Review*, *138*(4A), p.A1083. 1965.

[198] Birss, R.R. and Lee, E.W. The saturation magnetostriction constants of nickel within the temperature range-196 to 365 C. *Proceedings of the Physical Society*, *76*(4), p.502.1960.

[199] R. M. Bozorth. *Ferromagnetism*. Wiley-Blackwell, 1993.

[200] Hu, J.M. and Nan, C.W. Electric-field-induced magnetic easy-axis reorientation in ferromagnetic/ferroelectric layered heterostructures. *Physical Review B*, *80*(22), p.224416, 2009.

[201] R. Waser. *Nanoelectronic and information technology: advanced electronic material and novel devices*, Wiley-VCH, 2012.

[202] Ohtani, T., Kawai, T., Ohtake, M. and Futamoto, M. Magnetostriction of permalloy epitaxial and polycrystalline thin films. In *EPJ Web of Conferences* (Vol. 40, p. 11004). EDP Sciences, 2013.

[203] Savitha Pillai, S., Kojima, H., Itoh, M. and Taniyama, T. Lateral electric-field control of giant magnetoresistance in Co/Cu/Fe/BaTiO3 multiferroic heterostructure. *Applied Physics Letters*, *107*(7), p.072903, 2015.

[204] Wang, K.Y., Irvine, A.C., Wunderlich, J., Edmonds, K.W., Rushforth, A.W., Campion, R.P., Foxon, C.T., Williams, D.A. and Gallagher, B.L. Magnetic reversal under external field and current-driven domain wall motion in (Ga, Mn) As: influence of extrinsic pinning. *New Journal of Physics*, *10*(8), p.085007, 2008.

[205] Cavaco, C., Van Kampen, M., Lagae, L. and Borghs, G. A room-temperature electrical field–controlled magnetic memory cell. *Journal of materials research*, *22*(8), pp.2111-2115, 2007.

[206] Parkin, S.S. Systematic variation of the strength and oscillation period of indirect magnetic exchange coupling through the 3d, 4d, and 5d transition metals. *Physical Review Letters*, *67*(25), p.3598, 1991.

[207] Brüssing, F., Nowak, G., Schumann, A., Buschhorn, S., Zabel, H. and Theis-Bröhl, K. Magnetization reversal and magnetic interactions in patterned spin valve structures. *Journal of Physics D: Applied Physics*, *42*(16), p.165001, 2009.

[208] Wee, L., Stamps, R.L., Malkinski, L. and Celinski, Z., Rotatable anisotropy and mixed interfaces: Exchange bias in Fe/KNiF3. *Physical Review B*, *69*(13), p.134426, 2004.

[209] Celinski, Z., Urquhart, K.B. and Heinrich, B. Using ferromagnetic resonance to measure the magnetic moments of ultrathin films. *Journal of Magnetism and Magnetic Materials*, *166*(1-2), pp.6-26, 1997.

[210] Urban, R., Woltersdorf, G. and Heinrich, B. Gilbert damping in single and multilayer ultrathin films: Role of interfaces in non-local spin dynamics. *Physical review letters*, *87*(21), p.217204, 2001.

[211] Ben Youssef, J. and Layadi, A. Ferromagnetic resonance study of Permalloy/Cu/Co/NiO spin valve system. *Journal of Applied Physics*, *108*(5), p.053913, 2010.

[212] Parkes, D.E., Shelford, L.R., Wadley, P., Holý, V., Wang, M., Hindmarch, A.T., Van Der Laan, G., Campion, R.P., Edmonds, K.W., Cavill, S.A. and Rushforth, A.W. Magnetostrictive thin films for microwave spintronics. *Scientific reports*, *3*, p.2220, 2013.

[213] Kobayashi, K., Inaba, N., Fujita, N., Sudo, Y., Tanaka, T., Ohtake, M., Futamoto, M. and Kirino, F. Damping constants for permalloy single-crystal thin films. *IEEE transactions on magnetics*, *45*(6), pp.2541-2544, 2009.

[214] Behera, N., Kumar, A., Chaudhary, S. and Pandya, D.K. Two magnon scattering and anti-damping behavior in a two-dimensional epitaxial TiN/Py (t Py)/β-Ta (t Ta) system. *RSC advances*, *7*(14), pp.8106-8117, 2017.

[215] Heinrich, B., Tserkovnyak, Y., Woltersdorf, G., Brataas, A., Urban, R. and Bauer, G.E. Dynamic exchange coupling in magnetic bilayers. *Physical review letters*, *90*(18), p.187601, 2003.

[216] Tserkovnyak, Y., Brataas, A. and Bauer, G.E. Spin pumping and magnetization dynamics in metallic multilayers. *Physical Review B*, *66*(22), p.224403, 2002.

[217] Tokaç, M., Bunyaev, S.A., Kakazei, G.N., Schmool, D.S., Atkinson, D. and Hindmarch, A.T. Interfacial structure dependent spin mixing conductance in cobalt thin films. *Physical review letters*, *115*(5), p.056601, 2015.

[218] Lenz, K., Kosubek, E., Baberschke, K., Wende, H., Herfort, J., Schönherr, H.P. and Ploog, K.H. Magnetic properties of Fe 3 Si∕ Ga As (001) hybrid structures. *Physical Review B*, *72*(14), p.144411, 2005.

[219] Khomenko, E.V., Chechenin, N.G., Perov, N.S., Samsonova, V.V., Goĭkhman, A.Y. and Zenkevich, A.V. Magnetic anisotropy in IrMn/Co structures with an alternative sequence of deposition of antiferromagnetic and ferromagnetic layers. *Physics of the Solid State*, *52*(8), pp.1701-1708, 2010.

[220] Nosach, T., Mullady, G., Leifer, N., Adyam, V., Li, Q., Greenbaum, S. and Ren, Y. Angular dependence of spin-wave resonance and relaxation in half-metallic Sr 2 Fe Mo O 6 films. *Journal of Applied Physics*, *103*(7), p.07E311, 2008.

[221] Yuan, S.J., Sui, Y.X. and Zhou, S.M. Isotropic ferromagnetic resonance field shift in as-prepared permalloy/FeMn bilayers. *The European Physical Journal B-Condensed Matter and Complex Systems*, *44*(4), pp.557-562, 2005.

[222] Xi, H., Mountfield, K.R. and White, R.M. Ferromagnetic resonance studies of exchange biasing in Ni 81 Fe 19/Pt 10 Mn 90 bilayers. *Journal of Applied Physics*, *87*(9), pp.4367-4374, 2000.

[223] De Sihues, M.D., Durante-Rincón, C.A. and Fermin, J.R. A ferromagnetic resonance study of NiFe alloy thin films. *Journal of Magnetism and Magnetic Materials*, *316*(2), pp.e462-e465, 2007.

[224] Timopheev, A.A., Sobolev, N.A., Pogorelov, Y.G., Talalaevskij, A.V., Teixeira, J.M., Cardoso, S., Freitas, P.P. and Kakazei, G.N. Resonant and non-resonant microwave absorption as a probe of the magnetic

dynamics and switching in spin valves. *Journal of Applied Physics*, *114*(2), p.023906, 2013.

[225] Brandlmaier, A. *Electric-field control of magnetization in multifunctional hybrid devices* (Doctoral dissertation, Technische Universität München), 2011.

[226] Beaujour, J.M., Chen, W., Krycka, K., Kao, C.C., Sun, J.Z. and Kent, A.D. Ferromagnetic resonance study of sputtered Co| Ni multilayers. *The European Physical Journal B*, *59*(4), pp.475-483, 2007

[227] Mizukami, S., Ando, Y. and Miyazaki, T. The study on ferromagnetic resonance linewidth for NM/80NiFe/NM (NM= Cu, Ta, Pd and Pt) films. *Japanese journal of applied physics*, *40*(2R), p.580, 2001.

[228] Zakeri, K., Lindner, J., Barsukov, I., Meckenstock, R., Farle, M., Von Hörsten, U., Wende, H., Keune, W., Rocker, J., Kalarickal, S.S. and Lenz, K. Spin dynamics in ferromagnets: Gilbert damping and two-magnon scattering. *Physical Review B*, *76*(10), p.104416, 2007.

[229] Kurebayashi, H., Skinner, T.D., Khazen, K., Olejník, K., Fang, D., Ciccarelli, C., Campion, R.P., Gallagher, B.L., Fleet, L., Hirohata, A. and Ferguson, A.J. Uniaxial anisotropy of two-magnon scattering in an ultrathin epitaxial Fe layer on GaAs. *Applied Physics Letters*, *102*(6), p.062415, 2013.

[230] Dutoit, C.E., Dolocan, V.O., Kuzmin, M., Michez, L., Petit, M., Le Thanh, V., Pigeau, B. and Bertaina, S. Ferromagnetic resonance and magnetic damping in C-doped Mn5Ge3. *Journal of Physics D: Applied Physics*, *49*(4), p.045001, 2015.

[231] Li, Y., Liu, Q., Xie, Z.K., Vetter, E., Yuan, Z., He, W., Liu, H.L., Sun, D.L., Xia, K., Yu, W. and Sun, Y.B. Isotropic non-local Gilbert damping driven by spin pumping in epitaxial Pd/Fe films on MgO (001) substrates. *New Journal of Physics*, *21*(10), p.103040, 2019.

[232] Peria, W.K., Peterson, T.A., McFadden, A.P., Qu, T., Liu, C., Palmstrøm, C.J. and Crowell, P.A. The interplay of large two-magnon ferromagnetic resonance linewidths and low Gilbert damping in Heusler thin films. *arXiv preprint arXiv:1909.02738*, 2019.

[233] Rodríguez-Suárez, R.L., Vilela-Leão, L.H., Bueno, T., Oliveira, A.B., De Almeida, J.R.L., Landeros, P., Rezende, S.M. and Azevedo, A. Critical thickness investigation of magnetic properties in exchange-coupled bilayers. *Physical Review B*, *83*(22), p.224418, 2011.

[234] Dubowik, J., Załęski, K., Głowiński, H. and Gościańska, I. Angular dependence of ferromagnetic resonance linewidth in thin films. *Physical Review B*, *84*(18), p.184438, 2011.

[235] Kim, J.V. and Chappert, C. Magnetization dynamics in spin-valve structures with spin pumping. *Journal of magnetism and magnetic materials*, *286*, pp.56-60, 2005.

[236] Chiba, T., Bauer, G.E. and Takahashi, S. Magnetization damping in noncollinear spin valves with antiferromagnetic interlayer couplings. *Physical Review B*, *92*(5), p.054407, 2015.

[237] Mosendz, O., Pearson, J.E., Fradin, F.Y., Bader, S.D. and Hoffmann, A. Suppression of spin-pumping by a MgO tunnel-barrier. *Applied Physics Letters*, *96*(2), p.022502, 2010.